

Technical University of Cluj-Napoca, Romania

HABILITATION THESIS

Wavelets on Two-Dimensional Manifolds

author

Daniela Roşca

2012

Contents

Introduction	iii
1 Wavelets on domains of \mathbb{R}^2	1
1.1 Piecewise constant wavelet bases obtained by 1-3 splitting	1
1.1.1 Triangulations, 1-3 refinement and wavelets	1
1.1.2 Decomposition, compression, reconstruction	3
1.1.3 The compression error	5
1.1.4 A comparison of wavelets	6
1.2 Piecewise constant wavelet bases obtained by 1-4 splitting	8
1.2.1 Wavelet coefficients and wavelet decomposition matrices	8
1.2.2 Quaternions and orthogonal matrices	10
1.2.3 Optimal wavelet bases	12
1.3 Piecewise constant wavelet bases obtained by arbitrary splitting	14
1.3.1 Orthonormal wavelet bases	15
1.3.2 Construction of orthogonal matrices of arbitrary dimension	17
1.4 Sparse image representation using Easy Path Wavelet Transform	20
1.4.1 Notations and description of the EPWT	21
1.4.2 A hybrid-model for image approximation	24
2 Area preserving projections and uniform grids	41
2.1 Area preserving projection from square to disc	41
2.1.1 Calculation of the projection	41
2.1.2 Application 1: UR spherical grids	44
2.1.3 Application 2: geographic maps of a hemisphere	47
2.2 Area preserving projection from rectangle to ellipse	48
2.2.1 First method of construction	49
2.2.2 Second method for constructing the projection	50
2.3 Area preserving projection from cube to sphere	52
2.3.1 Mapping a square onto a curved square	53
2.3.2 The inverse map	57
2.3.3 Mapping the curved squares onto the sphere	59
2.4 Area preserving projection from surfaces of revolution	60
2.4.1 The general case	61
2.4.2 Projection from the paraboloid $a^2z = x^2 + y^2$ onto XOY	63
2.4.3 Projection from the hyperboloid $z = \sqrt{1 + (x^2 + y^2)/a^2}$ onto XOY	64
2.4.4 Projection from the conical surface $z = \sqrt{(x^2 + y^2)/a^2}$	65
2.4.5 Combining two area preserving projections	66

3	Cubature formulas on the sphere	69
3.1	Cubature formulas with fundamental systems of points	69
3.1.1	The matrix Φ_n	71
3.1.2	The matrix D_1^{-1}	74
3.1.3	The weights of the cubature formula	77
3.1.4	Cubature formulas with positive weights	79
3.1.5	Spherical designs	81
3.1.6	The degree of exactness of the positive cubature formula	83
3.2	Cubature formulas with equally spaced nodes on latitudinal circles	87
3.2.1	Spherical quadrature	87
3.2.2	Maximal degree of exactness which can be attained with equally spaced nodes at $n + 1$ latitudes	89
3.2.3	Spherical designs	92
3.2.4	Numerical examples	95
4	Wavelets on the unit sphere of \mathbb{R}^3	103
4.1	Wavelet bases on the sphere obtained by radial projection	103
4.1.1	An inner product in $L^2(\mathbb{S}^2)$	104
4.1.2	Continuous rational spline wavelets on spherical triangulations	105
4.1.3	Piecewise constant wavelets on spherical triangulations	107
4.1.4	From wavelets on an interval to wavelets on the sphere	109
4.2	Another weighted inner product and equivalent norms	116
4.3	Wavelets on sphere-like surfaces	120
4.3.1	Inner products and norms in $L^2(\mathcal{S})$	120
4.3.2	Orthogonality and Riesz stability	122
4.3.3	Some closed surfaces which assure the Riesz stability in $L^2(\mathcal{S})$	123
4.4	Locally supported wavelet bases on the sphere via stereographic projection	123
4.4.1	Preliminaries	125
4.4.2	Multiresolution analysis (MRA) and wavelet bases of $L^2(\mathbb{S}^2)$	126
4.4.3	Further comments	128
4.4.4	Examples	128
4.5	EPWT on triangulations of the sphere	132
4.5.1	Definitions and notations for the EPWT	133
4.5.2	Adaptive Haar wavelet bases on the sphere	136
4.5.3	Implementation issues	138
4.5.4	Numerical experiments	140
5	Wavelets on manifolds	143
5.1	Wavelet analysis on manifolds via projections onto a plane	144
5.1.1	Geometry of projections	144
5.1.2	Constructing a global CWT on the manifold \mathcal{M}	148
5.1.3	CWT on a general manifold: Local wavelet transform	149
5.1.4	Generalizations	152
5.1.5	Lifting the DWT onto \mathcal{M}	153
5.2	Wavelet analysis on some surfaces of revolution via area preserving projection	153
5.2.1	Multiresolution analysis of $L^2(\mathcal{M})$	153
5.2.2	Continuous wavelet transform on \mathcal{M}	156
5.2.3	Wavelets by combining two area preserving projections	159

Introduction

This habilitation thesis is the sum of 28 papers and contains the results obtained since 2004, after I obtained the PhD degree with the thesis *Approximation with Wavelets*. These results concern the 2D approximation and they focus on the following directions:

1. Wavelets on domains of \mathbb{R}^2

Whereas constructing wavelet bases via a multiresolution analysis on the whole plane \mathbb{R}^2 is easy with the tensor product method, the same problem on bounded domains is notoriously hard, because of the boundary conditions to be satisfied. And, indeed, few solutions are known in the literature. A method consists in dividing a domain in several smaller domains, but only limited results have been obtained. Along this line, our contribution consists in:

- *Construction of piecewise constant wavelet bases with 1-3 splitting (Section 1.1)*

We construct piecewise constant wavelet bases on planar domains, the refinement process consisting in dividing each subdomain (usually a triangle) in three subdomains having the same area. We showed the efficiency of our construction in compression and detection of singularities, by performing numerical experiments.

- *Construction of piecewise constant wavelet bases with 1-4 splitting (Section 1.2)*

We give the most general expression of orthonormal piecewise constant wavelet bases, in the case when the refinement process consists in dividing a domain into four subdomains having the same area. The construction of piecewise constant wavelets based on this technique is the subject of many papers [59, 68, 93, 99, 130], but all of them take only particular cases of wavelets. On the contrary, in **Section 1.2** we obtain *all* the possible orthonormal wavelet bases with 1-4 refinement.

- *Construction of piecewise constant wavelet bases with arbitrary splitting (Section 1.3)*

A natural question that arises is whether one can generalize the previous constructions to 1- n splitting. In [60], the authors construct directional Haar frames on triangles, starting from the classical tensor product Haar wavelets, using a 1-8 subdivision. We also mention [41], where the authors consider a triangular lattice with symmetry 6 and define on that lattice a so-called *intertwining multiresolution analysis*, a concept introduced by the same authors in [42]. By contrast, our construction applies to an arbitrary 1- n subdivision.

We give a method for constructing certain orthogonal matrices of arbitrary dimension, yielding piecewise constant orthonormal wavelet bases. In this case, the orthogonality of the wavelet bases reduces to the orthogonality of an $n \times n$ matrix with $1/\sqrt{n}$ on the first row and in **Section 1.3.2** we describe a method for generating orthogonal matrices of this type, of arbitrary dimension n .

- *A hybrid method for image approximation*

We combine some local smoothing filters (which separate the smooth part of the image) with the adaptive (EPWT) Easy Path Wavelet Transform (applied to the noisy part of the image, containing edges and textures). We have performed numerical tests and we compared our method with the curvelet transform and with some classical biorthogonal tensor product wavelets.

2. Approximation of spherical data

An important part of our research performed during the last ten years was dedicated to the approximation of data on the two-dimensional sphere \mathbb{S}^2 of \mathbb{R}^3 , a topic of the so-called Mathematical Geosciences or more generally, in Earth and Space Sciences. Many situations yield data on *spherical* surfaces (for instance in geography, geodesy, meteorology, astronomy, cosmology, etc.), in crystallography (texture analysis of crystals), in medicine (some organs are regarded as sphere-like surfaces), or in computer graphics (modelling of closed surfaces as the graph of a function defined on the sphere). Thus one needs suitable techniques for analyzing such data.

Our contributions in this field include:

- *Construction of spherical cubature formulas (Chapter 3)*

Some existing results include cubature formulas for special nodes [49, 57, 77, 78, 120] and integration on spherical triangulations [11]. The goal of our research was the construction of cubature formulas with positive nodes with high degree of exactness (i.e. which are exact for spherical polynomials up to a certain degree). The results are published in [90, 100, 104].

- *Construction of area preserving projections and uniform and refinable grids on the sphere (Sections 2.1.2, 2.1.3 and 2.3)*

In many applications one requires simple, uniform and refinable grids on the sphere. One simple method to construct such grids is to transfer existing planar grids. The standard manipulation of spherical data includes convolutions with local and global kernels, Fourier analysis with spherical harmonics, wavelet analysis, nearest neighbour search, etc. Some of these manipulations become very slow if the sampling of functions on the sphere and the related discrete data set are not well designed. Thus, the discrete data should have the following properties: (a) hierarchical tree structure (allowing construction of a multiresolution analysis); (b) equal area for the discrete elements of the partition of the sphere; (c) isolatitudinal distribution for the discrete area elements (essential for fast computations involving spherical harmonics).

Most grid constructions given so far do not provide an equal area partition. But this property is crucial for a series of applications including statistical computations and wavelet constructions, since non-equal area partitions can generate severe distortions at large distances. The existence of partitions of the sphere into regions of equal area and small diameter has been already used by Alexander [1], who derives lower bounds for the maximum sum of distances between points on the sphere. Based on the construction by Zhou [134], Leopardi derives a recursive zonal equal area sphere partitioning algorithm for the unit sphere \mathbb{S}^d embedded in \mathbb{R}^{n+1} , see [66]. The partition constructed in [66] for \mathbb{S}^2 consists of polar cups and rectilinear regions that are arranged in zonal collars. Besides the problem that we have to deal with different kinds of areas, the obtained partition is

not suitable for various applications where one needs to avoid that vertices of spherical rectangles lie on edges of neighboring rectangles.

There are plenty of spherical grids and sampling points, many of them mentioned in [48]. A complete description of all known spherical projections used in cartography is realized in [50, 121]. Until the construction of the HEALPix grid [48], no grid satisfied simultaneous the requirements (a), (b), (c). Besides the HEALPix grid, other constructions for equal area partitions of \mathbb{S}^2 used in astronomy include the icosahedron-based method by Tegmark [128], see also [129]. In [122], an equal area global partition method based upon circle edges is presented. Starting with a spherical triangulation, obtained e.g. by projecting the faces of an icosahedron to the sphere, a subdivision method is proposed to partition each spherical triangle into four equal area subtriangles.

In **Section 2.1.2** we give a method for constructing uniform grids and sampling points on the sphere, satisfying these requirements simultaneously. The idea is to use a projection (constructed in Section 2.1.1), which preserves areas and maps squares into discs. Thus, *any* uniform grid of the square can be mapped bijectively onto a uniform grid on the disc, and then onto a uniform grid on the sphere, via Lambert's azimuthal equal area projection. Compared to the projections used for HEALPix grids and to the planar domains mapped there, our method has the nice property that, besides the uniform grids and sampling points on the sphere, one can transport *any* function from the square to the sphere by the technique used in [105]. In addition, if we have a set of real functions defined on the square, the corresponding spherical functions preserve the following properties: orthonormal basis, Riesz basis, frame, and local support.

In **Section 2.1.3** we show how the same projection introduced in Section 2.1.1 can be useful for the construction of new geographical maps of a hemisphere of the Earth.

Another idea of construction of an area preserving map, this time from the cube to the sphere, is presented in **Section 2.3**. Thus, other *new* uniform and refinable grids on the sphere may be constructed by transporting grids from the cube.

- *Constructions of wavelets on the sphere (Chapter 4)*

In the spherical case, the Fourier transform amounts to an expansion in spherical harmonics, whose support is the whole sphere. Fourier analysis on the sphere is thus global and cumbersome. Therefore many different methods have been proposed to replace it with some sort of wavelet analysis. Several approaches have been used in the literature for designing spherical wavelets. The first and oldest one is by transferring constructions from $[0, \pi] \times [0, 2\pi]$ via spherical coordinates (see for example [31, 88, 131]). The disadvantages of these wavelets are the existence of distortions and singularities around the poles and the fact that they are not locally supported. Another approach uses spherical harmonics or kernels of spherical harmonics [45, 79]. A drawback is that the spherical harmonics are globally supported and suffer from the same difficulties as Fourier transform, such as ringing. Locally supported wavelets using spherical harmonics were constructed later in [44], but their implementation seems not to be so easy. Wavelets on spherical triangulations were constructed in [17, 81, 118], but no stability of wavelets was proved.

Continuous wavelet transforms on the sphere were constructed in [2, 3, 32, 54]. In practice one needs to discretize the continuous wavelet transform. For the construction in [2, 3], a discretization leading to spherical wavelet frames was realized in [13], but up to now no discretization leading to *bases* of wavelets is known. Distortions around one pole occur also in these constructions as soon as one starts to discretize.

As we have mentioned before, a drawback of the existing constructions is the occurrence of distortions around the poles. With the aim of avoiding these distortions and, at the same time using the existing constructions in one and two dimensions, we introduce a new approach (**Section 4.1**): the planar wavelet bases are first transferred to the faces of a certain polyhedron, and then to \mathbb{S}^2 by a radial projection. We also introduce some inner products associated to the polyhedron (**Section 4.1.1** and **4.2**), but for some particular polyhedrons (like the cube) this inner product is not needed any more if instead of the radial projection we use the area preserving projections constructed in Chapter 2. The new idea allowed us to construct new wavelet bases on the sphere, whose advantages were listed at the beginning of Section 4.1 (page 103). The method can be easily extended to sphere-like surfaces (**Section 4.3**).

The lack of smoothness and vanishing moments of the wavelets presented in Section 4.1 can be repaired if we consider the stereographic projection instead the radial one (**Section 4.4**), but the price we must pay in this case is the apparition of severe distortions around a pole. However, we show that this method can be useful for manipulation of data situated on a portion of the sphere.

Finally, in **Section 4.5** we exploit the idea of the planar Easy Path Wavelet Transform and by transferring it to spherical triangulations we obtain adaptive piecewise constant wavelet bases on the sphere.

3. Wavelets on manifolds

Some data may live on more complicated manifolds, such as a *two-sheeted hyperboloid*, in cosmology for instance, or a *paraboloid*. In optics also, data on such manifolds are essential for the treatment of omnidirectional images via the catadioptric procedure, for instance in robotic vision. This last topic is particularly relevant for engineering purposes, due to the many applications in navigation, surveillance, visualization. In the catadioptric image processing, a sensor overlooks a mirror, whose shape may be spherical, hyperbolic or parabolic. However, instead of projecting the data from that mirror onto a plane, an interesting alternative consists in processing them directly on the mirror, and thus wavelets on such manifolds are needed [16]. Among the three shapes, the parabolic one is the most common (think of the headlights of a car). It has been shown in [47] that the reconstruction of the orthographic (i.e., vertical) projection from a parabolic mirror can be computed as the inverse stereographic projection from the image plane onto the unit sphere.

In [8] we have explored this method systematically. In particular, for the manifolds mentioned above, we have described the vertical and the stereographic projections. While these projections have nice properties, they suffer from one major drawback, namely, they do not preserve areas. As a consequence, lifting the DWT via the inverse projections results in severe distortions at large distances (e.g. close to the North Pole in the case of the sphere).

Our contributions consist in:

- *A review of the existing results, published in [8], in a special volume in the honor of Jean Morlet*

In **Section 5.1.1**, we describe several types of projections from the manifold \mathcal{M} on a plane, namely stereographic, vertical, conical, radial. Then, in **Section 5.1.2**, we describe the construction of a *global* CWT on \mathcal{M} . We point the fact that the existing constructions of CWT have not been discretized yet, and therefore no DWT is known. In addition, in

all the existing methods, the measure is not dilation invariant and the projection does not preserve areas, which forces one to introduce correction factors.

- *Construction of an area preserving projection from a surface of revolution \mathcal{M} onto the plane perpendicular to the rotation axis (Section 2.4)*

The method applies to all 2D surfaces of revolution obtained by rotating a piecewise smooth plane curve around a line in its plane, such that one end point of the curve is the only point of intersection with the line and each plane perpendicular to the line intersects the curve at most once.

- *Construction of a multiresolution analysis and a continuous wavelet transform, starting from the existing planar constructions (Section 5.2)*

We use the projection introduced in Section 2.4, which induces a unitary map between $L^2(\mathcal{M})$ and $L^2(\mathbb{R}^2)$. Inverting the latter, we can then lift all operations from the plane to \mathcal{M} , in particular, producing unitary operators on $L^2(\mathcal{M})$ that implement translations, rotations and dilations in the plane. In this way, the representation of the similitude group of the plane, that underlines the 2D plane CWT, is lifted to \mathcal{M} as well. Thus we have all the necessary ingredients for constructing a multiresolution analysis and a DWT on \mathcal{M} (Section 5.2.1), and a CWT (Section 5.2.2) that does not show distortions, due to the area preserving property.

The wavelets on \mathcal{M} inherit all the properties of the corresponding planar wavelets. In fact, all calculations are performed in the plane, not on \mathcal{M} , and makes the method both simpler and more efficient. Finally we note that the definition of the continuous Fourier transform on \mathcal{M} given in formula (5.21) can be used for defining a much simpler discrete Fourier transform than the one in [27].

Chapter 1

Wavelets on domains of \mathbb{R}^2

1.1 Piecewise constant wavelet bases obtained by 1-3 splitting

We construct piecewise constant wavelets on a bounded planar triangulation, the refinement process consisting in dividing each triangle into three triangles having the same area. Thus, the wavelets depend on two parameters linked by a certain relation. We perform a compression and try to compare different norms of the compression error, when one wavelet coefficient is canceled.

The results of this section were published in [101], where the construction was also extended to spherical triangulations.

1.1.1 Triangulations, 1-3 refinement and wavelets

Let $\mathcal{T} = \{T_1, \dots, T_n\}$ be a triangulation in \mathbb{R}^2 and let Γ be the planar region covered by $\bigcup_{i=1}^n T_i$. Given $\mathcal{T} = \mathcal{T}^0$ we wish to consider a refinement \mathcal{T}^1 of \mathcal{T}^0 such that every triangle in \mathcal{T}^0 is the union of triangles in \mathcal{T}^1 . In this section the refinement consists in splitting each triangle into three triangles having the same area.

In the following we describe some possibilities to realize this splitting. Let $A_1A_2A_3$ be an arbitrary triangle. One possibility is to take the weight center G and to consider the triangles A_1A_2G , A_2A_3G and A_3A_1G . However, the drawback is that after some steps the refined triangles become long and thin. Another more convenient possibility is to take $M \in A_2A_3$ such that $A_2M = \frac{1}{3}A_2A_3$ and $N \in A_1A_3$ such that $A_1N = NA_3$, obtaining the refined triangles A_1A_2M , A_1MN , NMA_3 . Another choice of the point N could be as the mid point of the edge MA_3 or of the edge A_1M . Figure 1.1 shows some possible 1-3 splitting.

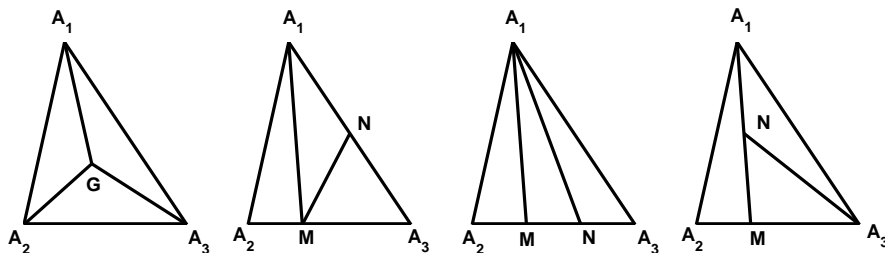


Figure 1.1: Examples of 1-3 splitting.

For a given triangle T , let \mathcal{R}_T denote the set of the three refined triangles in Γ , constructed

by a refinement process described above. The set $\mathcal{T}^1 = \bigcup_{T \in \mathcal{T}^0} \mathcal{R}_T$ is a triangulation and a refinement of \mathcal{T}^0 . Continuing the refinement process in the same manner, we obtain a triangulation \mathcal{T}^j of Γ , for $j \in \mathbb{N}$.

Let $\langle \cdot, \cdot \rangle_*$ be the following inner product, based on the initial coarsest triangulation \mathcal{T}^0

$$\langle f, g \rangle_* = \sum_{T \in \mathcal{T}^0} \frac{1}{\mathcal{A}(T)} \int_T f(\mathbf{x})g(\mathbf{x}) dx, \quad \text{for } f, g \in L^2(\Gamma). \quad (1.1)$$

Here $\mathcal{A}(T)$ denotes the area of the triangle T . Also we consider the induced norm

$$\| \cdot \|_* = \langle \cdot, \cdot \rangle_*^{1/2}, \quad (1.2)$$

which is equivalent with the usual L^2 -norm since

$$\frac{1}{\max_{T \in \mathcal{T}^0} \mathcal{A}(T)} \|f\|_2^2 \leq \langle f, f \rangle_* \leq \frac{1}{\min_{T \in \mathcal{T}^0} \mathcal{A}(T)} \|f\|_2^2,$$

for all $f \in L^2(\Gamma)$. This weighted norm is taken in computer graphics [71, 126] as it can reduce computational costs.

In the following we construct a wavelet basis which is orthogonal with respect to the inner product (1.1). Due to the above mentioned norm equivalence, this wavelet basis will be a Riesz basis of $L^2(\Gamma)$. For a fixed $j \in \mathbb{N}$, to each triangle $T_k^j \in \mathcal{T}^j$, $k \in \mathcal{N}_j^n := \{1, 2, \dots, n \cdot 3^j\}$, we associate the function $\varphi_{T_k^j} : \Gamma \rightarrow \mathbb{R}$,

$$\varphi_{T_k^j} = \begin{cases} 1, & \text{inside the triangle } T_k^j, \\ 0, & \text{elsewhere.} \end{cases}$$

Then we define the spaces of functions $V^j = \text{span}\{\varphi_{T_k^j}, k \in \mathcal{N}_j^n\}$, of dimension $n \cdot 3^j$, consisting of piecewise constant functions on the triangles of \mathcal{T}^j . Let $T^j \in \mathcal{T}^j$ and T_k^{j+1} , $k = 1, 2, 3$, the refined triangles obtained from T^j . The equalities

$$\varphi_{T^j} = \varphi_{T_1^{j+1}} + \varphi_{T_2^{j+1}} + \varphi_{T_3^{j+1}},$$

which hold in $L^2(\Gamma)$, implies the inclusions $V^j \subseteq V^{j+1}$, for all $j \in \mathbb{N}$. With respect to the inner product (1.1), the spaces V^j become Hilbert spaces, with the corresponding norm (1.2). Let W^j denote the orthogonal complement, with respect to $\langle \cdot, \cdot \rangle_*$, of the coarse space V^j in the fine space V^{j+1} , so that

$$V^{j+1} = V^j \oplus W^j.$$

The dimension of W^j is thus $\dim W^j = 2n \cdot 3^j$. The spaces W^j are called the *wavelet spaces*. In the following we construct an orthonormal basis of W^j . To each triangle T^j , two wavelets supported on T^j will be associated in the following way:

$$\begin{aligned} \psi_{T^j}^1 &= \alpha_1 \varphi_{T_1^{j+1}} + \alpha_2 \varphi_{T_2^{j+1}} + \alpha_3 \varphi_{T_3^{j+1}}, \\ \psi_{T^j}^2 &= \beta_1 \varphi_{T_1^{j+1}} + \beta_2 \varphi_{T_2^{j+1}} + \beta_3 \varphi_{T_3^{j+1}}, \end{aligned}$$

with $\alpha_i, \beta_i \in \mathbb{R}$, $i = 1, 2, 3$. Next we will find conditions on the coefficients α_i, β_i which assure that the set $\{\psi_{T^j}^l, l = 1, 2, T^j \in \mathcal{T}^j\}$ is an orthonormal basis of W^j with respect to the inner product (1.1). First we must have

$$\langle \psi_{T^j}^l, \varphi_{S^j} \rangle_* = 0, \quad \text{for } l = 1, 2 \text{ and } T^j, S^j \in \mathcal{T}^j. \quad (1.3)$$

If $T^j \neq S^j$, then the equality is immediate since $\text{supp } \psi_{T^j}^l = \text{supp } \varphi_{T^j}$ and $\text{supp } \varphi_{T^j} \cap \text{supp } \varphi_{S^j}$ is either empty or an edge, whose measure is zero. If $T^j = S^j$, evaluating the inner product (1.3) we obtain

$$\langle \psi_{T^j}^1, \varphi_{S^j} \rangle_* = \frac{\alpha_1 \mathcal{A}(T_1^{j+1}) + \alpha_2 \mathcal{A}(T_2^{j+1}) + \alpha_3 \mathcal{A}(T_3^{j+1})}{\mathcal{A}(T)},$$

T being the triangle of the initial triangulation \mathcal{T}^0 containing the triangle T^j . Since

$$\frac{\mathcal{A}(T_k^{j+1})}{\mathcal{A}(T)} = \frac{1}{3^{j+1}} \text{ for } k = 1, 2, 3,$$

the orthogonality conditions (1.3) reduce to $\alpha_1 + \alpha_2 + \alpha_3 = 0$ and $\beta_1 + \beta_2 + \beta_3 = 0$. Then, some simple calculations show that each of the orthogonality conditions

$$\langle \psi_{T^j}^1, \psi_{T^j}^2 \rangle_* = 0, \text{ for all } T^j \in \mathcal{T}^j,$$

is equivalent to $\alpha_1 \beta_1 + \alpha_2 \beta_2 + \alpha_3 \beta_3 = 0$. If we wish orthonormal bases, we have to impose that

$$\|s^{-j-1} \psi_{T^j}^l\|_* = 1, \text{ for } l = 1, 2, s = 1/\sqrt{3},$$

implying $\alpha_1^2 + \alpha_2^2 + \alpha_3^2 = 1$ and $\beta_1^2 + \beta_2^2 + \beta_3^2 = 1$, respectively.

Gathering all the above condition, we obtain the system

$$\begin{aligned} \alpha_1 + \alpha_2 + \alpha_3 &= 0, \\ \beta_1 + \beta_2 + \beta_3 &= 0, \\ \alpha_1 \beta_1 + \alpha_2 \beta_2 + \alpha_3 \beta_3 &= 0, \\ \alpha_1^2 + \alpha_2^2 + \alpha_3^2 &= 1, \\ \beta_1^2 + \beta_2^2 + \beta_3^2 &= 1, \end{aligned}$$

which has the solution

$$(\alpha_1, \alpha_2, \alpha_3, \beta_1, \beta_2, \beta_3) = \left(\alpha_1, \alpha_2, -(\alpha_1 + \alpha_2), \frac{\varepsilon}{\sqrt{3}}(\alpha_1 + 2\alpha_2), -\frac{\varepsilon}{\sqrt{3}}(2\alpha_1 + \alpha_2), \frac{\varepsilon}{\sqrt{3}}(\alpha_1 - \alpha_2) \right),$$

with $\varepsilon \in \{-1, 1\}$ and α_1, α_2 such that $\alpha_1^2 + \alpha_1 \alpha_2 + \alpha_2^2 = 1/2$. Without losing the generality, we can suppose that $\varepsilon = 1$, so finally we have the wavelets

$$\psi_{T^j}^1 = \alpha_1 \varphi_{T_1^{j+1}} + \alpha_2 \varphi_{T_2^{j+1}} - (\alpha_1 + \alpha_2) \varphi_{T_3^{j+1}}, \quad (1.4)$$

$$\psi_{T^j}^2 = s(\alpha_1 + 2\alpha_2) \varphi_{T_1^{j+1}} - s(2\alpha_1 + \alpha_2) \varphi_{T_2^{j+1}} + s(\alpha_1 - \alpha_2) \varphi_{T_3^{j+1}}, \quad (1.5)$$

with $s = 1/\sqrt{3}$ and α_1, α_2 such that $\alpha_1^2 + \alpha_1 \alpha_2 + \alpha_2^2 = 1/2$.

1.1.2 Decomposition, compression, reconstruction

Since we have an infinite number of wavelets, the goal now is to choose if possible, the best ones. We will focus in the following on the compression error. The idea of compression is to decompose a sequence of data f with respect to the wavelet basis, to cancel some wavelet coefficients which are small and then to reconstruct the data using the remaining coefficients. The result is a compressed sequence of data \hat{f} . We are interested in studying the error $f - \hat{f}$. Let $i \in \mathbb{N}^*$ be a given level. For our case, we suppose that the sequence $(f_k^i)_{k=1, \dots, n \cdot 3^i}$ is given

and it represents the values of the function φ^i , which is piecewise constant on the triangles at the level i ,

$$\varphi^i = \sum_{T^i \in \mathcal{T}^i} f_k^i \cdot \varphi_{T^i}.$$

Decomposition. Given the column vector $f^i = (f_k^i)_{k \in \mathcal{N}_i^n}$, we calculate the column vectors $w^{i-1}, w^{i-2}, \dots, w^0, f^0$ in the following way.

$$\begin{pmatrix} f^{j-1} \\ w^{j-1} \end{pmatrix} = D_j^T \cdot f^j, \quad (1.6)$$

for $j = i, i-1, \dots, 1$. Here f^{j-1} and w^{j-1} are column vectors which have the dimension $n \cdot 3^{j-1}$ and $2n \cdot 3^{j-1}$ respectively, and D_j is the block matrix

$$D_j = \left(P_j \mid Q_j \right) = \left(\text{diag } u \mid \text{diag } m \right), \text{ with}$$

$$u = \begin{pmatrix} s \\ s \\ s \end{pmatrix}, \quad m = \begin{pmatrix} \alpha_1 & s(\alpha_1 + 2\alpha_2) \\ \alpha_2 & -s(2\alpha_1 + \alpha_2) \\ -(\alpha_1 + \alpha_2) & s(\alpha_1 - \alpha_2) \end{pmatrix}.$$

The dimensions of the matrices P_j and Q_j are $n \cdot 3^j \times n \cdot 3^{j-1}$ and $n \cdot 3^j \times 2n \cdot 3^{j-1}$, respectively. Due to the orthogonality properties of our wavelets, the matrix D_j is orthogonal, meaning that $D_j \cdot D_j^T = D_j^T \cdot D_j = I_{n \cdot 3^j}$.

The components of the vectors $w^{i-1}, w^{i-2}, \dots, w^0$ are called the *wavelet coefficients* at the levels $i-1, i-2, \dots, 0$.

Compression. A common procedure is to cancel the smallest r ($r \in \mathbb{N}$ given number) wavelet coefficients. The result is contained in the vectors $\widehat{w}^{i-1}, \widehat{w}^{i-2}, \dots, \widehat{w}^0$, having the components

$$\widehat{w}_k^j = \begin{cases} 0, & \text{if } w_k^j \text{ is among the smallest } r \text{ coefficients,} \\ w_k^j, & \text{otherwise,} \end{cases}$$

$j = 0, \dots, i-1$, $k \in \mathcal{M}_j^n = \{1, \dots, 2n \cdot 3^{j-1}\}$.

Another procedure, called *hard thresholding*, is to cancel all the wavelet coefficients situated below a fixed number *thr*, called threshold:

$$\widehat{w}_k^j = \begin{cases} 0, & \text{if } |w_k^j| < thr, \\ w_k^j, & \text{otherwise.} \end{cases}$$

Reconstruction. With the help of the compressed wavelet coefficients in \widehat{w}^j , $j = 0, 1, \dots, i-1$, we can obtain an approximated version \widehat{f}^i of the initial vector f^i as follows:

$$\widehat{f}^j = D_j \cdot \begin{pmatrix} \widehat{f}^{j-1} \\ \widehat{w}^{j-1} \end{pmatrix}, \quad (1.7)$$

for $j = 1, 2, \dots, i$ and with the notation $\widehat{f}^0 = f^0$.

1.1.3 The compression error

The compression error can be measured by a norm of the vector $f^i - \widehat{f}^i$. In the following we consider the norms $\|\cdot\|_2$, $\|\cdot\|_\infty$ and $\|\cdot\|_1$ defined by

$$\begin{aligned}\|f^i - \widehat{f}^i\|_2 &= \left(\sum_{k \in \mathcal{N}_i^n} (f_k^i - \widehat{f}_k^i)^2 \right)^{1/2}, \\ \|f^i - \widehat{f}^i\|_\infty &= \max \left\{ |f_k^i - \widehat{f}_k^i|, k \in \mathcal{N}_i^n \right\}, \\ \|f^i - \widehat{f}^i\|_1 &= \sum_{k \in \mathcal{N}_i^n} |f_k^i - \widehat{f}_k^i|,\end{aligned}$$

and try to find out for which (α_1, α_2) (which of the wavelets) these norms are minimal, in the case when \widehat{f}^i is obtained from f^i by canceling one fixed wavelet coefficient $w_{k_0}^{i_0}$.

For all $j \in \{i, i-1, \dots, 1\}$, in the vector f^j having $n \cdot 3^j$ components, we make groups of three components and denote them by $\mathbf{f}_1^j, \mathbf{f}_2^j, \dots, \mathbf{f}_{n \cdot 3^{j-1}}^j$. More precisely, \mathbf{f}_k^j will be the vector

$$\mathbf{f}_k^j = \left(f_{3k-2}^j \quad f_{3k-1}^j \quad f_{3k}^j \right)^T, \quad k \in \mathcal{N}_{j-1}^n$$

and therefore we can write

$$D_j^T \cdot f^j = \left(u^T \mathbf{f}_1^j \mid u^T \mathbf{f}_2^j \mid \dots \mid u^T \mathbf{f}_{n \cdot 3^{j-1}}^j \mid m^T \mathbf{f}_1^j \mid m^T \mathbf{f}_2^j \mid \dots \mid m^T \mathbf{f}_{n \cdot 3^{j-1}}^j \right)^T.$$

Thus, the wavelet coefficients are the components of the vectors $m^T \mathbf{f}_k^j$, for $j = i, i-1, \dots, 1$ and $k \in \mathcal{M}_{j-1}^n$, as follows:

$$m^T \mathbf{f}_k^j = \begin{pmatrix} w_{2k-1}^{j-1} \\ w_{2k}^{j-1} \end{pmatrix} = \mathbf{w}_k^{j-1}, \quad \text{for } k \in \mathcal{N}_{j-1}^n.$$

Suppose that $w_{k_0}^{i_0}$ is the wavelet coefficient which is going to be canceled. There is a unique $p \in \mathbb{N}^*$ such that $k_0 = 2p - l$, with $l \in \{0, 1\}$ and we have

$$m^T \mathbf{f}_p^{i_0+1} = \begin{pmatrix} w_{2p-1}^{i_0} \\ w_{2p}^{i_0} \end{pmatrix} = \mathbf{w}_p^{i_0}.$$

Let $r = 2 - l$. Replacing $w_{k_0}^{i_0}$ by zero means replacement by zero of the r -th component of the vector in (3.30), obtaining a vector denoted by $\widehat{\mathbf{w}}_p^{i_0}$, which depends on k_0 . Thus, applying the relation (1.7) successively for $j = i_0 + 1, i_0 + 2, \dots, i$ we obtain

$$\begin{aligned}\widehat{f}^{i_0+1} &= \begin{pmatrix} u f_1^{i_0} + m \mathbf{w}_1^{i_0} \\ \dots \\ u f_{p-1}^{i_0} + m \mathbf{w}_{p-1}^{i_0} \\ u f_p^{i_0} + m \widehat{\mathbf{w}}_p^{i_0} \\ u f_{p+1}^{i_0} + m \mathbf{w}_{p+1}^{i_0} \\ \dots \\ u f_{n \cdot 3^{i_0}}^{i_0} + m \mathbf{w}_{n \cdot 3^{i_0}}^{i_0} \end{pmatrix} = \begin{pmatrix} \mathbf{f}_1^{i_0+1} \\ \dots \\ \mathbf{f}_{p-1}^{i_0+1} \\ \widehat{\mathbf{f}}_p^{i_0+1} \\ \mathbf{f}_{p+1}^{i_0+1} \\ \dots \\ \mathbf{f}_{n \cdot 3^{i_0}}^{i_0+1} \end{pmatrix}, \quad f^{i_0+1} = \begin{pmatrix} u f_1^{i_0} + m \mathbf{w}_1^{i_0} \\ \dots \\ u f_p^{i_0} + m \mathbf{w}_p^{i_0} \\ \dots \\ u f_{n \cdot 3^{i_0}}^{i_0} + m \mathbf{w}_{n \cdot 3^{i_0}}^{i_0} \end{pmatrix}, \\ \left\| f^{i_0+1} - \widehat{f}^{i_0+1} \right\| &= \left\| \mathbf{f}_p^{i_0+1} - \widehat{\mathbf{f}}_p^{i_0+1} \right\| = \left\| m \left(\mathbf{w}_p^{i_0} - \widehat{\mathbf{w}}_p^{i_0} \right) \right\| = |w_{k_0}^{i_0}| \cdot \|m_r\|,\end{aligned}$$

where m_r denotes the column r of the matrix m and $\|\cdot\|$ is an arbitrary vector norm. Further,

$$\begin{aligned} \widehat{f}^{i_0+2} &= \left(P_{i_0+2} \mid Q_{i_0+2} \right) \begin{pmatrix} \widehat{f}^{i_0+1} \\ \widehat{w}^{i_0+1} \end{pmatrix} = \left(P_{i_0+2} \mid Q_{i_0+2} \right) \begin{pmatrix} \widehat{f}^{i_0+1} \\ w^{i_0+1} \end{pmatrix} \\ &= \begin{pmatrix} u f_1^{i_0+1} + m \mathbf{w}_1^{i_0+1} \\ \dots \\ u f_{3p-3}^{i_0+1} + m \mathbf{w}_{3p-3}^{i_0+1} \\ u \widehat{f}_{3p-2}^{i_0+1} + m \mathbf{w}_{3p-2}^{i_0+1} \\ \widehat{f}_{3p-1}^{i_0+1} + m \mathbf{w}_{3p-1}^{i_0+1} \\ u \widehat{f}_{3p}^{i_0+1} + m \mathbf{w}_{3p}^{i_0+1} \\ u f_{3p+1}^{i_0+1} + m \mathbf{w}_{3p+1}^{i_0+1} \\ \dots \\ u f_{n \cdot 3^{i_0+1}}^{i_0+1} + m \mathbf{w}_{n \cdot 3^{i_0+1}}^{i_0+1} \end{pmatrix} = \begin{pmatrix} \mathbf{f}_1^{i_0+2} \\ \dots \\ \mathbf{f}_{3p-3}^{i_0+2} \\ \widehat{\mathbf{f}}_{3p-2}^{i_0+2} \\ \widehat{\mathbf{f}}_{3p-1}^{i_0+2} \\ \widehat{\mathbf{f}}_{3p}^{i_0+2} \\ \mathbf{f}_{3p+1}^{i_0+2} \\ \dots \\ \mathbf{f}_{n \cdot 3^{i_0+1}}^{i_0+2} \end{pmatrix} \end{aligned}$$

and analogous expression for f^{i_0+2} , with \mathbf{f} instead of $\widehat{\mathbf{f}}$. So

$$\|f^{i_0+2} - \widehat{f}^{i_0+2}\| = \left\| \begin{pmatrix} u(f_{3p-2}^{i_0+1} - \widehat{f}_{3p-2}^{i_0+1}) \\ u(f_{3p-1}^{i_0+1} - \widehat{f}_{3p-1}^{i_0+1}) \\ u(f_{3p}^{i_0+1} - \widehat{f}_{3p}^{i_0+1}) \end{pmatrix} \right\| = s \left\| \begin{pmatrix} \mathbf{f}_p^{i_0+1} - \widehat{\mathbf{f}}_p^{i_0+1} \\ \mathbf{f}_p^{i_0+1} - \widehat{\mathbf{f}}_p^{i_0+1} \\ \mathbf{f}_p^{i_0+1} - \widehat{\mathbf{f}}_p^{i_0+1} \end{pmatrix} \right\|,$$

whence

$$\begin{aligned} \|f^{i_0+2} - \widehat{f}^{i_0+2}\|_2 &= \|\mathbf{f}_p^{i_0+1} - \widehat{\mathbf{f}}_p^{i_0+1}\|_2 = \|f^{i_0+1} - \widehat{f}^{i_0+1}\|_2, \\ \|f^{i_0+2} - \widehat{f}^{i_0+2}\|_\infty &= s \|f^{i_0+1} - \widehat{f}^{i_0+1}\|_\infty, \\ \|f^{i_0+2} - \widehat{f}^{i_0+2}\|_1 &= \frac{1}{s} \|f^{i_0+1} - \widehat{f}^{i_0+1}\|_1. \end{aligned}$$

Repeating this procedure we finally obtain

$$\|f^i - \widehat{f}^i\|_2 = \|f^{i_0+1} - \widehat{f}^{i_0+1}\|_2 = |w_{k_0}^{i_0}| \cdot \|m_r\|_2, \quad (1.8)$$

$$\|f^i - \widehat{f}^i\|_\infty = s^{i-i_0-1} \|f^{i_0+1} - \widehat{f}^{i_0+1}\|_\infty = s^{i-i_0-1} |w_{k_0}^{i_0}| \cdot \|m_r\|_\infty, \quad (1.9)$$

$$\|f^i - \widehat{f}^i\|_1 = s^{-i+i_0+1} \|f^{i_0+1} - \widehat{f}^{i_0+1}\|_1 = s^{-i+i_0+1} |w_{k_0}^{i_0}| \cdot \|m_r\|_1. \quad (1.10)$$

1.1.4 A comparison of wavelets

Formulas (1.8)-(1.10) show that, in the case when only one wavelet coefficient is canceled, the compression errors depend on the wavelet coefficient which was canceled and on the matrix m . In the following we investigate for which parameters α_1, α_2 the norms of the vectors

$$m_1 = (\alpha_1, \alpha_2, -\alpha_1 - \alpha_2)^T \quad \text{and} \quad m_2 = (s(\alpha_1 + 2\alpha_2) - s(2\alpha_1 + \alpha_2)s(\alpha_1 - \alpha_2))^T$$

are minimal. First, it is easy to see that

$$\|m_1\|_2 = \|m_2\|_2 = 1,$$

so all the wavelets lead to the same 2-norm of the reconstruction error.

Then the calculations show that

$$\begin{aligned}\|m_1\|_\infty &= \max\{|\alpha_1|, |\alpha_2|, |\alpha_1 + \alpha_2|\} = \max\left\{|\alpha_1|, \frac{1}{2}|\alpha_1 \pm \sigma(\alpha_1)|\right\} = f_1(\alpha_1), \\ \|m_2\|_\infty &= s \max\{|\alpha_1 + 2\alpha_2|, |2\alpha_1 + \alpha_2|, |\alpha_1 - \alpha_2|\} \\ &= s \max\left\{\sigma(\alpha_1), \frac{1}{2}|3\alpha_1 \pm \sigma(\alpha_1)|\right\} = f_2(\alpha_1),\end{aligned}$$

where $\alpha_1 \in [-\sqrt{2/3}, \sqrt{2/3}]$ and $\sigma(\alpha_1) = \sqrt{2 - 3\alpha_1^2}$. The functions f_1 and f_2 defined on the interval $[-\sqrt{2/3}, \sqrt{2/3}]$ are both even, so we can restrict ourselves to the interval $[0, \sqrt{2/3}]$, where they have the expressions

$$\begin{aligned}f_1(\alpha_1) &= \max\left\{|\alpha_1|, \frac{1}{2}|\alpha_1 + \sigma(\alpha_1)|\right\}, \\ f_2(\alpha_1) &= s \max\left\{\sigma(\alpha_1), \frac{1}{2}|3\alpha_1 + \sigma(\alpha_1)|\right\}.\end{aligned}$$

From the graphs of these functions (Figure 1.2 left) we can conclude that their minimum and

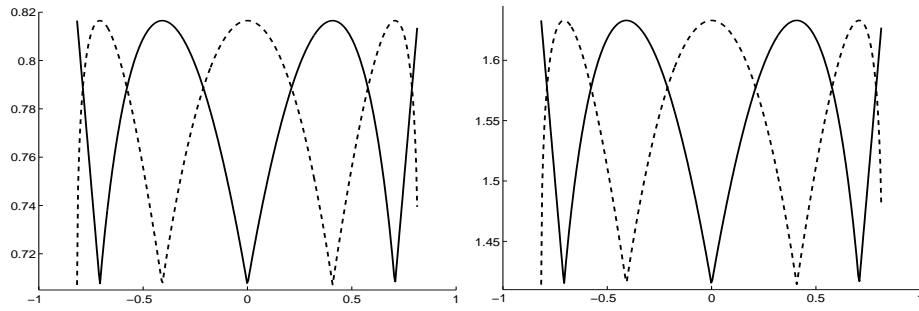


Figure 1.2: The graphs of the functions f_1 (—) and f_2 (- -) (left) and of g_1 (—) and g_2 (- -) (right).

maximum values are $1/\sqrt{2}$ and $\sqrt{2/3}$ respectively. Figure 1.3 show the points of the ellipse $\alpha_1^2 + \alpha_1\alpha_2 + \alpha_2^2 = 1/2$ where these extreme values are attained. More precisely, with the notations $\nu = 1/\sqrt{6}$, $\mu = 1/\sqrt{2}$, the points (α_1, α_2) in

$$\mathcal{P} = \{P_1(-\nu, 2\nu), P_2(\nu, \nu), P_3(2\nu, -\nu), P_4(\nu, -2\nu), P_5(-\nu, -\nu), P_6(-2\nu, \nu)\}$$

lead to the minimum of the norm $\|m_2\|_\infty$ and to the maximum of the norm $\|m_1\|_\infty$, while the points (α_1, α_2) in

$$\mathcal{R} = \{R_1(-\mu, \mu), R_2(0, \mu), R_3(\mu, 0), R_4(\mu, -\mu), R_5(0, -\mu), R_6(-\mu, 0)\}$$

lead to the minimum of the norm $\|m_1\|_\infty$ and to the maximum of the norm $\|m_2\|_\infty$. Unfortunately, we cannot obtain, for a chosen wavelet (a choice of the parameters α_1 and α_2), a minimum for the two norms $\|m_1\|_\infty$ and $\|m_2\|_\infty$ simultaneously.

Further, for the norm $\|\cdot\|_1$ we have

$$\begin{aligned}\|m_1\|_1 &= |\alpha_1| + |\alpha_2| + |\alpha_1 + \alpha_2| \\ &= |\alpha_1| + \frac{1}{2}|\alpha_1 + \sigma(\alpha_1)| + \frac{1}{2}|\alpha_1 - \sigma(\alpha_1)| = g_1(\alpha_1), \\ \|m_2\|_1 &= s(|\alpha_1 + 2\alpha_2| + |2\alpha_1 + \alpha_2| + |\alpha_1 - \alpha_2|) \\ &= s\left(\sigma(\alpha_1) + \frac{1}{2}|3\alpha_1 + \sigma(\alpha_1)| + \frac{1}{2}|3\alpha_1 - \sigma(\alpha_1)|\right) = g_2(\alpha_1).\end{aligned}$$

Again, from the graphs of the functions g_1 and g_2 (Figure 1.2 right) we can conclude that the extreme values are $\sqrt{2}$ and $2\sqrt{2/3}$ for both g_1 and g_2 . As in the previous case, the minimum of the norm $\|m_1\|_1$ and the maximum of the norm $\|m_2\|_1$ are taken for the points in \mathcal{R} , while the maximum of the norm $\|m_1\|_1$ and the minimum of the norm $\|m_2\|_1$ are taken for the points in \mathcal{P} .

Conclusion. Unlike the wavelets in [96, 97], in our case there are no optimal wavelets (no optimal choice of the parameters (α_1, α_2)) which minimize the norm $\|f^i - \widehat{f}^i\|_\infty$ no matter which wavelet coefficient $w_{k_0}^{i_0}$ is canceled. However, we can conclude the following. In the case when the canceled wavelet coefficient $w_{k_0}^{i_0}$ is taken such that k_0 is odd, then $r = 1$ and $\|m_1\|_\infty$ is minimum for $\alpha_1 \in \{\pm 1/\sqrt{2}, 0\}$. Therefore, if we chose $(\alpha_1, \alpha_2) \in \mathcal{R}$, we obtain the smallest possible value for the norm $\|f^i - \widehat{f}^i\|_\infty$. In the other case, when the canceled wavelet coefficient $w_{k_0}^{i_0}$ is taken such that k_0 is even, then $r = 2$ and $\|m_2\|_\infty$ is minimum for $\alpha_1 \in \{\pm 1/\sqrt{6}, \pm\sqrt{2/3}\}$. Therefore, if we chose $(\alpha_1, \alpha_2) \in \mathcal{P}$, we obtain the smallest possible value for the norm $\|f^i - \widehat{f}^i\|_\infty$. The same conclusion follows for the norm $\|f^i - \widehat{f}^i\|_1$.

In Section 4.1.3 we show how this construction can be adapted to spherical triangulations and give some numerical examples.

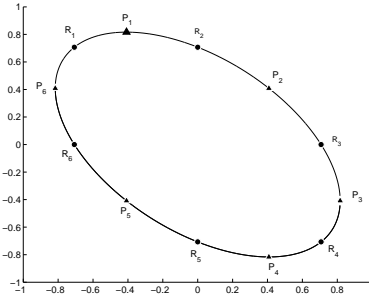


Figure 1.3: The ellipse $\alpha_1^2 + \alpha_1\alpha_2 + \alpha_2^2 = 1/2$ and the points which lead to minimum and maximum of the norms $\|m_r\|_\infty$ and $\|m_r\|_1$, $r = 1, 2$.

1.2 Piecewise constant wavelet bases obtained by 1-4 splitting

In this section we give the most general expression of orthonormal piecewise constant wavelet bases, in the case when the refinement process consists in dividing a domain into four subdomains having the same area. We show that the classical Haar bases are optimal with respect to the ∞ -norm of the reconstruction error, but not with respect to the 1-norm. The construction applies not only to planar domains, but also to surfaces of revolution, like sphere, cone, paraboloid, or two-sheeted hyperboloid. The results are published in [110].

1.2.1 Wavelet coefficients and wavelet decomposition matrices

Let $\mathcal{D} = \{D_1, \dots, D_n\}$ be a decomposition of a given domain $\Omega \subseteq \mathbb{R}^2$ ($\Omega = \cup_{i=1}^n D_i$). Given $\mathcal{D} = \mathcal{D}^0$, we consider a refinement \mathcal{D}^1 of \mathcal{D}^0 such that each domain in \mathcal{D}^0 is the union of four domains of \mathcal{D}^1 of equal areas. The most common cases are a square or rectangle divided by lines parallel to the edges or a triangle divided by its median lines.

For a given $D \in \mathcal{D}^0$, let \mathcal{R}_D denote the set of the four refined domains. The set $\mathcal{D}^1 = \cup_{D \in \mathcal{D}^0} \mathcal{R}_D$ is a refinement of \mathcal{D}^0 . Continuing the refinement process in the same manner, we

obtain a decomposition \mathcal{D}^j of Ω , for $j \in \mathbb{N}$.

Let $\langle \cdot, \cdot \rangle_*$ be the inner product defined in (1.1), based on the initial coarsest decomposition \mathcal{D}^0

$$\langle f, g \rangle_* = \sum_{D \in \mathcal{D}^0} \frac{1}{\mathcal{A}(D)} \int_D f(\mathbf{x})g(\mathbf{x}) \, d\mathbf{x}, \text{ for } f, g \in L^2(\Omega). \quad (1.11)$$

The induced norm $\| \cdot \|_*$ is again equivalent with the usual L^2 -norm.

In the sequel we construct a wavelet basis which is orthogonal with respect to the inner product (1.11). Due to the norm equivalence, this wavelet basis will be a Riesz basis of $L^2(\Omega)$, not an orthonormal one, but the most important fact is that in implementations one uses orthogonal matrices. Thus, the numerical behavior of our wavelet bases will be that of orthonormal bases. For a fixed $j \in \mathbb{N}$, we associate to each subdomain $D_k^j \in \mathcal{D}^j$, $k \in \mathcal{N}_j^n := \{1, 2, \dots, n \cdot 4^j\}$, the function $\varphi_{D_k^j} : \Omega \rightarrow \mathbb{R}$,

$$\varphi_{D_k^j} = 2^j \chi_{D_k^j},$$

where $\chi_{D_k^j}$ is the characteristic function of the domain D_k^j . Then we define the spaces of functions $V^j = \text{span}\{\varphi_{D_k^j}, k \in \mathcal{N}_j^n\}$, of dimension $n \cdot 4^j$, consisting of piecewise constant functions on the domains of \mathcal{D}^j . Moreover, we have $\|\varphi_{D_k^j}\|_* = 1$. Let $D^j \in \mathcal{D}^j$ and D_k^{j+1} , $k = 1, 2, 3, 4$ the refined subdomains obtained from D^j . Due to the equalities

$$\varphi_{D^j} = \frac{1}{2}\varphi_{D_1^{j+1}} + \frac{1}{2}\varphi_{D_2^{j+1}} + \frac{1}{2}\varphi_{D_3^{j+1}} + \frac{1}{2}\varphi_{D_4^{j+1}},$$

which hold in $L^2(\Omega)$, we have the inclusions $V^j \subseteq V^{j+1}$, for all $j \in \mathbb{N}$. With respect to the inner product (1.11), the spaces V^j become Hilbert spaces, with the corresponding norm $\| \cdot \|_*$. Let W^j denote the orthogonal complement, with respect to $\langle \cdot, \cdot \rangle_*$, of the coarse space V^j in the fine space V^{j+1} , so that

$$V^{j+1} = V^j \oplus W^j.$$

The dimension of W^j is thus $\dim W^j = 3n \cdot 4^j$. The spaces W^j are called the *wavelet spaces*. In the following we construct an orthonormal basis of W^j . To each domain D^j , three wavelets supported on D^j will be associated in the following way:

$$\psi_{D^j}^k = a_{k1}\varphi_{D_1^{j+1}} + a_{k2}\varphi_{D_2^{j+1}} + a_{k3}\varphi_{D_3^{j+1}} + a_{k4}\varphi_{D_4^{j+1}}, \text{ for } k = 1, 2, 3,$$

with $a_{ij} \in \mathbb{R}$, $i = 1, 2, 3, 4$, $j = 1, 2, 3$. Next we will find conditions on the coefficients a_{ij} which ensure that the set $\{\psi_{D^j}^k, k = 1, 2, 3, 4, D^j \in \mathcal{D}^j\}$ is an orthonormal basis of W^j with respect to the inner product (1.11). First we must have

$$\langle \psi_{D^j}^k, \varphi_{S^j} \rangle_* = 0, \text{ for } k = 1, 2, 3 \text{ and } T^j, S^j \in \mathcal{T}^j. \quad (1.12)$$

If $D^j \neq S^j$, then the equality is immediate since $\text{supp} \psi_{D^j}^k = \text{supp} \varphi_{D^j}$ and $\text{supp} \varphi_{D^j} \cap \text{supp} \varphi_{S^j}$ is either empty or an edge, whose measure is zero. If $D^j = S^j$, evaluating the inner product (1.12) we obtain

$$\begin{aligned} \langle \psi_{T^j}^1, \varphi_{S^j} \rangle_* &= \frac{2}{\mathcal{A}(D)} (a_{k1}\mathcal{A}(D_1^{j+1}) + a_{k2}\mathcal{A}(D_2^{j+1}) + a_{k3}\mathcal{A}(D_3^{j+1}) + a_{k4}\mathcal{A}(D_4^{j+1})), \\ &= \frac{1}{2}a_{k1} + \frac{1}{2}a_{k2} + \frac{1}{2}a_{k3} + \frac{1}{2}a_{k4}, \end{aligned}$$

D being the domain of the initial decomposition \mathcal{D}^0 containing D^j . Then, some simple calculations show that each of the orthogonality conditions

$$\langle \psi_{D^j}^k, \psi_{D^j}^l \rangle_* = \delta_{kl}, \text{ for all } D^j \in \mathcal{T}^j,$$

is equivalent to $a_{k1}a_{l1} + a_{k2}a_{l2} + a_{k3}a_{l3} + a_{k4}a_{l4} = \delta_{kl}$. In fact, one requires the orthogonality of the matrix

$$M = \begin{pmatrix} \frac{1}{2} & \frac{1}{2} & \frac{1}{2} & \frac{1}{2} \\ a_{11} & a_{12} & a_{13} & a_{14} \\ a_{21} & a_{22} & a_{23} & a_{24} \\ a_{31} & a_{32} & a_{33} & a_{34} \end{pmatrix}, \quad (1.13)$$

that is we look for the non-singular matrices M satisfying the condition $M^{-1} = M^T$. For orthogonal matrices M we have $\det M = \pm 1$ and in our case it will not be a restriction to impose only the requirement $\det M = 1$. A particular case is the Haar matrix

$$H = \frac{1}{2} \begin{pmatrix} 1 & 1 & 1 & 1 \\ 1 & 1 & -1 & -1 \\ 1 & -1 & -1 & 1 \\ 1 & -1 & 1 & -1 \end{pmatrix}, \quad (1.14)$$

and other particular cases have already been considered in [87, 103]. In the following we will determine all the orthogonal matrices M with $\det M = 1$.

1.2.2 Quaternions and orthogonal matrices

Let $O = (o_{ij})_{i,j=1,2,3,4}$ be an orthogonal matrix with $\det O = 1$. With the entries of its first row we construct the so-called quaternion matrix

$$Q = Q(o_{11}, o_{12}, o_{13}, o_{14}) = \begin{pmatrix} o_{11} & o_{12} & o_{13} & o_{14} \\ -o_{12} & o_{11} & -o_{14} & o_{13} \\ -o_{13} & o_{14} & o_{11} & -o_{12} \\ -o_{14} & -o_{13} & o_{12} & o_{11} \end{pmatrix},$$

having the inverse

$$Q^{-1} = \frac{1}{s} \begin{pmatrix} o_{11} & -o_{12} & -o_{13} & -o_{14} \\ o_{12} & o_{11} & o_{14} & -o_{13} \\ o_{13} & -o_{14} & o_{11} & o_{12} \\ o_{14} & o_{13} & -o_{12} & o_{11} \end{pmatrix} = \frac{1}{s} Q^T,$$

with $s = o_{11}^2 + o_{12}^2 + o_{13}^2 + o_{14}^2$. The matrix OQ^{-1} can be written as a block matrix

$$OQ^{-1} = \frac{1}{s} \begin{pmatrix} s & \mathbf{0}^T \\ \mathbf{0} & R \end{pmatrix}, \quad (1.15)$$

where R is an orthogonal matrix with $\det R = 1$ and $\mathbf{0}^T = (0, 0, 0)$. In our case $s = 1$ and the quaternion matrix associated to the orthogonal matrix M will be

$$Q_1 = Q\left(\frac{1}{2}, \frac{1}{2}, \frac{1}{2}, \frac{1}{2}\right) = \frac{1}{2} \begin{pmatrix} 1 & 1 & 1 & 1 \\ -1 & 1 & -1 & 1 \\ -1 & 1 & 1 & -1 \\ -1 & -1 & 1 & 1 \end{pmatrix},$$

satisfying $Q_1^{-1} = Q_1^T$. Now we can prove the following result:

Proposition 1.1 *Let B be 4×4 matrix with $1/2$ on the first row. Then B is orthogonal with $\det B = 1$ if and only if*

$$BQ_1^{-1} = \begin{pmatrix} 1 & \mathbf{0}^T \\ \mathbf{0} & R \end{pmatrix}, \quad (1.16)$$

with R a 3×3 rotation matrix, that is a 3×3 orthogonal matrix with $\det R = 1$.

Proof. Indeed, let $B = (b_{ij})_{ij}$ be a 4×4 orthogonal matrix with $\det B = 1$ and $b_{1j} = 1/2$ for $j = 1, 2, 3, 4$. Then, using (1.15), equality (1.16) is satisfied with

$$R = \frac{1}{2} \begin{pmatrix} -b_{21} + b_{22} - b_{23} + b_{24} & -b_{21} + b_{22} + b_{23} - b_{24} & -b_{21} - b_{22} - b_{23} + b_{24} \\ -b_{31} + b_{32} - b_{33} + b_{34} & -b_{31} - b_{32} + b_{33} - b_{34} & -b_{31} - b_{32} + b_{33} + b_{34} \\ -b_{41} + b_{42} - b_{43} - b_{44} & -b_{41} - b_{42} + b_{43} - b_{44} & -b_{41} - b_{42} + b_{43} + b_{44} \end{pmatrix}.$$

Conversely, given a 3×3 orthogonal matrix R with $\det R = 1$, the matrix

$$B = \begin{pmatrix} 1 & \mathbf{0}^T \\ \mathbf{0} & R \end{pmatrix} Q_1$$

has $1/2$ on the first row and is indeed orthogonal since

$$BB^T = \begin{pmatrix} 1 & \mathbf{0}^T \\ \mathbf{0} & R \end{pmatrix} Q_1 Q_1^T \begin{pmatrix} 1 & \mathbf{0}^T \\ \mathbf{0} & R^T \end{pmatrix} = \begin{pmatrix} 1 & \mathbf{0}^T \\ \mathbf{0} & RR^T \end{pmatrix} = \mathbf{I}_4.$$

■

Using this proposition, we conclude that each 3×3 rotation matrix will generate an orthogonal 4×4 matrix with $1/2$ on the first column, and therefore a wavelet basis.

It is known¹ that the most general expression of a 3×3 rotation matrix is

$$R = (r_{ij})_{i,j=1,2,3} = \begin{pmatrix} a^2 + b^2 - c^2 - d^2 & -2ad + 2bc & 2ac + 2bd \\ 2ad + 2bc & a^2 - b^2 + c^2 - d^2 & -2ab + 2cd \\ -2ac + 2bd & 2ab + 2cd & a^2 - b^2 - c^2 + d^2 \end{pmatrix}, \quad (1.17)$$

with $a, b, c, d \in \mathbb{R}$ satisfying $a^2 + b^2 + c^2 + d^2 = 1$. Thus, the matrix M of wavelet coefficients can be written as

$$M = \begin{pmatrix} 1 & \mathbf{0}^T \\ \mathbf{0} & R \end{pmatrix} Q_1, \quad (1.18)$$

¹This formula was first discovered by Euler in 1770 and later rediscovered independently by Rodrigues in 1840.

and with the notations in (1.13) we obtain:

$$\begin{aligned}
2a_{11} &= -a^2 - b^2 + c^2 + d^2 - 2ac + 2ad - 2bc - 2bd, \\
2a_{12} &= a^2 + b^2 - c^2 - d^2 - 2ac - 2ad + 2bc - 2bd, \\
2a_{13} &= -a^2 - b^2 + c^2 + d^2 + 2ac - 2ad + 2bc + 2bd, \\
2a_{14} &= -2(a_{11} + a_{12} + a_{13}) = a^2 + b^2 - c^2 - d^2 + 2ac + 2ad - 2bc + 2bd \\
2a_{21} &= -a^2 + b^2 - c^2 + d^2 + 2ab - 2ac - 2ad - 2bc, \\
2a_{22} &= a^2 - b^2 + c^2 - d^2 + 2ab + 2ad + 2bc - 2cd, \\
2a_{23} &= a^2 - b^2 + c^2 - d^2 - 2ab - 2ad - 2bc + 2cd, \\
2a_{24} &= -2(a_{21} + a_{22} + a_{23}) = -a^2 + b^2 - c^2 + d^2 - 2ab + 2ac + 2ad + 2bc \\
2a_{31} &= -a^2 + b^2 + c^2 - d^2 - 2ab + 2ac - 2bd - 2cd, \\
2a_{32} &= -a^2 + b^2 + c^2 - d^2 + 2ab - 2ac + 2bd + 2cd, \\
2a_{33} &= a^2 - b^2 - c^2 + d^2 + 2ab + 2ac - 2bd + 2cd, \\
2a_{34} &= -2(a_{31} + a_{32} + a_{33}) = a^2 - b^2 - c^2 + d^2 - 2ab - 2ac + 2bd - 2cd
\end{aligned}$$

Since $a^2 + b^2 + c^2 + d^2 = 1$, one can also express these entries using spherical coordinates:

$$\begin{aligned}
a &= \cos \alpha, \\
b &= \cos \beta \sin \gamma \sin \alpha, \\
c &= \sin \beta \sin \gamma \sin \alpha, \\
d &= \cos \gamma \sin \alpha,
\end{aligned}$$

with $\alpha, \gamma \in [0, \pi]$, $\beta \in [0, 2\pi]$.

As we have already mentioned, some particular cases were already studied. For example, the case when the matrix $\widetilde{M} = (a_{ij})_{i,j=2,3,4}$ is normal (i.e. $\widetilde{M}\widetilde{M}^T = \widetilde{M}^T\widetilde{M}$) was discussed in [103].

1.2.3 Optimal wavelet bases

For $k = 1, 2, 3$, let $a_k = (a_{k1}, a_{k2}, a_{k3}, a_{k4})$ be the vectors formed with the last three rows of the matrix M .

As we have already calculated in [101], the norm of the compression error, when we cancel one wavelet coefficient, depends on the norm of the vectors a_k . Therefore, we need to study the behavior of the norms $\|a_k\|_\infty$ and $\|a_k\|_1$.

The norm $\|\cdot\|_\infty$

We have

$$\begin{aligned}
2\|a_k\|_\infty &= 2 \max \{|a_{k1}|, |a_{k2}|, |a_{k3}|, |-a_{k1} - a_{k2} - a_{k3}|\} \\
&= 2 \max \{\max\{|a_{k1}|, |a_{k2}|\}, \max\{|a_{k3}|, |a_{k1} + a_{k2} + a_{k3}|\}\} \\
&= \max\{|a_{k1} + a_{k2}| + |a_{k1} - a_{k2}|, |a_{k1} + a_{k2} + 2a_{k3}| + |a_{k1} + a_{k2}|\} \\
&= |a_{k1} + a_{k2}| + \max\{|a_{k1} - a_{k2}|, |a_{k1} + a_{k2} + 2a_{k3}|\} \\
&= |a_{k1} + a_{k2}| + |a_{k2} + a_{k3}| + |a_{k1} + a_{k3}| \\
&= |r_{k1}| + |r_{k2}| + |r_{k3}| \\
&= \|r_k\|_1,
\end{aligned}$$

where $r_k = (r_{k1}, r_{k2}, r_{k3})$ is the k -th row of the matrix R .

For the Haar wavelets, which are the piecewise constant wavelets that are the most used in practice, one has $\|a_k^{\text{Haar}}\|_\infty = 1/2$.

Proposition 1.2 *One has $\|a_k\|_\infty \geq 1/2$ for all $k = 1, 2, 3$.*

Proof. If we suppose that there exists k such that $\|a_k\|_\infty < 1/2$, then $a_{ki} < 1/2$ for $i = 1, 2, 3, 4$, whence $a_{k1}^2 + a_{k2}^2 + a_{k3}^2 + a_{k4}^2 < 1$. This is a contradiction, since the orthogonality of the matrix M implies that $a_{k1}^2 + a_{k2}^2 + a_{k3}^2 + a_{k4}^2 = 1$. ■

Thus, the Haar wavelets minimize the ∞ -norm of the reconstruction error.

The norm $\|\cdot\|_1$

First let us note that for the Haar case we have $\|a_k^{\text{Haar}}\|_1 = 2$ for $k = 1, 2, 3$. In the general case we have

$$\begin{aligned} 2\|a_k\|_1 &= 2(|a_{k1}| + |a_{k2}| + |a_{k3}| + |a_{k4}|) \\ &= |r_{k1} + r_{k2} + r_{k3}| + |r_{k1} + r_{k2} - r_{k3}| + |r_{k1} - r_{k2} + r_{k3}| + |r_{k1} - r_{k2} - r_{k3}| \\ &= \left| r_{k1} + r_{k2} + \sqrt{1 - r_{k1}^2 - r_{k2}^2} \right| + \left| r_{k1} + r_{k2} - \sqrt{1 - r_{k1}^2 - r_{k2}^2} \right| + \\ &\quad \left| r_{k1} - r_{k2} + \sqrt{1 - r_{k1}^2 - r_{k2}^2} \right| + \left| r_{k1} - r_{k2} - \sqrt{1 - r_{k1}^2 - r_{k2}^2} \right|. \end{aligned}$$

Let us consider the function $f : \{(x, y) \in \mathbb{R}^2, x^2 + y^2 \leq 1\} \rightarrow \mathbb{R}$,

$$\begin{aligned} f(x, y) &= \left| x + y + \sqrt{1 - x^2 - y^2} \right| + \left| x + y - \sqrt{1 - x^2 - y^2} \right| + \\ &\quad \left| x - y + \sqrt{1 - x^2 - y^2} \right| + \left| x - y - \sqrt{1 - x^2 - y^2} \right|. \end{aligned}$$

This function has its minimum equal to $2\sqrt{2}$, which is attained at the points

$$(x, y) \in \{(0, t), (0, -t), (t, 0), (-t, 0), (t, t), (t, -t), (-t, t), (-t, -t)\},$$

where $t = 1/\sqrt{2}$.

Some calculations show that there exists no matrix M with the property that $\|a_k\|_1 = \sqrt{2}$, for all $k = 1, 2, 3$.

However, there exist matrices M for which $\|a_k\|_1 \leq 2 = \|a_k^{\text{Haar}}\|_1$ for all $k = 1, 2, 3$. For these matrices, the associated wavelets will lead to a smaller 1-norm of the reconstruction error, compared with the Haar classical wavelets, for which $\|a_k\|_1 = 2$.

In the following we will find all matrices M for which $\|a_1\|_1 = \sqrt{2}$. Due to the symmetry and taking into account the previous calculations, we can restrict ourselves to the matrices

$$R = \begin{pmatrix} 0 & s/\sqrt{2} & t/\sqrt{2} \\ r_{21} & r_{22} & r_{23} \\ r_{31} & r_{32} & r_{33} \end{pmatrix}, \text{ with } s, t \in \{-1, 1\}.$$

Then, any circular permutation of its columns leads to $\|a_1\|_1 = \sqrt{2}$.

From the orthogonality of the rows, we deduce that

$$r_{23} = -st r_{22}, \quad r_{32} = -st r_{33}.$$

Since $r_{21}^2 + r_{31}^2 = 1$, we can write $r_{21} = \cos \alpha$, $r_{31} = \sin \alpha$, $\alpha \in [0, 2\pi)$. Then, from the fact that the vector in the second column has norm 1, we deduce that $r_{22}^2 + r_{33}^2 = \frac{1}{2}$ and therefore one can write

$$r_{22} = \frac{1}{\sqrt{2}} \cos \varphi, \quad r_{33} = \frac{1}{\sqrt{2}} \sin \varphi, \quad \text{with } \varphi \in [0, 2\pi).$$

Further, the orthogonality of the vectors on the first and second column gives

$$\begin{aligned} \frac{1}{\sqrt{2}} \cos \alpha \cos \varphi - \frac{1}{\sqrt{2}} st \sin \alpha \sin \varphi &= 0, \\ \cos s\alpha \cos t\varphi - \sin s\alpha \sin t\varphi &= 0, \\ \cos(s\alpha + t\varphi) &= 0, \\ s\alpha + t\varphi &= \varepsilon \frac{\pi}{2} + 2k\pi, \quad \text{with } k \in \mathbb{Z}, \varepsilon \in \{-1, 1\}. \\ \alpha &= -st\varphi + s\varepsilon \frac{\pi}{2} + 2sk\pi. \end{aligned}$$

Therefore,

$$\begin{aligned} \sin \alpha &= \sin \left(s\varepsilon \frac{\pi}{2} - st\varphi \right) = \sin \left(s\varepsilon \frac{\pi}{2} \right) \cos(st\varphi) - \cos \left(s\varepsilon \frac{\pi}{2} \right) \sin(st\varphi) \\ &= s\varepsilon \cos \varphi, \\ \cos \alpha &= \cos \left(s\varepsilon \frac{\pi}{2} - st\varphi \right) = \cos \left(s\varepsilon \frac{\pi}{2} \right) \cos(st\varphi) + \sin \left(s\varepsilon \frac{\pi}{2} \right) \sin(st\varphi) \\ &= t\varepsilon \sin \varphi. \end{aligned}$$

Thus, the matrix R can be written as

$$R = \begin{pmatrix} 0 & \frac{s}{\sqrt{2}} & \frac{t}{\sqrt{2}} \\ t\varepsilon \sin \varphi & \frac{1}{\sqrt{2}} \cos \varphi & -\frac{st}{\sqrt{2}} \cos \varphi \\ s\varepsilon \cos \varphi & -\frac{st}{\sqrt{2}} \sin \varphi & \frac{1}{\sqrt{2}} \sin \varphi \end{pmatrix}$$

and one calculates $\det R = -\varepsilon st$. If we impose the condition $\det R = 1$, then $t\varepsilon = -s$, $s\varepsilon = -t$ and R becomes

$$R = \begin{pmatrix} 0 & \frac{s}{\sqrt{2}} & \frac{t}{\sqrt{2}} \\ -s \sin \varphi & \frac{1}{\sqrt{2}} \cos \varphi & -\frac{st}{\sqrt{2}} \cos \varphi \\ -t \cos \varphi & -\frac{st}{\sqrt{2}} \sin \varphi & \frac{1}{\sqrt{2}} \sin \varphi \end{pmatrix}.$$

Conclusion

We have presented the construction of piecewise constant orthonormal wavelet bases on 2D-domains, but they can be easily adapted to spherical domains, with subdivision performed either directly onto the sphere and using the uniform and refinable grids in [48, 107], or onto a polyhedron, using the technique in [93]. A recent result [109] allows us to extend them to other surfaces of revolution, such as a paraboloid, cone, or two-sheeted hyperboloid.

1.3 Piecewise constant wavelet bases obtained by arbitrary splitting

The results presented in this section were published in [87]. In the previous two sections we have investigated the construction of orthonormal wavelet bases on 2D domains, in the case

when the refinement process consists in 1-3 and 1-4 splitting. A natural question that arises is if one can generalize the construction to 1- n splitting. In [60], the authors construct directional Haar frames on triangles, starting from the classical tensor product Haar wavelets, using the 1-8 subdivision in Figure 1.4. We also mention [41], where the authors consider triangular lattice with symmetry 6, and define on that lattice a so-called *intertwining multiresolution analysis*, a concept introduced by the same authors in [42]. By contrast, our construction applies to the triangulation of *any* lattice.

In this section we give a method for constructing certain orthogonal matrices of arbitrary dimension, yielding piecewise constant orthonormal wavelet bases. The refinement step consists in dividing a domain into n sub-domains of equal areas.

Let $\mathcal{D} = \{D_1, \dots, D_N\}$ be a decomposition of a given domain $\Omega \subseteq \mathbb{R}^2$, i.e. $\Omega = \cup_{i=1}^N D_i$. Given $\mathcal{D} = \mathcal{D}^0$, we consider a refinement \mathcal{D}^1 of \mathcal{D}^0 such that each domain in \mathcal{D}^0 is the union of n domains of \mathcal{D}^1 of equal areas. For arbitrary n , a subdivision of a triangle $M_1M_2M_3$ into n smaller triangles of equal area can be done as follows (see Figure 1.5 for $n = 5$): on the longest edge, say M_1M_2 take the point P such that $M_1P = \frac{M_1M_2}{n}$. Thus, the area of M_1PM_3 will be $1/n$ of the area of $M_1M_2M_3$ and it remains to divide the triangle M_3PM_2 into $n - 1$ triangles of equal areas. This division will be performed in the same way, by taking on the longest edge, say M_2M_3 a point Q such that $M_3Q = \frac{M_2M_3}{n-1}$. Continuing in the same manner we obtain at the end a subdivision of $M_1M_2M_3$ into n triangles of the same area. Another subdivision into 2^k triangles (for arbitrary k) can be taken as in Figure 1.6.

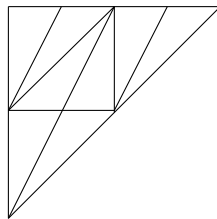


Figure 1.4: Subdivision into 8 triangles with the same area, used in [60].

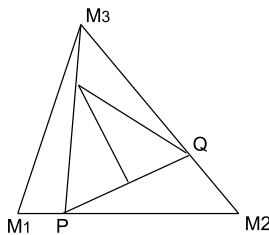


Figure 1.5: Example of subdivision into 5 triangles with the same area.

1.3.1 Orthonormal wavelet bases

For a given $D \in \mathcal{D}^0$, let \mathcal{R}_D denote the set of the n refined domains. The set $\mathcal{D}^1 = \cup_{D \in \mathcal{D}^0} \mathcal{R}_D$ is a refinement of \mathcal{D}^0 . Continuing the refinement process in the same manner, we obtain a decomposition \mathcal{D}^j of Ω , for $j \in \mathbb{N}$.

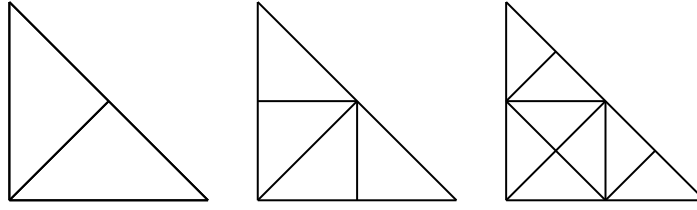


Figure 1.6: Example of subdivision into 2, 4 and 8 domains with the same area.

We consider again the inner product in (1.1)

$$\langle f, g \rangle_* = \sum_{D \in \mathcal{D}^0} \frac{1}{\mathcal{A}(D)} \int_D f(\mathbf{x})g(\mathbf{x}) \, d\mathbf{x}, \text{ for } f, g \in L^2(\Omega). \quad (1.19)$$

In the sequel, we construct a wavelet basis which is orthogonal with respect to this inner product. For a fixed $j \in \mathbb{N}$, to each subdomain $D_k^j \in \mathcal{D}^j$, $k \in \mathcal{N}_j^N := \{1, 2, \dots, N \cdot n^j\}$, we associate the function $\varphi_{D_k^j} : \Omega \rightarrow \mathbb{R}$,

$$\varphi_{D_k^j} = n^{\frac{j}{2}} \chi_{D_k^j},$$

where $\chi_{D_k^j}$ is the characteristic function of the domain D_k^j . Then we define the spaces of functions $V^j = \text{span}\{\varphi_{D_k^j}, k \in \mathcal{N}_j^N\}$, of dimension $N \cdot n^j$, consisting of piecewise constant functions on the domains of \mathcal{D}^j . Moreover, we have $\|\varphi_{D_k^j}\|_* = 1$. Let $D^j \in \mathcal{D}^j$ and D_k^{j+1} , $k = 1, \dots, n$, the refined subdomains obtained from D^j . Due to the equalities

$$\varphi_{D^j} = \frac{1}{\sqrt{n}} \sum_{k=1}^n \varphi_{D_k^{j+1}},$$

which hold in $L^2(\Omega)$, we have the inclusions $V^j \subseteq V^{j+1}$, for all $j \in \mathbb{N}$. With respect to the inner product (1.19), the spaces V^j become Hilbert spaces, with the corresponding norm $\|\cdot\|_*$. Let W^j denote the orthogonal complement, with respect to $\langle \cdot, \cdot \rangle_*$, of the coarse space V^j in the fine space V^{j+1} , so that

$$V^{j+1} = V^j \oplus W^j.$$

The dimension of W^j is thus $\dim W^j = (n-1)N \cdot n^j$. The spaces W^j are called the *wavelet spaces*. In the following we construct an orthonormal basis of W^j . To each domain D^j , $n-1$ wavelets supported on D^j will be associated in the following way:

$$\psi_{D^j}^k = \sum_{m=1}^n a_{km} \varphi_{D_m^{j+1}}, \text{ for } k = 1, \dots, n-1, \quad (1.20)$$

with $a_{km} \in \mathbb{R}$, $k = 1, \dots, n-1$, $m = 1, \dots, n$. Next we will find conditions on the coefficients a_{km} which assure that the set $\{\psi_{D^j}^k, D^j \in \mathcal{D}^j, k = 1, \dots, n-1\}$ is an orthonormal basis of W^j with respect to the inner product (1.19). First we must have $W^j \perp V^j$, meaning that

$$\langle \psi_{D^j}^k, \varphi_{S^j} \rangle_* = 0, \text{ for } k = 1, \dots, n-1 \text{ and } D^j, S^j \in \mathcal{D}^j. \quad (1.21)$$

If $D^j \neq S^j$, then the equality is immediate since $\text{supp } \psi_{D^j}^l = \text{supp } \varphi_{D^j}$ and $\text{supp } \varphi_{D^j} \cap \text{supp } \varphi_{S^j}$ is either empty or an edge, whose measure is zero. If $D^j = S^j$, by evaluating the inner product (1.21) we obtain

$$\langle \psi_{D^j}^k, \varphi_{S^j} \rangle_* = \frac{n^{\frac{2j+1}{2}}}{\mathcal{A}(D)} \sum_{m=1}^n a_{km} \mathcal{A}(D_m^{j+1}) = \frac{1}{\sqrt{n}} \sum_{m=1}^n a_{km},$$

D being the domain of the initial decomposition \mathcal{D}^0 containing D^j . This says that the mean value of each wavelet is zero. Then, it is immediate that

$$\langle \psi_{D^j}^k, \psi_{S^j}^l \rangle_* = 0, \text{ for all } D^j \neq S^j.$$

For $S^j = D^j$, each of the orthogonality conditions

$$\langle \psi_{D^j}^k, \psi_{D^j}^l \rangle_* = \delta_{kl}, \text{ for all } D^j \in \mathcal{D}^j,$$

is equivalent to

$$\sum_{m=1}^n a_{km} a_{lm} = \delta_{kl}.$$

In fact, one requires the orthogonality of the matrix

$$M = \begin{bmatrix} \frac{1}{\sqrt{n}} & \frac{1}{\sqrt{n}} & \cdots & \frac{1}{\sqrt{n}} \\ a_{11} & a_{12} & \cdots & a_{1n} \\ \vdots & \vdots & \cdots & \vdots \\ a_{n-1,1} & a_{n-1,2} & \cdots & a_{n-1,n} \end{bmatrix}, \quad (1.22)$$

more precisely we look for the non-singular matrices M satisfying the condition $M^{-1} = M^T$. A particular case is the Haar matrix

$$H = \frac{1}{2} \begin{bmatrix} 1 & 1 & 1 & 1 \\ 1 & 1 & -1 & -1 \\ 1 & -1 & -1 & 1 \\ 1 & -1 & 1 & -1 \end{bmatrix}, \quad (1.23)$$

for $n = 4$. The cases $n = 3$ and $n = 4$ were studied in the previous sections. In what follows we will give a method for generating orthogonal matrices of arbitrary dimension.

1.3.2 Construction of orthogonal matrices of arbitrary dimension

Let $n \in \mathbb{N}$, $n \geq 3$, be fixed. We denote by $\mathbf{O}_n(\mathbb{R})$ the set of real orthogonal matrices of dimension n and by $\mathbf{O}_n(\mathbf{x})$ the set of matrices whose first row is the vector

$$\mathbf{x} \in B_n(\mathbf{0}, 1) := \{(x_1, \dots, x_n) \in \mathbb{R}^n, x_1^2 + \dots + x_n^2 = 1\}.$$

We give a simple method for constructing orthogonal matrices in $\mathbf{O}_n(\mathbf{x})$, when \mathbf{x} is given. The main result is given in Theorem 1.5. To prove it, we need some preliminary results.

Proposition 1.3 Let $\mathbf{e}_1 = (1, 0, \dots, 0) \in B_n(\mathbf{0}, 1)$. Then every matrix $M \in \mathbf{O}_n(\mathbf{e}_1)$ can be written as

$$M = \left[\begin{array}{c|ccc} 1 & 0 & \dots & 0 \\ \hline 0 & & & \\ \vdots & & \widetilde{M} & \\ 0 & & & \end{array} \right], \text{ with } \widetilde{M} \in \mathbf{O}_{n-1}(\mathbb{R}).$$

Proof. The first component of the vectors in \mathbb{R}^n orthogonal to \mathbf{e}_1 is zero. ■

Remark: An immediate consequence of Proposition 1.3 is the fact that there exists a bijection $g : \mathbf{O}_n(\mathbf{e}_1) \rightarrow \mathbf{O}_{n-1}(\mathbb{R})$,

$$g(M) = \widetilde{M}.$$

Theorem 1.4 If $\mathbf{u} = (u_1, \dots, u_n) \in B_n(\mathbf{0}, 1)$, and $A_n \in \mathbf{O}_n(\mathbf{u})$, then the function $f_{A_n} : \mathbf{O}_n(\mathbf{e}_1) \rightarrow \mathbf{O}_n(\mathbf{u})$,

$$f_{A_n}(X) = XA_n,$$

is bijective.

Proof. First, let us remark that the function $h_{A_n} : \mathbf{O}_n(\mathbb{R}) \rightarrow \mathbf{O}_n(\mathbb{R})$, $h_{A_n}(X) = XA_n$ is a bijection (as a translation in the group $\mathbf{O}_n(\mathbb{R})$).

We denote by $\mathbf{c}_1, \mathbf{c}_2, \dots, \mathbf{c}_n$ the columns of A_n and by $\mathbf{l}_1, \mathbf{l}_2, \dots, \mathbf{l}_n$ the rows of A_n . Let $X \in \mathbf{O}_n(\mathbf{e}_1)$. The first row of the matrix XA_n has the entries

$$\langle \mathbf{e}_1, \mathbf{c}_1 \rangle = u_1, \langle \mathbf{e}_1, \mathbf{c}_2 \rangle = u_2, \dots, \langle \mathbf{e}_1, \mathbf{c}_n \rangle = u_n,$$

whence $XA_n \in \mathbf{O}_n(\mathbf{u})$.

Let $Y \in \mathbf{O}_n(\mathbf{u})$. There exists a unique $X \in \mathbf{O}_n(\mathbb{R})$ such that $XA_n = Y$. We have to prove that $X \in \mathbf{O}_n(\mathbf{e}_1)$. From $XA_n = Y$ we have $X = YA_n^{-1} = YA_n^T$. The components of the first row of X are

$$\begin{aligned} \langle \mathbf{u}, \mathbf{l}_1 \rangle &= \langle \mathbf{l}_1, \mathbf{l}_1 \rangle = 1, \\ \langle \mathbf{u}, \mathbf{l}_2 \rangle &= \langle \mathbf{l}_1, \mathbf{l}_2 \rangle = 0, \\ &\dots \\ \langle \mathbf{u}, \mathbf{l}_n \rangle &= \langle \mathbf{l}_1, \mathbf{l}_n \rangle = 0, \end{aligned}$$

and thus $X \in \mathbf{O}_n(\mathbf{e}_1)$. ■

Using Proposition 1.3, an immediate consequence is the following theorem.

Theorem 1.5 Let $\mathbf{u} \in B_n(\mathbf{0}, 1)$ and $A_n \in \mathbf{O}_n(\mathbf{u})$. Then every matrix $Y_n \in \mathbf{O}_n(\mathbf{x})$ can be written as

$$Y_n = X_n A_n, \text{ with } X_n = \left[\begin{array}{c|ccc} 1 & 0 & \dots & 0 \\ \hline 0 & & & \\ \vdots & & \widetilde{X}_{n-1} & \\ 0 & & & \end{array} \right] \in \mathbf{O}_n(\mathbf{e}_1), \quad \widetilde{X}_{n-1} \in \mathbf{O}_{n-1}(\mathbb{R}). \quad (1.24)$$

Thus, for arbitrary $n \in \mathbb{N}$ and for a given $\mathbf{x} \in B_n(\mathbf{0}, 1)$, we will be able to construct matrices in $\mathbf{O}_n(\mathbf{x})$ recursively, if only a matrix A_k in each set $\mathbf{O}_k(\mathbf{x})$, $k = 2, 3, \dots, n$, is given. A simple way of construction such matrices will be given in the next section.

A choice for the matrices A_n and \tilde{X}_{n-1}

As we have seen, in our particular problem we are interested in constructing matrices $A_k \in \mathbf{O}_k(\mathbf{u}_k)$, for $k = 2, 3, \dots, n$, where

$$\mathbf{u}_k = \frac{1}{\sqrt{k}} (1, 1, \dots, 1) \in B_k(\mathbf{0}, 1).$$

If one such matrix A_k is given for each $k = 2, 3, \dots, n$ then we can obtain a whole class of matrices in $\mathbf{O}_n(\mathbf{u}_n)$ by using formula (1.24). The entries of these matrices will lead to wavelets, by (1.20) and (1.22).

We define the following vectors in \mathbb{R}^k :

$$\begin{aligned} \mathbf{v}_1 &= (1, 1, 1, \dots, 1), & \|\mathbf{v}_1\| &= \sqrt{k}, \\ \mathbf{v}_2 &= (1, -1, 0, 0, \dots, 0), & \|\mathbf{v}_2\| &= \sqrt{2}, \\ \mathbf{v}_3 &= (1, 1, -2, 0, \dots, 0), & \|\mathbf{v}_3\| &= \sqrt{6}, \\ \mathbf{v}_4 &= (1, 1, 1, -3, 0, \dots, 0), & \|\mathbf{v}_4\| &= \sqrt{12}, \\ & \dots & & \\ \mathbf{v}_k &= (1, 1, \dots, 1, -k + 1), & \|\mathbf{v}_k\| &= \sqrt{k(k-1)}. \end{aligned}$$

A simple calculation shows that the matrix A_k , which has on the rows the normalized vectors $\mathbf{r}_i = \mathbf{v}_i / \|\mathbf{v}_i\|$, $i = 1, 2, \dots, k$, will belong to $\mathbf{O}_k(\mathbf{u}_k)$.

Let us remark the fact that one can obtain the matrix $A_{k+1} \in \mathbf{O}_{k+1}(\mathbf{u}_{k+1})$ from the already determined matrix A_k , as follows:

- replace the first row of A_k with $\frac{1}{\sqrt{k+1}}(1, 1, \dots, 1) \in \mathbb{R}^k$;
- add the row $k + 1$ containing the vector $\frac{1}{\sqrt{k(k+1)}}(1, 1, \dots, 1) \in \mathbb{R}^k$;
- add the column $k + 1$ containing the vector $\frac{1}{\sqrt{k+1}}(1, 0, \dots, 0, -\sqrt{k})^T \in \mathbb{R}^{k+1}$.

For example, the Haar matrix of dimension 4 given in (1.23) can be written as

$$H = \left[\begin{array}{c|ccc} 1 & 0 & \dots & 0 \\ \hline 0 & & & \\ \vdots & & \tilde{X}_3 & \\ 0 & & & \end{array} \right] A_4, \quad \text{with } \tilde{X}_3 = \begin{bmatrix} 0 & \frac{2}{\sqrt{6}} & \frac{1}{\sqrt{3}} \\ \frac{1}{\sqrt{2}} & \frac{1}{\sqrt{6}} & -\frac{1}{\sqrt{3}} \\ \frac{1}{\sqrt{2}} & -\frac{1}{\sqrt{6}} & \frac{1}{\sqrt{3}} \end{bmatrix} \in \mathbf{O}_3(\mathbb{R}). \quad (1.25)$$

Concerning the matrices \tilde{X}_{k-1} , any orthogonal matrix of dimension $k - 1$ is suitable, including A_k and the matrices obtained from A_k by permuting its rows and columns. An alternative is to apply Gram-Schmidt procedure to any given non-orthogonal matrix, but this can be computationally expensive. Another simple choice, easy to construct, is the following.

We define the following vectors in \mathbb{R}^k :

$$\begin{aligned} \mathbf{w}_1 &= (1, -1, 1, -1, \dots, (-1)^{k+1}), & \|\mathbf{w}_1\| &= \sqrt{k}, \\ \mathbf{w}_2 &= (1, 1, 0, 0, \dots, 0), & \|\mathbf{w}_2\| &= \sqrt{2}, \\ \mathbf{w}_3 &= (-1, 1, 2, 0, \dots, 0), & \|\mathbf{w}_3\| &= \sqrt{6}, \\ \mathbf{w}_4 &= (1, -1, 1, 3, 0, \dots, 0), & \|\mathbf{w}_4\| &= \sqrt{12}, \\ \mathbf{w}_5 &= (-1, 1, -1, 1, 4, 0, \dots, 0), & \|\mathbf{w}_5\| &= \sqrt{20}, \\ & \dots & & \\ \mathbf{w}_k &= ((-1)^k, (-1)^{k+1}, \dots, (-1)^{k+k-2}, k-1), & \|\mathbf{w}_k\| &= \sqrt{k(k-1)}. \end{aligned}$$

As before, the matrix \tilde{X}_k , whose rows and columns are the vectors $\mathbf{w}_i/\|\mathbf{w}_i\|$, $i = 1, 2, \dots, k$, belongs to $\mathbf{O}_k(\mathbb{R})$. One can consider, of course, any permutation of its rows and columns, and the matrix \tilde{X}_3 in (1.25) is one of these matrices.

Conclusions

The merit of our construction is that it extends the constructions of some piecewise constant orthonormal wavelet bases. By a suitable choice of the domains and their subdivision, one can obtain directional wavelet bases.

1.4 Sparse image representation using Easy Path Wavelet Transform

The **Easy Path Wavelet Transform** (EPWT) has recently been proposed by G. Plonka [83] as a tool for sparse representations of bivariate functions from discrete data, in particular from image data. The EPWT is a locally adaptive wavelet transform. It works along pathways through the array of function values and exploits the local correlations of the given data in a simple appropriate manner. However, the EPWT suffers from its adaptivity costs that arise from the storage of path vectors. In [85], we proposed a new hybrid method for image approximation that exploits the advantages of the usual tensor product wavelet transform for the representation of smooth images and uses the EPWT for an efficient representation of edges and texture. Numerical results show the efficiency of this procedure.

In the one-dimensional case, wavelets provide optimal representations of piecewise smooth functions. Unfortunately, in two dimensions, tensor product wavelet bases are suboptimal for representing geometric structures as edges and texture, since their support is not adapted to directional geometric properties. Only in case of globally smooth images, they provide optimally sparse representations.

Many different approaches have been developed to design approximation schemes that aim at a more efficient representation of two-dimensional data. Curvelets [22], shearlets [52], contourlets [38], wedgelets [39, 69] and directional wavelets on triangles [60] are examples of non-adaptive highly redundant function frames with a strong anisotropic directional selectivity. However, while theoretical results show their good performance for sparse representation of piecewise smooth images with discontinuities along smooth curves [22, 53], these frames cannot be applied for image compression. On the one hand, the known curvelet/shearlet algorithms do not get completely rid of the redundancy of the underlying function systems, see e.g. [26]. On the other hand, the almost optimal image representation has so far only been proven for images with edges along C^2 -curves.

Instead of choosing an a priori a basis or a frame to approximate an image u , one can rather adapt the approximation scheme to the image geometry. Different approaches have been developed in this direction [9, 30, 35, 39, 56, 61, 67, 74]. Le Pennec and Mallat [67] proposed bandelet orthogonal bases and frames that adapt the geometric regularity of the data. Dekel and Leviatan [35] introduced a geometric wavelet transform based on an adaptive binary partition of the image domain to match the geometric feature of the image. Krommweh [61] proposed an adaptive Haar-like wavelet transform, named tetrolet transform, which allows the so-called tetromino partitions such that the local image geometry is taken into account. In [36], an image compression scheme based on piecewise linear functions over an optimized triangulation has been constructed. Further, nonlinear edge adapted multiscale decompositions based on essentially non-oscillatory (ENO) schemes have been extensively investigated [9, 30].

The adaptive methods suggested so far either usually suffer from a time-consuming implementation and not negligible adaptivity cost [35, 39, 67, 74], or, if based on generalized lifting schemes where no adaptivity costs occur [9, 30], suffer from stability problems and do only slightly improve the results of tensor-product wavelet transform. For example, bandelets as described in [67] require an involved construction of wavelet bases along regularity flows of the image. The second generation bandelet transform [82] uses a usual wavelet filter bank followed by adaptively chosen directional orthogonal filters. A complete representation of an image in a bandelet basis is then composed of an image segmentation at each scale 2^j (by a quadtree) and, beside the bandelet coefficients, one has to store the segmentation and the polynomial flow for each dyadic square. The idea of a nonlinear locally adaptive easy path wavelet transform (EPWT) has been explored in [83] for sparse image representations. The EPWT is slightly related with the idea of grouplets [74], where one applies a weighted Haar wavelet transform to points that are grouped by a so-called association field. The main idea of the EPWT is as follows. In a first step, one determines a “path vector” through all indices of a given (two-dimensional) index set of the image. Starting with a suitable index (the corresponding image value), we apply a “best neighbor strategy” such that on the one hand adjacent pixels in the path are neighbor pixels in the image, and on the other hand the corresponding adjacent image values are strongly correlated. The complete path vector can be seen as a permutation of the original index vector. Then, one level of a (one-dimensional) wavelet transform is applied to the image values along the path vector and the choice of the path will ensure that most wavelet coefficients remain small. In the following levels, one needs to find path vectors through index sets of a low-pass image and applies again the wavelet transform. After a suitable number of iterations, we apply a shrinkage procedure to all wavelet coefficients in order to find a sparse digital representation of the function. For reconstruction one needs the path vector at each level in order to apply the inverse wavelet transform.

1.4.1 Notations and description of the EPWT

We remind the detailed description of the EPWT given in [83]. We start with the decomposition of the real data $\{\mathbf{f}(\nu), \nu \in J\}$, $J = \{1, 2, \dots, N\}$, and we assume that $N = |J|$ is a multiple of 2^L with $L \in \mathbb{N}$. Then we will be able to apply L levels of the EPWT. We denote by $\mathcal{N}(\nu)$, $\mathcal{N}(\nu) \subseteq J \setminus \{\nu\}$ the neighborhood of an index ν . For example, for a 2D image, one can choose $\mathcal{N}(\nu)$ as the set of eight pixels around ν . If \mathbf{f} represents the values of a function on a triangulation $\mathcal{T} = \{T_j, j \in J\}$, then one can define $\mathcal{N}(\nu)$ as the set of indices $\mu \neq \nu$ such that T_ν and T_μ have a common edge.

Decomposition

First level

We first determine a complete path vector \mathbf{p}^L through the index set J and then apply a suitable discrete one-dimensional (periodic) wavelet transform to the function values along this path \mathbf{p}^L .

We start with $\mathbf{f}^L = \mathbf{f}$ and $\mathbf{p}^L(1) = 1$. In order to determine the second index $\mathbf{p}^L(2)$, we seek the minimum of absolute differences of the function values corresponding to the neighborhood of the index 1, and put

$$\mathbf{p}^L(2) = \underset{k}{\operatorname{argmin}} \{|\mathbf{f}^L(1) - \mathbf{f}^L(k)|, k \in \mathcal{N}(1)\}.$$

We proceed in this manner, thereby determining a path vector through the index set J that is locally adapted to the function f (easy path). With the procedure above we obtain a pathway

such that the absolute differences between neighboring function values $\mathbf{f}^L(l)$ along the path stay as small as possible. Generally, having given the index $\mathbf{p}^L(l)$, $1 \leq l \leq N-1$, we determine the next value $\mathbf{p}^L(l+1)$ by

$$\mathbf{p}^L(l+1) = \operatorname{argmin}_k \{|\mathbf{f}^L(\mathbf{p}^L(l)) - \mathbf{f}^L(k)|, k \in \mathcal{N}(\mathbf{p}^L(l)), k \neq \mathbf{p}^L(\nu), \nu = 1, \dots, l\}.$$

It can happen that the choice of the next index value $\mathbf{p}^L(l+1)$ is not unique, if the above minimum is attained by more than one index. In this case, one may just fix favorite directions in order to determine a unique pathway.

Another situation can occur during the procedure, namely that all indices in the neighborhood of a considered index $\mathbf{p}^L(l)$ have already been used in the path \mathbf{p}^L . In this case we need to start with a new pathway, i.e., we have an interruption in the path vector. We need to choose one index $\mathbf{p}^L(l+1)$ from the remaining indices in J that have not been taken in \mathbf{p}^L yet. There are different possibilities for starting the next pathway. One simple choice is to take just the smallest index from J that has not been used so far. Another choice is to look for a next index, such that again the absolute difference $|\mathbf{f}^L(\mathbf{p}^L(l)) - \mathbf{f}^L(\mathbf{p}^L(l+1))|$ is minimal, i.e., we take in this case

$$\mathbf{p}^L(l+1) = \operatorname{argmin}_k \{|\mathbf{f}^L(\mathbf{p}^L(l)) - \mathbf{f}^L(k)|, k \in J, k \neq \mathbf{p}^L(\nu), \nu = 1, \dots, l\}.$$

We proceed in this manner and obtain finally a complete path vector $\mathbf{p}^L \in \mathbb{Z}^N$ that is a permutation of $(1, 2, \dots, N)$.

After having constructed the path \mathbf{p}^L , we apply one level of the discrete one-dimensional Haar wavelet transform or any other discrete orthogonal or biorthogonal periodic wavelet transform to the vector of function values $(\mathbf{f}^L(\mathbf{p}^L(l)))_{l=1}^N$ along the path \mathbf{p}^L . We find the vector $\mathbf{f}^{L-1} \in \mathbb{R}^{N/2}$ containing the low-pass part and the vector of wavelet coefficients $\mathbf{g}^{L-1} \in \mathbb{R}^{N/2}$. While the wavelet coefficients will be stored in \mathbf{g}^{L-1} , we proceed further with the low-pass vector \mathbf{f}^{L-1} at the second level.

Remark. For the numerical implementation, the method for choosing the start index of a new pathway has essential consequences. The simple method to take the smallest “free” index is also the cheapest with regard to the storing costs for the path, but for each new pathway one may produce a big wavelet coefficient. The second method (preferred here), avoids big wavelet coefficients but leads to higher costs for storing the path \mathbf{p}^L . Plonka [83] has proposed an efficient method for index selections, that finds a compromise between these issues.

Second level

Let us consider the index sets $J_l^{L-1} := \{\mathbf{p}^L(2l-1), \mathbf{p}^L(2l)\}$, $l = 1, \dots, N/2$, that determine a partition of J . Now, each such index set J_l^{L-1} corresponds to the function value $\mathbf{f}^{L-1}(l)$. We repeat the same procedure as in the first step, but replacing the single indices with corresponding function values by the new index sets J_l^{L-1} and the corresponding smoothed function values $\mathbf{f}^{L-1}(l)$. The new path vector $\mathbf{p}^{L-1} \in \mathbb{Z}^{N/2}$ should now be a permutation of $(1, 2, \dots, N/2)$. We start again with the first index set J_1^{L-1} , i.e., $\mathbf{p}^{L-1}(1) = 1$. Having already found $\mathbf{p}^{L-1}(l)$, $1 \leq l \leq N/2 - 1$, we determine the next value $\mathbf{p}^{L-1}(l+1)$ by

$$\begin{aligned} \mathbf{p}^{L-1}(l+1) &= \operatorname{argmin}_k \{|\mathbf{f}^{L-1}(\mathbf{p}^{L-1}(l)) - \mathbf{f}^{L-1}(k)|, J_k^{L-1} \in \mathcal{N}(J_{\mathbf{p}^{L-1}(l)}^{L-1}), \\ &\quad k \neq \mathbf{p}^{L-1}(\nu), \nu = 1, \dots, l\}. \end{aligned}$$

If the new value $\mathbf{p}^{L-1}(l+1)$ is not uniquely determined by the minimizing procedure, we can just fix favorite directions in order to obtain a unique path. If for the set $J_{\mathbf{p}^{L-1}(l)}^{L-1}$ there is

no neighbor index set that has not been used yet in the path vector \mathbf{p}^{L-1} , then we have to interrupt the path and to find a new good index set (that has been not used so far) to start a new pathway. As in the first level, we try to keep the differences of function values along the path small and may choose in this case

$$\mathbf{p}^{L-1}(l+1) = \underset{k}{\operatorname{argmin}} \{ |\mathbf{f}^{L-1}(\mathbf{p}^{L-1}(l)) - \mathbf{f}^{L-1}(k)|, 1 \leq k \leq N/2, \\ k \neq \mathbf{p}^{L-1}(\nu), \nu = 1, \dots, l \}.$$

After having completed the path vector \mathbf{p}^{L-1} , we apply again the chosen discrete (periodic) wavelet transform to the vector $(\mathbf{f}^{L-1}(\mathbf{p}^{L-1}(l)))_{l=1}^{N/2}$ along the path \mathbf{p}^{L-1} . Assuming that $N/4 \in \mathbb{N}$, i.e. $L \geq 2$, we obtain the vector $\mathbf{f}^{L-2} \in \mathbb{R}^{N/4}$ containing the low-pass part and the vector of wavelet coefficients $\mathbf{g}^{L-2} \in \mathbb{R}^{N/4}$. While the wavelet coefficients in \mathbf{g}^{L-2} will be stored, we proceed now again with the low-pass vector \mathbf{f}^{L-2} in the next step.

Further levels

If N is of the form $2^L s$ with $s \in \mathbb{N}$ being greater than or equal to the lengths of low-pass and high-pass filters in the chosen discrete wavelet transform, then we may apply the procedure L times. For a given vector \mathbf{f}^{L-j} , $0 < j < L$, we consider in the $(j+1)$ -th step the index sets

$$J_l^{L-j} = J_{\mathbf{p}^{L-j+1}(2l-1)}^{L-j+1} \cup J_{\mathbf{p}^{L-j+1}(2l)}^{L-j+1}, \quad l = 1, \dots, N/2^j,$$

with the corresponding function values $\mathbf{f}^{L-j}(l)$. Then we determine a path vector \mathbf{p}^{L-j} of length $N/2^j$ as a permutation of $(1, 2, \dots, N/2^j)$, as before. Finally, we apply the (periodic) wavelet transform to the vector $(\mathbf{f}^{L-j}(\mathbf{p}^{L-j}(l)))_{l=1}^{N/2^j}$ along the path \mathbf{p}^{L-j} , thereby obtaining the low-pass vector $\mathbf{f}^{L-j-1} \in \mathbb{R}^{N/2^{j+1}}$ and the vector of wavelet coefficients $\mathbf{g}^{L-j-1} \in \mathbb{R}^{N/2^{j+1}}$.

Output

As output of the complete procedure after L iterations we obtain the coefficient vector

$$\mathbf{g} = (\mathbf{f}^0, \mathbf{g}^0, \mathbf{g}^1, \dots, \mathbf{g}^{L-1}) \in \mathbb{R}^N$$

and the vector determining the paths in each iteration step

$$\mathbf{p} = (\mathbf{p}^1, \mathbf{p}^2, \dots, \mathbf{p}^L) \in \mathbb{R}^{2N(1-1/2^L)}.$$

These two vectors contain the entire information about the original function f .

In order to find a sparse representation of f , we apply a *shrinkage procedure* to the wavelet coefficients in the vectors \mathbf{g}^j , $j = 0, \dots, L-1$, and obtain $\tilde{\mathbf{g}}^j$. Here one can use the hard threshold function

$$S_\sigma(x) = \begin{cases} x, & |x| \geq \sigma, \\ 0, & |x| < \sigma. \end{cases}$$

Reconstruction

The reconstruction of (the approximation) \tilde{f} resp. $\tilde{\mathbf{f}}^L$ from $\tilde{\mathbf{g}}$ and \mathbf{p} is given as follows.

For $j = 0$ to $L-1$ do

Apply the inverse discrete wavelet transform to the vector $(\tilde{\mathbf{f}}^j, \tilde{\mathbf{g}}^j) \in \mathbb{R}^{r2^j}$

(with $\tilde{\mathbf{f}}^0 := \mathbf{f}^0$) in order to obtain $\tilde{\mathbf{f}}_p^{j+1} \in \mathbb{R}^{r2^{j+1}}$.

Apply the permutation

$$\tilde{\mathbf{f}}^{j+1}(\mathbf{p}^{j+1}(k)) = \tilde{\mathbf{f}}_p^{j+1}(k), \quad k = 1, \dots, r2^{j+1}.$$

end.

In Section 4.5 we illustrate the EPWT on triangulations of the sphere and we also take a simple example to illustrate the EPWT.

1.4.2 A hybrid-model for image approximation

In this section, we will exploit the advantages of the well-known tensor-product wavelet transform for representation of smooth images and the ability of the adaptive EPWT to represent edges and texture in images. For that purpose, we propose a new hybrid method for image approximation that (roughly) consists of the following steps.

For a given digital image $u^0 = (u^0(i, j))_{i=1, j=1}^{N_1, N_2}$, we first try to find a suitable separation $u^0 = u^{sm} + u^r$, where u^{sm} is globally smooth, and the difference image u^r contains the remaining part of the image (i.e. edges and texture). The separation will be done by a simple smoothing of u^0 based on local smoothing filters. Then the usual tensor product wavelet transform is applied to the smooth image u^{sm} . Here we exploit the fact that smooth functions can be optimally represented by an M -term wavelet expansion u_M^{sm} .

In the next step, the EPWT is applied to the (shrunk) difference image $u^0 - u_M^{sm}$. Assuming that the original image u^0 is piecewise smooth, the difference image $u^0 - u_M^{sm}$ contains a high number of components with very small absolute value. Therefore, we consider a shrunk version $\tilde{u}^r = S(u^0 - u_M^{sm})$ possessing a smaller number of nonzero values. In our numerical experiments, we shrink the difference, such that \tilde{u}^r contains only $N_1 N_2 / 4$ nonzero values. The EPWT is now applied only to the nonzero values of \tilde{u}^r , and the adaptivity costs can be strongly reduced compared with the EPWT for a full image.

Finally, we obtain a very good image approximation as a sum of the M -term wavelet expansion u_M^{sm} of the smooth image part and the N -term EPWT wavelet expansion u_N^r of the difference image.

The results are published in [85].

Separation of images and tensor-product wavelet transform

We are interested in a segmentation of our image u into a “smooth” part u^{sm} and a remainder u^r that contains information about edges and textures. Note that this separation issue is different from image separation problems usually considered for image denoising, where one aims to separate an image into a cartoon part, i.e. a piecewise smooth function (smooth part together with edges of finite length), and a texture part, see e.g. [18, 28, 124] and others.

We suppose that the main portion of the considered image is regular outside a set of (piecewise) regular curves and that the image contains only a small amount of texture.

In our experiments we iteratively apply a smoothing filter based on linear diffusion, namely

$$\begin{aligned} u^{k+1}(i, j) &= u^k(i, j) + \tau (u^k(i+1, j) + u^k(i-1, j) \\ &\quad + u^k(i, j-1) + u^k(i, j+1) - 4u^k(i, j)) \end{aligned} \quad (1.26)$$

for $i = 1, \dots, N_1, j = 1, \dots, N_2$, with Neumann boundary conditions. The parameter τ controls the amount of smoothing in each step. Using K iterations of the smoothing filter, we obtain a smoothed image $u^{sm} = (u^K(i, j))_{i=1, j=1}^{N_1, N_2}$, where K can be suitably taken depending on the image. Our numerical experiments show that $K = 5$ is already a good choice (compare Table 1.5).

Alternatively, other smoothing filters can be used at this step resulting in similar images u^{sm} . For example, a Gaussian standard smoothing filter can be applied, or we can use a low-pass image obtained by a translation-invariant wavelet transform.

Let a function f be Hölder-continuous of order α in $\Omega = [0, N_1] \times [0, N_2]$ and let the M -term separable wavelet approximation f_M be obtained by keeping only the M wavelet coefficients with the largest absolute value in a wavelet basis representation of f . Then for a sufficiently

smooth wavelet basis we have [72]

$$\|f - f_M\|_2^2 < CM^{-\alpha}.$$

The decay exponent $-\alpha$ is optimal, i.e., tensor product wavelet bases are optimal for sparse representation of smooth images. Therefore we apply the tensor product wavelet transform to the obtained smoothed digital image u^{sm} (or to a slightly different image \tilde{u}^{sm}). Using only a fixed number of M most significant wavelet coefficients in the wavelet representation, we obtain an approximation u_M^{sm} of u^{sm} after wavelet reconstruction. In our numerical experiments we use the well-known 9/7 biorthogonal filter bank and $D4$ orthonormal Daubechies wavelets. As usual, the image u_M^{sm} is then obtained by a decomposition algorithm, a shrinkage procedure and a wavelet reconstruction.

The EPWT for sparse edge representation

Let u be the original digital image and \tilde{u}_M^{sm} the M -term wavelet approximation of the smoothed image \tilde{u}^{sm} obtained by a linear smoothing process (and a slight modification based on shrinkage). Now we consider the difference image $u^r = u - \tilde{u}_M^{sm}$ that mostly contains edges and texture. We want to apply a new locally adaptive wavelet transform to this difference image, the easy path wavelet transform (EPWT). While the EPWT has been shown to be very efficient for sparse image representation [83, 86], we have to keep in mind its adaptivity costs for the storage of path vectors. In order to exploit the ability of the EPWT to sparsely represent edges and texture and, at the same time, to keep adaptivity costs small, we suggest to apply the EPWT not to the complete image u^r , but only to the part with essential image information.

Supposing that the original image u mainly contains piecewise regular regions, which will be hardly changed by the smoothing process, the difference image $u^r = u - \tilde{u}_M^{sm}$ possesses many very small image values. Therefore, we apply first a shrinkage procedure to u^r and obtain $\tilde{u}^r = (\tilde{u}^r(i, j))_{i=1, j=1}^{N_1, N_2}$ with $\tilde{u}^r(i, j) := S_\theta u^r(i, j)$, where

$$S_\theta x := \begin{cases} x, & \text{if } |x| \geq \theta, \\ 0, & \text{if } |x| < \theta. \end{cases} \quad (1.27)$$

The shrinkage parameter θ should be chosen dependently on the image at hand in such a way that \tilde{u}^r contains exactly 2^J nonzero image values, where $2^J < N_1 N_2$. In our numerical experiments, we have taken θ such that \tilde{u}^r has only $\frac{1}{4} N_1 N_2$ nonzero values; these values are situated along the edges/texture of u . Now we apply the EPWT only along the nonzero values of \tilde{u}^r while the vanishing values remain untouched. More precisely, we only consider the partial image \tilde{u}^r containing the image values corresponding to the index set

$$I_J := \{(i, j) \mid 1 \leq i \leq N_1, 1 \leq j \leq N_2, |u^r(i, j)| \geq \theta\} \quad (1.28)$$

of size 2^J .

In order to obtain a sparse representation of \tilde{u}^r , we again apply the hard threshold function S_σ in (1.27), to the EPWT-wavelet coefficients. By taking only a fixed number of N most significant EPWT wavelet coefficients, we obtain an EPWT approximation \tilde{u}_N^r of the difference image \tilde{u}^r (after reconstruction).

Algorithm 1 (New hybrid algorithm)

Input: digital image $u^0 = (u^0(i, j))_{i=1, j=1}^{N_1, N_2}$.

1 Apply an iterative local smoothing filter for image separation:

Fix $\tau > 0$ and $K \in \mathbb{N}$.

For $k = 1, \dots, K$ **do**

$u^k(i, j) := u^{k-1}(i, j) + \tau(u^{k-1}(i+1, j) + u^{k-1}(i-1, j) + u^{k-1}(i, j-1) + u^{k-1}(i, j+1) - 4u^{k-1}(i, j))$, using Neumann boundary conditions.

end

Put $u^{sm} := (u^K(i, j))_{i=1, j=1}^{N_1, N_2}$.

2 Apply a shrinkage procedure to the difference image $d = u^0 - u^{sm}$ by a hard threshold procedure.

Choose a θ such that $\tilde{d}(i, j) := S_\theta d(i, j)$ possesses exactly 2^J nonzero image values, where $2^J < N_1 N_2$.

Now compute a (slightly changed) smooth part of the original image u^0 , namely $\tilde{u}^{sm} := u^0 - \tilde{d} = u^0 - S_\theta d$.

3 Apply a usual wavelet shrinkage procedure to the smoothed image \tilde{u}^{sm} using an orthogonal or biorthogonal two-dimensional wavelet transform. Let \tilde{u}_M^{sm} be the approximation of \tilde{u}^{sm} that is reconstructed using only the M most significant wavelet coefficients.

4 Consider the difference image $u^r := u^0 - \tilde{u}_M^{sm}$ that contains edges and texture. Apply again a shrinkage procedure to u^r obtaining $\tilde{u}^r = S_\theta u^r$, where \tilde{u}^r possesses exactly 2^J nonzero image values.

5 Apply the EPWT with shrinkage to the detail image \tilde{u}^r , where only the nonzero coefficients of \tilde{u}^r are used. Let \tilde{u}_N^r be the approximation of \tilde{u}^r using only the N most significant EPWT wavelet coefficients.

Output: Then $\tilde{u}^0 := \tilde{u}_M^{sm} + \tilde{u}_N^r$ is an approximation of u^0 where we have used only $M + N$ wavelet coefficients.

For the illustration of the above algorithm, we present an example, where the partial results after each step of the algorithm are displayed.

The original image u^0 in Figure 1.7(a) shows a 256×256 -part of the image “sails”. After the first step of our algorithm, we get a smoothed version u^{sm} , see Figure 1.7(b). In this example, we have used the smoothing filter in (1.26) with $\tau = 0.17$ and $K = 5$. Now we apply the second step, i.e., we calculate a difference image, keep the 16384 components with largest absolute values, and add the other values to u^{sm} . In this way we obtain a slightly changed smooth image \tilde{u}^{sm} , see Figure 1.7(c). Compared with u^{sm} , it contains slightly more details; the numbers on the sails are a bit less blurry now.

According to step 3 of the algorithm, we apply a wavelet shrinkage procedure with a hard threshold to \tilde{u}^{sm} , and keep only 1200 coefficients; here we use 5 levels of the biorthogonal 9/7-wavelet filter bank. We obtain \tilde{u}_{1200}^{sm} , see Figure 1.7(d). The difference image $u^r = u^0 - \tilde{u}_{1200}^{sm}$ is presented in Figure 1.7(e). (The image shown here contains the absolute values of the difference and is inverted, i.e., white stands for 0 and black for 255). We apply again a shrinkage to this difference image keeping only $16384 = (256 \times 256)/4$ nonzero coefficients according to step 4 of the algorithm. Figure 1.7(f) shows an inverted version of the obtained difference $|\tilde{u}^r|$.

We apply the EPWT, and a hard threshold to keep only 800 EPWT wavelet coefficients of \tilde{u}^r . The reconstruction \tilde{u}_{800}^r is shown in Figure 1.7(g), again we present here the absolute values of its components, where white stands for zero and black for 255. Finally, we add the results of wavelet shrinkage \tilde{u}_{1200}^{sm} in Figure 1.7(d) and the result \tilde{u}_{800}^r of the EPWT shrinkage in Figure 1.7(g) and obtain the result in Figure 1.7(h). For comparison, we show in Figure 1.7(i)

the wavelet approximation of the original image by the 9/7-transform using 2000 nonzero-coefficients.

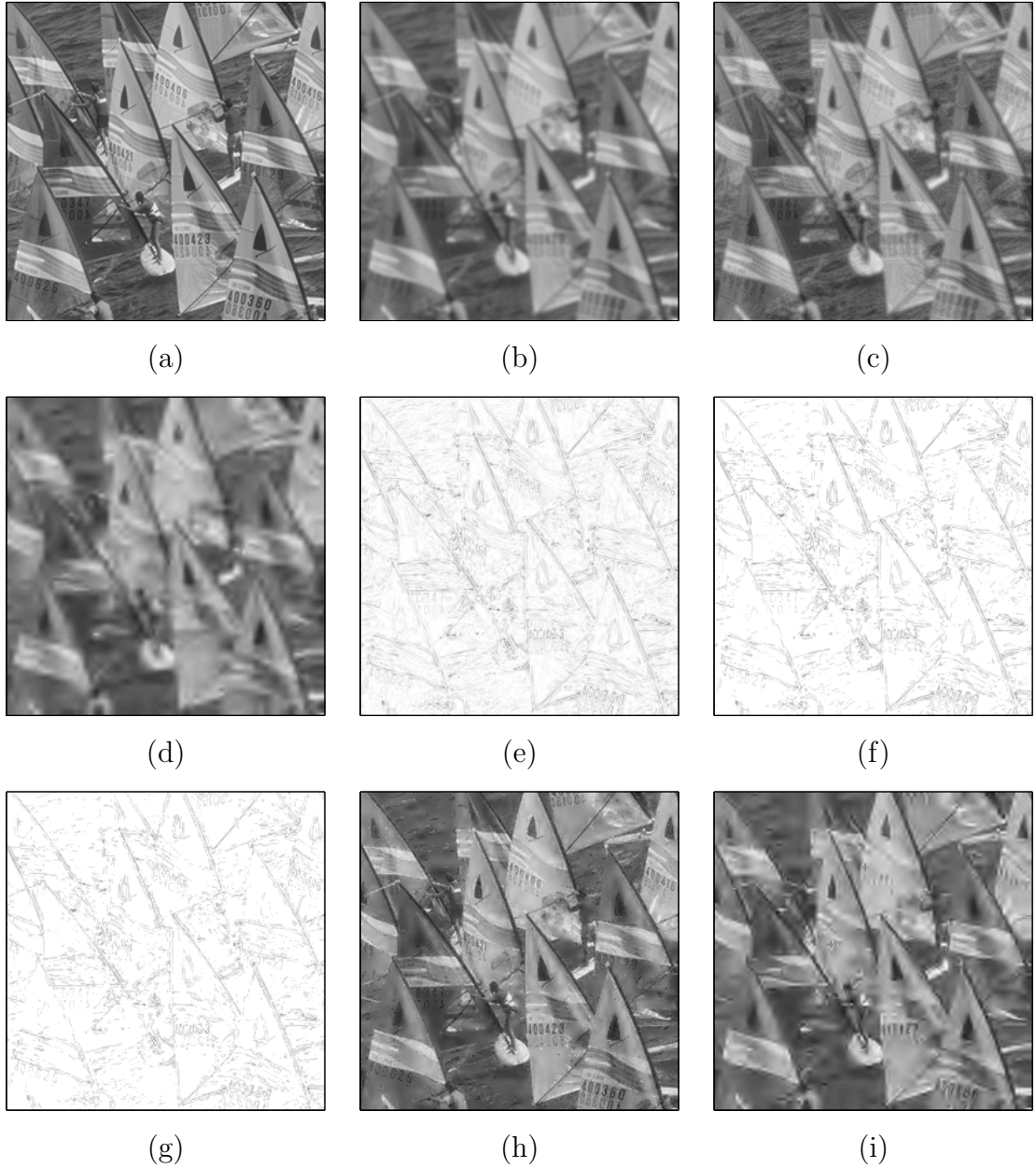


Figure 1.7: Illustration of the steps in Algorithm 1. (a) Original image, (b) smoothed image u^{sm} , (c) smoothed image \tilde{u}^{sm} , (d) wavelet approximation \tilde{u}_{1200}^{sm} , (e) difference u^r , absolute values, inverted, (f) shrunken difference \tilde{u}^r , inverted, (g) EPWT approximation \tilde{u}_{800}^r , inverted, (h) our approximation $\tilde{u}_{1200}^{sm} + \tilde{u}_{800}^r$ with 2000 coefficients, (i) tensor product biorthogonal 9/7 wavelet approximation with 2000 coefficients.

Application of the EPWT

In the sequel we describe the EPWT algorithm that we need to adapt here to a partial difference image. Let $I_J \subset \{(i, j) \mid i = 1, \dots, N_1, j = 1, \dots, N_2\}$ given in (1.28) with $|I_J| = 2^J < N_1 N_2$ be the index set of nonzero image values in the thresholded difference image $\tilde{u}^r = \tilde{u}^J = (\tilde{u}^J(i, j))_{(i, j) \in I_J}$.

We say that the nonzero value $\tilde{u}^J(i, j)$ corresponds to the index $(i, j) \in I_J$.

We define a neighborhood of an index $(i, j) \in I_J$ by

$$N(i, j) := \{(i_1, j_1) \in I_J \setminus \{(i, j)\} : |i - i_1| \leq 1, |j - j_1| \leq 1\}.$$

A vector of indices $(l_k, l_{k+1}, \dots, l_{k+n})$ with $l_k = (i_k, j_k)$ and with $1 \leq k < k+n \leq 2^J$ is called *connected* if we have $l_{r+1} \in N(l_r)$ for $r = k, \dots, k+n-1$. A connected vector of indices is called *pathway*.

For application of the first level of the EPWT, we need to find a complete path vector \mathbf{p}^J through the index set I_J . This first path vector $\mathbf{p}^J = (\mathbf{p}^J(n))_{n=1}^{2^J}$ is a suitable permutation of all indices in I_J , and contains the information on the position of the corresponding image values as well as about the order, in which the image values of \tilde{u}^r have to be used in the first level of the EPWT. In order to determine \mathbf{p}^J , we want to adapt the idea of the relaxed EPWT which has been introduced in [83] and use the following strategy.

Start with an arbitrary pixel $(i, j) \in I_J$, e.g., with $(i, j) \in I_J$ such that $i + N_1(j-1)$ is minimal, and put $\mathbf{p}^J(1) = (i, j)$. Now, for a given n th component $\mathbf{p}^J(n) = (\tilde{i}, \tilde{j})$, we choose the path vector's next component $\mathbf{p}^J(n+1)$ as follows. We consider the set of all pixels (i_1, j_1) in the neighborhood of $\mathbf{p}^J(n) = (\tilde{i}, \tilde{j})$ that are in I_J and have not been used yet in the path \mathbf{p}^J , i.e.

$$\tilde{N}(\mathbf{p}^J(n)) := (N(\mathbf{p}^J(n)) \cap I_J) \setminus \{\mathbf{p}^J(1), \dots, \mathbf{p}^J(n)\}.$$

The indices in $\tilde{N}(\mathbf{p}^J(n))$ are called “admissible” neighbor indices for $\mathbf{p}^J(n)$. If $\mathbf{p}^J(n)$ was in the neighborhood of $\mathbf{p}^J(n-1)$, i.e. $\mathbf{p}^J(n) \in \tilde{N}(\mathbf{p}^J(n-1))$, then we try to keep the “direction” of the path if the correlation of the corresponding image values is good enough, i.e., if the absolute value of the difference of the corresponding image values is smaller than a predetermined bound ϑ_1 . If this procedure is not possible since the wanted index is not admissible or the corresponding function values differ too much, then look clockwise through the admissible neighbor index of $\mathbf{p}^J(n)$ to find the first index that meets the bounding condition for the image values. If the set of admissible neighbors $\tilde{N}(\mathbf{p}^J(n))$ is empty, we have to start a new pathway. For example, one may take the new starting index of the next pathway such that its Euclidean distance to the last index of the preceding pathway is smallest. For other possible choices of a new starting index that can be coded efficiently, we refer to [83]. Indeed, the strategy above ensures that \mathbf{p}^J can be cheaply stored since keeping of path direction is preferred, and the bounding condition for the image values of adjacent indices in \mathbf{p}^J ensures mostly small differences of function values along the path and hence a small amount of significant wavelet coefficients. As it is extensively explained in [83], one may store only directions of the path, and non-changing directions in the path can be encoded with 0.

We proceed in this manner and determine a complete path vector $\mathbf{p}^J \in \mathbb{Z}^{2^J}$ that contains all indices of I_J as components. Let us illustrate the first path in the EPWT in a small example. We consider the difference between the original image in Figure 1.8(a) and the smoothed image in Figure 1.8(b), and apply a shrinkage keeping only 64 nonzero coefficients. In Figure 1.8(c), we show a model of the obtained thresholded difference image and the corresponding path vector $\mathbf{p}^6 \in \mathbb{Z}^{64}$ for the first level of EPWT. Here, gray corresponds to zero values, the darker pixels correspond to negative values and the brighter entries to positive values of the difference image.

Now we apply one level of a (periodic) discrete one-dimensional orthogonal or biorthogonal wavelet transform to the vector of function values $(\tilde{u}^J(\mathbf{p}^J(n)))_{n=1}^{2^J}$. We obtain a vector $\tilde{u}^{J-1} \in \mathbb{R}^{2^{J-1}}$ containing the low pass part and a vector of wavelet coefficients $g^{J-1} \in \mathbb{R}^{2^{J-1}}$. Then we proceed further with the low pass vector \tilde{u}^{J-1} at the second level.

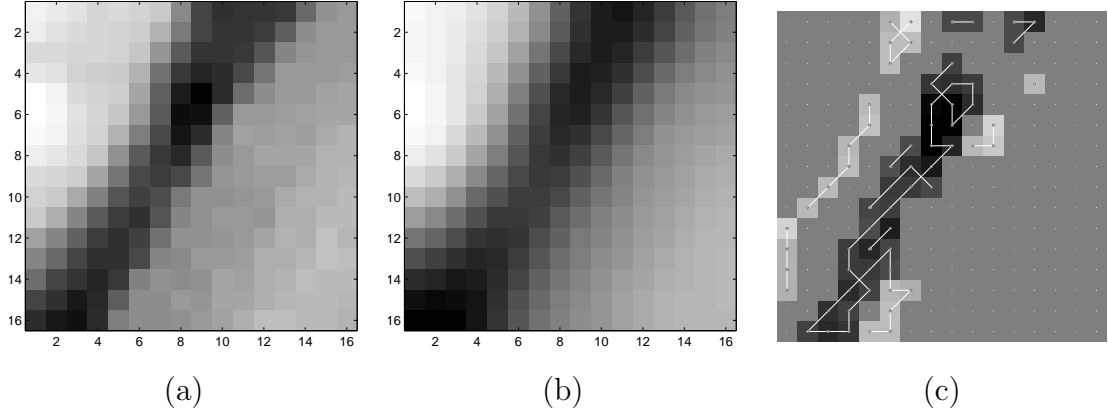


Figure 1.8: (a) Original image 16×16 , (b) Smoothed image, (c) Illustration of the shrunk difference with 64 nonzero values and of the first path of the EPWT.

The procedure for all further levels is now analogous as described in [83], where more details and simple examples are given. We may apply $J - s$ levels of the EPWT, supposing that the length of the used wavelet filters is smaller than or equal to 2^s .

At the second level we define the index sets

$$I_n^{J-1} := \mathbf{p}^J(2n-1) \cup \mathbf{p}^J(2n) \quad n = 1, \dots, 2^{J-1},$$

and we say that I_n^{J-1} corresponds to the low-pass value $\tilde{u}^{J-1}(n)$. Observe that, since adjacent indices in the path are usually neighbors in the image, I_n^{J-1} is (usually) a set of two adjacent pixels. Again we are looking for a path $\mathbf{p}^{J-1} \in \mathbb{Z}^{2^{J-1}}$ through the index sets I_n^{J-1} , where the components $\mathbf{p}^{J-1}(n)$ form now a permutation of the set $\{1, \dots, 2^{J-1}\}$. As before, this path vector should be cheap to store and the difference of function values of adjacent index sets in the path vector should be small in order to avoid large wavelet coefficients. We illustrate the idea in a further example at the end of the section.

Generally, for a given low pass vector \tilde{u}^{J-j} , $1 < j < J - s$, we consider the index sets

$$I_n^{J-j} := I_{\mathbf{p}^{J-j+1}(2n-1)}^{J-j+1} \cup I_{\mathbf{p}^{J-j+1}(2n)}^{J-j+1} \quad n = 1, \dots, 2^{J-j},$$

such that the low-pass value $\tilde{u}^{J-j}(n)$ corresponds to I_n^{J-j} .

If in the $(j+1)$ th level of the EPWT a path vector $\mathbf{p}^{J-j} \in \mathbb{Z}^{2^{J-j}}$ through the index sets I_n^{J-j} has been determined, then the wavelet transform is applied to the vector of function values $(\tilde{u}^{J-j}(\mathbf{p}^{J-j}(n)))_{n=1}^{2^{J-j}}$ along the path vector and we obtain the low pass values $\tilde{u}^{J-j-1} \in \mathbb{R}^{2^{J-j-1}}$ and the wavelet vector $g^{J-j-1} \in \mathbb{R}^{2^{J-j-1}}$.

For determining a path $\mathbf{p}^{J-j} \in \mathbb{Z}^{2^{J-j}}$ we fix again a starting index set, e.g. $\mathbf{p}^{J-j}(1) = 1$ (corresponding to I_1^{J-j}). Then for given $\mathbf{p}^{J-j}(n)$ we choose the next index set as follows.

First we determine all neighbor index sets of $I_{\mathbf{p}^{J-j}(n)}^{J-j}$, where we say that I_n^{J-j} and I_m^{J-j} are *neighbors* if there exist indices $k_1 \in I_n^{J-j}$ and $k_2 \in I_m^{J-j}$ with $k_1 \in N(k_2)$. Then these neighbor index sets can e.g. be ordered by “strength” of neighborhood, i.e. by the number of indices that are direct neighbors of a pixel in $I_{\mathbf{p}^{J-j}(n)}^{J-j}$. Finally, we define the next index $\mathbf{p}^{J-j}(n+1)$ from the set of admissible neighbor indices such that the corresponding image values are well correlated. Further strategies for determining path vectors that can be coded efficiently are described later, when we will present some numerical results.

Algorithm 2 (Forward EPWT algorithm)

Input: Decomposition level s , index set I_J , data $\tilde{u}^r = \tilde{u}^J := (\tilde{u}^J(i, j))_{(i, j) \in I_J}$.
For $j = 0, 1, \dots, s - 1$ **do**

- 1 Find a suitable path vector \mathbf{p}^{J-j} through the index set I_j (for $j = 0$), resp. through $\{I_n^{J-j} : n = 1, \dots, 2^{J-j}\}$.
- 2 Apply the 1D periodic wavelet transform (e.g. Daubechies D_4 or $9/7$ filter bank) to the vector $(\tilde{u}^{J-j}(\mathbf{p}^{J-j}(n)))_{n=1}^{2^{J-j}}$, i.e., to the vector of function values \tilde{u}^{J-j} along the path \mathbf{p}^{J-j} to obtain the vector of low-pass coefficients $\tilde{u}^{J-j-1} \in \mathbb{R}^{2^{J-j-1}}$ and the vector of EPWT wavelet coefficients $g^{J-j-1} \in \mathbb{R}^{2^{J-j-1}}$.
- 3 Store the wavelet coefficients in g^{J-j-1} and the path vector \mathbf{p}^{J-j} and go to the first step for low-pass components.

end

Output: EPWT wavelet vector $g = (g^{J-1}, g^{J-2}, \dots, g^{J-s})$, vector of low-pass coefficients \tilde{u}^{J-s} , path vector $\mathbf{p} = (\mathbf{p}^J, \mathbf{p}^{J-1}, \dots, \mathbf{p}^{J-s+1})$.

Algorithm 3 (Inverse EPWT algorithm)

Input: coefficient vectors \tilde{u}^{J-s} and $g^{J-s}, \dots, g^{J-2}, g^{J-1}$, path vector \mathbf{p} , decomposition level s .

For $j = J - s, \dots, J - 1$

- 1 Apply the inverse 1D periodic wavelet transform to the vector (\tilde{u}^j, g^j) in order to obtain $\tilde{u}_{\mathbf{p}}^{j+1}$.
- 2 Apply a permutation to reorder the data $\tilde{u}^{j+1}(\mathbf{p}^{j+1}(k)) := \tilde{u}_{\mathbf{p}}^{j+1}(k)$.

end

Output: reconstructed data \tilde{u}^J .

In order to illustrate the levels of the EPWT, we consider the small example in Figure 1.9. The numbered pixels in Figure 1.9(a) belong to the non-zero coefficients of the difference image, and pixels of the difference image that we do not consider are represented as white unnumbered squares. Gray values represent the image values. For simplicity, we have used here a one-dimensional numbering of the index set obtained by the bijective mapping $\gamma : (i, j) \rightarrow i + N_1(j - 1)$. To obtain the next components of the path, we apply the procedure described above. We start with $\mathbf{p}^4(1) = 1$. Since $\tilde{N}(\mathbf{p}^4(1)) = \{9\}$, it follows that $\mathbf{p}^4(2) = 9$. In this way we further find $\mathbf{p}^4(3) = 17$, $\mathbf{p}^4(4) = 25$, $\mathbf{p}^4(5) = 34$. Since $\tilde{N}(\mathbf{p}^4(5)) = \{35, 43\}$, we choose now the next path component such that $|\tilde{u}^4(\mathbf{p}^4(5)) - \tilde{u}^4(\mathbf{p}^4(6))|$ is minimal. Therefore, $\mathbf{p}^4(6) = 35$. Again, we have $\tilde{N}(\mathbf{p}^4(6)) = \{28, 43\}$, and looking at the corresponding image values, we find $\mathbf{p}^4(7) = 43$. Thus $\mathbf{p}^4(8) = 51$. Now $\tilde{N}(\mathbf{p}^4(8))$ is empty, and we need to start with a new pathway. We choose here the starting index with smallest Euclidean distance to $\mathbf{p}^4(8)$, i.e., $\mathbf{p}^4(9) = 28$. The complete path vector \mathbf{p}^4 is represented in Figure 1.9(a). Now, Figure 1.9(b) illustrates the obtained index sets $I_n^3 = \mathbf{p}^4(2n - 1) \cup \mathbf{p}^4(2n)$, $n = 1, \dots, 8$. After application of a one-dimensional (periodic) wavelet transform to $\tilde{u}^4(\mathbf{p}^4(n))_{n=1}^{16}$ along the path, we obtain 8 wavelet coefficients $(g^3(n))_{n=1}^8$ that need to be stored, and 8 low-pass coefficients $(\tilde{u}^3(n))_{n=1}^8$, where the values $\tilde{u}^3(n)$ correspond now to I_n^3 , $n = 1, \dots, 8$, and are illustrated by gray values in Figure 1.9(b).

At the second level of the EPWT, we have to choose a path \mathbf{p}^3 through the index sets I_n^3 in Figure 1.9(b). The simplest idea is to take $\mathbf{p}^3 = (1, 2, 3, 4, 5, 6, 7, 8)$, then the second level of wavelet transform would be just applied to $(\tilde{u}^3(n))_{n=1}^8$, and there are no further storage costs for the path (simple hybrid method). A better path \mathbf{p}^3 is illustrated in Figure 1.9(c). Since $|\tilde{u}^3(3) - \tilde{u}^3(5)| < |\tilde{u}^3(3) - \tilde{u}^3(4)|$, we take here $\mathbf{p}^3 = (1, 2, 3, 5, 6, 7, 8, 4)$. Finally, Figure 1.9(d) shows the new index sets $I^2(n)$, $n = 1, 2, 3, 4$ obtained from \mathbf{p}^3 in Figure 1.9(c). The path

vectors can efficiently be coded, see [83]. For example, in a rather naive approach, one may encode the path \mathbf{p}^4 in a first step by

$$((1, 1), 0, 0, 0, 1, 1, -2, 0; (1, -3), -3, -2, 0, -1, -1, -2, -2).$$

Here, $(1, 1)$ is the starting index, $(1, -3)$ encodes the difference between $\mathbf{p}^4(8)$ and $\mathbf{p}^4(9)$, and the numbers $-3, \dots, 3$ encode the directions of the path, where the path direction formed by the previous step is always encoded by 0, and for starting pathways, the 0-direction is “going to the right”. The above code also contains complete information about the index set I_4 itself, i.e., about the difference image. If the index set I_J is known in advance, then the storage of \mathbf{p}^4 can of course be managed in a more efficient manner.

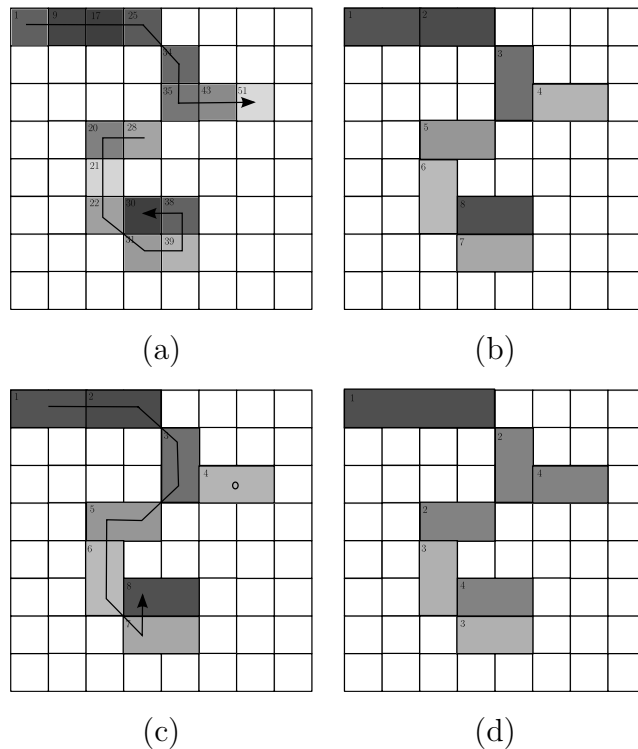


Figure 1.9: (a) The numbered pixels belong to the shrunk difference image that we consider, the first path is indicated, (b) the index sets after applying the EPWT once, (c) the second path, (d) the new index sets.

Numerical results

We give some numerical examples of our proposed hybrid method. We apply the algorithm to different images and especially compare the results with the compression results of the 9/7 tensor product wavelet transform. We consider several images of size 256×256 (65536 coefficients), namely **cameraman**, **clock**, **lena**, **pepper** and 256×256 -details of the **barbara**, **goldhill** and **sails** image, respectively.

The PSNR (peak-signal-to-noise-ratio) is defined by

$$\text{PSNR} = 20 \log_2 \frac{m}{\|f - \tilde{f}\|_2},$$

where m is the maximum possible pixel value of the image, $\|\cdot\|_2$ is the Euclidean norm and f and \tilde{f} are the original data and the reconstructed sparse image, respectively. The entropy of

the path vector \mathbf{p} (i.e. a concatenation of path vectors in all levels) for the EPWT is calculated by

$$\text{entropy} := - \sum_{j=0}^n \frac{h_j}{N_1 N_2} \log_2 \frac{h_j}{l}, \quad (1.29)$$

where l denotes the length of the path vector, n is the number of different values that appear in the path vector and h_1, \dots, h_n denote the frequencies of their occurrence. We observe that the entropy computed in (1.29) heavily overestimates the indeed encoding costs for the path since it does not take into account that adjacent components in the path are usually strongly correlated.

In a first experiment we compute a sparse representation of the image using only 500 wavelet coefficients. In the first step of Algorithm 1, we apply 5 iterations of the smoothing filter with time step $\tau = 0.17$. The threshold parameters θ and $\tilde{\theta}$ in step 2 and in step 4 of Algorithm 1 are chosen in such a way that 16384 nonzero coefficients are kept in \tilde{u}^{sm} and \tilde{u}^r , respectively. We approximate the smooth part of the image (step 3 of the algorithm) using 5 levels of the 9/7-biorthogonal tensor product filter bank and applying a shrinkage procedure to keep only 300 coefficients. Further, we apply the EPWT with 11 iterations of the one-dimensional 9/7-filter bank to the texture part \tilde{u}^r and keep 200 coefficients in step 5. Table 1.1 shows the total number of nonzero coefficients (nzc, second column) and the PSNR-values for the hybrid methods “Hybrid”, “Center Hybrid”, and “Simple Hybrid” that differ only by the choice of the EPWT path vectors in the further levels (levels 2, \dots , 11), see detailed explanations below. Further, the entropy (according to formula (1.29)) of the path vectors of the EPWT for the hybrid methods are given. For comparison, the PSNR obtained using a tensor product wavelet shrinkage with 9/7-filter and with 500 kept nonzero wavelet coefficients is given in the third column of Table 1.1.

In a second experiment, we apply the hybrid algorithms (with same parameters) to the example images, but keep 1200 coefficients for the approximation of the smooth image and 800 EPWT coefficients for approximating the difference image, see Table 1.1.

We present in Figures 1.10 and 1.11 the images corresponding to the method “Hybrid”, where we keep only 500 nonzero coefficients out of 65536. The original images are presented in the first column, whereas in the second and third column, we show the approximation results using 9/7-tensor product wavelet transform and the proposed hybrid method, respectively.

Let us give some remarks about the entropy of the path vector for the EPWT. Taking only a partial image \tilde{u}^r in step 5 of Algorithm 1, we also have to store the positions of the pixels with nonzero image values in the difference image. Using the EPWT, this can be done by a suitable encoding of the first path vector p^J . In order to minimize the entropy of the path vector, we bound the number n of different values in the stored path. In fact, the path is coded using only the values $-3, \dots, 4$ that correspond to the different possible directions of index neighbors.

Recall that we determine the path vector for the first EPWT iteration by looking for a certain “well-suited” successor of a certain pixel $l_1 = (i_1, j_1)$. As illustrated already, we do not store the position $l_2 = (i_2, j_2) \in I_J$ of the selected successor, but its position in the ordered neighborhood $\tilde{N}(l_1)$. Here, we order the neighborhood in such a way that the first pixel maintains the direction of the path. Then we store a zero if we walk into the same direction as before (which happens often when we walk along edges). If the neighborhood is empty, then we need to start a new pathway. If the index set I_J is known, then there are more efficient ways to determine and to store the starting index of a new pathway (instead of storing the position difference with respect to the last index). For example, we consider 7 equally distributed pixels in the set of remaining admissible pixels in I_J as possible starting indices (beginning with the first “admissible” pixel in the ordered set I_J), and again code the choice

image	nzc	9/7	Hybrid		Center Hybrid		Simple Hybrid	
		PSNR	PSNR	entropy	PSNR	entropy	PSNR	entropy
barbara	500	23.33	27.34	1.0497	27.28	1.0070	24.42	0.4010
cameraman	500	22.54	27.61	1.0714	27.49	0.9893	23.79	0.3794
clock	500	24.61	31.06	1.0163	30.87	0.8742	26.69	0.3014
goldhill	500	24.18	28.18	0.9918	28.19	0.8408	25.98	0.3300
lena	500	23.21	28.02	1.0343	27.91	0.9022	24.66	0.3313
pepper	500	23.41	28.07	1.0286	28.03	0.8795	24.89	0.3143
sails	500	21.32	25.52	1.0179	25.42	0.9190	22.95	0.3664
barbara	2000	26.07	30.50	1.1097	30.50	1.0950	28.12	0.4411
cameraman	2000	27.17	31.46	1.1033	31.35	1.0472	28.36	0.4153
clock	2000	29.93	35.48	1.0416	35.55	0.9329	32.49	0.3266
goldhill	2000	27.82	31.41	0.9860	31.37	0.8986	29.90	0.3556
lena	2000	28.16	32.66	1.0715	32.52	0.9699	29.97	0.3790
pepper	2000	28.84	32.97	1.0488	33.01	0.9385	30.62	0.3632
sails	2000	24.57	28.30	1.0195	28.26	0.9666	26.77	0.3916

Table 1.1: Comparison of 9/7-transform and our hybrid method for several images.

of the next pixel in the path by a value from $\{-3, \dots, 3\}$. From this easy-to-store-version of \mathbf{p} we can later reconstruct the original pixel indices of the path.

In the further levels of the EPWT, one may apply different strategies for efficient encoding of the path vectors. In the method “Hybrid”, we apply simply the so-called rigorous EPWT in the second level and in all further levels, see [83]. That means, for determining a next component in the path vector, we just look at all adjacent index sets that have not been used in the path so far and choose the index set, where the difference of the corresponding (low-pass) image values is minimal.

A more efficient method, called “Center Hybrid”, is to compute the centers of index sets and to order neighbor index sets of I_n by the Euclidean distance of their centers to the center of I_n . (Here, the center of an index set is computed as the arithmetical mean of all indices belonging to the set.) Then, not necessarily the neighbor index set with the most similar image value is taken but the first neighbor index set, for which the difference of corresponding image values is smaller than a certain bound (here $\vartheta_1 = 13$ in the first two experiments). In the path vector, we only store the position of the chosen index set in the ordered set of neighbor index sets.

However, in our application, where the EPWT is only applied along edges and texture, one may expect already good approximation results if all levels of the EPWT use the same path vector \mathbf{p}^J , obtained in the first level of the procedure (see columns 8 and 9 of Table 1.1). This method is called “Simple Hybrid”. In this case, only \mathbf{p}^J has to be stored.

In Tables 1.2 and 1.3 we present some results that are obtained using different wavelet filter banks for approximation of the smooth image and the difference image. In this experiment we also use $\tau = 0.17$, five iterations of the smoothing process, and we apply 5 iterations of a tensor-product wavelet transform to approximate the smoothed image. As bound for the first level of EPWT we have chosen $\vartheta_1 = 13$. For further levels, simply the adjacent index set



Figure 1.10: (Left) Original image; (middle) tensor product wavelet transform with 9/7 filter, keeping only 500 nonzero coefficients (nzc); (right) our hybrid method with 9/7 filter, keeping only 500 nzc.



Figure 1.11: (Left) Original image; (middle) tensor product wavelet transform with 9/7 filter, keeping only 500 nonzero coefficients (nzc); (right) our hybrid method with 9/7 filter, keeping only 500 nzc.

		Hybrid		Center Hybrid		Simple Hybrid	
smo	dif	PSNR	entropy	PSNR	entropy	PSNR	entropy
D4	D4	27.23	1.0274	27.05	0.8921	24.41	0.3262
D4	7-9	26.86	1.0295	26.92	0.8929	24.13	0.3262
D4	9/7	27.23	1.0248	27.18	0.8909	24.36	0.3262
7-9	D4	26.82	1.0200	26.76	0.8806	24.02	0.3175
7-9	7-9	26.65	1.0132	26.62	0.8820	24.16	0.3175
7-9	9/7	26.90	1.0125	26.86	0.8735	24.30	0.3175
9/7	D4	28.01	1.0273	27.92	0.8772	24.96	0.3143
9/7	7-9	27.67	1.0253	27.65	0.8824	24.68	0.3143
9/7	9/7	28.07	1.0286	28.03	0.8795	24.89	0.3143
Tensor prod		PSNR					
D4		22.51					
7-9		22.15					
9/7		23.41					

Table 1.2: Different wavelet transforms used for approximation of the **pepper** image.

with the most similar value is taken, i.e. no bound is applied (see “Hybrid” in columns 3 and 4); the “Center Hybrid” strategy with bound 13 is used (columns 5 and 6); and in columns 7 and 8 the results of the “Simple Hybrid” strategy are shown. The tensor product wavelet transform for approximating the smooth image is given in the first column, while the one-dimensional wavelet transform used for EPWT (11 iterations) is given in the second column. For comparison, we also mention the PSNR-values that are obtained by applying a $D4$ -, $7-9$ - and $9/7$ -tensor-product wavelet transform to the original image. In all cases we have used a hard threshold in order to keep only 500 nonzero-coefficients; the original images **pepper** and **lena** are each of size 256×256 .

Tables 1.4 and 1.5 illustrate the dependence of the results from the choice of the parameter τ and from the number of iterations in the smoothing process. Here the clock image of size 256×256 is used. In Table 1.4, five iterations of the smoothing filter are applied but with different time steps τ . All other parameters are the same as for the first experiment, where 500 nonzero coefficients are kept. For comparison, the PSNR-value obtained by applying a $9/7$ tensor product wavelet transform to the original image is 24.61 dB. We see that the results only slightly depend on τ (if τ stays in a certain range). Table 1.5 presents the PSNR- and entropy-values that result from the fixed time step $\tau = 0.17$, but different numbers of iterations of the smoothing process (the other parameters are chosen as above). Our numerical results suggest that we can take five iterations of the smoothing filter with a fixed $\tau = 0.17$ to obtain satisfying results for all considered images.

While the adaptivity costs of the method, i.e. the extra costs for path storing are lower than for the original EPWT algorithm in [83], these costs are still not negligible. In fact, the bottleneck of the proposed method is that the index set I_J determining the positions of nonzero elements in the difference image \tilde{u}^r needs to be coded in the path.

For a rough comparison of the encoding costs using the new hybrid algorithm (center hybrid)

		Hybrid		Center Hybrid		Simple Hybrid	
smo	dif	PSNR	entropy	PSNR	entropy	PSNR	entropy
D4	D4	26.60	1.0097	26.47	0.8775	23.74	0.3216
D4	7-9	26.34	1.0044	26.42	0.8851	23.75	0.3216
D4	9/7	26.70	1.0051	26.57	0.8768	23.97	0.3216
7-9	D4	26.51	1.0016	26.47	0.8771	23.94	0.3191
7-9	7-9	26.33	1.0081	26.31	0.8779	23.88	0.3191
7-9	9/7	26.63	1.0137	26.55	0.8742	23.99	0.3191
9/7	D4	27.90	1.0318	27.75	0.9043	24.66	0.3313
9/7	7-9	27.62	1.0307	27.54	0.9067	24.57	0.3313
9/7	9/7	28.02	1.0343	27.91	0.9022	24.66	0.3313
Tensor prod		PSNR					
D4		22.13					
7-9		22.02					
9/7		23.21					

Table 1.3: Different wavelet transforms used for approximation of the lena image.

τ	Hybrid		Center Hybrid		Simple Hybrid	
	PSNR	entropy	PSNR	entropy	PSNR	entropy
0.04	30.95	1.0203	30.81	0.8656	26.65	0.3008
0.08	30.94	1.0209	30.95	0.8738	26.66	0.3047
0.12	30.89	1.0156	30.77	0.8650	26.58	0.2988
0.14	30.90	1.0224	30.67	0.8688	26.68	0.2958
0.18	30.93	1.0186	30.92	0.8744	26.62	0.2978
0.20	30.91	1.0197	31.03	0.8820	26.67	0.3016
0.22	31.09	1.0256	31.14	0.8841	26.74	0.3041
0.24	31.02	1.0235	30.98	0.8798	26.46	0.2982

Table 1.4: PSNR- and entropy results for different values of τ .

Iterations	Hybrid		Center Hybrid		Simple Hybrid	
	PSNR	entropy	PSNR	entropy	PSNR	entropy
1	30.81	1.0186	30.84	0.8688	26.56	0.3072
3	30.92	1.0221	30.80	0.8691	26.67	0.3033
5	31.06	1.0163	30.87	0.8742	26.69	0.3014
8	31.02	1.0321	30.99	0.8784	26.42	0.3008
12	30.86	1.0297	31.25	0.8795	26.43	0.2939
20	31.03	1.0269	31.09	0.8871	26.15	0.2912
24	31.17	1.0318	31.02	0.8878	26.19	0.2883
28	30.94	1.0298	31.03	0.8891	26.04	0.2929

Table 1.5: PSNR- and entropy results for different numbers of iterations of the smoothing process.

with the tensor product 9/7 wavelet transform and with the curvelet transform, we apply the following simplified scheme. We compute the cost for encoding of the position of M nonzero wavelet coefficients by

$$-\frac{M}{N} \log_2 \frac{M}{N} - \frac{(N-M)}{N} \log_2 \frac{(N-M)}{N},$$

where $N = 256 \times 256$ is the number of coefficients in the image. Further, we use 16 bits for encoding of one wavelet coefficient. For the tensor product wavelet transform, the storing costs (in bpp) are composed of the costs for encoding of the position of the nonzero coefficients and the costs for storage of these coefficients, i.e. $16M/N$. For the new hybrid EPWT algorithm, we take into account the storing costs of the wavelet transformed part u_M^{sm} (computed as above) and the cost for the EPWT part \tilde{u}_N^r , where (beside of encoding of position and values of the EPWT wavelet coefficients) we need to consider the additional cost for the path. Here, we estimate the extra cost for path encoding with 0.5 bpp. Applying the redundant curvelet transform (see MATLAB toolbox in www.curvelet.org), the function `fdct_wrapping_demo_recon.m` obtains 184985 curvelet coefficients for a 256×256 image. This redundancy leads to rather poor compression results compared to the other methods. In Table 1.6 we summarize the encoding costs in order to present an (almost) fair comparison of the methods. For the usual tensor product wavelet transform 2000 most significant wavelet coefficients are used while we use only 500 coefficients for the hybrid method. We see that encoding of the EPWT path (0.5 bpp) constitutes the main portion of the complete storage costs (0.6880 bpp). The results in Table 1.6 impressively show, that some more effort towards an efficient path encoding can essentially improve the proposed method.

Conclusion

Similarly as most known adaptive transforms for image approximation, the EPWT provides very good approximation results but produces a non-negligible amount of extra costs due to the adaptivity of the method. Incorporating these “adaptivity costs”, adaptive methods only slightly outperform the non-adaptive methods but with essentially higher computational costs. One way to obtain a real improvement for image approximation may be to study hybrid methods as we did in this section. Also here, the remaining adaptivity costs are not negligible but considerably smaller than for the “pure” EPWT for image approximation. In particular, a

image	9/7			Curvelets			Center Hybrid with 9/7		
	nzc	PSNR	cost	nzc	PSNR	cost	nzc	PSNR	cost
barbara	2000	26.07	0.6853	2000	22.84	0.7028	500	27.28	0.6880
cameraman	2000	27.17	0.6853	2000	22.69	0.7028	500	27.49	0.6880
clock	2000	29.93	0.6853	2000	21.25	0.7028	500	30.87	0.6880
goldhill	2000	27.82	0.6853	2000	23.25	0.7028	500	28.19	0.6880
lena	2000	28.16	0.6853	2000	22.04	0.7028	500	27.91	0.6880
pepper	2000	28.84	0.6853	2000	21.77	0.7028	500	28.03	0.6880
sails	2000	24.57	0.6853	2000	20.75	0.7028	500	25.42	0.6880

Table 1.6: Comparison of storing costs for 9/7-transform, curvelets and our hybrid method for several images.

further improvement of pathway determination and path encoding may lead to a compression algorithm that is truly interesting for practical purposes.

Chapter 2

Area preserving projections and uniform grids

A uniform grid of a 2D domain Ω is a grid all of whose cells have the same area. This fact is required in statistical applications and in construction of wavelet bases of $L^2(\Omega)$, where we wish to use the standard 2-norm and inner product instead of a weighted norm dependent on the grid. A refinement process is needed for a multiresolution analysis or for multigrid methods, when a grid is not fine enough to solve a problem accurately. A uniform refinement consist in dividing each cell into a given number of smaller cells with the same area. To be efficient in practice, a refinement procedure should also be a simple one.

While on a rectangle or on other polygonal domains the construction of uniform and refinable (UR) grids is trivial, it is not immediate on a disc, an elliptic domain, a sphere or on some surfaces, even symmetric. A simple procedure for constructing such UR grids would be therefore to define maps defined on rectangles to the desired domain D , that preserves areas, and then to transport rectangular UR grids onto UR grids on D .

In this chapter we present four different ideas of constructions of such area preserving maps, sometimes called *equal area projections* or *area preserving projections*. Combined with Lambert's azimuthal equal area projection, some of our projections allows us to construct new UR grids on the sphere.

2.1 Area preserving projection from square to disc

2.1.1 Calculation of the projection

The results presented in this section were published in [107]. Consider the square of edge $2L$ and the circle with the same area, both centred on the origin O (Figure 2.1). The radius of the circle will be $R = 2L/\sqrt{\pi}$. We want to construct a continuous bijective transform $T : \mathbb{R}^2 \rightarrow \mathbb{R}^2$ which maps, for each $L > 0$, the domain

$$S_L = \{(x, y) \in \mathbb{R}^2, |x| \leq L, |y| \leq L\}$$

onto the disc of radius R ,

$$C_L = \left\{ (x, y) \in \mathbb{R}^2, x^2 + y^2 \leq \frac{4L^2}{\pi} \right\}.$$

At the same time we require the area preserving property

$$\mathcal{A}(D) = \mathcal{A}(T(D)) \text{ for every domain } D \subseteq \mathbb{R}^2. \quad (2.1)$$

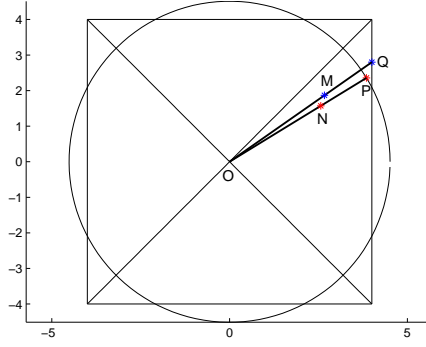


Figure 2.1: The action of the transform T . Points N and P are the images of M and Q , respectively.

Here $\mathcal{A}(D)$ denotes the area of D .

The first idea is to construct a map by keeping the direction of the position vector, that is, for $M \in \mathbb{R}^2$ to take $T(M)$ on the half-line OM . If we define such an application which maps the square

$$\partial S_L = \{(x, y) \in \mathbb{R}^2, |x| = L, |y| = L\},$$

into the circle

$$\partial C_L = \left\{ (x, y) \in \mathbb{R}^2, x^2 + y^2 = \frac{4L^2}{\pi} \right\},$$

for every $L > 0$ we see that such an application does not satisfy (2.1). Therefore, an alternative would be to take a rotation around O , followed by an appropriate move along the radius. This construction is described bellow.

Let $L > 0$. We focus for the moment on the first octant I of the plane, intersected with the square S_L ,

$$I = \{(u, v) \in \mathbb{R}^2, 0 \leq v \leq u\}.$$

The map T will be defined in such a way that each half-line $d_m \subset I$ of equation $y = mx$ ($0 \leq m \leq 1$) is mapped into the half-line $d_{k(m)}$ of equation $y = k(m)x$, with

$$k(m) = \tan \frac{m\pi}{4}.$$

In this way, the half lines $y = 0$ and $y = x$, situated on the boundary of I are invariant under T and $d_{k(m)} \subset I$ for all $m \in [0, 1]$. We want T to map ∂S_L onto ∂C_L , therefore the other boundary edge $x = L$ situated in I must be mapped on the arc of the circle of ∂C_L situated in I. So, let $M(u, v) \in I \cap S_L$ and let $Q(L, mL) \in \partial S_L$ be the intersection of OM with the square ∂S_L (see Figure 2.1), where

$$m = \frac{v}{u}.$$

The point Q will be mapped on the point $P(X, Y)$, the intersection of the half-line $d_{k(m)}$ with the circle ∂C_L . Thus, we have $X^2 + k(m)^2 X^2 = R^2$, whence

$$X = \frac{R}{\sqrt{1 + k(m)^2}} = \frac{R}{\sqrt{1 + \tan^2 \frac{m\pi}{4}}} = R \cos \frac{m\pi}{4}.$$

Therefore, the point P has the coordinates

$$P \left(R \cos \frac{m\pi}{4}, R \sin \frac{m\pi}{4} \right).$$

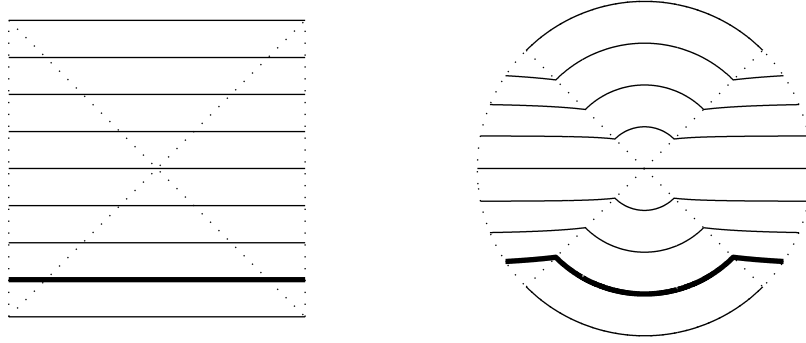


Figure 2.2: A horizontal grid and its image grid on the disc. The image of the bold line on the left is the bold curve on the right.

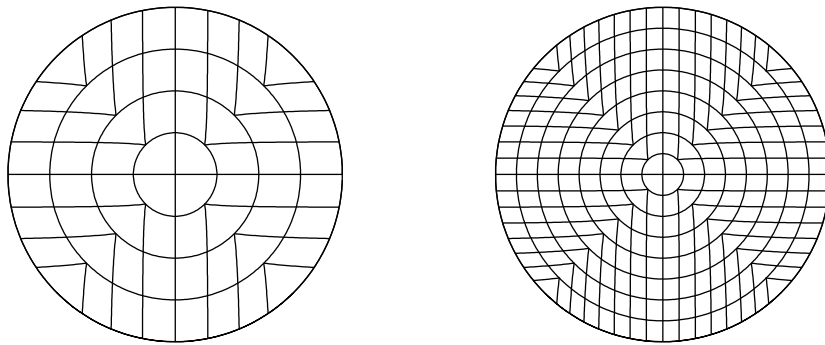


Figure 2.3: Two uniform grids of the disc, where the right one is the refinement of the left one.

We define $N = T(M)$ such that $N \in OP$ and $\frac{ON}{OP} = \frac{OM}{OQ}$. A simple calculation gives $\frac{OM}{OQ} = \frac{u}{L}$, and therefore we find

$$N \left(\frac{2u}{\sqrt{\pi}} \cos \frac{v\pi}{4u}, \frac{2u}{\sqrt{\pi}} \sin \frac{v\pi}{4u} \right).$$

Straightforward calculations show that the Jacobian of the map T , restricted to I , is indeed 1, and therefore T preserves the areas of the domains situated in the first octant I .

By similar arguments for the seven other octants, we find that the map T preserving areas is defined as follows:

1. For $|v| \leq |u|$,

$$(u, v) \mapsto (U, V) = \left(\frac{2u}{\sqrt{\pi}} \cos \frac{v\pi}{4u}, \frac{2u}{\sqrt{\pi}} \sin \frac{v\pi}{4u} \right); \quad (2.2)$$

2. For $|u| \leq |v|$,

$$(u, v) \mapsto (U, V) = \left(\frac{2v}{\sqrt{\pi}} \sin \frac{u\pi}{4v}, \frac{2v}{\sqrt{\pi}} \cos \frac{u\pi}{4v} \right). \quad (2.3)$$

For the origin we take $T(0,0) = (0,0)$. One can prove that T is continuous and that the Jacobian of T is 1. Figure 2.2 shows the images of the horizontal lines. Figure 2.3 show images of two uniform grids of S_L , each obtained from uniform grids on the square consisting of lines parallel to the edges.

The inverse of T is given by the following formulas:

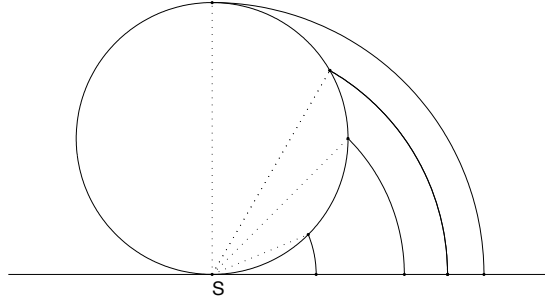


Figure 2.4: Lambert azimuthal projection.

1. For $|V| \leq |U|$,

$$(U, V) \mapsto (u, v) = \text{sign}(U) \sqrt{U^2 + V^2} \left(\frac{\sqrt{\pi}}{2}, \frac{2}{\sqrt{\pi}} \arctan \frac{V}{U} \right); \quad (2.4)$$

2. For $|U| \leq |V|$,

$$(U, V) \mapsto (u, v) = \text{sign}(V) \sqrt{U^2 + V^2} \left(\frac{2}{\sqrt{\pi}} \arctan \frac{U}{V}, \frac{\sqrt{\pi}}{2} \right). \quad (2.5)$$

2.1.2 Application 1: UR spherical grids

In this section we combine the area preserving projection T constructed in the previous section with the Lambert azimuthal equal area projection. Thus, *any* uniform grid on the square can be mapped bijectively onto a uniform grid on the disc and then onto a uniform grid on the sphere. Thus, one can obtain spherical grids with the following properties: (a) hierarchical tree structure (allowing construction of a multiresolution analysis); (b) equal area for the spherical cells; (c) isolatitudinal distribution of the cells (essential for fast computations involving spherical harmonics). Compared to the HealPix grid (the first one satisfying simultaneously these properties) and the planar domains mapped there, our construction is much simpler and allows the transportation of any function from the square to the sphere, keeping the properties of orthogonality, basis, frame, local support.

Lambert's azimuthal equal area projection

This projection was constructed in 1772 by J.H. Lambert, and it is the most used projection in cartography for mapping one hemisphere of the Earth onto a disc. It establishes a bijection between a sphere of radius r , without a point, and the interior of a disc of radius $2r$, and it preserves areas. To define the Lambert azimuthal projection (see Figure 2.4), we need the plane tangent to the sphere at some point S of the sphere, called antipode. Let P be an arbitrary point on the sphere other than the antipode of S . Let d be the Euclidean distance between S and P (not the distance along the sphere surface). The projection of P will be the point P' on the plane, such that $SP' = d$. Geometrically, it can be constructed as follows. We consider the unique circle centred on S , passing through P and perpendicular to the plane. This circle intersects the plane at two points and we take P' those point that is closer to P . This is the projected point (Figure 2.4). The antipode of S is excluded from the projection because the required circle is not unique. The projection of S is taken as S .

If we take the sphere \mathbb{S}_r^2 of equation $x^2 + y^2 + z^2 = r^2$ and $S(0, 0, -r)$ the south pole, then Lambert's projection and its inverse can be described, in Cartesian coordinates, by the following formulas:

$$(x, y, z) \mapsto (X, Y) = \left(\sqrt{\frac{2r}{r-z}} x, \sqrt{\frac{2r}{r-z}} y \right) \quad (2.6)$$

and

$$(X, Y) \mapsto (x, y, z) = \left(\sqrt{1 - \frac{X^2 + Y^2}{4r^2}} X, \sqrt{1 - \frac{X^2 + Y^2}{4r^2}} Y, -r + \frac{X^2 + Y^2}{2r} \right). \quad (2.7)$$

Spherical uniform grids using Lambert's azimuthal projection for the whole sphere

We want to construct a uniform grid on the sphere \mathbb{S}_r^2 starting from a uniform grid of the square $S_{r\sqrt{\pi}}$ of edge $2r\sqrt{\pi}$. By combining the formulas (2.7) and (2.2)-(2.3), we obtain that a point $(u, v) \in S_{r\sqrt{\pi}}$ is mapped into the point $(x, y, z) \in \mathbb{S}_r^2$ with the following coordinates:

1. For $|v| \leq |u| \leq r\sqrt{\pi}$,

$$(x, y, z) = \left(\frac{2u}{\pi} \sqrt{\pi - \frac{u^2}{r^2}} \cos \frac{v\pi}{4u}, \frac{2u}{\pi} \sqrt{\pi - \frac{u^2}{r^2}} \sin \frac{v\pi}{4u}, \frac{2u^2}{\pi r} - r \right); \quad (2.8)$$

2. For $|u| \leq |v| \leq r\sqrt{\pi}$,

$$(x, y, z) = \left(\frac{2v}{\pi} \sqrt{\pi - \frac{v^2}{r^2}} \sin \frac{u\pi}{4v}, \frac{2v}{\pi} \sqrt{\pi - \frac{v^2}{r^2}} \cos \frac{u\pi}{4v}, \frac{2v^2}{\pi r} - r \right). \quad (2.9)$$

The point $(0, 0)$ is mapped into $(0, 0, -r)$. For the inverse, combining formulas (2.6) and (2.4)-(2.5), we obtain that a point $(x, y, z) \in \mathbb{S}_r^2$ is mapped onto the point $(u, v) \in S_{r\sqrt{\pi}}$ with the following coordinates:

1. For $|y| \leq |x|$,

$$(u, v) = \text{sign}(x) \sqrt{2r(r+z)} \left(\frac{\sqrt{\pi}}{2}, \frac{2}{\sqrt{\pi}} \arctan \frac{y}{x} \right); \quad (2.10)$$

2. For $|x| \leq |y|$

$$(u, v) = \text{sign}(y) \sqrt{2r(r+z)} \left(\frac{2}{\sqrt{\pi}} \arctan \frac{x}{y}, \frac{\sqrt{\pi}}{2} \right). \quad (2.11)$$

Two examples of such spherical uniform grids are given in Figure 2.5. One can see that, because of the Lambert projection, the distortion of shape increases towards the north pole. For this reason, one can construct another type of spherical grids, by applying the Lambert projection separately for the two hemispheres.

Spherical grid using Lambert's azimuthal projection for each of the hemispheres

When we use Lambert's projection, we can choose to map only the southern hemisphere with respect to the south pole, and separately, the northern hemisphere with respect to the north pole. If the sphere has the radius r , then the projected discs of each hemisphere have the radius $\sqrt{2}r$ and therefore the corresponding square will be $S_{r\sqrt{\pi/2}}$ of edge $r\sqrt{2\pi}$. The formula for the

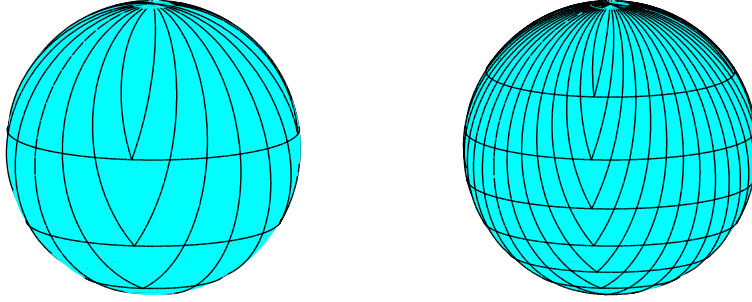


Figure 2.5: The grids in Figure 2.3, projected on the sphere by Lambert's projection.

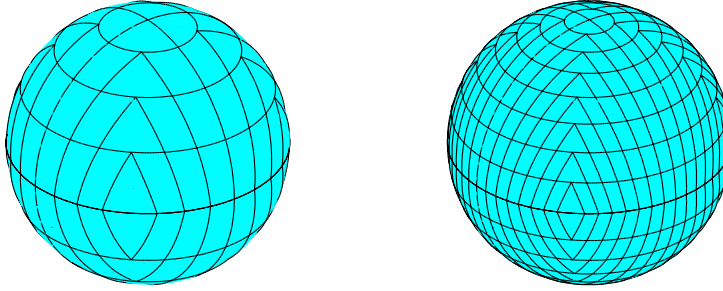


Figure 2.6: The grids in Figure 2.3, projected on the sphere by Lambert's projection, separately for the northern and southern hemispheres.

spherical image (x, y, z) of a point (X, Y) of the disc $C_{r\sqrt{2}}$ are the one given in (2.7) for (x, y, z) in the southern hemisphere, while for the northern hemisphere it is given by

$$(x, y, z) = \left(\sqrt{1 - \frac{X^2 + Y^2}{4r^2}} X, \sqrt{1 - \frac{X^2 + Y^2}{4r^2}} Y, r - \frac{X^2 + Y^2}{2r} \right). \quad (2.12)$$

For the inverse projection, a point (x, y, z) on the southern hemisphere projects according to formula (2.6), while for a point (x, y, z) on the northern hemisphere, the projection onto the disc $C_{r\sqrt{2}}$ is given by

$$(x, y, z) \mapsto (X, Y) = \left(\sqrt{\frac{2r}{r+z}} x, \sqrt{\frac{2r}{r+z}} y \right). \quad (2.13)$$

Similarly, formulas (2.8)-(2.9) are the ones used for the points (x, y, z) on the southern hemisphere, while for the northern hemisphere, only the sign of z changes in both of these formulas. As for the images in the square $S_{r\sqrt{\pi/2}}$ of a point (x, y, z) on the northern hemisphere, the formulas are similar to (2.10)-(2.11), with $(r + z)$ replaced with $(r - z)$. Such uniform spherical grids are depicted in Figure 2.6.

The number of cells at each latitude for the square grid

We focus on the spherical grid with $8n^2$ cells, for which the grid on each hemisphere is the image of a uniform grid of the square $[-L, L]$, with $L = r\sqrt{\pi/2}$. On this square we consider

the grid containing $(2n)^2$ small squares of the same area, formed by lines parallel to the edges. The centres of the cells of the spherical grid are equally distributed on $2n$ latitudinal circles, symmetric with respect to the equator. The latitudinal circles are, in fact, images of squares centred on O . The number of cells in the northern hemisphere (and of course, symmetric on the southern hemisphere) will be $4(2i - 1)$ on the i -th latitudinal circle.

We presented here only the pictures for the spherical grid generated by a square grid with square cells, but of course there are many other uniform grids on the square, which can be mapped to nice uniform grids on the sphere.

There are still many open questions. Do the centers of some spherical grid cells constitute fundamental systems of points? How do cubature formulas with such points behave? Which wavelets on the interval can be efficiently mapped on the sphere? How efficient are the new grids for geo-statistical applications? In which applications are our grids preferable to other grids?

2.1.3 Application 2: geographic maps of a hemisphere

Another application of the map T constructed in Section 2.1.1 is to map a hemisphere of the Earth onto a disc by Lambert projection and then onto a square by T^{-1} . In this way we can obtain a geographic square map of one hemisphere of the Earth, more suitable for computer manipulation than a circular one.

We mention that the problem of finding an analytic function that maps a disc onto the interior of any convex polygon was first solved independently by E.B. Christoffel(1867) and H.A. Schwarz(1869). Their map is a complex integral which is conformal (i.e. preserves angles), but it does not preserve areas. In fact, it is known that no conformal map can preserve areas. Another drawback is that it has no explicit formula, requiring to solve a system of nonlinear equations.

Some well-known projections mapping a hemisphere onto a square are Pierce quincuncial(1879 - conformal except four points), Guyou (1886 - conformal), Adams (1925 - conformal), Collignon (1865 - area preserving). An area preserving projection from a sphere to a rectangle is Lambert Cylindrical projection. A complete description of all known map projections used in cartography can be found in [50, 121].

Consider the sphere \mathbb{S}_r^2 of radius r centered at the origin, with the parametrization

$$\begin{aligned}x &= r \sin \theta \cos \varphi, \\y &= r \sin \theta \sin \varphi, \\z &= r \cos \theta,\end{aligned}$$

with $\theta \in [0, \pi)$ the colatitude and $\varphi \in [-\pi, \pi]$ the longitude. We focus on the northern hemisphere \mathbb{S}_r^+ (i.e. $\theta \in [0, \pi/2]$), and we recall the formulas deduced in (2.8) and (2.9) by combining the Lambert azimuthal projection and the projection T . A point $(X, Y) \in S_L$ is mapped onto the point $(x, y, z) \in \mathbb{S}_r^+$ given by

$$(x, y, z) = \begin{cases} \left(\frac{2X}{\pi} \sqrt{\pi - \frac{X^2}{r^2}} \cos \frac{Y\pi}{4X}, \frac{2X}{\pi} \sqrt{\pi - \frac{X^2}{r^2}} \sin \frac{Y\pi}{4X}, r - \frac{2X^2}{\pi r} \right), & |Y| \leq |X|, \\ \left(\frac{2Y}{\pi} \sqrt{\pi - \frac{Y^2}{r^2}} \sin \frac{X\pi}{4Y}, \frac{2Y}{\pi} \sqrt{\pi - \frac{Y^2}{r^2}} \cos \frac{X\pi}{4Y}, r - \frac{2Y^2}{\pi r} \right), & |X| \leq |Y|. \end{cases} \quad (2.14)$$

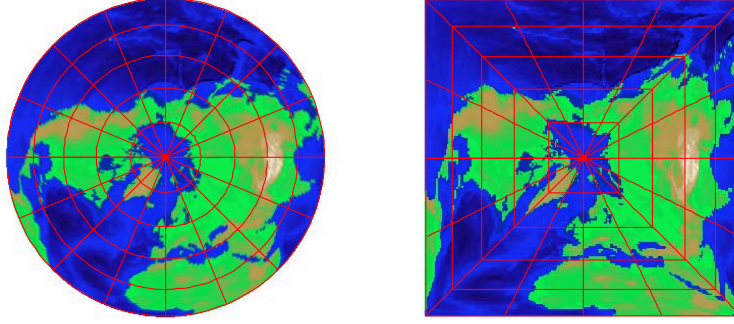


Figure 2.7: The northern hemisphere of the Earth, projected on a disc with Lambert projection (left) and on a square with our projection (2.16) (right). The image of the meridians $\varphi_k = \frac{k\pi}{8}$, $k = -7, -6, \dots, 6, 7, 8$, are segments through the origin forming an angle φ_k with OX , while the image of the parallels $\theta_j = \frac{j\pi}{10}$, $j = 1, 2, \dots, 5$ are squares centered at the origin.

For the inverse, a point $(x, y, z) \in \mathbb{S}_r^+$ is mapped onto $(X, Y) \in S_L$ with

$$(X, Y) = \begin{cases} \operatorname{sgn}(x)\sqrt{2r(r-z)} \left(\frac{\sqrt{\pi}}{2}, \frac{2}{\sqrt{\pi}} \arctan \frac{y}{x} \right), & \text{if } |y| \leq |x|, \\ \operatorname{sgn}(y)\sqrt{2r(r-z)} \left(\frac{2}{\sqrt{\pi}} \arctan \frac{x}{y}, \frac{\sqrt{\pi}}{2} \right), & \text{if } |x| \leq |y|. \end{cases} \quad (2.15)$$

In spherical coordinates θ, φ , formula (2.15) writes

$$(X, Y) = \begin{cases} \operatorname{sgn}(\sin \varphi) 2r \sin \frac{\theta}{2} \left(\frac{2}{\sqrt{\pi}} \arctan(\cot \varphi), \frac{\sqrt{\pi}}{2} \right), & \text{if } \frac{\pi}{4} \leq |\varphi| \leq \frac{3\pi}{4}, \\ \operatorname{sgn}(\cos \varphi) 2r \sin \frac{\theta}{2} \left(\frac{\sqrt{\pi}}{2}, \frac{2}{\sqrt{\pi}} \arctan(\tan \varphi) \right), & \text{otherwise.} \end{cases} \quad (2.16)$$

Conversely, given the point $(X, Y) \in S_L$, it will be mapped on the point of the hemisphere \mathbb{S}_r^+ , with $r = L\sqrt{2/\pi}$, of spherical coordinates

$$\theta = \arccos \frac{z}{r} = \begin{cases} \arccos \left(1 - \frac{2X^2}{\pi r^2} \right), & |Y| \leq |X| \\ \arccos \left(1 - \frac{2Y^2}{\pi r^2} \right), & |X| < |Y| \end{cases} = \arccos \left(1 - \frac{2}{\pi r^2} \max\{|X|^2, |Y|^2\} \right),$$

$$\varphi = \begin{cases} \frac{\pi Y}{4X}, & X > 0, |Y| \leq X, \\ \frac{\pi}{2} - \frac{\pi X}{4Y}, & Y > 0, Y \geq |X|, \\ -\pi + \frac{\pi Y}{4X}, & X < 0, -X \geq |Y|, \\ -\frac{\pi}{2} - \frac{\pi X}{4Y}, & Y < 0, -Y \geq |X|. \end{cases}$$

In [112] we also give the formulas for the geographical parametrization of the sphere.

Figure 2.7 shows the Lambert projection (left) and our projection given in formulas (2.15) (right) of the northern hemisphere of the Earth. The red lines are the images of some meridians and parallels of the northern hemisphere, using formulas (2.15).

2.2 Area preserving projection from rectangle to ellipse

In this section we construct a bijection from \mathbb{R}^2 to \mathbb{R}^2 , which maps rectangles onto ellipses and preserves area. This allows us to transport a rectangular grid to an elliptic grid, preserving the area of the cells. In particular, any uniform rectangular grid is mapped into a uniform elliptic grid. In the particular case of the square and disc, such a bijection reduces to that constructed in Section 2.1.1.

2.2.1 First method of construction

Consider the ellipse $\mathcal{E}_{a,b}$ of semi-axes a and b , $a, b > 0$, of equation

$$\frac{x^2}{a^2} + \frac{y^2}{b^2} = 1,$$

and the rectangle \mathcal{R}_{L_1, L_2} with edges $2L_1$ and $2L_2$, defined as

$$\mathcal{R}_{L_1, L_2} = \{(x, y) \in \mathbb{R}^2, |x| = L_1, |y| = L_2\}.$$

The domains enclosed by $\mathcal{E}_{a,b}$ and \mathcal{R}_{L_1, L_2} will be denoted by $\bar{\mathcal{E}}_{a,b}$ and $\bar{\mathcal{R}}_{L_1, L_2}$, respectively.

We will construct a bijection $T_{L_1, L_2}^{a,b} : \mathbb{R}^2 \rightarrow \mathbb{R}^2$ which maps each rectangle $\mathcal{R}_{\alpha L_1, \alpha L_2}$ onto the ellipse $\mathcal{E}_{\alpha a, \alpha b}$ and has the area preserving property

$$\mathcal{A}(D) = \mathcal{A}(T_{L_1, L_2}^{a,b}(D)), \text{ for every domain } D \subseteq \mathbb{R}^2. \quad (2.17)$$

Here $\mathcal{A}(D)$ denotes the area of D . Thus, $\mathcal{A}(\bar{\mathcal{R}}_{L_1, L_2}) = \mathcal{A}(\bar{\mathcal{E}}_{a,b})$ implies

$$\pi ab = 4L_1 L_2.$$

In (2.2) and (2.3) we have defined the bijection $T_L : \mathbb{R}^2 \rightarrow \mathbb{R}^2$, given by

$$T_L(x, y) = \begin{cases} \frac{2x}{\sqrt{\pi}} \left(\cos \frac{\pi y}{4x}, \sin \frac{\pi y}{4x} \right), & \text{for } 0 \leq |y| \leq |x|, \\ \frac{2y}{\sqrt{\pi}} \left(\sin \frac{\pi x}{4y}, \cos \frac{\pi x}{4y} \right), & \text{for } 0 \leq |x| \leq |y|. \end{cases}$$

For the origin we take $T_L(0, 0) = (0, 0)$. This function maps each square $\mathcal{R}_{\alpha L, \alpha L}$ onto the circle $\mathcal{E}_{\alpha R, \alpha R}$, with $\pi R^2 = 4L^2$ and has the property (2.17). The map $T_{L_1, L_2}^{a,b}$ will be defined as

$$T_{L_1, L_2}^{a,b} = S_2 \circ T_L \circ S_1,$$

where $S_1, S_2 : \mathbb{R}^2 \rightarrow \mathbb{R}^2$ preserve areas and are defines as

$$S_1(x, y) = \left(\frac{Lx}{L_1}, \frac{Ly}{L_2} \right),$$

$$S_2(x, y) = \frac{\sqrt{\pi}}{2L} (ax, by).$$

More precisely, S_1 maps rectangles $\mathcal{R}_{\alpha L_1, \alpha L_2}$ onto squares $\mathcal{R}_{\alpha L, \alpha L}$ with $L_1 L_2 = L^2$, while S_2 maps circles $\mathcal{E}_{\alpha R, \alpha R}$ onto ellipses $\mathcal{E}_{\alpha a, \alpha b}$, with $R^2 = ab$. A simple calculation shows that $T_{L_1, L_2}^{a,b}$ can be written as follows:

For $L_1 |y| \leq L_2 |x|$,

$$(x, y) \mapsto (X, Y) = \left(2x \sqrt{\frac{aL_2}{bL_1\pi}} \cos \frac{\pi L_1 y}{4L_2 x}, 2x \sqrt{\frac{bL_2}{aL_1\pi}} \sin \frac{\pi L_1 y}{4L_2 x} \right); \quad (2.18)$$

For $L_2 |x| \leq L_1 |y|$,

$$(x, y) \mapsto (X, Y) = \left(2y \sqrt{\frac{aL_1}{bL_2\pi}} \sin \frac{\pi L_2 x}{4L_1 y}, 2y \sqrt{\frac{bL_1}{aL_2\pi}} \cos \frac{\pi L_2 x}{4L_1 y} \right). \quad (2.19)$$

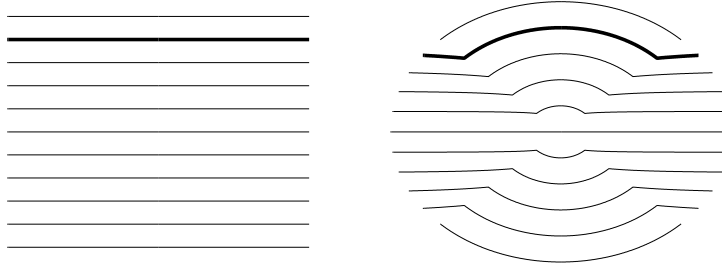


Figure 2.8: A horizontal grid and its image grid on the elliptic domain. The image of the bold line on the left is the bold curve on the right.

For the origin we take $T_{L_1, L_2}^{a, b}(0, 0) = (0, 0)$. Obviously, $T_{L_1, L_2}^{a, b}$ is continuous and bijective and its inverse is given by the following formulas:

For $a|Y| \leq b|X|$,

$$(X, Y) \mapsto (x, y) = \text{sign}(X) \sqrt{X^2 + \frac{a^2}{b^2} Y^2} \left(\frac{\sqrt{\pi}}{2}, \frac{2b}{a\sqrt{\pi}} \arctan \frac{aY}{bX} \right);$$

For $b|X| \leq a|Y|$,

$$(X, Y) \mapsto (x, y) = \text{sign}(Y) \sqrt{\frac{b^2}{a^2} X^2 + Y^2} \left(\frac{2a}{b\sqrt{\pi}} \arctan \frac{bX}{aY}, \frac{\sqrt{\pi}}{2} \right).$$

Since the Jacobians of S_1, S_2 and T_L are 1, the Jacobian of $T_{L_1, L_2}^{a, b}$ is also equal to 1 and therefore relation (2.17) is fulfilled for arbitrary domains $D \subseteq I$.

Figure 2.8 shows the image of horizontal lines by an application $T_{L_1, L_2}^{a, b}$. In Figures 2.9 and 2.10 we show two grids on an elliptic domain and its refinement, both images of a rectangular grid. Of course, other 2D uniform grids on a rectangle can be constructed, including triangular grids with different types of refinements. An example of triangular grid is depicted in Figure 2.11.

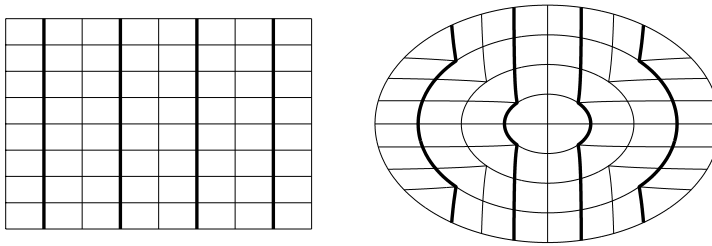


Figure 2.9: A uniform rectangular grid and its image - a uniform grid on the elliptic domain.

2.2.2 Second method for constructing the projection

In this section we present another idea for deducing formulas (2.18) and (2.19). The result is published in [111]. We construct an area preserving bijection from \mathbb{R}^2 to \mathbb{R}^2 , which again maps rectangles of arbitrary edges $\mathcal{R}_{\alpha L_1, \alpha L_2}$ onto ellipses $\mathcal{E}_{\alpha a, \alpha b}$, with a, b satisfying $4L_1 L_2 = \pi ab$.

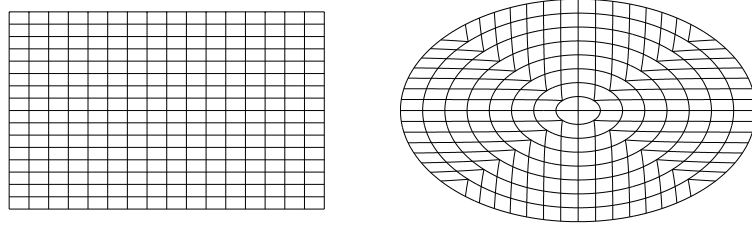


Figure 2.10: A refinement of the grid in Figure 2.9 and its image - a refinement of the elliptic grid in Figure 2.9.

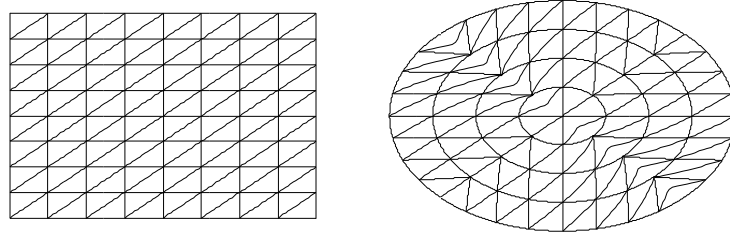


Figure 2.11: A triangular grid and its image - a uniform grid on the elliptic domain.

We focus for the moment on the first octant I of the plane,

$$I = I_{L_1, L_2} = \{(x, y) \in \mathbb{R}^2, 0 \leq L_1 y \leq L_2 x\}.$$

The map $T_{L_1, L_2}^{a, b}$ will be defined in such a way that each half-line $d_m \subset I$ of equation $y = mx$ ($0 \leq m \leq L_2/L_1$) is mapped onto the half-line $d_{\varphi(m)}$ of equation $Y = \varphi(m)X$, such that

$$0 \leq \varphi(m) \leq \frac{b}{a}, \quad \text{for } 0 \leq m \leq \frac{L_2}{L_1}.$$

Let $Q = Q(L_1, mL_1)$ and let $Q' = Q'(L_1, 0)$ be its projection on Ox . The area of the triangle OQQ' is

$$\mathcal{A}_\Delta = \frac{mL_1^2}{2} = \frac{yL_1^2}{2x}.$$

We denote by $(X, \varphi(m)X)$ the coordinates of the point $P = T_{L_1, L_2}^{a, b}(Q) \in \mathcal{E}_{a, b}$. The area of the portion of the elliptic domain $\bar{\mathcal{E}}_{a, b}$ located between the axis OX and the line $Y = \varphi(m)X$ will be

$$\mathcal{A}_e = \frac{ab\theta}{2},$$

where

$$\theta = \arctan \frac{a\varphi(m)}{b}.$$

Here $\varphi(m)$ is the angle between the axis OX and OP and θ is the parametric angle (i.e. the angle used in the following parametric equations of $\bar{\mathcal{E}}_{a, b}$: $x = a\rho \cos \theta$, $y = b\rho \sin \theta$, $\rho \in [0, 1]$, $\theta \in [0, 2\pi)$).

Next, we impose the area preserving property $\mathcal{A}_\Delta = \mathcal{A}_e$, which yields

$$\theta = \frac{\pi L_1 y}{4L_2 x},$$

and therefore

$$\varphi(m) = \frac{b}{a} \tan \frac{\pi L_1 y}{4L_2 x}.$$

It is easy to see that φ has the following properties:

$$\begin{aligned} \varphi(0) &= 0, \quad \varphi\left(\frac{L_2}{L_1}\right) = \frac{b}{a}, \quad \text{and} \\ 0 \leq \varphi(m) &\leq \frac{b}{a}, \quad \text{for } 0 \leq m \leq \frac{L_2}{L_1}. \end{aligned}$$

Consider now $M = M(x, mx)$ and $N = T_{L_1, L_2}^{a, b}(M) = (X, \varphi(m)X)$, which belongs to an ellipse $\mathcal{E}_{\alpha a, \alpha b}$ for a certain α . The portion of the elliptic domain $\overline{\mathcal{E}}_{\alpha a, \alpha b}$, located between ON and OX , has the area

$$\mathcal{A}_{e, \alpha} = \frac{ab\theta\alpha^2}{2},$$

whereas the area of the triangle OMM' , with $M' = M'(x, 0)$ is $mx^2/2$.

Again, the area preserving property implies this time

$$\alpha = x \sqrt{\frac{m}{ab\theta}} = 2x \sqrt{\frac{L_2}{L_1} \cdot \frac{1}{\pi ab}}.$$

Finally, from $N \in \mathcal{E}_{\alpha a, \alpha b}$ we obtain

$$\frac{X^2}{a^2} + \frac{X^2 \varphi^2(m)}{b^2} = \alpha^2,$$

and therefore

$$\begin{aligned} X &= \frac{ab\alpha}{\sqrt{b^2 + a^2\varphi^2(m)}} = \frac{a\alpha}{\sqrt{1 + \tan^2\theta}} = a\alpha \cos\theta = 2x \sqrt{\frac{aL_2}{bL_1\pi}} \cos \frac{\pi L_1 y}{4L_2 x}, \\ Y &= \varphi(m)X = 2x \sqrt{\frac{bL_2}{aL_1\pi}} \sin \frac{\pi L_1 y}{4L_2 x}. \end{aligned}$$

Thus, we have reobtained formulas (2.18) and (2.19).

2.3 Area preserving projection from cube to sphere

We construct an area preserving map from the cube to the unit sphere \mathbb{S}^2 , both centered at the origin. More precisely, each face F_i of the cube is first projected to a curved square \mathcal{S}_i of the same area, and then each \mathcal{S}_i is projected onto the sphere by inverse Lambert azimuthal equal area projection, with respect to the points situated at the intersection of the coordinate axes with \mathbb{S}^2 . This map is then used to construct uniform and refinable grids on a sphere, starting from any grid on a square. The results were published in [113].

Our construction scheme will therefore consists of two steps. In the first step, we construct in Section 2.3.1 a bijection T from each face F_i of the cube, onto a curved square \mathcal{S}_i . In Section 2.3.2 we construct the inverse T^{-1} . In the second step, we combine T with the inverse Lambert azimuthal projection, in order to map each face F_i of the cube onto a subset \mathcal{F}_i of the sphere, such that $\cup_{i=1}^6 \mathcal{F}_i = \mathbb{S}^2$. Finally, we present some examples of the obtained spherical grids.

Consider the unit sphere \mathbb{S}^2 centered at the origin O and the cube \mathbb{K} centered at O , with the same area. Thus, the edge of the cube has the length $a = \sqrt{2\pi/3}$. Denote $\beta = a/2 = \sqrt{\pi/6}$.

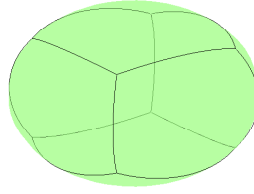


Figure 2.12: The curves of intersection of the cube with the diagonal plans.

We cut the sphere with the six diagonal planes $z = \pm x$, $z = \pm y$, $y = \pm x$ and obtain the curves in Figure 2.12.

Let us focus on one of these curves \mathcal{C}_1 , given by the equations

$$\begin{cases} x^2 + y^2 + z^2 = 1, \\ z = x > 0, \\ y \in \left[-\frac{1}{\sqrt{3}}, \frac{1}{\sqrt{3}}\right]. \end{cases}$$

The Lambert projection (2.13) of the curve \mathcal{C}_1 onto the plane $z = 1$ has the equations

$$x_L = \frac{\sqrt{2 - 2t^2}}{\sqrt{2 + \sqrt{2 - 2t^2}}}, \quad (2.20)$$

$$y_L = \frac{2t}{\sqrt{2 + \sqrt{2 - 2t^2}}}, \quad (2.21)$$

$$z_L = 1,$$

with $t \in [-1/\sqrt{3}, 1/\sqrt{3}]$. The calculations show that

$$x_L^2 + y_L^2 = 2 - \sqrt{2 - 2t^2}, \quad (2.22)$$

$$\frac{y_L}{x_L} = \frac{\sqrt{2}t}{\sqrt{1 - t^2}}. \quad (2.23)$$

We denote by \mathcal{S}_a the curved square in the tangent plane $z = 1$, formed by the curved edge of equations (2.20)-(2.21) and three other curved edges obtained in the same manner by intersecting the sphere with the half-planes $z = -x > 0$, $z = y > 0$ and $z = -y > 0$, respectively (Figure 2.13). Because of the area-preserving property of the Lambert projection, the area $\mathcal{A}(\mathcal{S}_a)$ of the obtained curved square \mathcal{S}_a is exactly $\frac{2\pi}{3} = a^2$. With the help of this projection, we have simplified the problem of finding an area preserving map from the cube to the sphere \mathbb{S}^2 to a problem of finding a two-dimensional map from a square, i.e., a face of the cube, to the curved square \mathcal{S}_a .

2.3.1 Mapping a square onto a curved square

In this section we derive an area preserving bijection $T : \mathbb{R}^2 \rightarrow \mathbb{R}^2$, which maps the square

$$S_a = \{(x, y) \in \mathbb{R}^2, |x| \leq a, |y| \leq a\}$$

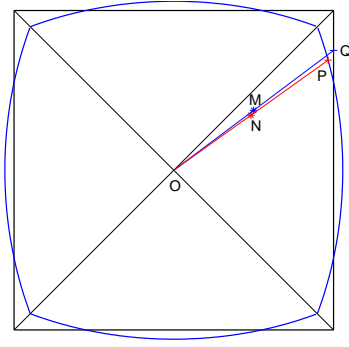


Figure 2.13: The square S_a , the curved square \mathcal{S}_a and the action of the transform T . Points N and P are the images of M and Q .

onto the curved square \mathcal{S}_a .

Since we consider only the two-dimensional problem in this section, we will work in the (x, y) -plane for simplicity, i.e., the curved boundary \mathcal{C}_a of \mathcal{S}_a is given by (2.20) and (2.21) with the notation $x = x_L$ and $y = y_L$, and analogously for the three other curves.

We focus for the moment on the first octant of the (x, y) -plane

$$I = \{(x, y) \in \mathbb{R}^2, 0 < y \leq x\}$$

with origin $O = (0, 0)$ and take a point $M = (x_M, y_M) = (x_M, mx_M) \in I$, where m is a parameter with $0 \leq m \leq 1$, see Figure 2.13. The map T will be defined in such a way that each half-line d_m of equation $y = mx$ ($0 \leq m \leq 1$) is mapped onto the half-line $d_{\varphi(m)}$ of equation $y = \varphi(m)x$, where $\varphi : [0, 1] \rightarrow \mathbb{R}$ is a differentiable function that satisfies

$$\varphi(0) = 0, \quad \varphi(1) = 1 \quad \text{and} \quad 0 \leq \varphi(m) \leq 1. \quad (2.24)$$

This condition ensures that the diagonal of the square S_a and the axis x are invariant under φ . We denote by (x_N, y_N) the coordinates of the point $N = T(M)$. Let Q be the intersection of OM with the square S_a (see Figure 2.13). The point Q has the coordinates $(x_Q, y_Q) = (\beta, m\beta)$, where $\beta = \frac{a}{2} = \sqrt{\frac{\pi}{6}}$, and the line ON has the equation $y = \varphi(m)x$. Further, let the point $P = (x_P, y_P) = P(x_P, \varphi(m)x_P)$ be the intersection of ON with the curved square \mathcal{S}_a . Thus, the coordinates of P satisfy the equations (2.22) and (2.23) with some $t_P \in [0, \frac{1}{\sqrt{3}}]$, and from (2.23) we have

$$\varphi(m) = \frac{\sqrt{2}t_P}{\sqrt{1-t_P^2}}, \quad \text{whence} \quad t_P = \frac{\varphi(m)}{\sqrt{2+\varphi^2(m)}}.$$

Replacing t_P in (2.20) and (2.21), we obtain the coordinates of P in the form

$$x_P = \frac{\sqrt{2}}{\sqrt{2+\varphi^2(m)}\sqrt{1+\frac{1}{\sqrt{2+\varphi^2(m)}}}},$$

$$y_P = \frac{\sqrt{2}\varphi(m)}{\sqrt{2+\varphi^2(m)}\sqrt{1+\frac{1}{\sqrt{2+\varphi^2(m)}}}}.$$

Some simple calculations yield the distances

$$\begin{aligned} OM &= x_M \sqrt{1 + m^2}, \\ OQ &= \beta \sqrt{1 + m^2}, \\ ON &= x_N \sqrt{1 + \varphi^2(m)}, \\ OP &= \left(2 - \frac{2}{\sqrt{2 + \varphi^2(m)}} \right)^{1/2}. \end{aligned}$$

We want to determine the map T such that

$$\frac{ON}{OP} = \frac{OM}{OQ}.$$

From the above calculations we then obtain

$$\begin{aligned} x_N &= \frac{x}{\beta} \frac{1}{\sqrt{1 + \varphi^2(m)}} \sqrt{2 - \frac{2}{\sqrt{2 + \varphi^2(m)}}}, \\ y_N &= \varphi(m) x_N = \frac{x}{\beta} \frac{\varphi(m)}{\sqrt{1 + \varphi^2(m)}} \sqrt{2 - \frac{2}{\sqrt{2 + \varphi^2(m)}}}. \end{aligned}$$

With this assertion, the map T is now completely described by means of the function φ , and we obtain that T maps the point $(x, y) \in I$ onto the point (X, Y) given by

$$X = \frac{x}{\beta} \frac{1}{\sqrt{1 + \varphi^2(\frac{y}{x})}} \sqrt{2 - \frac{2}{\sqrt{2 + \varphi^2(\frac{y}{x})}}}, \quad (2.25)$$

$$Y = \frac{x}{\beta} \frac{\varphi(\frac{y}{x})}{\sqrt{1 + \varphi^2(\frac{y}{x})}} \sqrt{2 - \frac{2}{\sqrt{2 + \varphi^2(\frac{y}{x})}}}. \quad (2.26)$$

Next we impose the area preserving property by a suitable determination of φ . For this purpose, we define the function φ such that the Jacobian of T is 1. After simplification, the Jacobian writes as

$$J(T) = \det \begin{pmatrix} \frac{\partial X}{\partial x} & \frac{\partial X}{\partial y} \\ \frac{\partial Y}{\partial x} & \frac{\partial Y}{\partial y} \end{pmatrix} = \frac{2}{\beta^2} \frac{\varphi'(\frac{y}{x})}{2 + \varphi^2(\frac{y}{x}) + \sqrt{2 + \varphi^2(\frac{y}{x})}}.$$

For solving the equation $J(T) = 1$ we substitute $v := \frac{y}{x}$, and thus, in the considered case $0 < y \leq x$ we have $v \in (0, 1]$. Hence, with the simplified notation $\varphi = \varphi(v)$, we get

$$\frac{\varphi'}{2 + \varphi^2 + \sqrt{2 + \varphi^2}} = \frac{\beta^2}{2}.$$

Integration gives

$$\arctan \varphi - \arctan \frac{\varphi}{\sqrt{2 + \varphi^2}} = \frac{\beta^2}{2} v + C.$$

The condition $\varphi(0) = 0$ yields $C = 0$. Next, in order to determine φ we use the formula

$$\arctan a - \arctan b = \arctan \frac{a - b}{1 + ab} \quad \text{for all } a, b \in \mathbb{R}, \quad ab > -1$$

and we further obtain

$$\frac{\varphi(\sqrt{2+\varphi^2}-1)}{\sqrt{2+\varphi^2}+\varphi^2} = \tan \frac{\beta^2 v}{2}. \quad (2.27)$$

To simplify this term, we introduce the notation $\gamma = \tan \frac{\beta^2 v}{2} = \tan \frac{\pi}{12} v$, and equality (2.27) yields

$$\sqrt{2+\varphi^2}(\varphi-\gamma) = \varphi(\gamma\varphi+1). \quad (2.28)$$

From the requirements (2.24) we can deduce that, for $(x, y) \in I$ with $y > 0$, both sides of equality (2.28) are positive. Thus, (2.28) is equivalent with

$$\begin{aligned} (2+\varphi^2)(\varphi-\gamma)^2 &= \varphi^2(\gamma\varphi+1)^2 \\ (\varphi^2+1)((1-\gamma^2)\varphi^2-4\varphi\gamma+2\gamma^2) &= 0, \end{aligned}$$

which gives

$$\varphi_{1,2}(v) = \frac{2\gamma \pm \sqrt{2}\gamma\sqrt{1+\gamma^2}}{1-\gamma^2}.$$

We denote $\alpha = \frac{\beta^2}{2}v = \frac{\beta^2 y}{2x}$. Thus $\gamma = \tan \alpha$ and some calculations show that the function φ becomes

$$\varphi_{1,2}(v) = \varphi_{1,2}\left(\frac{y}{x}\right) = \frac{\sqrt{2}\sin \alpha}{\sqrt{2}\cos \alpha \pm 1}, \quad \text{with } \alpha = \frac{\pi y}{12x}.$$

If we take into account the condition $\varphi(1) = 1$ and the equality

$$\sqrt{2}\sin \frac{\pi}{12} = \sqrt{2}\cos \frac{\pi}{12} - 1,$$

the only convenient solution is

$$\varphi\left(\frac{y}{x}\right) = \frac{\sqrt{2}\sin \alpha}{\sqrt{2}\cos \alpha - 1}, \quad \text{with } \alpha = \frac{\pi y}{12x}.$$

Finally, we need to replace φ in the equations (2.25)-(2.26). Some straightforward calculations show that

$$\begin{aligned} \sqrt{\varphi^2+2} &= \frac{2-\sqrt{2}\cos \alpha}{\sqrt{2}\cos \alpha-1}, \\ \sqrt{\varphi^2+1} &= \frac{\sqrt{3-2\sqrt{2}\cos \alpha}}{\sqrt{2}\cos \alpha-1}, \\ \frac{\varphi}{\sqrt{\varphi^2+1}} &= \frac{\sqrt{2}\sin \alpha}{\sqrt{3-2\sqrt{2}\cos \alpha}}. \end{aligned}$$

Hence, for $(x, y) \in I$, the formulas for the desired area preserving map $T(x, y) = (X, Y)$ are given by

$$\begin{aligned} X &= 2^{1/4} \frac{x}{\beta} \frac{\sqrt{2}\cos \alpha - 1}{\sqrt{\sqrt{2} - \cos \alpha}}, \\ Y &= 2^{1/4} \frac{x}{\beta} \frac{\sqrt{2}\sin \alpha}{\sqrt{\sqrt{2} - \cos \alpha}}, \quad \text{with } \alpha = \frac{y\pi}{12x}, \quad \beta = \sqrt{\frac{\pi}{6}}. \end{aligned}$$

Similar arguments for the other seven octants show that the area preserving map $T: \mathbb{R}^2 \rightarrow \mathbb{R}^2$ which maps squares into curved squares is defined as follows:

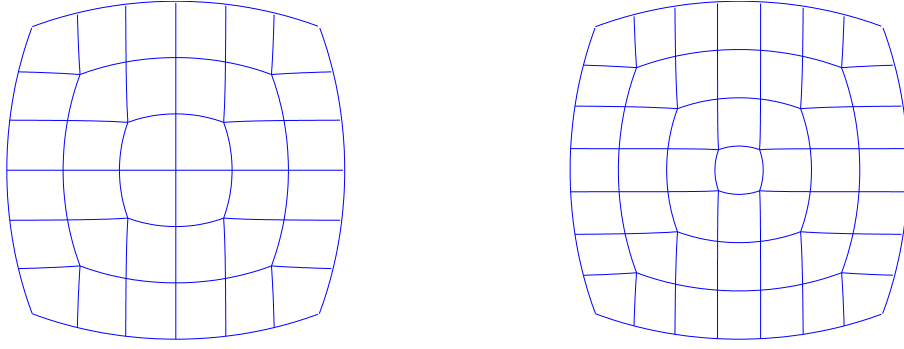


Figure 2.14: Two grids on the curved square, with seven and eight equidistant horizontal and vertical lines.

For $|y| \leq |x|$,

$$(x, y) \mapsto (X, Y) = \left(\frac{2^{1/4}x}{\beta} \frac{\sqrt{2} \cos \frac{y\pi}{12x} - 1}{\sqrt{\sqrt{2} - \cos \frac{y\pi}{12x}}}, \frac{2^{1/4}x}{\beta} \frac{\sqrt{2} \sin \frac{y\pi}{12x}}{\sqrt{\sqrt{2} - \cos \frac{y\pi}{12x}}} \right); \quad (2.29)$$

For $|x| \leq |y|$,

$$(x, y) \mapsto (X, Y) = \left(\frac{2^{1/4}y}{\beta} \frac{\sqrt{2} \sin \frac{x\pi}{12y}}{\sqrt{\sqrt{2} - \cos \frac{x\pi}{12y}}}, \frac{2^{1/4}y}{\beta} \frac{\sqrt{2} \cos \frac{x\pi}{12y} - 1}{\sqrt{\sqrt{2} - \cos \frac{x\pi}{12y}}} \right). \quad (2.30)$$

Figure 2.14 shows two grids on the curved square.

2.3.2 The inverse map

To make the area preserving map T applicable in practice, we need also to derive a closed simple form for the inverse mapping T^{-1} . Let us consider first the case when $x \geq y > 0$, when the map T is given by formula (2.29).

With the notation

$$\eta = \cos \frac{y\pi}{12x}, \quad (2.31)$$

we have

$$X^2 = \frac{\sqrt{2}x^2 (\sqrt{2}\eta - 1)^2}{\beta^2 \sqrt{2} - \eta}, \quad Y^2 = \frac{\sqrt{2}x^2 2(1 - \eta^2)}{\beta^2 \sqrt{2} - \eta}.$$

In particular,

$$\begin{aligned} X^2 + Y^2 &= \frac{\sqrt{2}x^2}{\beta^2} \frac{3 - 2\sqrt{2}\eta}{\sqrt{2} - \eta}, \\ X^2 + \frac{1}{2}Y^2 &= \frac{\sqrt{2}x^2}{\beta^2} (\sqrt{2} - \eta), \\ X^2 - \frac{1}{2}Y^2 &= \frac{\sqrt{2}x^2}{\beta^2} \frac{\eta(3\eta - 2\sqrt{2})}{\sqrt{2} - \eta}. \end{aligned} \quad (2.32)$$

We define

$$B := \frac{X^2 + \frac{1}{2}Y^2}{X^2 + Y^2} = \frac{(\sqrt{2} - \eta)^2}{3 - 2\sqrt{2}\eta}.$$

Hence, we obtain the equation in η

$$\eta^2 - 2\sqrt{2}(1 - B)\eta + 2 - 3B = 0$$

with the solutions

$$\eta_{1,2} = \sqrt{2}(1 - B) \pm \sqrt{B(2B - 1)}.$$

In our case, $\eta \in (\cos \frac{\pi}{12}, 1)$, therefore the only convenient solution is $\eta = \sqrt{2}(1 - B) + \sqrt{B(2B - 1)}$. Then, from

$$1 - B = \frac{Y^2}{2(X^2 + Y^2)} \quad \text{and} \quad 2B - 1 = \frac{X^2}{X^2 + Y^2}$$

it follows that

$$\eta = \frac{Y^2 + X\sqrt{2X^2 + Y^2}}{\sqrt{2}(X^2 + Y^2)}. \quad (2.33)$$

For simplicity we introduce the notation $w := Y/X$. Thus, we have $w \in [0, 1]$ and

$$\frac{\pi y}{12x} = \arccos \eta = \arccos \left(\frac{w^2}{\sqrt{2}(1 + w^2)} + \frac{\sqrt{2 + w^2}}{\sqrt{2}(1 + w^2)} \right).$$

Now we use the identity

$$\arccos(ab + \sqrt{1 - a^2}\sqrt{1 - b^2}) = \arccos a - \arccos b, \quad \forall \quad 0 \leq a \leq b \leq 1,$$

for $a = \frac{w}{\sqrt{2(1+w^2)}}$ and $b = \frac{w}{\sqrt{1+w^2}}$ and obtain

$$\frac{\pi y}{12x} = \arccos \frac{w}{\sqrt{2(1+w^2)}} - \arccos \frac{w}{\sqrt{1+w^2}}.$$

Other possible expressions are

$$\begin{aligned} \frac{\pi y}{12x} &= \arctan \frac{\sqrt{2 + w^2}}{w} - \arctan \frac{1}{w} \\ &= \arctan w - \arctan \frac{w}{\sqrt{2 + w^2}} \\ &= \arctan \frac{Y}{X} - \arctan \frac{Y}{\sqrt{2X^2 + Y^2}}. \end{aligned} \quad (2.34)$$

For the calculation of x from X and Y , we use the second equality in (2.32) and $\eta = \frac{w^2 + \sqrt{2 + w^2}}{\sqrt{2}(1 + w^2)}$ in order to find

$$\begin{aligned} x^2 &= \frac{\beta^2}{\sqrt{2}} \frac{X^2 + \frac{Y^2}{2}}{\sqrt{2} - \eta} = \frac{\beta^2 X^2}{2\sqrt{2}} \frac{2 + w^2}{\sqrt{2} - \eta} \\ &= \frac{\beta^2 X^2 (1 + w^2)\sqrt{2 + w^2}}{2 \sqrt{w^2 + 2} - 1} \\ &= \frac{\beta^2 X^2}{2} \sqrt{2 + w^2} (\sqrt{2 + w^2} + 1) \\ &= \frac{\beta^2}{2} \sqrt{2X^2 + Y^2} (\sqrt{2X^2 + Y^2} + X). \end{aligned}$$

Finally, from (2.31) and (2.34) we find

$$\begin{aligned} y &= \frac{12x}{\pi} \arccos \eta = \frac{12x}{\pi} \left(\arctan w - \arctan \frac{w}{\sqrt{2+w^2}} \right) \\ &= \frac{12}{\pi} \frac{\beta X}{\sqrt{2}} \sqrt[4]{2+w^2} \sqrt{1+\sqrt{2+w^2}} \left(\arctan w - \arctan \frac{w}{\sqrt{2+w^2}} \right) \\ &= \frac{\sqrt{2}}{\beta} \sqrt[4]{2X^2+Y^2} \sqrt{X+\sqrt{2X^2+Y^2}} \left(\arctan \frac{Y}{X} - \arctan \frac{Y}{\sqrt{2X^2+Y^2}} \right). \end{aligned}$$

Using similar arguments for the other seven octants, we obtain that the inverse $T^{-1} : \mathbb{R}^2 \rightarrow \mathbb{R}^2$ has the expressions

For $|Y| \leq |X|$,

$$\begin{aligned} (X, Y) \mapsto (x, y) &= \left(\frac{\beta}{\sqrt{2}} \operatorname{sign}(X) \sqrt[4]{2X^2+Y^2} \sqrt{|X|+\sqrt{2X^2+Y^2}}, \right. \\ &\quad \left. \frac{\sqrt{2}}{\beta} \sqrt[4]{2X^2+Y^2} \sqrt{|X|+\sqrt{2X^2+Y^2}} \left(\operatorname{sign}(X) \arctan \frac{Y}{X} - \arctan \frac{Y}{\sqrt{2X^2+Y^2}} \right) \right); \end{aligned}$$

For $|X| \leq |Y|$,

$$\begin{aligned} (X, Y) \mapsto (x, y) &= \left(\frac{\sqrt{2}}{\beta} \sqrt[4]{X^2+2Y^2} \sqrt{|Y|+\sqrt{X^2+2Y^2}} \left(\operatorname{sign}(Y) \arctan \frac{X}{Y} - \arctan \frac{X}{\sqrt{X^2+2Y^2}} \right), \right. \\ &\quad \left. \frac{\beta}{\sqrt{2}} \operatorname{sign}(Y) \sqrt[4]{X^2+2Y^2} \sqrt{|Y|+\sqrt{X^2+2Y^2}} \right). \end{aligned}$$

2.3.3 Mapping the curved squares onto the sphere

The complete mapping from the cube to the sphere \mathbb{S}^2 is now described in two steps. In the first step, each face F_i of the cube \mathbb{K} will be mapped onto a domain \tilde{F}_i , bounded by a curved square, using the transformation T . In the second step, each \tilde{F}_i will be mapped onto $\mathcal{F}_i \subseteq \mathbb{S}^2$ by the inverse Lambert azimuthal projection, with respect to the center of F_i . Obviously

$$\bigcap_{i=1}^6 \operatorname{int} \mathcal{F}_i = \emptyset \quad \text{and} \quad \bigcup_{i=1}^6 \mathcal{F}_i = \mathbb{S}^2.$$

We denote by $L_{(0,0,1)}$ the Lambert azimuthal area preserving projection with respect to the North Pole $N = (0, 0, 1)$. Remember that $L_{(0,0,1)}$ maps a point $(x, y, z) \in \mathbb{S}^2$ onto the point $(X_L, Y_L, 1)$ situated in the tangent plane at N , as given in (2.13) for $r = 1$.

Applying the inverse Lambert projection $L_{(0,0,1)}^{-1}$, the point $(X, Y, 1)$, situated in the tangent plane to \mathbb{S}^2 at the pole N , maps onto $(x_L, y_L, z_L) \in \mathbb{S}^2$ given by

$$x_L = \sqrt{1 - \frac{X^2 + Y^2}{4}} X, \quad (2.35)$$

$$y_L = \sqrt{1 - \frac{X^2 + Y^2}{4}} Y, \quad (2.36)$$

$$z_L = 1 - \frac{X^2 + Y^2}{2}. \quad (2.37)$$

Thus, the application $L_{(0,0,1)}^{-1} \circ T$ maps the upper face of the cube onto $\mathcal{F}_1 \subset \mathbb{S}^2$. The formulas for $L_{(0,0,1)}^{-1} \circ T(x, y)$ are given by (2.35), (2.36) and (2.37), where X, Y are calculated

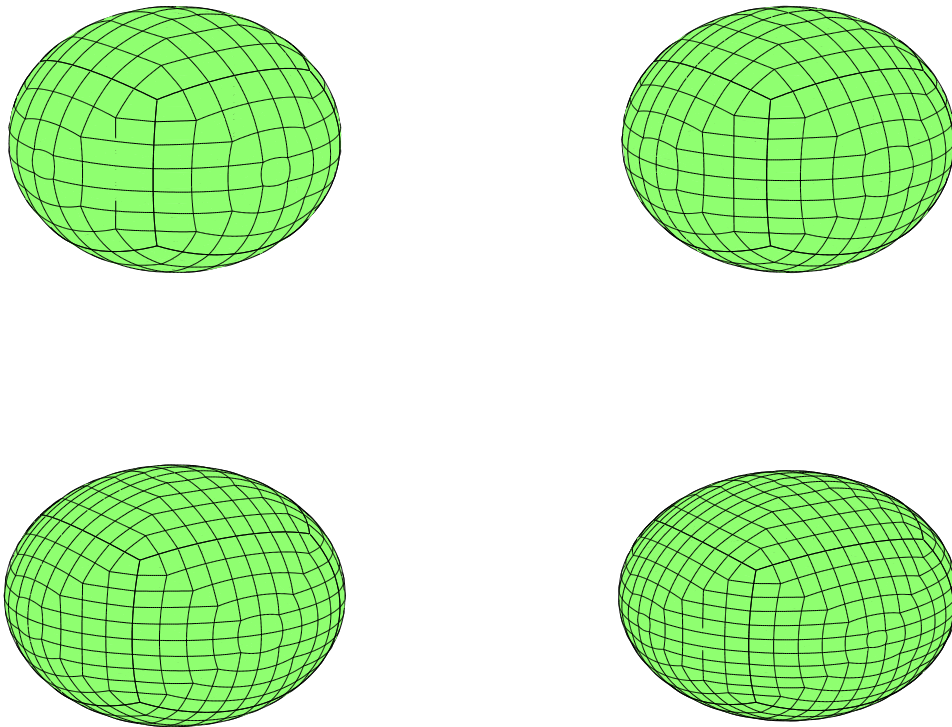


Figure 2.15: Grids on the sphere.

with formulas (2.29), (2.30). One can easily obtain similar formulas for $L_{(0,0,-1)}^{-1} \circ T$, $L_{(0,1,0)}^{-1} \circ T$, $L_{(0,-1,0)}^{-1} \circ T$, $L_{(1,0,0)}^{-1} \circ T$ and $L_{(-1,0,0)}^{-1} \circ T$. Figure 2.15 shows some grids of the sphere, where a regular partition of the faces of the cube into 49, 64, 121 and 144 equal area squares has been applied.

2.4 Area preserving projection from surfaces of revolution

In this section we present the construction of a projection from a surface of revolution onto the plane perpendicular to the rotation axis, that preserves areas. Then we will give the expression of the projection and its inverse in the cases of the paraboloid, the upper sheet of two-sheeted hyperboloid and the positive part of the cone, since these cases are the most useful in practice. The results were published in [109].

2.4.1 The general case

Consider the surface of revolution

$$\mathcal{M} : \begin{cases} x = \rho \cos t, \\ y = \rho \sin t, \\ z = \varphi(\rho), \quad t \in [0, 2\pi), \rho \in I = [0, b) \text{ or } [0, \infty). \end{cases}$$

obtained by rotating the planar curve of equation $z = \varphi(x)$ around Oz . We suppose that $\varphi \geq 0$, φ is piecewise smooth and increasing on I .

Our goal is to construct a bijection \mathbf{p} from \mathcal{M} to a subset of the plane XOY which preserves the areas. More precisely, for every portion \mathcal{S} of \mathcal{M} we must have $\mathcal{A}(\mathcal{S}) = \mathcal{A}(\mathbf{p}(\mathcal{S}))$, where $\mathcal{A}(\mathcal{S})$ denotes the area of \mathcal{S} .

The intersection of \mathcal{M} with the plane $z = z_0$, $z_0 \in \varphi(I)$, $z_0 \neq \varphi(0)$, will be a circle of radius $\rho_0 = \varphi^{-1}(z_0)$. In particular, if we consider the portion \mathcal{M}_0 situated under the plane $z = z_0$,

$$\mathcal{M}_0 : \begin{cases} z = \varphi(\sqrt{x^2 + y^2}), \\ z \leq z_0, \end{cases}$$

then we must have $\mathcal{A}(\mathcal{M}_0) = \mathcal{A}(\mathbf{p}(\mathcal{M}_0))$. In fact, we calculate $\mathcal{A}(\mathcal{M}_0)$ and determine the radius R_0 of the circle with area equal to $\mathcal{A}(\mathcal{M}_0)$. Next, the projection $M' = \mathbf{p}(M)$ of a point $M(x, y, \varphi(\sqrt{x^2 + y^2})) \in \mathcal{M}$, $x, y \neq 0$, will be defined as follows (see Figure 2.16):

1. Consider $N(x, y, 0)$ the vertical projection of M ;
2. Take M' on the half line ON , such that $OM' = R_0$.

In this way, the area of $\mathbf{p}(\mathcal{M}_0)$ will be πR_0^2 , which is exactly $\mathcal{A}(\mathcal{M}_0)$.

So, let us calculate $\mathcal{A}(\mathcal{M}_0)$. We have

$$\mathcal{A}(\mathcal{M}_0) = \iint_{\mathcal{M}_0} dS = \int_0^{2\pi} dt \int_0^{\varphi^{-1}(z_0)} \sqrt{EG - F^2} d\rho,$$

with

$$\begin{aligned} E &= (x'_t)^2 + (y'_t)^2 + (z'_t)^2 = \rho^2, \\ F &= x'_t x'_\rho + y'_t y'_\rho + z'_t z'_\rho = 0, \\ G &= (x'_\rho)^2 + (y'_\rho)^2 + (z'_\rho)^2 = 1 + (\varphi'(\rho))^2. \end{aligned}$$

Next we have, with the notation $\rho_0 = \varphi^{-1}(z_0)$,

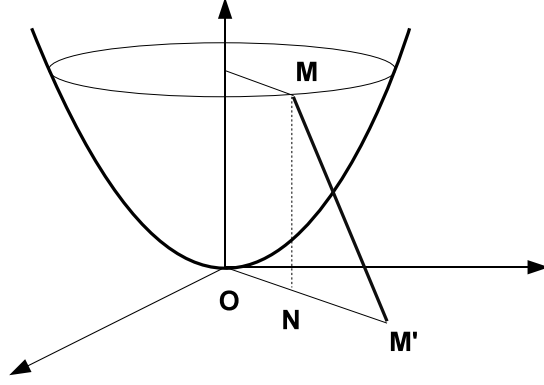
$$\mathcal{A}(\mathcal{M}_0) = \int_0^{2\pi} dt \int_0^{\rho_0} \rho \sqrt{1 + (\varphi'(\rho))^2} d\rho = \pi h(\rho_0),$$

where $h : I \rightarrow h(I) \subseteq [0, \infty)$ satisfies the equality

$$h'(\rho) = 2\rho \sqrt{1 + (\varphi'(\rho))^2}. \quad (2.38)$$

It is immediate that the function h is increasing and continuous, therefore bijective. The radius R_0 of the disc $\mathbf{p}(\mathcal{M}_0)$ is

$$R_0 = \sqrt{h(\rho_0)}.$$

Figure 2.16: The projection M' of a point $M \in \mathcal{M}$.

If we denote by (X, Y) the coordinates of $M' \neq O$, then one can easily deduce that

$$\begin{aligned} X &= R \cos t = \frac{x}{\rho} \sqrt{h(\rho)}, \\ Y &= R \sin t = \frac{y}{\rho} \sqrt{h(\rho)}. \end{aligned}$$

In the case when $\rho = 0$ we take $\mathbf{p}(0, 0, f(0)) = (0, 0)$.

In order to determine the inverse, we first observe that $X^2 + Y^2 = h(\rho)$, whence

$$\rho = h^{-1}(X^2 + Y^2).$$

Then, the inverse \mathbf{p}^{-1} can be written as

$$x = \frac{X}{\sqrt{X^2 + Y^2}} h^{-1}(X^2 + Y^2), \quad (2.39)$$

$$y = \frac{Y}{\sqrt{X^2 + Y^2}} h^{-1}(X^2 + Y^2), \quad (2.40)$$

$$z = \varphi(h^{-1}(X^2 + Y^2)). \quad (2.41)$$

Finally, we have to prove that our projection \mathbf{p} preserves the areas. Indeed,

$$\begin{aligned} E &= (x'_X)^2 + (y'_X)^2 + (z'_X)^2 = Y^2 A^2(X, Y) + X^2 B(X, Y) \\ F &= x'_X x'_Y + y'_X y'_Y + z'_X z'_Y = XY(B(X, Y) - A^2(X, Y)) \\ G &= (x'_Y)^2 + (y'_Y)^2 + (z'_Y)^2 = X^2 A^2(X, Y) + Y^2 B(X, Y), \end{aligned}$$

with

$$\begin{aligned} A(X, Y) &= \frac{h^{-1}(X^2 + Y^2)}{X^2 + Y^2} = \frac{\rho}{h(\rho)}, \\ B(X, Y) &= (1 + (\varphi'(h^{-1}(X^2 + Y^2)))^2) ((h^{-1})'(X^2 + Y^2))^2 \\ &= (1 + (\varphi'(\rho))^2) ((h^{-1})'(h(\rho)))^2 = \frac{1}{4\rho^2(1 + (\varphi'(\rho))^2)}. \end{aligned}$$

The last equality was obtained from the relation

$$(h^{-1})'(h(\rho)) \cdot h'(\rho) = 1,$$

obtained from (2.38) and by differentiating the equality $h^{-1}(h(\rho)) = \rho$.

Then, a straightforward calculation gives that $EG - F^2 = 1$, so that indeed our projection \mathbf{p} preserves the area. In the case when the curve defined by the function φ has infinite length, the area preserving property allows us to construct on \mathcal{M} a uniform grid simply by lifting a uniform grid on the plane via \mathbf{p}^{-1} . Thus we obtain the essential ingredient for defining a multiresolution analysis on \mathcal{M} , as will be done in Section 5.2.1.

2.4.2 Projection from the paraboloid $a^2z = x^2 + y^2$ onto XOY

Consider the paraboloid $\mathcal{P} : z = (x^2 + y^2)/a^2$. We use the following parametrization of \mathcal{P}_0 :

$$\mathcal{P}_0 : \begin{cases} x = a\rho \cos t \\ y = a\rho \sin t \\ z = \rho^2 \end{cases}, \quad t \in [0, 2\pi), \rho \in [0, \sqrt{z_0}].$$

We have

$$\begin{aligned} \mathcal{A}(\mathcal{P}_0) &= \int_0^{2\pi} dt \int_0^{\sqrt{z_0}} a\rho \sqrt{4\rho^2 + a^2} d\rho = 2\pi \cdot \frac{a}{12} (a^2 + 4\rho^2)^{3/2} \Big|_{\rho=0}^{\rho=\sqrt{z_0}} \\ &= \frac{a\pi}{6} ((4z_0 + a^2)^{3/2} - a^2), \end{aligned}$$

and therefore the radius R_0 of the disc $\mathbf{p}(\mathcal{P}_0)$ is

$$R_0 = \sqrt{a \cdot \frac{(4z_0 + a^2)^{3/2} - a^2}{6}}.$$

For the projection \mathbf{p} we deduce the formulas

$$X = R \cos t = \sqrt{\frac{(4z + a^2)^{3/2} - a^2}{6a}} \cdot \frac{x}{\sqrt{z}}, \quad (2.42)$$

$$Y = R \sin t = \sqrt{\frac{(4z + a^2)^{3/2} - a^2}{6a}} \cdot \frac{y}{\sqrt{z}}. \quad (2.43)$$

For the origin O we take $\mathbf{p}(O) = O$, that is $\mathbf{p}(0, 0, 0) = (0, 0)$.

The coordinates (x, y, z) of $M = \mathbf{p}^{-1}(M')$, where $M' = M'(X, Y)$, are

$$x = \frac{a^{2/3}}{2} X \sqrt{\frac{(6X^2 + 6Y^2 + a^3)^{2/3} - a^{8/3}}{X^2 + Y^2}}, \quad (2.44)$$

$$y = \frac{a^{2/3}}{2} Y \sqrt{\frac{(6X^2 + 6Y^2 + a^3)^{2/3} - a^{8/3}}{X^2 + Y^2}}, \quad (2.45)$$

$$z = \frac{(6X^2 + 6Y^2 + a^3)^{2/3} - a^{8/3}}{4a^{2/3}}. \quad (2.46)$$

An example of uniform grid on \mathcal{P} is given in Figure 2.17.

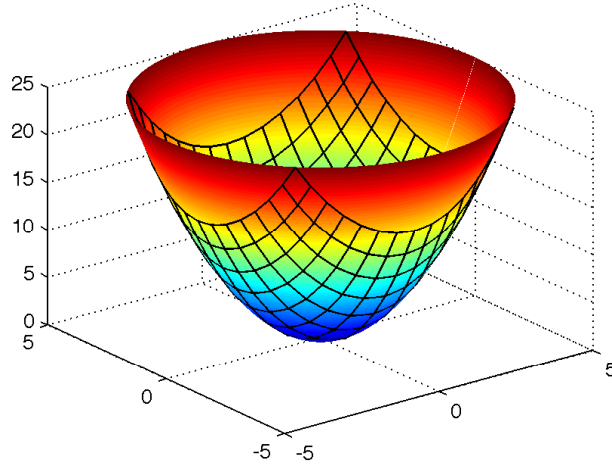


Figure 2.17: A uniform grid on the paraboloid $\mathcal{P} : z = x^2 + y^2$, formed by applying the projection \mathfrak{p}^{-1} given in (2.44)-(2.46) to the planar grid $G = \{x = -35 + 5i, i = 0, 1, \dots, 14\} \cup \{y = -35 + 5j, j = 0, 1, \dots, 14\}$.

2.4.3 Projection from the hyperboloid $z = \sqrt{1 + (x^2 + y^2)/a^2}$ onto XOY

We consider the (upper sheet) of the hyperboloid, $\mathcal{H} : z = \sqrt{1 + (x^2 + y^2)/a^2}$, with $a > 0$, and we try to perform the same steps as before. The intersection of \mathcal{H} with the plane $z = z_0, z_0 > 1$, is a circle of radius $r_0 = \sqrt{z_0^2 - 1}$. We calculate again the area of

$$\mathcal{H}_0 : \begin{cases} z = \sqrt{1 + \frac{x^2 + y^2}{a^2}}, \\ z \leq z_0. \end{cases}$$

We use the parametric equations

$$\mathcal{H}_0 : \begin{cases} x = a\rho \cos t \\ y = a\rho \sin t \\ z = \sqrt{\rho^2 + 1} \end{cases}, \quad t \in [0, 2\pi), \rho \in [0, r_0].$$

We obtain, after simple calculations,

$$EG - F^2 = a^2 \rho^2 \frac{(a^2 + 1)\rho^2 + a^2}{\rho^2 + 1}$$

and further

$$\mathcal{A}(\mathcal{H}_0) = 2\pi \int_0^{r_0} a\rho \sqrt{\frac{(a^2 + 1)\rho^2 + a^2}{\rho^2 + 1}} d\rho = \frac{\pi}{2} f(r_0) = \frac{\pi}{2} g(z_0),$$

where $f : (0, \infty) \rightarrow \mathbb{R}, g : (1, \infty) \rightarrow \mathbb{R}$,

$$\begin{aligned} f(r) &= \frac{2}{\sqrt{a^2 + 1}} \log(\sqrt{(1 + a^2)(1 + r^2)} - \sqrt{a^2 + (1 + a^2)r^2}) \\ &+ 2\sqrt{(1 + r^2)(1 + (1 + a^2)r^2)} + \frac{2}{\sqrt{a^2 + 1}} \log(a + \sqrt{a^2 + 1}) - 2a, \end{aligned}$$

$$g(z) = \frac{2}{\sqrt{1+a^2}} \log(z\sqrt{1+a^2} - \sqrt{(1+a^2)z^2-1}) \\ + 2z\sqrt{(1+a^2)z^2-1} + \frac{2}{\sqrt{a^2+1}} \log(a + \sqrt{1+a^2}) - 2a.$$

In conclusion, the radius of the disc $\mathfrak{p}(\mathcal{H}_0)$ is

$$R_0 = \sqrt{\frac{g(z_0)}{2}}.$$

Again, if we denote by (X, Y) the coordinates of $M' = \mathfrak{p}(M)$, for $M(x, y, z) \in \mathcal{H}$, $M \neq (0, 0, 1)$, then one can easily deduce that

$$X = R \cos t = \sqrt{\frac{g(z)}{2}} \cdot \frac{x}{a\sqrt{z^2-1}}, \quad (2.47)$$

$$Y = R \sin t = \sqrt{\frac{g(z)}{2}} \cdot \frac{y}{a\sqrt{z^2-1}}. \quad (2.48)$$

The projection of $(0, 0, 1)$ is taken $(0, 0)$.

Unfortunately, in the case of the hyperboloid, an explicit expression for the inverse \mathfrak{p}^{-1} cannot be determined as for the paraboloid. Indeed, we have

$$X^2 + Y^2 = \frac{g(z)}{2},$$

and since we cannot have an explicit expression of g^{-1} , we cannot obtain z as an explicit function of $X^2 + Y^2$. However, we can solve numerically the nonlinear equation $g(z) = b$, for fixed $b > 0$, by applying the Newton-Raphson method or the secant method, since $g \in C^2[1, \infty)$ and both g' and g'' have constant sign.

The coordinates (x, y, z) of $M = \mathfrak{p}^{-1}(M')$, $M'(X, Y) \neq (0, 0)$, are

$$x = aX \sqrt{\frac{(g^{-1}(2X^2 + 2Y^2))^2 - 1}{X^2 + Y^2}}, \quad (2.49)$$

$$y = aY \sqrt{\frac{(g^{-1}(2X^2 + 2Y^2))^2 - 1}{X^2 + Y^2}}, \quad (2.50)$$

$$z = g^{-1}(2X^2 + 2Y^2). \quad (2.51)$$

An example of uniform grid on \mathcal{H} is given in Figure 2.18.

2.4.4 Projection from the conical surface $z = \sqrt{(x^2 + y^2)/a^2}$

Consider the cone \mathcal{C} of equation $z = \sqrt{(x^2 + y^2)/a^2}$, with $a > 0$, and for the portion \mathcal{C}_0 with $z < z_0$ we use the parametric equations

$$\mathcal{C}_0 : \begin{cases} x = a\rho \cos t \\ y = a\rho \sin t \\ z = \rho \end{cases}, \quad t \in [0, 2\pi), \quad \rho \in [0, z_0].$$

For the radius of the disc $\mathfrak{p}(\mathcal{C}_0)$ we obtain

$$R_0 = a^{1/2}(a^2 + 1)^{1/4}z_0,$$

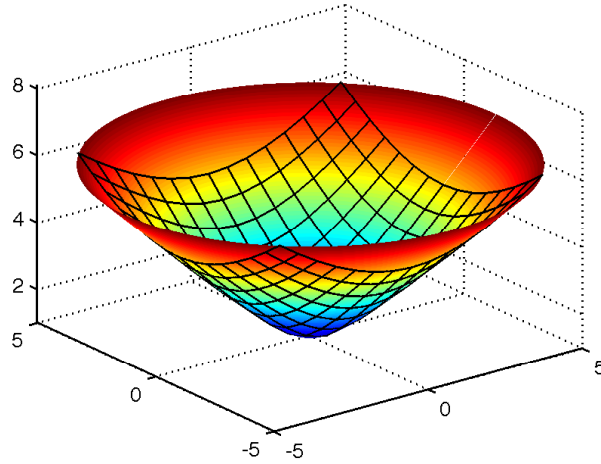


Figure 2.18: A uniform grid on the hyperboloid $\mathcal{H} : z = \sqrt{1 + x^2 + y^2}$, formed by applying the projection \mathbf{p}^{-1} given in (2.49)-(2.51) to the planar grid $G = \{x = -5 + 5i/7, i = 0, 1, \dots, 14\} \cup \{y = -5 + 5j/7, j = 0, 1, \dots, 14\}$.

and for the projection \mathbf{p} and its inverse we obtain, respectively

$$\begin{aligned} X &= R \cos t = a^{1/2}(a^2 + 1)^{1/4}z \cdot \frac{x}{az} = x a^{-1/2}(a^2 + 1)^{1/4}, \\ Y &= R \sin t = a^{1/2}(a^2 + 1)^{1/4}z \cdot \frac{y}{az} = y a^{-1/2}(a^2 + 1)^{1/4} \end{aligned}$$

and

$$x = a^{1/2}(a^2 + 1)^{-1/4}X \tag{2.52}$$

$$y = a^{1/2}(a^2 + 1)^{-1/4}Y \tag{2.53}$$

$$z = a^{-1/2}(a^2 + 1)^{-1/4}\sqrt{X^2 + Y^2}. \tag{2.54}$$

An example of uniform grid on \mathcal{C} is given in Figure 2.19.

2.4.5 Combining two area preserving projections

The grids obtained by transporting square grids onto surfaces of revolution (see Figures 2.17, 2.18, 2.19) can rise some problems when we want to handle only a finite part of the surface of revolution \mathcal{M} . A classical example that occurs in practice is the case when the rotation curve has finite length. In this case, in order to obtain a grid that covers completely the finite surface, one can combine two area preserving projections: projection T presented in Section 2.1.1 with projection \mathbf{p} described in Section 2.4. Figures 2.20 right, and 2.21 show three examples of such grids.

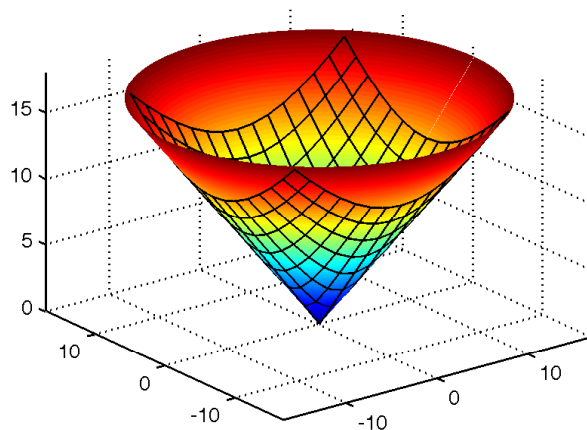


Figure 2.19: A uniform grid on the cone $\mathcal{C} : z = \sqrt{x^2 + y^2}$, formed by applying the projection \mathbf{p}^{-1} given in (2.52)-(2.54) to the planar grid $G = \{x = -14 + 2i, i = 0, 1, \dots, 14\} \cup \{y = -14 + 2j, j = 0, 1, \dots, 14\}$.

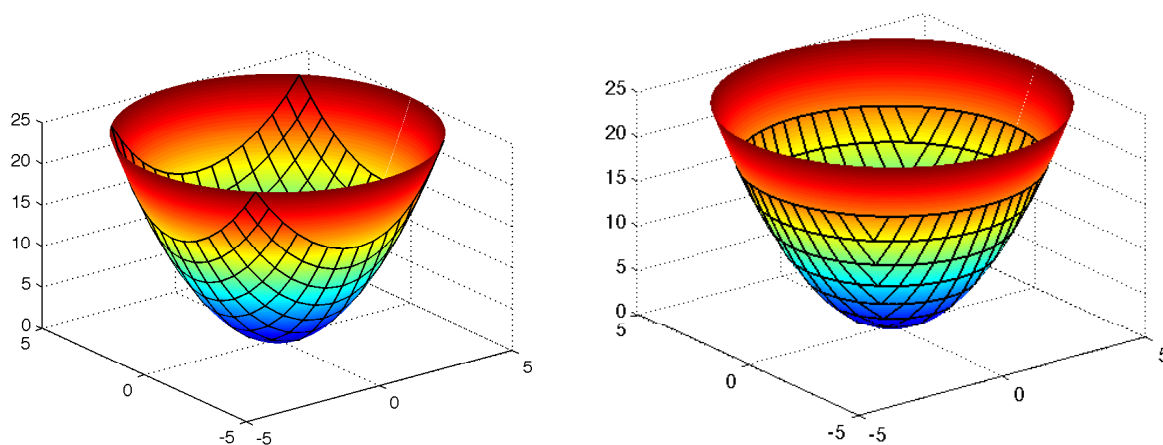


Figure 2.20: Uniform grids on the paraboloid $\mathcal{P} : z = x^2 + y^2$, formed by applying the projection \mathbf{p}^{-1} (left) and $\mathbf{p}^{-1} \circ T$ (right) to the planar grid $G = \{x = -35 + 5i, i = 0, 1, \dots, 14\} \cup \{y = -35 + 5j, j = 0, 1, \dots, 14\}$.

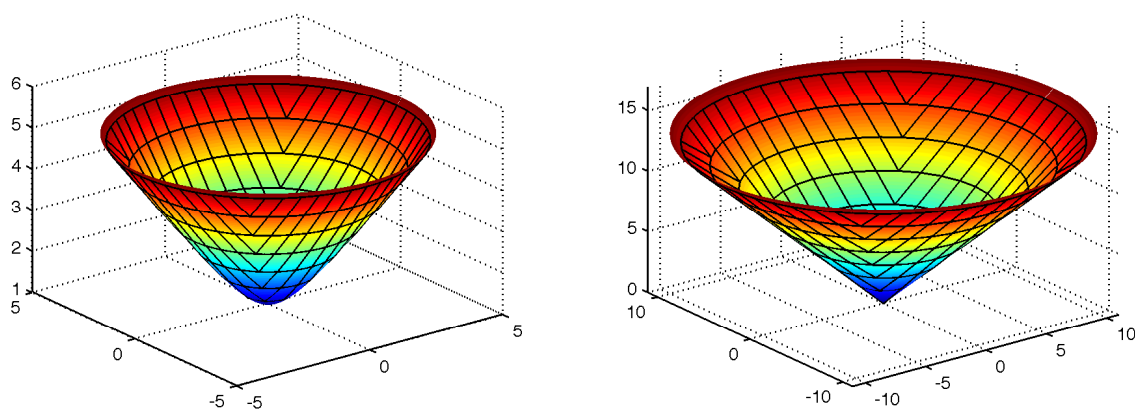


Figure 2.21: Uniform grids on the hyperboloid $\mathcal{H} : z = \sqrt{1 + x^2 + y^2}$ (left) and cone $\mathcal{C} : z = \sqrt{x^2 + y^2}$ (right), formed by applying the projection $\mathbf{p}^{-1} \circ T$ to the planar grids $G = \{x = -5 + 5i/7, i = 0, 1, \dots, 14\} \cup \{y = -5 + 5j/7, j = 0, 1, \dots, 14\}$ and $G = \{x = -14 + 2i, i = 0, 1, \dots, 14\} \cup \{y = -14 + 2j, j = 0, 1, \dots, 14\}$, respectively.

Chapter 3

Cubature formulas on the sphere

When evaluating the wavelet coefficients, in the case of wavelet approximation of functions defined on a two-dimensional sphere \mathbb{S}^2 , one needs to approximate some integrals on \mathbb{S}^2 , i.e. to construct cubature rules on \mathbb{S}^2 . If one uses some fundamental system of points, the weights of the cubature rules can be calculated explicitly.

In Section 3.1 we investigate the cubature formulas generated by a fundamental system of points obtained by Laín Fernández in [64, 65] and we also discuss the cases when this cubature leads to positive weights. An important point is the question whether spherical designs, i.e., cubature rules with equal weights, can be constructed out of these point systems. For $(n+1)^2$ points with $n = 1, 3, 5, 7, 9$ we can create such spherical designs. For larger n point systems of this type cannot lead to spherical designs. However, as a byproduct of our approach for arbitrary odd n , we obtain positive cubature rules. The crucial relation used in obtaining these cubature results is some simplification of the addition formula evaluated at these point systems presented in Lemma 3.2. The results presented in this section were published in [90, 95].

An improvement of the degree of exactness can be achieved by taking more equidistributed points on each latitudinal circle [104]. Thus we do not use fundamental systems of points anymore and therefore the corresponding cubature formulas are not interpolatory. In this way, in the Section 3.2 we show how we can obtain positive cubature formulas with higher degree of exactness.

3.1 Cubature formulas with fundamental systems of points

Let $\mathbb{S}^2 = \{x \in \mathbb{R}^3 : \|x\|_2 = 1\}$ denote the unit sphere of the Euclidean space \mathbb{R}^3 and let

$$\begin{aligned}\Psi : [0, \pi] \times [0, 2\pi) &\rightarrow \mathbb{S}^2 \\ (\rho, \theta) &\mapsto (\sin \rho \cos \theta, \sin \rho \sin \theta, \cos \rho)\end{aligned}$$

be its parametrization in spherical coordinates (ρ, θ) . The coordinate ρ of a point $\xi (\Psi(\rho, \theta)) \in \mathbb{S}^2$ is usually called the *latitude* of ξ . For given functions $f, g : \mathbb{S}^2 \rightarrow \mathbb{C}$, we consider the inner product and norm

$$\begin{aligned}\langle f, g \rangle &= \int_{\mathbb{S}^2} f(\xi) \overline{g(\xi)} d\omega(\xi), \\ \|f\| &= \sqrt{\langle f, f \rangle},\end{aligned}$$

where $d\omega(\xi)$ stands for the surface element of the sphere. We denote by \mathbb{P}_n the set of univariate polynomials of degree $\leq n$. Then, let P_k , $k = 0, 1, \dots$, denote the Legendre polynomials of

degree k on $[-1, 1]$, normalized within the condition $P_k(1) = 1$ and let V_n be the space of spherical polynomials of degree less than or equal to n . The dimension of V_n is $\dim V_n = (n+1)^2 = N$ and the reproducing kernel of V_n is defined by

$$K_n(\xi, \eta) = \sum_{k=0}^n \frac{2k+1}{4\pi} P_k(\xi \cdot \eta) = k_n(\xi \cdot \eta), \quad \xi, \eta \in \mathbb{S}^2.$$

Then for given n we consider a set of points $\{\xi_i\}_{i=1, \dots, N} \subset \mathbb{S}^2$ and the polynomial functions $\varphi_i^n : \mathbb{S}^2 \rightarrow \mathbb{C}$, $i = 1, \dots, N$, defined by

$$\varphi_i^n(\circ) = K_n(\xi_i, \circ) = \sum_{k=0}^n \frac{2k+1}{4\pi} P_k(\xi_i \cdot \circ), \quad i = 1, \dots, N.$$

These polynomials are called *scaling functions*. A set of points $\{\xi_i\}_{i=1, \dots, N}$ for which the scaling functions $\{\varphi_i^n\}_{i=1, \dots, N}$ constitute a basis for V_n is called a *fundamental system* for V_n .

The Gram matrix Φ associated to the scaling functions $\{\varphi_i^n\}_{i=1, \dots, N}$ has the entries

$$\Phi_n(r, s) = \langle \varphi_r^n, \varphi_s^n \rangle = K_n(\xi_r, \xi_s).$$

and it is positive definite when $\{\xi_i\}_{i=1, \dots, N}$ is a fundamental system for V_n .

Given the fundamental system $\{\varphi_i^n\}_{i=1, \dots, N}$ of V_n , we can construct unique spherical polynomials $L_j^n : \mathbb{S}^2 \rightarrow \mathbb{C}$ in V_n satisfying the condition $L_j^n(\xi_i) = \delta_{ij}$. These functions are called Lagrangians and the set $\{L_j^n\}_{j=1, \dots, N}$ constitutes a basis of V_n . Furthermore, any $f \in V_n$ can be written as

$$f = \sum_{i=1}^N f(\xi_i) L_i^n. \quad (3.1)$$

It is easy to verify that the Gram matrix of the Lagrangians, defined by $\mathbf{L}_n = (\langle L_i^n, L_j^n \rangle)_{i, j=1, \dots, N} \in \mathbb{C}^{N \times N}$, satisfies

$$\Phi \mathbf{L}_n = \mathbf{I}_N.$$

Here \mathbf{I}_N denotes the $N \times N$ dimensional identity matrix. This means that the Lagrangians $\{L_j^n\}_{j=1, \dots, N}$ are the dual functions of the scaling functions $\{\varphi_i^n\}_{i=1, \dots, N}$.

We wish to find appropriate numerical procedures for approximating the value of the integral

$$I(F) = \int_{\mathbb{S}^2} F(\xi) d\omega(\xi), \quad F \in C(\mathbb{S}^2).$$

This can be achieved by considering cubature formulas of the type

$$I_L(F) = \sum_{i=1}^L w_i F(\zeta_i), \quad (3.2)$$

where the L pairwise different points $\{\zeta_i\}_{i=1, \dots, L} \subset \mathbb{S}^2$ are the so-called *cubature nodes* and the coefficients $\{w_i\}_{i=1, \dots, L}$ are called the *cubature weights*. The basic problem in numerical integration consists in choosing appropriate nodes and weights such that the sum (3.2) approximates $I(F)$ for a large class of functions, as $L \rightarrow \infty$.

Let $f \in V_n$ and let $\{L_i^n\}_{i=1, \dots, N}$ be the Lagrangians associated to a fundamental system $\{\xi_i\}_{i=1, \dots, N}$. By integrating the formula (3.1) we obtain

$$\int_{\mathbb{S}^2} f(\xi) d\omega(\xi) = \sum_{i=1}^N f(\xi_i) \int_{\mathbb{S}^2} L_i^n(\xi) d\omega(\xi).$$

Therefore, the weights can be defined as

$$w_i^n = \int_{\mathbb{S}^2} L_i^n(\xi) d\omega(\xi) = \langle L_i^n, 1 \rangle, \quad i = 1, \dots, N,$$

yielding the following cubature formula

$$\int_{\mathbb{S}^2} F(\xi) d\omega(\xi) \approx \sum_{i=1}^N w_i^n F(\xi_i). \quad (3.3)$$

On the other hand, taking $f \equiv 1 \in V_n$ in (3.1), we obtain $\sum_{i=1}^N L_i^n \equiv 1$ and therefore

$$w_i^n = \langle L_i^n, 1 \rangle = \langle L_i^n, \sum_{k=1}^N L_k^n \rangle = \sum_{k=1}^N \langle L_i^n, L_k^n \rangle.$$

This means that the weight w_i^n can be calculated as the sum of the entries of the i -th row of the matrix \mathbf{L}_n , which is the inverse of the Gram matrix Φ_n . Consequently, we obtain

$$\Phi_n (w_1^n, w_2^n, \dots, w_N^n)^T = (1, 1, \dots, 1)^T. \quad (3.4)$$

N. Laín Fernández proved the following result.

Proposition 3.1 [64, 65] *Let $n \in \mathbb{N}$ be an odd number, $\alpha \in (0, 2)$ and let $0 < \rho_1 < \rho_2 < \dots < \rho_{\frac{n+1}{2}} < \pi/2$, $\rho_{n+2-j} = \pi - \rho_j$, $j = 1, \dots, (n+1)/2$, denote a system of symmetric latitudes. Then the set of points*

$$S_n(\alpha) = \{ \xi_{j,k} = \Psi(\rho_j, \theta_k^j) : j, k = 1, \dots, n+1 \},$$

where

$$\theta_k^j = \begin{cases} \frac{2k\pi}{n+1}, & \text{if } j \text{ is odd,} \\ \frac{2(k-1)+\alpha}{n+1}\pi, & \text{if } j \text{ is even,} \end{cases}$$

constitutes a fundamental system for V_n .

In the following we will study the cubature formula (3.3) for odd n , with the nodes in $S_n(\alpha)$.

3.1.1 The matrix Φ_n

Due to the symmetry of the fundamental system of points in $S_n(\alpha)$ we expect equal weights on each latitude. However, for further considerations, we need to calculate these weights explicitly. We consider the following numbering of the points of $S_n(\alpha)$

$$\begin{aligned} \eta_1 &= \xi_{1,1}, & \eta_2 &= \xi_{1,2}, & \dots, & \eta_{n+1} &= \xi_{1,n+1}, \\ \eta_{n+2} &= \xi_{2,1}, & \eta_{n+3} &= \xi_{2,2}, & \dots, & \eta_{2(n+1)} &= \xi_{2,n+1}, \\ & \dots & & & & & \\ \eta_{(n+1)n+1} &= \xi_{n+1,1}, & \eta_{(n+1)n+2} &= \xi_{n+1,2}, & \dots, & \eta_{(n+1)^2} &= \xi_{n+1,n+1}. \end{aligned}$$

For a given point $\xi_{i,j} \in S_n(\alpha)$, the corresponding numbered point is $\eta_{(n+1)(j-1)+k}$. Reciprocally, given the point η_l , then l can be uniquely written as $l = k + (n+1)(j-1)$, with $k, j \in \mathbb{N}$,

$0 \leq k < n + 1$, and thus $\eta_l = \xi_{j,k}$. With this numbering, the matrix Φ_n can be regarded as a block matrix with circulant blocks of dimension $m \times m$, with $m = n + 1$,

$$\Phi_n = \begin{pmatrix} A_{11} & A_{12} & \dots & A_{1m} \\ \vdots & \vdots & & \vdots \\ A_{m1} & A_{m2} & \dots & A_{mm} \end{pmatrix}.$$

Indeed, the entries of the block A_{ij} are

$$(A_{ij})_{r,s} = K_n(\eta_{(i-1)m+r}, \eta_{(j-1)m+s}) = k_n(\eta_{(i-1)m+r} \cdot \eta_{(j-1)m+s}),$$

where

$$\begin{aligned} \eta_{(i-1)m+r} &= \xi_{i,r} = \Psi(\rho_i, \theta_r^i), \\ \eta_{(j-1)m+s} &= \xi_{j,s} = \Psi(\rho_j, \theta_s^j) \end{aligned}$$

and

$$\eta_{(i-1)m+r} \cdot \eta_{(j-1)m+s} = \sin \rho_i \sin \rho_j \cos(\theta_r^i - \theta_s^j) + \cos \rho_i \cos \rho_j. \quad (3.5)$$

Evaluating $\theta_r^i - \theta_s^j$ we obtain

$$\theta_r^i - \theta_s^j = \begin{cases} \frac{2(r-s)\pi}{m}, & \text{for } i - j \text{ even,} \\ \frac{2(r-s)\pi}{m} + \frac{(\alpha-2)\pi}{m}(-1)^i, & \text{for } i - j \text{ odd.} \end{cases}$$

Thus, for fixed i and j , the inner product (3.5) depends only on the difference $r - s$, so we can denote it by $E_{ij}(r - s)$. It is immediate that

$$E_{ij}(r - s - mk) = E_{ij}(r - s), \text{ for all } k \in \mathbb{Z}.$$

With these considerations, the entries of the matrix A_{ij} are

$$(A_{ij})_{r,s} = (k_n \circ E_{ij})(r - s),$$

and therefore the matrix A_{ij} is circulant.

Consider now the Fourier matrix $F_m \in \mathbb{C}^{m \times m}$, with the entries

$$(F_m)_{jk} = \frac{1}{\sqrt{m}} \omega^{-(j-1)(k-1)}, \text{ where } \omega = \exp(2\pi i/m).$$

The matrix Φ_n can be written as

$$\begin{aligned} \Phi_n &= (I_m \otimes F_m)^* \Lambda (I_m \otimes F_m) \\ &= \text{diag}(F_m^*, \dots, F_m^*) \begin{pmatrix} \Lambda_{11} & \Lambda_{12} & \dots & \Lambda_{1m} \\ \vdots & \vdots & & \vdots \\ \Lambda_{m1} & \Lambda_{m2} & \dots & \Lambda_{mm} \end{pmatrix} \text{diag}(F_m, \dots, F_m) \\ &= \mathbf{F}_N^* \Lambda \mathbf{F}_N, \end{aligned}$$

with $\mathbf{F}_N = \text{diag}(F_m, \dots, F_m)$, $A_{ij} = F_m^* \Lambda_{ij} F_m$ and $\Lambda_{ij} = \text{diag}(\lambda_1(A_{ij}), \dots, \lambda_m(A_{ij}))$. Here $\lambda_k(A_{ij})$, $k = 1, \dots, m$ denote the eigenvalues of the circulant matrix A_{ij} and they are given by

$$\lambda_k(A_{ij}) = p_{A_{ij}}(\omega^{k-1}),$$

with

$$p_{A_{ij}}(x) = \sum_{\mu=1}^m (A_{ij})_{1,\mu} x^{\mu-1} = \sum_{\mu=1}^m K_n(\eta_{(i-1)m+1}, \eta_{(j-1)m+\mu}) x^{\mu-1}.$$

Consider the permutation matrix \mathbf{P} obtained from \mathbf{I}_N by re-ordering its columns \mathbf{c}_i , $i = 1, \dots, N$, as follows

$$\mathbf{P} = \begin{pmatrix} \mathbf{c}_1, \mathbf{c}_{m+1}, \mathbf{c}_{2m+1}, \dots, \mathbf{c}_{(m-1)m+1}, \mathbf{c}_2, \mathbf{c}_{m+2}, \\ \dots, \mathbf{c}_{(m-1)m+2}, \dots, \mathbf{c}_m, \mathbf{c}_{2m}, \mathbf{c}_{3m}, \dots, \mathbf{c}_{m^2} \end{pmatrix}.$$

The product $\mathbf{P}\mathbf{A}\mathbf{P}$ will be the diagonal block matrix $\mathbf{D}_N = \text{diag}(D_1, D_2, \dots, D_m)$, with

$$(D_k)_{ij} = p_{A_{ij}}(\omega^{k-1}), \quad k = 1, 2, \dots, m.$$

For the cubature formulas we are interested in evaluating the vector

$$(w_1^n, w_2^n, \dots, w_N^n)^T = \mathbf{\Phi}_n^{-1} \mathbf{u}_N,$$

where $\mathbf{u}_N = (1, 1, \dots, 1)^T \in \mathbb{R}^N$. We have shown that the matrix $\mathbf{\Phi}_n$ can be written as

$$\mathbf{\Phi}_n = \mathbf{F}_N^* \mathbf{\Lambda}_N \mathbf{F}_N = \mathbf{F}_N^* \mathbf{P} \mathbf{D}_N \mathbf{P} \mathbf{F}_N$$

and thus, using the property $\mathbf{P}^{-1} = \mathbf{P}$, we obtain

$$\mathbf{\Phi}_n^{-1} = \mathbf{F}_N^* \mathbf{P} \mathbf{D}_N^{-1} \mathbf{P} \mathbf{F}_N.$$

Then, with the notation $\mathbf{e}_1 = (1, 0, \dots, 0) \in \mathbb{R}^m$ we compute

$$\begin{aligned} F_m \mathbf{u}_m &= \frac{1}{\sqrt{m}} (m, 0, \dots, 0)^T = \sqrt{m} \mathbf{e}_1^T, \\ \mathbf{F}_N \mathbf{u}_N &= (\sqrt{m}, 0, \dots, 0 \mid \dots \mid \sqrt{m}, 0, \dots, 0)^T = \sqrt{m} (\mathbf{e}_1 \mid \mathbf{e}_1 \mid \dots \mid \mathbf{e}_1)^T, \\ \mathbf{P} \mathbf{F}_N \mathbf{u}_N &= \sqrt{m} (\underbrace{1, 1, \dots, 1}_m \mid \underbrace{0, 0, \dots, 0}_m \mid \dots \mid \underbrace{0, 0, \dots, 1}_m)^T = \sqrt{m} (\mathbf{u}_m^T \mid \mathbf{0} \mid \dots \mid \mathbf{0})^T, \\ \mathbf{D}_N^{-1} \mathbf{P} \mathbf{F}_N \mathbf{u}_N &= \sqrt{m} \text{diag}(D_1^{-1}, D_2^{-1}, \dots, D_m^{-1}) (\mathbf{u}_m^T \mid \mathbf{0} \mid \dots \mid \mathbf{0})^T \\ &= \sqrt{m} ((D_1^{-1} \mathbf{u}_m)^T \mid \mathbf{0} \mid \dots \mid \mathbf{0})^T. \end{aligned}$$

Denoting $D_1^{-1} \mathbf{u}_m = \mathbf{s} = (s_1, s_2, \dots, s_m)^T$, we further obtain

$$\mathbf{P} \mathbf{D}_N^{-1} \mathbf{P} \mathbf{F}_N \mathbf{u}_N = \sqrt{m} (\underbrace{s_1, 0, \dots, 0}_m \mid \underbrace{s_2, 0, \dots, 0}_m \mid \dots \mid \underbrace{s_m, 0, \dots, 0}_m)^T,$$

and finally

$$\mathbf{\Phi}_n^{-1} \mathbf{u}_N = \mathbf{F}_N^* \mathbf{P} \mathbf{D}_N^{-1} \mathbf{P} \mathbf{F}_N \mathbf{u}_N = (\underbrace{s_1, s_1, \dots, s_1}_m \mid \underbrace{s_2, s_2, \dots, s_2}_m \mid \dots \mid \underbrace{s_m, s_m, \dots, s_m}_m)^T.$$

In conclusion, the weights $(w_1^n, w_2^n, \dots, w_N^n)$ take at most m distinct values, contained in the vector $\mathbf{s} = (s_1, s_2, \dots, s_m)^T = D_1^{-1} \mathbf{u}_m$.

3.1.2 The matrix D_1^{-1}

We focus now on the matrix D_1 having the entries

$$\begin{aligned} (D_1)_{ij} &= \sum_{k=1}^m K_n(\eta_{(i-1)m+1}, \eta_{(j-1)m+k}) \\ &= \sum_{k=1}^m \sum_{l=0}^n \frac{2l+1}{4\pi} P_l(\eta_{(i-1)m+1} \cdot \eta_{(j-1)m+k}) \\ &= \frac{1}{4\pi} \sum_{l=0}^n (2l+1) \sum_{k=1}^m P_l(\eta_{(i-1)m+1} \cdot \eta_{(j-1)m+k}). \end{aligned}$$

At this point we prove the following result.

Lemma 3.2 *Let $\{\xi_k\}_{k=0, \dots, n}$ be $n+1$ equidistant points on a circle of \mathbb{S}^2 , situated at the latitude ρ^* . Then for every point $\xi(\Psi(\theta, \rho)) \in \mathbb{S}^2$ we have*

$$\sum_{k=0}^n P_l(\xi \cdot \xi_k) = (n+1) P_l(\cos \rho) P_l(\cos \rho^*) \text{ for } l = 0, 1, \dots, n.$$

Proof. The spherical coordinates of the point ξ_k are (θ_k, ρ^*) , with

$$\theta_k = (\beta + 2k\pi) / (n+1), \quad \beta \in [0, 2\pi), \quad k = 0, 1, \dots, n.$$

Using the associated Legendre functions P_k^j , defined by

$$P_k^j(t) = \left(\frac{(k-j)!}{(k+j)!} \right)^{1/2} (1-t^2)^{j/2} \frac{d^j}{dt^j} P_k(t), \quad j = 0, \dots, k, \quad t \in [-1, 1],$$

we can write

$$\begin{aligned} P_l(\xi \cdot \xi_k) &= \sum_{s=-l}^l P_l^{|s|}(\cos \rho) P_l^{|s|}(\cos \rho^*) e^{is\theta - is\theta_k}, \\ \sum_{k=0}^n P_l(\xi \cdot \xi_k) &= \sum_{s=-l}^l P_l^{|s|}(\cos \rho) P_l^{|s|}(\cos \rho^*) e^{is\theta - is\frac{\beta}{n+1}} \sum_{k=0}^n \left(e^{-is\frac{2\pi}{n+1}} \right)^k. \end{aligned}$$

Since $-n \leq -l \leq s \leq l \leq n$, it follows that the only non-zero term of the sum $\sum_{s=-l}^l$ is the one corresponding to $s = 0$. In this case, the sum $\sum_{k=0}^n$ equals $n+1$ and thus

$$\sum_{k=0}^n P_l(\xi \cdot \xi_k) = (n+1) P_l(\cos \rho) P_l(\cos \rho^*) \text{ for } l = 0, 1, \dots, n.$$

■

As an immediate consequence we prove the following result.

Lemma 3.3 *Let $\{\xi_k, \tilde{\xi}_k, k = 0, 1, \dots, n\}$ be $n+1$ equidistant points situated on circles which are symmetric with respect to the equator, at the latitudes ρ^* and $\pi - \rho^*$ respectively. Then*

$$\sum_{k=0}^n \left(P_{2p+1}(\xi \cdot \xi_k) + P_{2p+1}(\xi \cdot \tilde{\xi}_k) \right) = 0 \text{ for } p = 0, 1, \dots, (n+1)/2 - 1.$$

Proof. Since P_{2p+1} is an odd polynomial, we obtain

$$P_{2p+1}(\cos \rho^*) + P_{2p+1}(-\cos \rho^*) = 0.$$

Then, multiplying it by $P_{2p+1}(\cos \rho)$, the conclusion follows immediately. ■

Let us come back to the matrix D_1 . Its entries are

$$(D_1)_{ij} = \frac{n+1}{4\pi} \sum_{l=0}^n (2l+1) P_l(\cos \rho_i) P_l(\cos \rho_j).$$

With the notations $n+1 = m$, $q = (n+1)/2$ and $\cos \rho_i = r_i$, $i = 1, \dots, q$, it can be written as $D_1 = \mathbf{G} \cdot \mathbf{G}^T$, with

$$\mathbf{G} = \sqrt{\frac{m}{4\pi}} \begin{pmatrix} P_0(r_1) & \sqrt{3}P_1(r_1) & \sqrt{5}P_2(r_1) & \cdots & \sqrt{2n+1}P_n(r_1) \\ P_0(r_2) & \sqrt{3}P_1(r_2) & \sqrt{5}P_2(r_2) & \cdots & \sqrt{2n+1}P_n(r_2) \\ \vdots & \vdots & \vdots & \cdots & \vdots \\ P_0(r_q) & \sqrt{3}P_1(r_q) & \sqrt{5}P_2(r_q) & \cdots & \sqrt{2n+1}P_n(r_q) \\ P_0(-r_q) & \sqrt{3}P_1(-r_q) & \sqrt{5}P_2(-r_q) & \cdots & \sqrt{2n+1}P_n(-r_q) \\ \vdots & \vdots & \vdots & \cdots & \vdots \\ P_0(-r_2) & \sqrt{3}P_1(-r_2) & \sqrt{5}P_2(-r_2) & \cdots & \sqrt{2n+1}P_n(-r_2) \\ P_0(-r_1) & \sqrt{3}P_1(-r_1) & \sqrt{5}P_2(-r_1) & \cdots & \sqrt{2n+1}P_n(-r_1) \end{pmatrix}.$$

Consider the matrix \mathbf{P}_1 , obtained from the identity matrix \mathbf{I}_m by the transformations row $(n+1) \leftarrow$ row $(n+1) -$ row 1, row $n \leftarrow$ row $n -$ row 2, \dots , row $(q+1) \leftarrow$ row $(q+1) -$ row q . Then the matrix $\mathbf{G}_1 = \mathbf{P}_1 \mathbf{G}$ has the form

$$\mathbf{G}_1 = \sqrt{\frac{m}{4\pi}} \begin{pmatrix} P_0(r_1) & \sqrt{3}P_1(r_1) & \sqrt{5}P_2(r_1) & \cdots & \sqrt{2n+1}P_n(r_1) \\ \vdots & \vdots & \vdots & \cdots & \vdots \\ P_0(r_q) & \sqrt{3}P_1(r_q) & \sqrt{5}P_2(r_q) & \cdots & \sqrt{2n+1}P_n(r_q) \\ 0 & -2\sqrt{3}P_1(r_q) & 0 & \cdots & -2\sqrt{2n+1}P_n(r_q) \\ \vdots & \vdots & \vdots & \cdots & \vdots \\ 0 & -2\sqrt{3}P_1(r_1) & 0 & \cdots & -2\sqrt{2n+1}P_n(r_1) \end{pmatrix}.$$

By multiplying it by a permutation matrix \mathbf{P}_2 we can write

$$\mathbf{G}_2 = \mathbf{G}_1 \mathbf{P}_2 = c_n \left(\begin{array}{c|c} \mathbf{X}_q & \mathbf{P}_3 \mathbf{Y}_q \\ \hline \mathbf{0}_q & -2\mathbf{Y}_q \end{array} \right),$$

where $c_n = \sqrt{\frac{n+1}{4\pi}}$,

$$\mathbf{X}_q = \begin{pmatrix} 1 & \sqrt{5}P_2(r_1) & \cdots & \sqrt{2n-1}P_{n-1}(r_1) \\ \vdots & \vdots & & \vdots \\ 1 & \sqrt{5}P_2(r_q) & \cdots & \sqrt{2n-1}P_{n-1}(r_q) \end{pmatrix}, \quad (3.6)$$

$$\mathbf{Y}_q = \begin{pmatrix} \sqrt{3}P_1(r_q) & \sqrt{7}P_3(r_q) & \dots & \sqrt{2n+1}P_n(r_q) \\ \vdots & \vdots & & \vdots \\ \sqrt{3}P_1(r_1) & \sqrt{7}P_3(r_1) & \dots & \sqrt{2n+1}P_n(r_1) \end{pmatrix},$$

and $\mathbf{P}_3 \in \mathbb{R}^{q \times q}$ is a permutation matrix which changes the rows $(1, \frac{n+1}{2}), (2, \frac{n-1}{2}), \dots, (\frac{q}{2}, \frac{q+1}{2})$.

We wish to evaluate $D_1^{-1}\mathbf{u}_m$, so we write

$$\begin{aligned} D_1 &= \mathbf{G}\mathbf{G}^T = \mathbf{P}_1^{-1}\mathbf{G}_1(\mathbf{P}_1^{-1}\mathbf{G}_1)^T = \mathbf{P}_1^{-1}\mathbf{G}_1\mathbf{G}_1^T(\mathbf{P}_1^T)^{-1} \\ &= \mathbf{P}_1^{-1}\mathbf{G}_2\mathbf{P}_2^T(\mathbf{G}_2\mathbf{P}_2^T)^T(\mathbf{P}_1^{-1})^T = \mathbf{P}_1^{-1}\mathbf{G}_2\mathbf{G}_2^T(\mathbf{P}_1^{-1})^T \end{aligned}$$

and finally

$$D_1^{-1} = \mathbf{P}_1^T(\mathbf{G}_2^{-1})^T\mathbf{G}_2^{-1}\mathbf{P}_1.$$

Then $\mathbf{P}_1\mathbf{u}_m = (\mathbf{u}_q|\mathbf{0}_q)^T$, and

$$\begin{aligned} \mathbf{G}_2^{-1} &= \frac{1}{c_n} \begin{pmatrix} \mathbf{X}_q & \mathbf{P}_3\mathbf{Y}_q \\ \mathbf{0}_q & -2\mathbf{Y}_q \end{pmatrix}^{-1} \\ &= \frac{1}{c_n} \begin{pmatrix} \mathbf{X}_q^{-1} & \frac{1}{2}\mathbf{X}_q^{-1}(\mathbf{P}_3\mathbf{Y}_q)\mathbf{Y}_q^{-1} \\ \mathbf{0}_q & -\frac{1}{2}\mathbf{Y}_q^{-1} \end{pmatrix} = \frac{1}{c_n} \begin{pmatrix} \mathbf{X}_q^{-1} & \frac{1}{2}\mathbf{X}_q^{-1}\mathbf{P}_3 \\ \mathbf{0}_q & -\frac{1}{2}\mathbf{Y}_q^{-1} \end{pmatrix}. \end{aligned}$$

Moreover, we obtain

$$\begin{aligned} \mathbf{G}_2^{-1}\mathbf{P}_1\mathbf{u}_m &= \frac{1}{c_n} \begin{pmatrix} \mathbf{X}_q^{-1}\mathbf{u}_q \\ \mathbf{0}_q \end{pmatrix}, \\ (\mathbf{G}_2^{-1})^T\mathbf{G}_2^{-1}\mathbf{P}_1\mathbf{u}_m &= \frac{1}{c_n^2} \begin{pmatrix} (\mathbf{X}_q^{-1})\mathbf{X}_q^{-1}\mathbf{u}_q \\ \frac{1}{2}(\mathbf{X}_q^{-1}\mathbf{P}_3)^T\mathbf{u}_q \end{pmatrix} \\ &= \frac{1}{c_n^2} \begin{pmatrix} (\mathbf{X}_q\mathbf{X}_q^T)^{-1}\mathbf{u}_q \\ \frac{1}{2}\mathbf{P}_3(\mathbf{X}_q\mathbf{X}_q^T)^{-1}\mathbf{u}_q \end{pmatrix} \end{aligned}$$

and

$$\mathbf{P}_1^T(\mathbf{G}_2^{-1})^T\mathbf{G}_2^{-1}\mathbf{P}_1\mathbf{u}_m = \frac{1}{c_n^2} \begin{pmatrix} \frac{1}{2}(\mathbf{X}_q\mathbf{X}_q^T)^{-1}\mathbf{u}_q \\ \frac{1}{2}\mathbf{P}_3(\mathbf{X}_q\mathbf{X}_q^T)^{-1}\mathbf{u}_q \end{pmatrix} = D_1^{-1}\mathbf{u}_m.$$

Denoting

$$\mathbf{a} = (a_1, a_2, \dots, a_q)^T = (\mathbf{X}_q\mathbf{X}_q^T)^{-1}\mathbf{u}_q,$$

the vector $\mathbf{P}_3(\mathbf{X}_q\mathbf{X}_q^T)^{-1}\mathbf{u}_q$ is equal to $(a_q, \dots, a_2, a_1)^T$ and thus

$$D_1^{-1}\mathbf{u}_m = \frac{2\pi}{m} (a_1, a_2, \dots, a_q, a_q, a_{q-1}, \dots, a_2, a_1).$$

In conclusion, the cubature weights w_i^n take at most q distinct values and in order to evaluate them it is enough to evaluate the components of the vector $\mathbf{a} = (\mathbf{X}_q\mathbf{X}_q^T)^{-1}\mathbf{u}_q$.

3.1.3 The weights of the cubature formula

The matrix \mathbf{X}_q given in (3.6) can be written as $\mathbf{X} = \mathbf{X}_q = \mathbf{V} \cdot \mathbf{U}$, with

$$\mathbf{V} = \begin{pmatrix} 1 & r_1^2 & r_1^4 & \cdots & r_1^{n-1} \\ 1 & r_2^2 & r_2^4 & \cdots & r_2^{n-1} \\ \vdots & & & & \vdots \\ 1 & r_q^2 & r_q^4 & \cdots & r_q^{n-1} \end{pmatrix}, \quad (3.7)$$

$$\mathbf{U} = \begin{pmatrix} b_{00} & \sqrt{5}b_{02} & \sqrt{9}b_{04} & \cdots & \sqrt{2n-1}b_{0,n-1} \\ & \sqrt{5}b_{12} & \sqrt{9}b_{14} & \cdots & \sqrt{2n-1}b_{1,n-1} \\ & & & \vdots & \\ & & & & \sqrt{2n-1}b_{q-1,n-1} \end{pmatrix},$$

the entries of the matrix \mathbf{U} being the coefficients of the Legendre polynomials

$$P_{2l}(x) = \sum_{k=0}^l b_{k,2l} x^{2k}.$$

Since the vector \mathbf{a} is the solution of the system

$$\mathbf{X} \mathbf{X}^T \mathbf{a} = \mathbf{u}_q, \quad (3.8)$$

using the Cramer's rule, the component a_i can be written as

$$a_i = \frac{\det(\mathbf{Y}_i)}{\det(\mathbf{X} \mathbf{X}^T)},$$

where \mathbf{Y}_i is the matrix obtained by replacing in $\mathbf{Y} = \mathbf{X} \mathbf{X}^T$ the column i by the vector \mathbf{u}_q . One can prove that the matrix \mathbf{Y}_i can be written as $\mathbf{X} \mathbf{X}_i^T$, where \mathbf{X}_i^T is the matrix obtained from \mathbf{X}^T by replacing the column i by the column vector $\mathbf{e}_1^T = (1, 0, \dots, 0)$. Consequently,

$$a_i = \frac{\det(\mathbf{X}) \cdot \det(\mathbf{X}_i^T)}{\det(\mathbf{X}) \cdot \det(\mathbf{X}^T)} = \frac{\det(\mathbf{X}_i^T)}{\det(\mathbf{X}^T)} = \frac{\det(\mathbf{Z}_i^T)}{\det(\mathbf{Z}^T)},$$

where

$$\mathbf{Z} = \begin{pmatrix} 1 & P_2(r_1) & \cdots & P_{n-1}(r_1) \\ 1 & P_2(r_2) & \cdots & P_{n-1}(r_2) \\ \vdots & \vdots & & \cdots \\ 1 & P_2(r_q) & \cdots & P_{n-1}(r_q) \end{pmatrix}$$

and the matrix \mathbf{Z}_i^T is obtained from the matrix \mathbf{Z}^T by replacing the column i by the vector $(1, 0, \dots, 0)^T$. Thus, the vector \mathbf{a} becomes the solution of the system

$$\mathbf{Z}^T \cdot \mathbf{a} = \mathbf{e}_1,$$

which implies $\mathbf{a} = (\mathbf{Z}^T)^{-1} \mathbf{e}_1$. The matrix \mathbf{Z}^T can be written as $\mathbf{Z}^T = \mathbf{L} \cdot \mathbf{V}^T$, where \mathbf{V} is defined in (3.7) and

$$\mathbf{L} = \begin{pmatrix} 1 & 0 & 0 & \cdots & 0 \\ b_{02} & b_{12} & 0 & \cdots & 0 \\ b_{04} & b_{14} & b_{24} & \cdots & 0 \\ \vdots & & & & \\ b_{0,n-1} & b_{1,n-1} & b_{2,n-1} & \cdots & b_{q-1,n-1} \end{pmatrix}.$$

So, $\mathbf{a} = (\mathbf{V}^T)^{-1} \mathbf{L}^{-1} \mathbf{e}_1$, the vector $\mathbf{g} = \mathbf{L}^{-1} \mathbf{e}_1$ being the first column of the matrix \mathbf{L}^{-1} .

In order to calculate the first column of \mathbf{L}^{-1} we use the orthogonality property of Legendre polynomials. Since P_{2l} is an even polynomial, orthogonal to P_0 on the interval $[-1, 1]$ for $l \neq 0$, we can write

$$0 = \int_0^1 P_{2l}(x) dx = \int_0^1 \sum_{k=0}^l b_{k,2l} x^{2k} dx = \sum_{k=0}^l \frac{1}{2k+1} b_{k,2l}.$$

Hence, the row l , $l \neq 1$ of the matrix \mathbf{L} is orthogonal to the vector $\mathbf{v} = \left(1, \frac{1}{3}, \frac{1}{5}, \dots, \frac{1}{2q-1}\right)^T$ and thus the first column of \mathbf{L}^{-1} will be \mathbf{v} .

We have now to evaluate the vector $\mathbf{a} = \mathbf{V}^{-1} \mathbf{v}$. Using again the Cramer's rule, we can calculate a_i by replacing the vector \mathbf{v} into the i -th column of \mathbf{V}^T , as follows

$$\begin{aligned} a_i &= \frac{1}{\det(\mathbf{V})} \cdot \begin{vmatrix} 1 & 1 & \dots & 1 & 1 & 1 & \dots & 1 \\ r_1^2 & r_2^2 & \dots & r_{i-1}^2 & \frac{1}{3} & r_{i+1}^2 & \dots & r_q^2 \\ r_1^4 & r_2^4 & \dots & r_{i-1}^4 & \frac{1}{5} & r_{i+1}^4 & \dots & r_q^4 \\ \vdots & \vdots & \dots & \vdots & \vdots & \vdots & \dots & \vdots \\ r_1^{n-1} & r_2^{n-1} & \dots & r_{i-1}^{n-1} & \frac{1}{2q-1} & r_{i+1}^{n-1} & \dots & r_q^{n-1} \end{vmatrix} \\ &= (-1)^{i+1} \left(V_0^i - \frac{1}{3} V_1^i + \frac{1}{5} V_2^i + \dots + (-1)^{q-1} \frac{1}{2q-1} V_q^i \right), \end{aligned}$$

where V_k^i , $k = 0, 1, \dots, q-1$, denote the lacunary Vandermonde determinants, obtained from the matrix V by eliminating the row $k+1$ together with the column i . Regarding the lacunary Vandermonde determinants, the following result is known.

Lemma 3.4 *Let $x_1, x_2, \dots, x_p \in \mathbb{C}$ and $V = V(x_1, x_2, \dots, x_p) \in \mathbb{C}$ their Vandermonde determinant. Let V_k denote the following lacunary determinant*

$$V_k = V_k(x_1, \dots, x_p) = \begin{vmatrix} 1 & 1 & \dots & 1 \\ x_1 & x_2 & \dots & x_p \\ \vdots & \vdots & \dots & \vdots \\ x_1^{k-1} & x_2^{k-1} & \dots & x_p^{k-1} \\ x_1^{k+1} & x_2^{k+1} & \dots & x_p^{k+1} \\ \vdots & \vdots & \dots & \vdots \\ x_1^p & x_2^p & \dots & x_p^p \end{vmatrix}, \quad k = 0, 1, \dots, p.$$

Then $V_k = V \cdot S_{p-k}$, where S_k , $k = 0, 1, \dots, p$, denote the Viète sums of the numbers x_1, \dots, x_p .

Using Lemma 3.4, the numbers a_i can be expressed as

$$\begin{aligned} a_i &= (-1)^{i+1} \frac{V(r_1^2, \dots, r_{i-1}^2, r_{i+1}^2, \dots, r_q^2)}{V(r_1^2, \dots, r_q^2)} \\ &\times \left(S_q^i - \frac{1}{3} S_{q-1}^i + \frac{1}{5} S_{q-2}^i - \dots + \frac{(-1)^{q-2}}{2q-3} S_1^i + \frac{(-1)^{q-1}}{2q-1} \right), \end{aligned}$$

where S_k^i , $k = 1, \dots, q$, are the Viète sums of the numbers $r_1^2, \dots, r_{i-1}^2, r_{i+1}^2, \dots, r_q^2$. Replacing the values $\frac{1}{2l+1}$, $l = 0, 1, \dots, q-1$, with $\int_0^1 x^{2l} dx$, we further obtain

$$\begin{aligned} a_i &= \frac{(-1)^{i+1}(-1)^{q-i}(-1)^{q-1}}{(r_i^2 - r_1^2) \dots (r_i^2 - r_{i-1}^2)(r_i^2 - r_{i+1}^2) \dots (r_i^2 - r_q^2)} \\ &\times \int_0^1 (x^{2q-2} - S_1^i x^{2q-4} + S_2^i x^{2q-6} - \dots + (-1)^{q-2} x^2 S_{q-1}^i + (-1)^{q-1} S_q^i) dx \\ &= \int_0^1 \frac{(x^2 - r_1^2) \dots (x^2 - r_{i-1}^2)(x^2 - r_{i+1}^2) \dots (x^2 - r_q^2)}{(r_i^2 - r_1^2) \dots (r_i^2 - r_{i-1}^2)(r_i^2 - r_{i+1}^2) \dots (r_i^2 - r_q^2)} dx \\ &= \int_0^1 l_i(x^2) dx, \end{aligned}$$

where $l_i(x)$ are the fundamental Lagrange polynomials associated to the points r_1^2, \dots, r_q^2 .

Further, the vector $\mathbf{l} = (l_1(x^2), l_2(x^2), \dots, l_q(x^2))^T$ can be regarded as the solution of the system

$$\mathbf{V}^T \mathbf{l} = (1, x^2, x^4, \dots, x^{2(q-1)})^T, \quad (3.9)$$

with \mathbf{V} given in (3.7). By integrating from 0 to 1 the equations of the system (3.9) we obtain that the weights $\{a_i, i = 1, \dots, q\}$ and the cosines of the latitudes, $\{r_j, j = 1, \dots, q\}$, should satisfy the following conditions

$$\begin{aligned} a_1 + a_2 + \dots + a_q &= 1, \\ a_1 r_1^2 + a_2 r_2^2 + \dots + a_q r_q^2 &= 1/3, \\ a_1 r_1^4 + a_2 r_2^4 + \dots + a_q r_q^4 &= 1/5, \\ &\dots \\ a_1 r_1^{2(q-1)} + a_2 r_2^{2(q-1)} + \dots + a_q r_q^{2(q-1)} &= 1/(2q-1). \end{aligned} \quad (3.10)$$

Thus, for the quadrature formula

$$\int_0^1 f(x) dx \approx \sum_{i=1}^q a_i f(r_i), \quad (3.11)$$

the equations of the system (3.10) are equivalent to the requirements that the quadrature formula (3.11) is exact for the monomials $1, x^2, x^4, \dots, x^{2q-2}$.

On the other hand, if we denote $v_1 = -r_q, v_2 = -r_{q-1}, \dots, v_q = -r_1, v_{q+1} = r_1, v_{q+2} = r_2, \dots, v_{2q} = r_q$, then the numbers v_i can be regarded as the nodes of the quadrature formula

$$\int_{-1}^1 f(x) dx \approx \sum_{i=1}^{2q} a_i f(v_i), \quad (3.12)$$

with $a_{n+2-i} = a_i$ for $i = 1, \dots, q$, and the system (3.10) is equivalent to the requirement that the quadrature formula (3.12) is exact for the monomials $1, x, x^2, \dots, x^{2q-1}$.

3.1.4 Cubature formulas with positive weights

We are particularly interested in the positivity of the weights $w_i^n = \frac{2\pi}{n+1} a_i$, $i = 1, \dots, q$. Consider the interpolating cubature formula

$$\int_{\mathbb{S}^2} F(\xi) d\omega(\xi) \approx \sum_{i=1}^{n+1} \sum_{k=1}^{n+1} w_{i,k}^n F(\xi_{i,k}), \quad (3.13)$$

with $\xi_{i,k} \in S_n(\alpha)$, for which we have proved the equalities $w_{i,k}^n = w_i^n$ for $i, k \in \{1, \dots, n\}$ and the fact that the weights w_i^n , $i = 1, \dots, n+1$ take q distinct values denoted $\frac{2\pi}{n+1}a_i$, $i = 1, \dots, q$. Let us denote $r_i = \cos \rho_i$ for $i = 1, \dots, q$, $v_1 = -r_q, v_2 = -r_{q-1}, \dots, v_q = -r_1, v_{q+1} = r_1, v_{q+2} = r_2, \dots, v_{2q} = r_q$. The following theorem describes three possible cases in which the weights are positive.

Theorem 3.5 *With the above notations, the cubature formula (3.13) is positive in the following cases.*

1. The numbers v_i are the roots of the Legendre polynomial P_{n+1} and

$$a_i = \frac{2}{(1 - v_i^2) (P'_{n+1}(v_i))^2}, \text{ for } i = 1, \dots, q.$$

2. The numbers r_i are taken as $r_i = \frac{t_i+1}{2}$, where t_i are the roots of the Legendre polynomial P_q , and

$$a_i = \frac{1}{(1 - t_i^2) (P'_q(t_i))^2}, \text{ for } i = 1, \dots, q.$$

3. More general, the numbers r_i are taken as $r_i = \frac{t_i+1}{2}$, where t_i are the roots of the polynomial $Q_q = P_q + \rho P_{q-1}$, with $\rho \in (-1, 1)$ and

$$a_i = \frac{1}{(1 - t_i^2) (P'_q(t_i))^2}, \text{ for } i = 1, \dots, q.$$

Proof. 1. Choosing the latitudes $\{\rho_i, i = 1, \dots, n+1\}$ such that $\cos \rho_i = v_i$, the matrix D_1 becomes diagonal with positive entries and therefore the vector $D_1^{-1} \mathbf{u}_m$ has positive components.
2. With the notation $g(t) = \frac{1}{2}f\left(\frac{t+1}{2}\right)$ we have

$$\begin{aligned} \int_0^1 f(x)dx &= \frac{1}{2} \int_{-1}^1 f\left(\frac{t+1}{2}\right) dt = \int_{-1}^1 g(t)dt \approx \sum_{i=1}^q \alpha_i g(t_i) \\ &= \frac{1}{2} \sum_{i=1}^q \alpha_i f\left(\frac{t_i+1}{2}\right) = \sum_{i=1}^q a_i f(r_i). \end{aligned}$$

Thus, the quadrature formula (3.11) has positive weights given by

$$a_i = \frac{\alpha_i}{2} = \frac{1}{(1 - t_i^2) (P'_q(t_i))^2}$$

and it is exact for $f \in \mathbb{P}_{2q-1}$, since the quadrature formula

$$\int_{-1}^1 g(t)dt \approx \sum_{i=1}^q \alpha_i g(t_i)$$

is exact for $g \in \mathbb{P}_{2q-1}$.

3. It is known (see [127], Th. 3.3.4, [133]) that the polynomial Q_q has distinct zeros, all situated in $(-1, 1)$ if and only if $\rho \in (-1, 1)$. In this case, the quadrature formula (3.11) has positive weights and is exact for $f \in \mathbb{P}_{2q-2}$. ■

3.1.5 Spherical designs

A spherical design is a set of points of \mathbb{S}^2 which generates a cubature formula with equal weights, which is exact for spherical polynomial up to a certain degree. We try to find conditions on the latitudes ρ_i , which assure that the set $S_n(\alpha)$ is a spherical design. So we suppose

$$w_1^n = w_2^n = \dots = w_N^n = w_n,$$

implying $a_1 = a_2 = \dots = a_q = 1/q$. We make again the notations $\cos \rho_i = r_i$, $r_i^2 = \gamma_i$, for $i = 1, \dots, q$. In the trivial case $n = 1$, we obtain a spherical design if and only if $w_1 = \pi$ and $\rho_1 = \pi/6$.

Next we focus on the case $n \geq 3$. In this case the numbers γ_i should satisfy the following conditions

$$\begin{aligned} \gamma_1 + \gamma_2 + \dots + \gamma_q &= q/3, \\ \gamma_1^2 + \gamma_2^2 + \dots + \gamma_q^2 &= q/5, \\ &\dots \\ \gamma_1^{q-1} + \gamma_2^{q-1} + \dots + \gamma_q^{q-1} &= q/n, \end{aligned} \tag{3.14}$$

equivalent to the requirement that the quadrature formula (cf. (3.12))

$$\int_{-1}^1 f(x) dx \approx \frac{1}{q} \sum_{i=1}^q (f(r_i) + f(-r_i)) \tag{3.15}$$

is exact for the monomials $1, x, \dots, x^{2q-1}$. Let us mention here that, unlike the classical Chebyshev quadrature, we impose in (3.15) for our purpose only $q - 1$ conditions for q unknowns.

The purpose now is to show how to solve the system (3.14), containing $q - 1$ equations and q unknowns. A way to do it is described in the following.

We introduce the notations $W_0 = q$,

$$W_k = \gamma_1^k + \gamma_2^k + \dots + \gamma_q^k, \quad k = 1, 2, \dots, q$$

and the parameter $\beta = W_q$. The solutions of the system (3.14) are the roots of the polynomial

$$T_q(x) = x^q + S_1 x^{q-1} + S_2 x^{q-2} + \dots + S_q,$$

where $(-1)^k S_k$ denotes the Viète sums of order k associated to the numbers $\gamma_1, \dots, \gamma_q$. They are related to the sums W_k through the following relations

$$\begin{aligned} W_1 + S_1 &= 0, \\ W_2 + S_1 W_1 + 2S_2 &= 0, \\ W_3 + S_1 W_2 + S_2 W_1 + 3S_3 &= 0, \\ &\dots \\ W_q + S_1 W_{q-1} + S_2 W_{q-2} + \dots + S_q W_0 &= 0. \end{aligned} \tag{3.16}$$

Thus, in order to solve the system (3.14), we first calculate recursively the numbers S_1, S_2, \dots, S_q using the relations (3.16) and then determine the roots of the polynomial T_q . This polynomial depends on the parameter β , which appears only in the free term S_q .

For our purposes we need to find those values of β for which the polynomial T_q has all the roots located in $(0, 1)$. The following theorem discusses all the cases for which the set $S_n(\alpha)$ defined in Theorem 3.1 constitutes a spherical design.

Theorem 3.6 Let $n \in \mathbb{N}$, $n \geq 3$, be an odd number, $q = (n+1)/2$ and consider the set $S_n(\alpha)$, defined in Proposition 3.1, with arbitrary $\alpha \in (0, 2)$ and with the latitudes $\{\rho_i, i = 1, \dots, q\}$ taken such that $\cos \rho_i = \sqrt{\gamma_i}$, where γ_i are the roots of the polynomial

$$T_q(x) = x^q + S_1x^{q-1} + S_2x^{q-2} + \dots + S_q.$$

The polynomial T_q has all the roots located in $(0, 1)$ – and hence $S_n(\alpha)$ constitutes a spherical design – in the following four cases.

1. For $n = 3$, the polynomial $T_2(x) = x^2 - \frac{2x}{3} + \frac{1}{2}(\frac{4}{9} - \beta)$ has all the roots located in $(0, 1)$ if and only if $\beta \in (\frac{2}{9}, \frac{4}{9})$.
2. For $n = 5$, the polynomial $T_3(x) = x^3 - x^2 + \frac{x}{5} + \frac{1}{3}(\frac{2}{5} - \beta)$ has all the roots located in $(0, 1)$ if and only if $\beta \in (0.4, 0.433996\dots)$.
3. For $n = 7$, the polynomial $T_4(x) = x^4 - \frac{4x^3}{3} + \frac{22x^2}{45} - \frac{148x}{2835} + \frac{1}{4}(\frac{18728}{42525} - \beta)$ has all the roots located in $(0, 1)$ if and only if $\beta \in (0.4336145\dots, 0.4403997\dots)$.
4. For $n = 9$, the polynomial $T_5(x) = x^5 - \frac{5x^4}{3} + \frac{8x^3}{9} - \frac{100x^2}{567} + \frac{17x}{1701} + \frac{1}{5}(\frac{2300}{5103} - \beta)$ has all the roots located in $(0, 1)$ if and only if $\beta \in (0.4507152\dots, 0.4515677\dots)$.

For $n \geq 11$, the polynomial T_q cannot have all the roots located in $(0, 1)$.

Proof. The results in the first four cases are immediate consequences of the application of Rolle's sequence. In order to prove that for $n \geq 11$ the system (3.14) has no real solution in $(0, 1)$, we use the results proved by S.N. Bernstein in [12]. Here the author treated the quadrature formula

$$\int_0^1 f(x) dx \approx \frac{1}{n+1} \sum_{i=1}^{n+1} f(x_i) \quad (0 < x_i < 1). \quad (3.17)$$

By making the linear transform $x = (y+1)/2$, it is immediate that (3.17) is equivalent to the quadrature formula

$$\int_{-1}^1 f(y) dy \approx \frac{2}{n+1} \sum_{i=1}^{n+1} f(y_i) \quad (-1 < y_i < 1). \quad (3.18)$$

If we denote $\gamma_i = y_i^2$, $i = 1, \dots, q$, then the system (3.14) is equivalent to the requirement that (3.17) or (3.18) are exact for the monomials $1, x, \dots, x^n$.

In [12] the degree of exactness of (3.17) was denoted by M_{n+1} . For our purposes we have to prove that, for n odd, $n \geq 11$, we have $M_{n+1} < n$, implying the incompatibility of the system (3.14). The main result of [12] is the inequality

$$M_{n+1} < \pi\sqrt{2(n+1)}. \quad (3.19)$$

Since $\pi\sqrt{2(n+1)} \leq n$ for $n \geq 21$, the system (3.14) will be incompatible for $n \geq 21$. Also, the following inequalities were proved

$$M_{12} < 12, \quad M_{14} < 13, \quad M_{16} < 15, \quad M_{18} < 15, \quad M_{20} < 20.$$

Since our goal is to prove that $M_{n+1} < n$, it remains to prove that $M_{12} < 11$ and $M_{20} < 19$. In these cases, the associated polynomials T_q are

$$T_6(x) = x^6 - 2x^5 + \frac{7x^4}{5} - \frac{44x^3}{105} + \frac{9x^2}{175} - \frac{2x}{825} + \frac{1}{6} \left(\frac{92956}{202125} - \beta \right)$$

and

$$\begin{aligned} T_{10}(x) &= x^{10} - \frac{10x^9}{3} + \frac{41x^8}{9} - \frac{1880x^7}{567} + \frac{2378x^6}{1701} - \frac{19556x^5}{56133} \\ &+ \frac{2308918x^4}{45972927} - \frac{544840x^3}{137918781} + \frac{936619x^2}{7033857831} - \frac{384505294x}{25258583471121} \\ &+ \frac{1}{10} \left(\frac{396816635954996}{833533254546993} - \beta \right), \end{aligned}$$

respectively. An application of the Rolle's sequence shows that these polynomials cannot have all the roots located in $(0, 1)$. ■

3.1.6 The degree of exactness of the positive cubature formula

The cubature formula on the sphere (3.3) with the nodes in $\xi_{j,k} \in S_n(\alpha)$ reduces to

$$\int_{\mathbb{S}^2} f(\xi) d\omega(\xi) \approx \sum_{j=1}^{n+1} w_j \sum_{k=1}^{n+1} f(\xi_{j,k}). \quad (3.20)$$

It is exact for $f_n \in V_n$, since it is an interpolatory one. The question which arises is whether it can be exact for all $f \in V_\mu$ with $\mu > n$. The answer is given in the following theorem.

Theorem 3.7 *Consider the interpolatory cubature formula (3.20), associated to the system of points $S_n(\alpha)$ given in Proposition 3.1, which is exact for $f \in V_n$ and suppose that the weights w_j are positive. Then the cubature formula is exact for $f \in V_{n+1}$ if and only if $\alpha = 1$ and*

$$\sum_{j=1}^{n+1} w_j P_{n+1}(\cos \rho_j) = 0, \quad (3.21)$$

where P_{n+1} denotes the Legendre polynomial of degree $n + 1$.

Proof. Let $f \in V_{n+1}$. Then f can be written as

$$f = f_n + g_n,$$

where g_n is an element of the wavelet space $\text{Harm}_n = V_{n+1} \ominus V_n$. It is well known that a basis in Harm_n is given by the set

$$\{P_{n+1}^j(\cos \rho) \cos j\theta, j = 0, 1, \dots, n+1\} \cup \{P_{n+1}^j(\cos \rho) \sin j\theta, j = 1, \dots, n+1\},$$

where P_{n+1}^j are the associated Legendre functions. Therefore the polynomial g_n can be written as

$$g_n = \sum_{j=0}^{n+1} P_{n+1}^j(\cos \rho) (b_j \cos j\theta + c_j \sin j\theta),$$

with $b_j, c_j \in \mathbb{R}$. We suppose the cubature formula (3.20) to be exact for f , meaning that

$$\int_{\mathbb{S}^2} f(\xi) d\omega(\xi) = \sum_{i=1}^N w_i^n f(\eta_i). \quad (3.22)$$

Since

$$\int_{\mathbb{S}^2} f(\xi) d\omega(\xi) = \int_{\mathbb{S}^2} f_n(\xi) d\omega(\xi),$$

formula (3.22) reduces to

$$\int_{\mathbb{S}^2} f_n(\xi) d\omega(\xi) = \sum_{i=1}^N w_i^n (f_n(\eta_i) + g_n(\eta_i)).$$

But $f_n \in V_n$ implies

$$\int_{\mathbb{S}^2} f_n(\xi) d\omega(\xi) = \sum_{i=1}^N w_i^n f_n(\eta_i),$$

so we have

$$\sum_{i=1}^N w_i^n g_n(\eta_i) = 0.$$

Further, using the fact that the weights corresponding to the points situated at the same latitude ρ_j are equal, we obtain

$$\sum_{j=1}^{n+1} \sum_{k=1}^{n+1} w_j \sum_{l=0}^{n+1} P_{n+1}^l(\cos \rho_j) (b_l \cos l\theta_k^j + c_l \sin l\theta_k^j) = 0,$$

for all $b_l, c_l \in \mathbb{R}$, which is equivalent to

$$\begin{aligned} \sum_{j=1}^{n+1} w_j \sum_{k=1}^{n+1} P_{n+1}^l(\cos \rho_j) \cos l\theta_k^j &= 0, \text{ for } l = 0, 1, \dots, n+1, \\ \sum_{j=1}^{n+1} w_j \sum_{k=1}^{n+1} P_{n+1}^l(\cos \rho_j) \sin l\theta_k^j &= 0, \text{ for } l = 1, \dots, n+1. \end{aligned} \quad (3.23)$$

For $l = 0$ it means that

$$\sum_{j=1}^{n+1} w_j P_{n+1}^0(\cos \rho_j) = 0, \quad (3.24)$$

and thus conditions (3.21) are satisfied. For $l = 1, 2, \dots, n+1$ we have

$$\sum_{j=1}^{n+1} w_j \sum_{k=1}^{n+1} P_{n+1}^l(\cos \rho_j) e^{il\theta_k^j} = 0. \quad (3.25)$$

Replacing now

$$\theta_k^j = \frac{\beta_j + 2k\pi}{n+1}, \text{ with } \beta_j = \begin{cases} 0, & \text{if } j \text{ is odd,} \\ (\alpha - 2)\pi, & \text{if } j \text{ is even,} \end{cases}$$

we get, for $l = 1, 2, \dots, n+1$,

$$\sum_{j=1}^{n+1} w_j P_{n+1}^l(\cos \rho_j) \sum_{k=1}^{n+1} e^{il \frac{\beta_j + 2k\pi}{n+1}} = 0.$$

The sum $\sum_{k=1}^{n+1}$ will be zero for all l , except $l = n + 1$, when it equals $(n + 1)e^{i\beta_j}$. So we have

$$\sum_{j=1}^{n+1} w_j (\sin \rho_j)^{n+1} e^{i\beta_j} = 0,$$

implying

$$\begin{aligned} \sin \alpha \pi \sum_{j=1, j \text{ even}}^{n+1} w_j (\sin \rho_j)^{n+1} &= 0, \\ \sum_{j=1, j \text{ odd}}^{n+1} w_j (\sin \rho_j)^{n+1} + \cos \alpha \pi \sum_{j=1, j \text{ even}}^{n+1} w_j (\sin \rho_j)^{n+1} &= 0. \end{aligned}$$

One can obtain positive weights only in the case $\alpha = 1$, implying further that

$$\sum_{j=1, j \text{ odd}}^{n+1} w_j (\sin \rho_j)^{n+1} = \sum_{j=1, j \text{ even}}^{n+1} w_j (\sin \rho_j)^{n+1}.$$

This condition is satisfied for our cubature formula, since we have proved in Section 3.1.2 that the weights corresponding to the points situated on symmetric latitudes are equal.

Conversely, if $\alpha = 1$ and (3.21) is satisfied, then relations (3.24) and (3.25) are satisfied, implying further that the cubature formula is exact for all $f \in V_{n+1}$. ■

A possible case is when ρ_j are taken as the roots of the Legendre polynomial P_{n+1} . In the sequel we intend to investigate whether the degree of exactness can be greater than $n + 1$, i.e. it can have positive weights and at the same time can be exact for all spherical polynomials in V_{n+2} . So we need to suppose $\alpha = 1$ and that condition (3.21) is fulfilled. Therefore

$$\theta_k^j = \frac{\beta_j + 2k\pi}{n+1}, \text{ with } \beta_j = \begin{cases} 0, & \text{if } j \text{ is odd,} \\ -\pi, & \text{if } j \text{ is even.} \end{cases}$$

In addition, we impose exactness for the spherical polynomials

$$\{Y_{n+2}^l(\theta, \rho), l = -n - 2, \dots, n + 2\},$$

knowing that this set constitutes a basis of the space $\text{Harm}V_{n+1} = V_{n+2} \ominus V_{n+1}$. On the one hand, evaluating the integral in (3.21) for these spherical polynomials we get

$$\int_{\mathbb{S}^2} P_{n+2}^{|l|}(\cos \rho) e^{il\theta} d\omega(\xi) = \int_0^\pi P_{n+2}^{|l|}(\cos \rho) \sin \rho d\rho \int_0^{2\pi} e^{il\theta} d\theta.$$

But

$$\int_0^{2\pi} e^{il\theta} d\theta = \begin{cases} 2\pi, & \text{for } l = 0, \\ 0, & \text{otherwise.} \end{cases}$$

On the other hand, evaluating the sums in (3.21) for these spherical polynomials we get

$$\begin{aligned} \sum_{j=1}^{n+1} \sum_{k=1}^{n+1} w_j P_{n+2}^{|l|}(\cos \rho_j) e^{i\theta_k^j} &= \sum_{j=1}^{n+1} w_j P_{n+2}^{|l|}(\cos \rho_j) \sum_{k=1}^{n+1} e^{il \frac{\beta_j + 2k\pi}{n+1}} \\ &= \sum_{j=1}^{n+1} w_j P_{n+2}^{|l|}(\cos \rho_j) e^{il \frac{\beta_j}{n+1}} \sum_{k=1}^{n+1} e^{il \frac{2k\pi}{n+1}}. \end{aligned}$$

The last sum is zero if $l \notin (n+1)\mathbb{Z}$ and is $n+1$ if $l \in (n+1)\mathbb{Z}$.

With the above remarks, the quadrature formula (3.21) is exact for Y_{n+2}^l with $l \neq 0$ and $|l| \neq n+1$. It remains to impose that (3.21) is exact for Y_{n+2}^0 and $Y_{n+2}^{\pm(n+1)}$.

- In order to be exact for $l = 0$, we should have

$$2\pi \int_0^\pi P_{n+2}(\cos \rho) \sin \rho d\rho = (n+1) \sum_{j=1}^{n+1} w_j \sum_{k=1}^{n+1} P_{n+2}(\cos \rho_j),$$

which yields

$$(0 =) \int_{-1}^1 P_{n+2}(x) dx = \frac{n+1}{2\pi} \sum_{j=1}^{n+1} w_j P_{n+2}(\cos \rho_j).$$

With the notations $\cos \rho_j = r_j$, $a_j = \frac{n+1}{2\pi} w_j$, we get

$$\sum_{j=1}^{n+1} a_j P_{n+2}(r_j) = 0. \quad (3.26)$$

This last condition, added to the conditions of exactness for the polynomials Y_j^0 for $j = 0, \dots, n+1$, conditions which can be written as

$$\sum_{j=1}^{n+1} a_j P_k(r_j) = 0, \text{ for } k = 0, 1, \dots, n+1, \quad (3.27)$$

means that the one-dimensional quadrature formula

$$\int_{-1}^1 f(x) dx \approx \sum_{j=1}^{n+1} a_j f(r_j) \quad (3.28)$$

should be exact for the Legendre polynomials P_0, \dots, P_{n+2} and therefore for all univariate polynomials in \mathbb{P}_{n+2} . Actually, condition (3.26) brings the additional condition that formula (3.28) is exact for the monomial x^{n+2} . This fact is true for odd n , due to the symmetry of the weights and of the latitudinal circles. In conclusion formula (3.21) is exact for the spherical polynomial Y_{n+2}^0 .

- In order to be exact for the spherical polynomials $Y_{n+2}^{\pm(n+1)}$, we should have

$$\sum_{j=1}^{n+1} a_j P_{n+2}^{n+1}(\cos \rho_j) e^{i\beta_j} = 0,$$

and further, replacing P_{n+2}^{n+1} and β_j , this condition becomes

$$\sum_{j=1}^{n+1} (-1)^j a_j (1 - r_j^2)^q r_j = 0, \quad (3.29)$$

again with $r_j = \cos \rho_j$ for $j = 1, \dots, n+1$ and $q = (n+1)/2$. Moreover, it can be rewritten as

$$\sum_{j=1, j \text{ even}}^{n+1} a_j (1 - r_j^2)^q r_j - \sum_{j=1, j \text{ odd}}^{n+1} a_j (1 - r_j^2)^q r_j = 0. \quad (3.30)$$

On the other hand, using the fact that (3.28) is exact for the odd polynomial $(1 - x^2)^q x$, we obtain that

$$\sum_{j=1}^{n+1} a_j r_j (1 - r_j^2)^q = 0,$$

whence

$$- \sum_{j=1, j \text{ odd}}^{n+1} a_j (1 - r_j^2)^q r_j = \sum_{j=1, j \text{ even}}^{n+1} a_j (1 - r_j^2)^q r_j.$$

Thus (3.21) becomes

$$\sum_{j=1, j \text{ even}}^{n+1} a_j (1 - r_j^2)^q r_j = 0.$$

This equality cannot be true under the assumption that the weights are positive, therefore formula (5.2) cannot be exact for the spherical polynomials $Y_{n+2}^{\pm(n+1)} \in V_{n+2}$.

In conclusion the maximal degree attained by the interpolatory positive cubature formula (3.21) is $n + 1$.

An improvement of the degree of exactness can be however achieved by taking more than $n + 1$ equidistributed points on each latitudinal circle and arbitrary deviations β_j . Thus we do not use fundamental systems of points anymore and therefore the corresponding cubature formulas are not interpolatory. In this way, in the next section we show how we can obtain positive cubature formulas with $(n + 1)(2n + 1)$ points and degree of exactness $2n + 1$.

3.2 Cubature formulas with equally spaced nodes on latitudinal circles

In the previous section we have constructed quadrature formulas based on some fundamental systems of $(n + 1)^2$ points on the sphere ($n + 1$ equally spaced points taken on $n + 1$ latitudinal circles), constructed by Laín-Fernández. In this section we improve the exactness by taking more equally spaced points on each latitude and equal weights for each latitude. We study the maximal degree of exactness which can be attained with $n + 1$ latitudes. As a particular case, we study the maximal exactness of the spherical designs with equally spaced points at each latitude. Of course all these quadratures are not interpolatory any more.

We remind that V_n , the space of spherical polynomials of degree less than or equal to n , has the dimension $\dim V_n = (n + 1)^2$ and an orthogonal basis of V_n is given by

$$\{Y_m^l(\theta, \rho) = P_m^{|l|}(\cos \rho) e^{il\theta}, \quad -m \leq l \leq m, \quad 0 \leq m \leq n\}.$$

3.2.1 Spherical quadrature

Let $n, p \in \mathbb{N}^*$, $\boldsymbol{\beta}_n = (\beta_1, \dots, \beta_{n+1}) \in [0, 2\pi)^{n+1}$, $\boldsymbol{\rho}_n = (\rho_1, \dots, \rho_{n+1})$, $0 < \rho_1 < \rho_2 < \dots < \rho_{n+1} < \pi$ and let

$$S(\boldsymbol{\beta}_n, \boldsymbol{\rho}_n, p) = \{\xi_{j,k}(\rho_j, \theta_k^j), \theta_k^j = \frac{\beta_j + 2k\pi}{p + 1}, j = 1, \dots, n + 1, k = 1, \dots, p + 1\}$$

be a system of $(p + 1)$ equally spaced nodes at each of the latitudes ρ_j . We consider the quadrature formula

$$\int_{\mathbb{S}^2} F(\xi) d\omega(\xi) \approx \sum_{j=1}^{n+1} w_j \sum_{k=1}^{p+1} F(\xi_{j,k}), \quad (3.31)$$

with $\xi_{j,k} \in S(\boldsymbol{\beta}_n, \boldsymbol{\rho}_n, p)$.

A particular case, when n is odd, $p = n$, $\beta_j = \begin{cases} \alpha\pi, & \text{for } j \text{ even} \\ 0 & \text{for } j \text{ odd} \end{cases}$, with $\alpha \in [0, 2)$ was already considered in the previous section. As we have seen in the previous section, the quadrature formulas are interpolatory and therefore the degree of exactness is at least n . In [95] we proved that $n + 1$ is the maximal degree of exactness attained in this particular case.

In the following, for a fixed n , we wish to study the maximum degree of exactness which can be achieved with such a formula. This means to impose (3.31) be exact for the spherical polynomials Y_m^l , for $l = -m, \dots, m$, and to specify which is the maximum value of m which makes (3.31) exact.

On the one hand, evaluating the integral in (3.31) for these spherical polynomials, we get

$$\int_{\mathbb{S}^2} P_m^{|l|}(\cos \rho) e^{il\theta} d\omega(\xi) = \int_0^\pi P_m^{|l|}(\cos \rho) \sin \rho d\rho \int_0^{2\pi} e^{il\theta} d\theta.$$

But

$$\int_0^{2\pi} e^{il\theta} d\theta = \begin{cases} 2\pi, & \text{for } l = 0, \\ 0, & \text{otherwise.} \end{cases}$$

On the other hand, evaluating the sum in (3.31) for these spherical polynomials, we get

$$\begin{aligned} \sum_{j=1}^{n+1} w_j \sum_{k=1}^{p+1} P_m^{|l|}(\cos \rho_j) e^{il\theta_k^j} &= \sum_{j=1}^{n+1} w_j P_m^{|l|}(\cos \rho_j) \sum_{k=1}^{p+1} e^{il \frac{\beta_j + 2k\pi}{p+1}} \\ &= \sum_{j=1}^{n+1} w_j P_m^{|l|}(\cos \rho_j) e^{il \frac{\beta_j}{p+1}} \sum_{k=1}^{p+1} e^{il \frac{2k\pi}{p+1}}. \end{aligned}$$

The last sum is zero if $l \notin (p + 1)\mathbb{Z}$ and is $p + 1$ if $l \in (p + 1)\mathbb{Z}$.

With the above remarks, the quadrature formula (3.31) is exact for Y_m^l with $l \neq 0$, in the case when $m < p + 1$. In order to be exact for $l = 0$ we should have

$$\int_{\mathbb{S}^2} P_m(\cos \rho) d\omega(\xi) = \sum_{j=1}^{n+1} w_j \sum_{k=1}^{p+1} P_m(\cos \rho_j),$$

which yields

$$\int_{-1}^1 P_m(x) dx = \frac{p+1}{2\pi} \sum_{j=1}^{n+1} w_j P_m(\cos \rho_j).$$

With the notations $\cos \rho_j = r_j$, $a_j = \frac{p+1}{2\pi} w_j$, we arrive at

$$\int_{-1}^1 P_m(x) dx = \sum_{j=1}^{n+1} a_j P_m(r_j). \quad (3.32)$$

In conclusion, we proved the following result.

Proposition 3.8 *Let $n, p, s \in \mathbb{N}^*$ such that $s < p + 1$, and consider the spherical quadrature formula (3.31) with $\xi_{j,k} \in S(\beta_n, \rho_n, p)$. This formula is exact for the spherical polynomials in V_s if and only if the quadrature formula*

$$\int_{-1}^1 f(x) dx \approx \sum_{j=1}^{n+1} a_j f(r_j) \quad (3.33)$$

is exact for all polynomials in \mathbb{P}_s .

Let us remark that, taking $m = 0, 1, \dots, p$ in (3.32) (or, equivalently, taking $f = 1, x, \dots, x^p$ in (3.33)), we obtain the system

$$\sum_{j=1}^{n+1} a_j r_j^\lambda = ((-1)^\lambda + 1) \frac{1}{\lambda + 1}, \quad (3.34)$$

for $\lambda = 0, \dots, p$. This system has $p + 1$ equations and $2n + 2$ unknowns a_j, r_j , $j = 1, \dots, n + 1$.

Next it is natural to ask when formula (3.31) is exact for spherical polynomials in V_s with $s \geq p + 1$. If we further impose that formula (3.31) is exact for the spherical polynomials Y_{p+1}^l , $l = -p - 1, \dots, p + 1$, then we have

$$\sum_{j=1}^{n+1} a_j r_j^{p+1} = ((-1)^{p+1} + 1) \frac{1}{p + 2}, \quad (3.35)$$

$$\sum_{j=1}^{n+1} a_j (\sin \rho_j)^{p+1} e^{i\beta_j} = 0. \quad (3.36)$$

Equation (3.35) follows from the fact that (3.31) is exact for Y_{p+1}^0 , while equation (3.36) results from the fact that formula (3.31) is exact for the spherical polynomials Y_{p+1}^{p+1} and Y_{p+1}^{-p-1} . For $l = -p, \dots, -1, 1, \dots, p$ both sides of quadrature (3.31) are zero, therefore it is exact.

In conclusion the following proposition holds.

Proposition 3.9 *Let $n, p \in \mathbb{N}^*$. Then formula (3.31) is exact for all spherical polynomials in V_p if and only if conditions (3.34) are satisfied for $\lambda = 0, \dots, p$. Moreover, formula (3.31) is exact for all spherical polynomials in V_{p+1} if and only if supplementary conditions (3.35) and (3.36) are fulfilled.*

3.2.2 Maximal degree of exactness which can be attained with equally spaced nodes at $n + 1$ latitudes

In this section we establish which is the maximum degree of exactness that can be obtained by taking the same number of equally spaced nodes on each of the $n + 1$ latitudinal circles and then we construct quadrature formulas with maximal degree of exactness.

What is well known is that the system (3.34) is solvable for a maximal number of conditions $2n + 2$ (for $\lambda = 0, 1, \dots, 2n + 1$), when it solves uniquely. This is the case of the univariate Gauss quadrature formula. In this case, the maximal value for p which can be taken in (3.34) is $p = 2n + 1$, implying that (3.31) is exact for all spherical polynomials in V_{2n+1} . In conclusion, the following result holds.

Proposition 3.10 *Let $n \in \mathbb{N}^*$ and consider the quadrature formula (3.31). Its maximal degree of exactness is $2n + 1$ and if we want it be attained, then we must take the cosines of the latitudes, $\cos \rho_j = r_j$, as the roots of the Legendre polynomial P_{n+1} and the weights as [127]*

$$w_j = \frac{2\pi}{p+1} a_j, \text{ with } a_j = \frac{2(1-r_j^2)}{(n+2)^2(P_{n+2}(r_j))^2} > 0. \quad (3.37)$$

One possible case when it can be attained is by taking $2n+2$ equally spaced nodes at each latitude and arbitrary deviations $\beta_j \in [0, 2\pi)$.

The question which naturally arises is if we can obtain degree of exactness $2n + 1$ with less than $2n + 2$ points at each latitude.

(a) Maximal exactness $2n + 1$ with only $2n + 1$ nodes at each latitude

Consider $2n + 1$ equally spaced nodes on each latitude. If we suppose conditions (3.34) satisfied for $\lambda = 0, 1, \dots, 2n$, then formula (3.31) will be exact for all spherical polynomial in V_{2n} . From Proposition 3.9 we deduce that, if we want it to be exact for all polynomials in V_{2n+1} , then we should add the conditions

$$\sum_{j=1}^{n+1} a_j r_j^{2n+1} = 0, \quad (3.38)$$

$$\sum_{j=1}^{n+1} a_j (\sin \rho_j)^{2n+1} e^{i\beta_j} = 0. \quad (3.39)$$

In this case the quadrature formula (3.32) becomes the Gauss quadrature formula. Thus, r_j will be the roots of the Legendre polynomial P_{n+1} and a_j are given in (3.37). Since $a_{n+2-j} = a_j$ and $\rho_j = \pi - \rho_{n+2-j}$ for $j = 1, \dots, n + 1$ and $r_{\frac{n}{2}+1} = 0$ for even n , condition (3.39) can be written as

$$\sum_{j=1}^{(n+1)/2} a_j (\sin \rho_j)^{2n+1} (e^{i\beta_j} + e^{i\beta_{n+2-j}}) = 0, \text{ for } n \text{ odd}, \quad (3.40)$$

$$a_{\frac{n}{2}+1} e^{i\beta_{\frac{n}{2}+1}} + \sum_{j=1}^{n/2} a_j (\sin \rho_j)^{2n+1} (e^{i\beta_j} + e^{i\beta_{n+2-j}}) = 0, \text{ for } n \text{ even}. \quad (3.41)$$

For n odd, equation (3.40) is always solvable and possible solutions are discussed in Appendix 1. For n even the solvability of equation (3.41) is discussed in Appendix 2. Numerical tests performed for $n \leq 100$ show that inequality (3.64) in Appendix 2 holds only for $n \geq 12$, therefore the equation (3.41) is not solvable for $n \in \{2, 4, \dots, 10\}$ and solvable for $12 \leq n \leq 100$. In conclusion, the following result holds.

Proposition 3.11 *Let $n \in \mathbb{N}^*$ and consider the quadrature formula (3.31) with $2n + 1$ equally spaced nodes at each latitude. For $n \in \{2, 4, 6, 8, 10\}$ one cannot attain exactness $2n + 1$. For n odd and for $n \in \{12, 14, \dots, 100\}$, if $\cos \rho_j$ are the roots of the Legendre polynomial P_{n+1} , the weights are as in (3.37), the numbers β_j are solutions of equation (3.39) (given in Appendices 1 and 2), then the quadrature formula (3.31) has the degree of exactness $2n + 1$.*

We further want to know if it is possible to obtain the maximal degree of exactness $2n + 1$ with less points at each latitude.

(b) Maximal exactness $2n + 1$ with $2n$ points at each latitude

Let us consider $2n$ points ($p = 2n - 1$) at each latitude. If we suppose conditions (3.34) satisfied for $\lambda = 0, 1, \dots, 2n - 1$, then formula (3.31) will be exact for all polynomials in V_{2n-1} . If we want it to be exact for Y_{2n}^l , for $l = -2n, \dots, 2n$, then we should add the conditions

$$\sum_{j=1}^{n+1} a_j r_j^{2n} = \frac{2}{2n+1}, \quad (3.42)$$

$$\sum_{j=1}^{n+1} a_j (\sin \rho_j)^{2n} e^{i\beta_j} = 0. \quad (3.43)$$

Further, if we want the formula (3.31) exact for all Y_{2n+1}^l , for $l = -2n - 1, \dots, 2n + 1$, then we should impose the conditions

$$\sum_{j=1}^{n+1} a_j r_j^{2n+1} = 0, \quad (3.44)$$

$$\sum_{j=1}^{n+1} a_j (\sin \rho_j)^{2n} \cos \rho_j e^{i\beta_j} = 0. \quad (3.45)$$

From conditions (3.42) and (3.44) we get again that $\cos \rho_j = r_j$ are the roots of the Legendre polynomial P_{n+1} and a_j are as in (3.37). Therefore, formula (3.31) has the degree of exactness $2n + 1$ if and only if equations (3.43) and (3.45) are simultaneously satisfied. Due to the symmetry, they reduce to the system

$$\sum_{j=1}^{(n+1)/2} a_j (\sin \rho_j)^{2n} (e^{i\beta_j} + e^{i\beta_{n+2-j}}) = 0, \quad (3.46)$$

$$\sum_{j=1}^{(n+1)/2} a_j (\sin \rho_j)^{2n} \cos \rho_j (e^{i\beta_j} - e^{i\beta_{n+2-j}}) = 0, \quad (3.47)$$

for n odd, and respectively to the system

$$a_{\frac{n}{2}+1} e^{i\beta_{\frac{n}{2}+1}} + \sum_{j=1}^{n/2} a_j (\sin \rho_j)^{2n} (e^{i\beta_j} + e^{i\beta_{n+2-j}}) = 0,$$

$$\sum_{j=1}^{n/2} a_j (\sin \rho_j)^{2n} \cos \rho_j (e^{i\beta_j} - e^{i\beta_{n+2-j}}) = 0,$$

for n even.

For n odd, we give some conditions on the solvability or non-solvability of this system in Appendix 3 (Proposition 3.16). Numerical tests performed for $n \in \{1, 3, 5, \dots, 99\}$ show that the hypotheses (2.44) in Appendix 3 are fulfilled only for $n \in \{1, 3, \dots, 13\}$, in each of these cases the index k being $k = (n + 1)/2$. In conclusion, for these values of n , the above system has no solution and therefore the quadrature formula cannot have maximal exactness $2n + 1$.

For $n \in \{15, 17, \dots, 41\}$ the system is solvable since hypotheses (3.71)–(3.72) in Appendix 3 are fulfilled, each time for $v = (n + 1)/2$. In the proof of Proposition 3.16, 3 in Appendix 3, we give a possible solution of the system. For $n \in \{43, 45, \dots, 99\}$, the solvability is not clear

nr. of nodes at each latitude	n	β_j
$2n + 2$	\mathbb{N}^*	$[0, 2\pi)$
$2n + 1$	odd $\{2, 4, 6, 8, 10\}$ $\{12, 14, \dots, 100\}$	Appendix 1 \emptyset (cf. Appendix 2) Appendix 2
$2n$	$\{1, 3, \dots, 13\}$ $\{15, 17, \dots, 41\}$ $\{43, 45, \dots, 99\}$ even	\emptyset (cf. Appendix 3, Prop. 3.16, 1) Appendix 3, Prop. 3.16, 3 no answer no answer

Table 3.1: Some choices for which the maximal degree of exactness $2n + 1$ is attained, for $P_{n+1}(\cos \rho_j) = 0$, $j \in \{1, \dots, n + 1\}$, $n \leq 100$.

yet. In this case, both sequences $\{\alpha_j, j = 1, \dots, (n + 1)/2\}$ and $\{\mu_j, j = 1, \dots, (n + 1)/2\}$ satisfy the triangle inequality.

In Table 3.1 we summarize all the cases discussed above.

As a final remark, we mention that the improvement brought to the interpolatory quadrature formulas in [90], which were established only for n odd, is the following: In [90], for attaining the degree of exactness $2n + 1$ one needs $(2n + 2)^2$ nodes. The quadrature formulas presented here can attain this degree of exactness with only $(2n + 2)(n + 1)$ nodes (for arbitrary choices of the deviations β_j) and with only $(2n + 1)(n + 1)$ nodes or only $2n(n + 1)$ nodes (for some special cases summarized in Table 3.1).

3.2.3 Spherical designs

For a fixed $n \in \mathbb{N}^*$, we intend to specify the maximal degree of exactness that can be attained by a spherical design with the points in $S(\beta_n, \rho_n, p)$ and show for which choices of the parameters β_n, ρ_n, p this maximal degree can be attained. So let us consider the quadrature formula

$$\int_{\mathbb{S}^2} F(\xi) d\omega(\xi) \approx w_{n,p} \sum_{j=1}^{n+1} \sum_{k=1}^{p+1} F(\xi_{j,k}), \quad \text{with } \xi_{j,k} \in S(\beta_n, \rho_n, p). \quad (3.48)$$

If we impose that this formula is exact for constant functions, we obtain

$$w_{n,p} = \frac{4\pi}{(n+1)(p+1)}.$$

As in the general case, we obtain that formula (3.48) is exact for the spherical polynomials Y_m^l for $m < p + 1$ and $-m \leq l \leq m$, $l \neq 0$. In order to be exact for Y_m^0 for $m < p + 1$ we should have

$$\int_{-1}^1 P_m(x) dx = \frac{2}{n+1} \sum_{j=1}^{n+1} P_m(r_j),$$

where $r_j = \cos \rho_j$, for $j = 1, \dots, n + 1$. In conclusion, if the quadrature formula

$$\int_{-1}^1 f(x) dx \approx \frac{2}{n+1} \sum_{j=1}^{n+1} f(r_j) \quad (3.49)$$

is exact for all univariate polynomials in \mathbb{P}_s , $s < p + 1$, then the quadrature formula (3.48) will be exact for all spherical polynomials in V_s . If in (3.49) we take $f(x) = x^m$ for $m = 1, \dots, p$, we obtain the system

$$\sum_{j=1}^{n+1} r_j^\lambda = \frac{(-1)^\lambda + 1}{\lambda + 1} \cdot \frac{n + 1}{2}, \quad (3.50)$$

with $\lambda = 1, \dots, p$. This system has $n + 1$ unknowns. The maximal degree of exactness of the quadrature formula (3.49) (respectively the maximal value of p) is obtained in the classical case of Chebyshev one-dimensional quadrature formula, when the system (3.50) solves uniquely. In this case $p = n + 1$ since the number of conditions needed to solve uniquely the quadrature formula is $n + 1$. More precisely, in the one-dimensional case of Chebyshev quadrature, it is known that $r_j = r_{n+2-j}$ for $j = 1, \dots, [n/2]$ and that system (3.50) has no solution for $n = 7$ and $n > 8$. For $n \in \{2, 4, 6, 8\}$, the quadrature formula (3.49) has the degree of exactness $n + 1$ if the conditions in (3.50) are fulfilled for $\lambda = 1, \dots, n + 1$. For $n \in \{1, 3, 5\}$, if the same conditions are fulfilled, the degree of exactness is $n + 2$ since one additional condition in (3.50) for $\lambda = n + 2$ is satisfied.

In conclusion, the following result hold.

Proposition 3.12 *Let $n \in \{1, 2, 3, 4, 5, 6, 8\}$ and consider the quadrature formula (3.48) with $p + 1$ equally spaced nodes at each latitudes. Its maximal degree of exactness is*

$$\mu_{max} = \begin{cases} n + 1, & \text{for } n \in \{2, 4, 6, 8\}, \\ n + 2, & \text{for } n \in \{1, 3, 5\}. \end{cases} \quad (3.51)$$

It can be attained, for example, by taking $n + 2$ equally spaced nodes at each latitude ($p = n + 1$), for all choices of the deviations β_j in $[0, 2\pi)$ and for $\cos \rho_j$ the nodes of the classical one-dimensional Chebyshev quadrature formula.

We wish to investigate if the maximal degree of exactness μ_{max} can be obtained with less than $n + 2$ points at each latitude.

(a) Maximal degree of exactness attained with only $n + 1$ points at each latitude

Suppose $p = n$ and suppose (3.50) fulfilled for $\lambda = 1, \dots, n$. This implies that (3.48) is exact for the spherical polynomials Y_λ^0 , for $\lambda = 1, \dots, n$. We want again to precise if the maximal degree of exactness μ_{max} can be attained with only $n + 1$ points at each latitude.

Case 1: n even. If we want formula (3.48) be exact for all spherical polynomials in $V_{n+1} = V_{\mu_{max}}$, it remains to impose that (3.48) is exact for Y_{n+1}^0 and $Y_{n+1}^{\pm(n+1)}$. Exactness for Y_{n+1}^0 means $\sum_{j=1}^{n+1} r_j^{n+1} = 0$, which, together with (3.50) fulfilled for $\lambda = 1, \dots, n$, leads finally to the system in the classical one-dimensional Chebyshev case. Thus $r_j = r_{n+2-j}$, for $j = 1, \dots, n/2$, $r_{\frac{n}{2}+1} = 0$ and a solution exists only for $n \in \{2, 4, 6, 8\}$. Further, exactness for $Y_{n+1}^{\pm(n+1)}$ reduces to

$$e^{i\beta_{\frac{n}{2}+1}} + \sum_{j=1}^{n/2} (\sin \rho_j)^{n+1} (e^{i\beta_j} + e^{i\beta_{n+2-j}}) = 0. \quad (3.52)$$

Numerical tests show that condition (3.64) in Appendix 2 is fulfilled for $n \in \{2, 4, 6, 8\}$, therefore equation (3.52) is solvable.

Case 2: n odd. In this case, if we want formula (3.48) be exact for all spherical polynomials in $V_{n+2} = V_{\mu_{max}}$, it remains to impose that it is exact for Y_{n+1}^0 , Y_{n+2}^0 , $Y_{n+1}^{\pm(n+1)}$ and $Y_{n+2}^{\pm(n+1)}$.

Exactness for the spherical polynomial Y_{n+1}^0 reduces to the condition

$$\sum_{j=1}^{n+1} r_j^{n+1} = \frac{n+1}{n+2},$$

which, added to conditions (3.50) for $\lambda = 1, \dots, n$, leads again to the system in the classical one-dimensional Chebyshev case (which solves uniquely).

Exactness for Y_{n+2}^0 reduces to condition

$$\sum_{j=1}^{n+1} r_j^{n+2} = 0,$$

which is automatically satisfied.

Further, exactness for $Y_{n+1}^{\pm(n+1)}$ and $Y_{n+2}^{\pm(n+1)}$ means, respectively,

$$\sum_{j=1}^{(n+1)/2} (\sin \rho_j)^{n+1} (e^{i\beta_j} + e^{i\beta_{n+2-j}}) = 0. \quad (3.53)$$

$$\sum_{j=1}^{(n+1)/2} (\sin \rho_j)^{n+1} \cos \rho_j (e^{i\beta_j} - e^{i\beta_{n+2-j}}) = 0. \quad (3.54)$$

In conclusion, the maximal degree of exactness $n+2$ is attained if and only if r_j are the nodes in the univariate Chebyshev quadrature and the system (3.53)–(3.54) is solvable. The solvability of this system is discussed in Appendix 3 in the general case. For $n = 1$, the non-solvability is clear. For $n = 3$, the system is again not solvable (cf. Proposition 3.16, Appendix 3, since $\mu_1 < \mu_2$). For $n = 5$, it is solvable since the hypotheses (3.69)–(3.70) in Proposition 3.16 are satisfied, with $v = 2$.

To summarize the above considerations, we state the following result.

Proposition 3.13 *Let $n \in \{1, 2, 3, 4, 5, 6, 8\}$ and consider the quadrature formula (3.48) with $n+1$ equally spaced nodes at each latitude. Then the maximal degree of exactness μ_{max} given in Proposition 3.12 can be attained for $n = 2, 4, 6, 8$ if $\cos \rho_j$ are chosen as nodes of the classical one-dimensional Chebyshev quadrature formula and the numbers β_j are chosen as described in Appendix 2. For $n = 1, 3$ the maximal degree of exactness cannot be attained, while for $n = 5$ it can be attained if the deviations β_j , $j = 1, \dots, 6$ are taken as described in Appendix 3, Proposition 3.16, 2.*

The natural question which arises now is: it is possible to have maximal degree of exactness $n+1$ with only n points at each latitude? The answer is given in the following section.

(b) Maximal degree of exactness with only n points at each latitude

Let us consider n points at each latitude ($p = n - 1$) and suppose (3.50) fulfilled for $\lambda = 1, \dots, n - 1$. We want to see if the maximal degree of exactness μ_{max} can be attained with only n points at each latitude.

Case 1: n odd. In this case, if we want formula (3.48) to be exact for all spherical polynomials in $V_{n+2} = V_{\mu_{max}}$, it remains to impose that it is exact for Y_{n+1}^0 , Y_{n+2}^0 , $Y_n^{\pm n}$, $Y_{n+1}^{\pm n}$ and $Y_{n+2}^{\pm n}$.

Altogether, they imply that $r_j = \cos \rho_j$ are the abscissa in the classical univariate Chebyshev case, and the deviations β_j should satisfy the system

$$\sum_{j=1}^{(n+1)/2} (\sin \rho_j)^n (e^{i\beta_j} + e^{i\beta_{n+2-j}}) = 0, \quad (3.55)$$

$$\sum_{j=1}^{(n+1)/2} (\sin \rho_j)^n \cos \rho_j (e^{i\beta_j} - e^{i\beta_{n+2-j}}) = 0, \quad (3.56)$$

$$\sum_{j=1}^{(n+1)/2} (\sin \rho_j)^n P_{n+2}^{(n)}(\cos \rho_j) (e^{i\beta_j} + e^{i\beta_{n+2-j}}) = 0.$$

Since $P_{n+2}^{(n)}(\cos \rho)$ is an even polynomial of degree two in $\cos \rho$, using equation (3.55), we can replace the last equation with

$$\sum_{j=1}^{(n+1)/2} (\sin \rho_j)^n (\cos \rho_j)^2 (e^{i\beta_j} + e^{i\beta_{n+2-j}}) = 0. \quad (3.57)$$

For $n = 1$, the system is clearly not solvable.

For $n = 3$, the system is solvable since $\sin^3 \rho_1 \cos \rho_1 = \sin^3 \rho_2 \cos \rho_2$. A solution can be written as

$$\beta_1 \in [0, 2\pi), \quad \beta_3 = \beta_1, \quad \beta_2 = \beta_4 = \beta_1 + \pi \pmod{2\pi}.$$

For $n = 5$, up to now we do not have a result regarding the solvability of the system.

Case 2: n even. If we want formula (3.48) to be exact for all spherical polynomials in $V_{n+1} = V_{\mu_{max}}$, it remains to impose that (3.48) is exact for $Y_n^0, Y_{n+1}^0, Y_n^{\pm n}$ and $Y_{n+1}^{\pm n}$. Exactness for Y_n^0 and Y_{n+1}^0 means $\sum_{j=1}^{n+1} r_j^n = 1$ and $\sum_{j=1}^{n+1} r_j^{n+1} = 0$, respectively. Together with (3.50) fulfilled for $\lambda = 1, \dots, n-1$, they lead to the system in the classical one-dimensional Chebyshev case. Thus $r_j = r_{n+2-j}$, for $j = 1, \dots, n/2$, $r_{\frac{n}{2}+1} = 0$ and a solution exists only for $n \in \{2, 4, 6, 8\}$. Further, using again the symmetry of the latitudes, exactness for $Y_n^{\pm n}$ and $Y_{n+1}^{\pm n}$ reduces to

$$e^{i\beta_{\frac{n}{2}+1}} + \sum_{j=1}^{n/2} (\sin \rho_j)^n (e^{i\beta_j} + e^{i\beta_{n+2-j}}) = 0, \quad (3.58)$$

$$\sum_{j=1}^{n/2} (\sin \rho_j)^n \cos \rho_j (e^{i\beta_j} - e^{i\beta_{n+2-j}}) = 0. \quad (3.59)$$

In conclusion, the maximal degree of exactness $\mu_{max} = n + 1$ can be attained if and only if the system (3.58)-(3.59) is solvable. Unfortunately we could not give a result regarding the solvability of this system.

All these cases are summarized in Table 3.2.

3.2.4 Numerical examples

In order to demonstrate the efficiency of our formulas, we consider the quadrature formula

$$\int_{\mathbb{S}^2} F(\xi) d\omega(\xi) \approx \sum_{j=1}^{m+1} w_j \sum_{k=1}^{p+1} F(\xi_{j,k}),$$

with $\xi_{j,k}(\rho_j, \theta_k^j) \in \mathbb{S}^2$, in the following cases:

number of nodes at each latitude	n	β_j
$n + 2$	$\{1, 2, 3, 4, 5, 6, 8\}$	$[0, 2\pi)$
$n + 1$	$\{2, 4, 6, 8\}$ $\{1, 3\}$ 5	$[0, 2\pi)$ \emptyset (cf. Appendix 3, Prop. 3.16, 2) no answer
n	1 3 $\{2, 4, 6, 8\}$	\emptyset $\beta_1 \in [0, 2\pi), \beta_3 = \beta_1, \beta_2 = \beta_4 = \beta_1 + \pi$ no answer

Table 3.2: Some choices for which the maximal degree of exactness μ_{\max} is attained, for $\cos \rho_j$, $j \in \{1, \dots, n + 1\}$ the nodes in the case of classical Chebyshev quadrature.

1. The classical Gauss-Legendre quadrature formula, with $m = n$, $p = 2n + 1$, $\cos \rho_j = r_j$ the roots of Legendre polynomial P_{n+1} ,

$$\theta_k^j = \frac{k\pi}{n+1},$$

$$w_j = \frac{2\pi}{2n+2} a_j, \text{ with } a_j = \frac{2(1-r_j^2)}{(n+2)^2(P_{n+2}(r_j))^2},$$

$j = 1, \dots, n + 1$, $k = 1, \dots, 2n + 2$. This formula has $2n^2 + 4n + 2$ nodes and is exact for polynomials in V_{2n+1} . It is in fact a particular case of the quadratures given in Proposition 3.10, when all deviations β_j are zero.

2. The Clenshaw-Curtis formula¹, with $m = 2n$, $p = 2n + 1$,

$$\theta_k^j = \frac{k\pi}{n+1}, \quad \rho_j = \frac{(j-1)\pi}{2n} \text{ for } j = 1, \dots, 2n + 1, \quad k = 1, \dots, 2n + 2,$$

$$w_j = w_{2n+1-j} = \frac{4\pi\varepsilon_j^{2n+1}}{n(n+1)} \sum_{l=0}^n \varepsilon_{l+1}^{n+1} \frac{1}{1-4l^2} \cos \frac{(j-1)l\pi}{n}, \text{ for } j = 1, \dots, n,$$

where

$$\varepsilon_j^J = \begin{cases} \frac{1}{2} & \text{if } j = 1 \text{ or } j = J, \\ 1 & \text{if } 0 < j < J. \end{cases}$$

This formula has $4n^2 + 6n + 2$ nodes and is exact for polynomials in V_{2n+1} .

In our numerical experiments we have considered the following test functions:

$$\begin{aligned} f_1(\mathbf{x}) &= -5 \sin(1 + 10x_3), \\ f_2(\mathbf{x}) &= \|\mathbf{x}\|_1/10, \\ f_3(\mathbf{x}) &= 1/\|\mathbf{x}\|_1, \\ f_4(\mathbf{x}) &= \exp(x_1^2), \end{aligned}$$

where $\mathbf{x} = (x_1, x_2, x_3) \in \mathbb{S}^2$.

¹This formula is sometimes called Chebyshev formula, since in the one-dimensional case it is based on the expansion of a function in terms of Chebyshev polynomials T_i of the first kind. The nodes $\cos j\pi/2n$ are the extrema of the Chebyshev polynomial T_{2n} of degree $2n$.

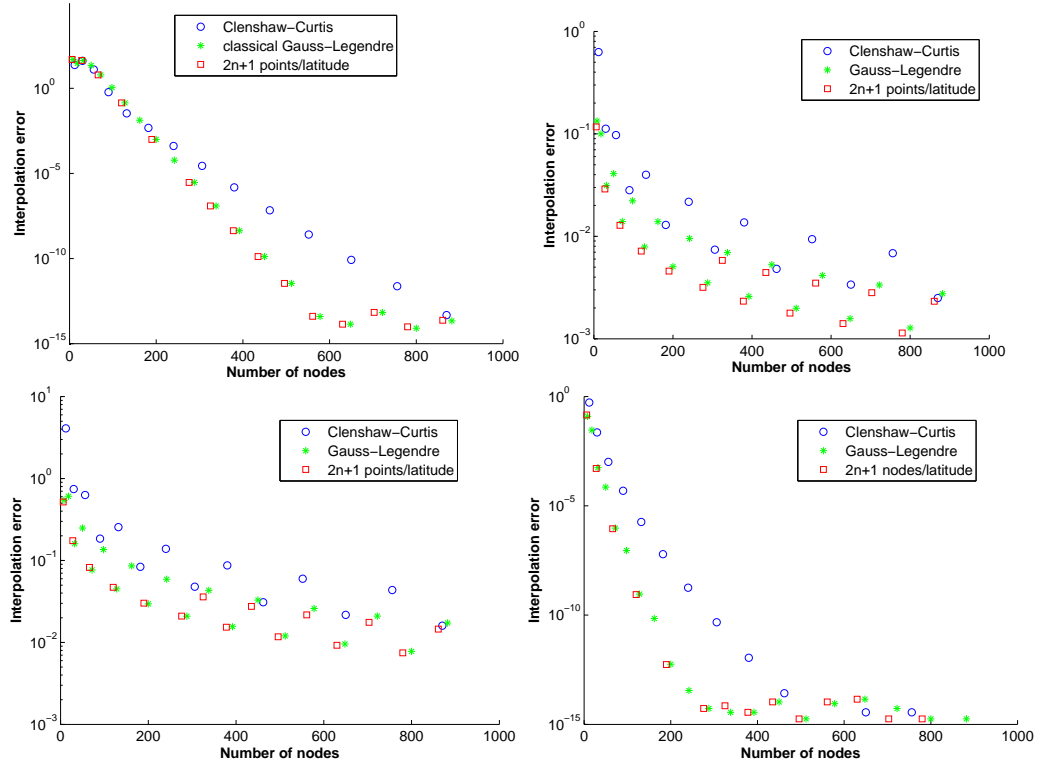


Figure 3.1: Approximation errors (logarithmic scales) for the test functions f_1, f_2, f_3, f_4 .

From the quadrature formulas constructed in this section, we consider those from Section 3.2.2 (a) and we compare them with the Gauss-Legendre and Clenshaw-Curtis quadratures mentioned above. We do not present here quadratures from Proposition 3.10 for deviations β_j different from zero, since in this case, for the above test functions, the errors are comparable with the ones obtained for Gauss-Legendre (when all β_j equal to zero).

Figure 3.1 show the approximation errors (logarithmic scale) for each of the functions f_1, f_2, f_3, f_4 , respectively.

Appendix 1

For n odd, we give solutions of the equation

$$\sum_{j=1}^q \alpha_j (e^{i\beta_j} + e^{i\beta_{n+2-j}}) = 0, \quad (3.60)$$

with $q = (n + 1)/2$, $\alpha_j > 0$ given and the unknowns β_j , $j = 1, \dots, n + 1$. For this we need the following result.

Lemma 3.14 *Let $A > 0$ be given. Then, for every number $z = \tau e^{i\theta} \in \mathbb{C}$ with $0 \leq \tau \leq 2A$, $\theta \in [0, 2\pi)$, there exist the numbers $\omega_j = \omega_j(\tau, \theta) \in [0, 2\pi)$, $j = 1, 2$, such that*

$$A(e^{i\omega_1} + e^{i\omega_2}) = z. \quad (3.61)$$

Proof. Indeed, denoting

$$\gamma = \arccos \frac{\tau}{2A} \in \left[0, \frac{\pi}{2}\right],$$

a possible choice of the numbers ω_1, ω_2 which satisfy relation (3.61) is the following:

1. If $\theta - \gamma \geq 0$ and $\theta + \gamma < 2\pi$, then $(\omega_1, \omega_2) \in \{(\theta + \gamma, \theta - \gamma), (\theta - \gamma, \theta + \gamma)\}$;
2. If $\theta - \gamma < 0$, then $(\omega_1, \omega_2) \in \{(\theta + \gamma, \theta - \gamma + 2\pi), (\theta - \gamma + 2\pi, \theta + \gamma)\}$;
3. If $\theta + \gamma \geq 2\pi$, then $(\omega_1, \omega_2) \in \{(\theta + \gamma - 2\pi, \theta - \gamma), (\theta - \gamma, \theta + \gamma - 2\pi)\}$,

or, shorter,

$$\begin{cases} \omega_1 = \theta + \varepsilon\gamma \pmod{2\pi}, \\ \omega_2 = \theta - \varepsilon\gamma \pmod{2\pi}, \end{cases} \quad \text{with } \varepsilon \in \{-1, 1\}.$$

Equality (3.61) can be verified by direct calculations. \blacksquare

Let us come back to the equation (3.60). For $j = 1, \dots, q$, we consider the numbers $z_j = \tau_j e^{i\theta_j} \in \mathbb{C}$ with $0 \leq \tau_j \leq 2\alpha_j$, such that

$$z_1 + \dots + z_q = 0.$$

In fact we take $q-1$ arbitrary complex numbers $z_j^* = \tau_j^* e^{i\theta_j}$, $\tau_j^* \geq 0$, $j = 1, \dots, q-1$, and then consider $z_q^* = -z_1^* - \dots - z_{q-1}^*$. The numbers $z_j = \tau_j e^{i\theta_j}$, $j = 1, \dots, q$, satisfying the inequalities $\tau_j \leq 2\alpha_j$ are taken such that

$$\tau_j = \tau_j^* B, \quad \text{with } B = \min_{k=1, \dots, q} \frac{2\alpha_k}{\tau_k^*}, \\ \tau_k^* > 0$$

Denoting

$$\gamma_j = \arccos \frac{\tau_j}{2\alpha_j}, \quad j = 1, \dots, q,$$

and applying Lemma 3.14, we can write a solution of equation (3.60) as

$$\begin{cases} \beta_j = \theta_j + \varepsilon_j \gamma_j \pmod{2\pi}, \\ \beta_{n+2-j} = \theta_j - \varepsilon_j \gamma_j \pmod{2\pi}, \end{cases} \quad \text{with } \varepsilon_j \in \{-1, 1\}.$$

Appendix 2

For n even, we discuss the equation

$$\alpha_{q+1} e^{i\beta_{q+1}} + \sum_{j=1}^q \alpha_j (e^{i\beta_j} + e^{i\beta_{n+2-j}}) = 0, \quad (3.62)$$

with $q = n/2$, $\alpha_j > 0$ given and the unknowns β_j , $j = 1, \dots, q+1$. For determining a non-trivial solution we need the following result.

Lemma 3.15 *Let $a, b_1, \dots, b_q > 0$ such that $a \leq b_1 + \dots + b_q$. Then there exist numbers $t_j \in [0, 1]$ (not all of them equal) for $j \in \{1, \dots, q\}$, such that*

$$a = \sum_{j=1}^q t_j b_j. \quad (3.63)$$

Proof. Of course, a trivial solution, when all t_j are equal, is

$$t_j = t^* = \frac{a}{b_1 + \dots + b_q} \in (0, 1], \text{ for } j = 1, 2, \dots, q + 1,$$

and it leads to a trivial solution of (3.41).

For non-trivial solutions, let $t = a(b_1 + \dots + b_q)^{-1} \in (0, 1]$. There exist numbers $\varepsilon_j \in [0, t]$, $j = 1, \dots, q - 1$ such that

$$c := \frac{\sum_{j=1}^{q-1} \varepsilon_j b_j}{b_q} \leq 1 - t.$$

The numbers t_j defined as

$$t_\nu = \begin{cases} t - \varepsilon_\nu, & \text{for } \nu \neq q, \\ t + c, & \text{for } \nu = q \end{cases}$$

satisfy the equality (3.63). ■

We will prove that equation (3.62) is solvable if and only if

$$\alpha_{q+1} \leq 2 \sum_{j=1}^q \alpha_j. \quad (3.64)$$

Indeed, if the equation is solvable, (3.64) follows immediately by applying the triangle inequality. Conversely, suppose that (3.64) hold. From the previous lemma, there exist numbers $t_j \in [0, 1]$ such that $\alpha_{q+1} = 2 \sum_{j=1}^q \alpha_j t_j$. Then a solution of equation (3.62) is

$$\begin{aligned} \beta_j &= \arccos t_j, \quad \beta_{n+2-j} = 2\pi - \beta_j \pmod{2\pi}, \text{ for } j = 1, \dots, q, \\ \beta_{q+1} &= \pi. \end{aligned}$$

Appendix 3

For n odd, we discuss the solutions of the system

$$\sum_{j=1}^q \alpha_j (e^{ix_j} + e^{iy_j}) = 0, \quad (3.65)$$

$$\sum_{j=1}^q \mu_j (e^{ix_j} - e^{iy_j}) = 0, \quad (3.66)$$

with $q = \frac{n+1}{2}$, $\alpha_j, \mu_j > 0$ given and $x_j, y_j \in [0, 2\pi)$ unknowns. Due to our particular problems (systems (3.46)–(3.47) and (3.53)–(3.54)), we will also suppose that

$$\frac{\alpha_{j+1}}{\mu_{j+1}} \geq \frac{\alpha_j}{\mu_j} \quad \text{for all } j = 1, \dots, q - 1. \quad (3.67)$$

For $n = 1$ the incompatibility is immediate, so let us suppose in the sequel that $n \geq 3$.

Proposition 3.16 *Under the above assumptions, the following statements are true:*

1. *If there exists $k \in \{1, \dots, q\}$ such that*

$$\alpha_k \mu_k > \alpha_k \sum_{j=1}^{k-1} \mu_j + \mu_k \sum_{j=k+1}^q \alpha_j, \quad (3.68)$$

then the system (3.65) – (3.66) is not solvable.

2. If there exists $v \in \{1, \dots, q\}$ such that

$$\mu_v \geq \sum_{j=1, j \neq v}^q \mu_j, \quad (3.69)$$

$$\alpha_v \leq \sum_{j=1, j \neq v}^q \alpha_j, \quad (3.70)$$

then the system is solvable.

3. If there exists $v \in \{1, \dots, q\}$ such that

$$\alpha_v \geq \sum_{j=1, j \neq v}^q \alpha_j, \quad (3.71)$$

$$\mu_v \leq \sum_{j=1, j \neq v}^q \mu_j, \quad (3.72)$$

then the system is solvable.

Proof.

1. We suppose that the system is solvable and let $x_j, y_j, j = 1, \dots, q$, be a solution. If we multiply the equations (3.65)–(3.66) by μ_k and α_k respectively and then we add them, we get, for all $k = 1, \dots, q$,

$$2\alpha_k \mu_k e^{ix_k} = \sum_{j=1, j \neq k}^q -(\alpha_k \mu_j + \alpha_j \mu_k) e^{ix_j} + (\alpha_k \mu_j - \alpha_j \mu_k) e^{iy_j}.$$

Using the triangle inequality and the identity $a + b + |a - b| = 2 \max\{a, b\}$ we obtain

$$\alpha_k \mu_k \leq \sum_{j=1, j \neq k}^q \max\{\alpha_k \mu_j, \alpha_j \mu_k\}.$$

Using now the hypothesis (3.67), this inequality can be written as

$$\alpha_k \mu_k \leq \alpha_k \sum_{j=1}^{k-1} \mu_j + \mu_k \sum_{j=k+1}^q \alpha_j,$$

which contradicts (3.68). In conclusion the system is incompatible.

2. Applying Lemma 3.15, there are numbers $t_j \in [0, 1], j = 1, \dots, q, j \neq v$, such that

$$\alpha_v = \sum_{j=1, j \neq v} \alpha_j t_j.$$

We define the function $\varphi : [0, 2] \rightarrow \mathbb{R}$,

$$\varphi(t) = \sum_{j=1, j \neq v}^q \mu_j \sqrt{4 - t_j^2 t^2} - \mu_v \sqrt{4 - t^2}.$$

Since $\varphi(0) \cdot \varphi(2) \leq 0$, there exists $t_0 \in [0, 2]$ such that $\varphi(t_0) = 0$. A simple calculation shows that a solution of the system can be written as

$$\begin{aligned} x_j &= \arccos \frac{t_0 t_j}{2}, \quad y_j = 2\pi - x_j \pmod{2\pi}, \quad \text{for } j \neq v, \\ x_v &= \pi + \arccos \frac{t_0}{2}, \quad y_v = \pi - \arccos \frac{t_0}{2}. \end{aligned}$$

3. Consider the number $t_1 = \alpha_v^{-1} \sum_{j=1, j \neq v}^q \alpha_j \leq 1$ and define the function $\varphi : [0, 1] \rightarrow \mathbb{R}$,

$$\varphi(t) = \sqrt{1-t^2} \sum_{j=1, j \neq v}^q \mu_j - \mu_v \sqrt{1-t_1^2 t^2}.$$

Since $\varphi(0) \cdot \varphi(1) \leq 0$, there exists $t_0 \in [0, 1]$ such that $\varphi(t_0) = 0$. Then we define the numbers

$$\delta_\nu = \begin{cases} 2\alpha_\nu t_0, & \text{for } \nu \neq v, \\ 2t_0 \sum_{j=1, j \neq v}^q \alpha_j, & \text{for } \nu = v. \end{cases}$$

A simple calculation shows that a solution of the system can be written as

$$\begin{aligned} x_j &= \arccos \frac{\delta_j}{2\alpha_j}, \quad y_j = 2\pi - x_j \pmod{2\pi}, \quad \text{for } j \neq v, \\ x_v &= \pi + \arccos \frac{\delta_v}{2\alpha_v}, \quad y_v = \pi - \arccos \frac{\delta_v}{2\alpha_v}. \quad \blacksquare \end{aligned}$$

Chapter 4

Wavelets on the unit sphere of \mathbb{R}^3

4.1 Wavelet bases on the sphere obtained by radial projection

We present a method for constructing wavelet bases on the unit sphere \mathbb{S}^2 of \mathbb{R}^3 , using the radial projection and an inner product associated to a convex polyhedron having the origin inside. The main advantage of this method is the avoidance of singularities and distortions around poles, which occur in other approaches. Also, we can obtain spherical wavelets with small support, a fact which is crucial in working with large amounts of data, since the algorithms deal with sparse matrices.

With the aim of avoiding these distortions around the poles and at the same time using the existing constructions in one and two dimensions, we considered another approach, where the planar wavelet bases are first transferred to the faces of a certain polyhedron and then to \mathbb{S}^2 by a radial projection. We present here three possible ways of exploiting this idea. The strengths in all these constructions are:

- the avoidance of distortions around the poles
- a stationary multiresolution analysis
- the scaling functions and wavelets are locally supported
- Riesz stability of wavelet bases
- simple implementation and fast algorithms
- the constructions can be easily adapted to other closed surfaces [94].

The price to pay for all these advantages is the lack of smoothness. We do not have yet a clear answer regarding the possibility of obtaining smooth wavelets for other cases than those illustrated here, but we believe that, along the radial projections of the polyhedral edges, it is impossible to have smoothness for the wavelets.

Let $\mathbb{S}^2 = \{\mathbf{x} \in \mathbb{R}^3, \|\mathbf{x}\| = 1\}$ be the unit sphere of \mathbb{R}^3 centered at the origin. We consider the real Hilbert space $L^2(\mathbb{S}^2)$ of square-integrable functions defined on \mathbb{S}^2 , with the usual scalar product $\langle \cdot, \cdot \rangle_{L^2(\mathbb{S}^2)}$ and the usual 2-norm $\|\cdot\|_{L^2(\mathbb{S}^2)}$ defined as

$$\begin{aligned}\langle F, G \rangle_{L^2(\mathbb{S}^2)} &= \int_{\mathbb{S}^2} F(\eta)G(\eta) d\omega(\eta), \\ \|F\|_{L^2(\mathbb{S}^2)} &= \langle F, F \rangle_{L^2(\mathbb{S}^2)}^{1/2},\end{aligned}$$

where $F, G \in L^2(\mathbb{S}^2)$ and $d\omega(\eta)$ stands for the surface element of the sphere \mathbb{S}^2 .

By definition, a *multiresolution analysis* of the space $L^2(\mathbb{S}^2)$ is a sequence of subspaces $\{\mathcal{V}^j : j \geq 0\}$ of $L^2(\mathbb{S}^2)$ which satisfy the following requirements:

1. $\mathcal{V}^j \subseteq \mathcal{V}^{j+1}$ for all $j \in \mathbb{N}_0$,
2. $\text{clos}_{L^2(\mathbb{S}^2)} \bigcup_{j=0}^{\infty} \mathcal{V}^j = L^2(\mathbb{S}^2)$,
3. There are index sets $\mathcal{K}_j \subseteq \mathcal{K}_{j+1}$ such that, for every level j , there exists a Riesz basis $\{\varphi_v^j, v \in \mathcal{K}_j\}$ of the space \mathcal{V}^j . This means that there exist constants $0 < C_1 \leq C_2 < \infty$, independent of the level j , such that

$$C_1 2^{-j} \left\| \{c_v^j\}_{v \in \mathcal{K}_j} \right\|_{l_2(\mathcal{K}_j)} \leq \left\| \sum_{v \in \mathcal{K}_j} c_v^j \varphi_v^j \right\|_{L^2(\mathbb{S}^2)} \leq C_2 2^{-j} \left\| \{c_v^j\}_{v \in \mathcal{K}_j} \right\|_{l_2(\mathcal{K}_j)},$$

for all $\{c_v^j\}_{v \in \mathcal{K}_j} \in l_2(\mathcal{K}_j)$. We do not require the scaling functions φ_v^j to be translations and dilations of the same function φ . In some papers the authors replace the translation requirement with a rotational one [2], but in most of the research on multiresolution and wavelets on the sphere, this requirement is not demanded, since it is difficult to be satisfied.

Once the multiresolution analysis is determined, we construct the wavelet spaces \mathcal{W}^j . Every wavelet space \mathcal{W}^j will be the orthogonal complement, with respect to a certain weighted L^2 -inner product which will be defined in Section 4.1.1, of the coarse space \mathcal{V}^j into the finest space \mathcal{V}^{j+1} . The basis functions of each space \mathcal{W}^j are commonly called *wavelets*. In Sections 4.1.2 and 4.1.3 we describe a construction of some wavelet bases on triangulations and in Section 4.1.4 we show how we can construct spherical wavelets starting from wavelets on an interval.

4.1.1 An inner product in $L^2(\mathbb{S}^2)$

Let Π be a convex polyhedron having all the vertices situated on \mathbb{S}^2 and triangular faces, such that no face contains the origin and the origin is situated inside the polyhedron. The case when some faces are not triangles is also allowed, if these faces are triangulated and each triangle is considered as a face (some triangular faces of the polyhedron are allowed to be coplanar). In the sequel, we consider this last condition satisfied without mentioning it explicitly. We denote by $\mathcal{T} = \{T_1, T_2, \dots, T_n\}$ the set of the faces of Π and by Ω the boundary of Π . Then we consider the following inner product in $L^2(\Omega)$:

$$\langle f, g \rangle_{\mathcal{T}} = \sum_{T \in \mathcal{T}} \frac{1}{\mathcal{A}(T)} \int_T f(\mathbf{x}) g(\mathbf{x}) d\mathbf{x}, \quad f, g \in L^2(\Omega),$$

where $\mathcal{A}(T)$ is the area of the triangle T . Let us define the radial projection $p : \Omega \rightarrow \mathbb{S}^2$,

$$p(x, y, z) = \left(\frac{x}{\sqrt{x^2 + y^2 + z^2}}, \frac{y}{\sqrt{x^2 + y^2 + z^2}}, \frac{z}{\sqrt{x^2 + y^2 + z^2}} \right),$$

$(x, y, z) \in \Omega$, and its inverse $p^{-1} : \mathbb{S}^2 \rightarrow \Omega$,

$$p^{-1}(\eta_1, \eta_2, \eta_3) = \left(-\frac{\eta_1 d}{a\eta_1 + b\eta_2 + c\eta_3}, -\frac{\eta_2 d}{a\eta_1 + b\eta_2 + c\eta_3}, -\frac{\eta_3 d}{a\eta_1 + b\eta_2 + c\eta_3} \right),$$

where $ax + by + cz + d = 0$ is the equation of that face of Π onto which the point $(\eta_1, \eta_2, \eta_3) \in \mathbb{S}^2$ projects. In the case when the point (η_1, η_2, η_3) projects onto an edge, then we may choose one of its adjacent faces to express the function p^{-1} . If we define $U_i = p(T_i)$ for $i = 1, \dots, n$, then $\mathcal{U} = \{U_1, \dots, U_n\}$ is a triangulation of \mathbb{S}^2 . For a given triangle $T \in \mathcal{T}$ having the vertices $M_i(x_i, y_i, z_i)$, $i = 1, 2, 3$, we consider the function $w_T : p(T) \rightarrow \mathbb{R}$, defined by

$$w_T(\eta) = \frac{2d_T^2}{|a_T\eta_1 + b_T\eta_2 + c_T\eta_3|^3}, \quad (4.1)$$

where $\eta = (\eta_1, \eta_2, \eta_3) \in p(T) \subseteq \mathbb{S}^2$ and a_T, b_T, c_T, d_T are the coefficients of $x, y, z, 1$ respectively, of the polynomial function

$$\begin{vmatrix} x & y & z & 1 \\ x_1 & y_1 & z_1 & 1 \\ x_2 & y_2 & z_2 & 1 \\ x_3 & y_3 & z_3 & 1 \end{vmatrix}.$$

With $d\omega(\eta)$ denoting the area element of \mathbb{S}^2 , the following weighted scalar product in $L(\mathbb{S}^2)$ was introduced in [92]:

$$\begin{aligned} \langle F, G \rangle_{\mathcal{U}} &= \langle F \circ p, G \circ p \rangle_{\mathcal{T}} \\ &= \sum_{T \in \mathcal{T}} \int_{p(T)} F(\eta)G(\eta)w_T(\eta) d\omega(\eta), \end{aligned} \quad (4.2)$$

for $F, G \in L^2(\mathbb{S}^2)$. There we proved that this inner product induces a norm,

$$\|\cdot\|_{\mathcal{U}} = \langle \cdot, \cdot \rangle_{\mathcal{U}}^{1/2}, \quad (4.3)$$

which is equivalent to the usual 2-norm of $L^2(\mathbb{S}^2)$. More precisely the following inequalities are true

$$m_{\mathcal{U}}\|F\|_{L^2(\mathbb{S}^2)}^2 \leq \|F\|_{\mathcal{U}}^2 \leq M_{\mathcal{U}}\|F\|_{L^2(\mathbb{S}^2)}^2, \quad (4.4)$$

with

$$m_{\mathcal{U}} = \min_{T \in \mathcal{T}} m_{\mathcal{U}}^T, \quad \text{with} \quad m_{\mathcal{U}}^T = \frac{d_T^2}{4(\mathcal{A}(T))^3} = \frac{\text{dist}^2(O, T)}{\mathcal{A}(T)}, \quad (4.5)$$

$$M_{\mathcal{U}} = \max_{T \in \mathcal{T}} M_{\mathcal{U}}^T, \quad \text{with} \quad M_{\mathcal{U}}^T = \frac{2}{|d_T|} = \frac{1}{\mathcal{A}(T)\text{dist}(O, T)}. \quad (4.6)$$

Here $\mathcal{A}(T)$ denotes the area of the triangle T and $\text{dist}(O, T)$ represents the distance from the origin to the plane of T . One has $|d_T| = 2\mathcal{A}(T)\text{dist}(O, T)$. In [106] we considered the case when the convex polyhedron Π is not necessarily inscribed in the sphere; then the conditions imposed on Π are that the origin O is situated inside Π and no face contains O . In this case inequalities (4.4) hold, with the constants $m_{\mathcal{U}} > 0$ and $M_{\mathcal{U}} < \infty$ given later in Section 4.2, Theorem 4.3.

4.1.2 Continuous rational spline wavelets on spherical triangulations

For the convex polyhedron Π satisfying the requirements in Section 4.1.1, we denote by E the set of edges and by V the set of vertices. For a vertex $v \in V$ the set of neighbors of v is $V_v = \{w \in V : [v, w] \in E\}$. For $v \in V$ we consider the piecewise linear ‘‘pyramidal’’ function

ϕ_v equal to 1 at the vertex v and 0 at the other vertices. Specifically, the function $\phi_{M_1} : \Omega \rightarrow \mathbb{R}$ associated to the vertex $M_1(x_1, y_1, z_1) \in \Omega$ is given by

$$\phi_{M_1}(x, y, z) = \begin{cases} \frac{\begin{vmatrix} x & y & z \\ x_i & y_i & z_i \\ x_k & y_k & z_k \end{vmatrix}}{\begin{vmatrix} x_1 & y_1 & z_1 \\ x_i & y_i & z_i \\ x_k & y_k & z_k \end{vmatrix}}, & \text{on each triangle } [M_1 M_i M_k] \text{ of } \mathcal{T}, \\ 0, & \text{on the triangles that do not contain } M_1. \end{cases}$$

The functions $\varphi_v : \mathbb{S}^2 \rightarrow \mathbb{R}$, $\varphi_v = \phi_v \circ p^{-1}$, for $v \in V$, are continuous on \mathbb{S}^2 and their supports are \mathcal{M}_v , the set of all spherical triangles of \mathcal{U} that contain the vertex v . Thus φ_v are local around the vertex v . If $[M_1 M_i M_k]$ is a triangle of \mathcal{T} and $[M'_1 M'_i M'_k]$ its radial projection onto \mathbb{S}^2 , then after some calculations we obtain that the restriction to $[M'_1 M'_i M'_k]$ of φ_{M_1} will be

$$\varphi_{M_1}(\eta_1, \eta_2, \eta_3) = \begin{vmatrix} \eta_1 & \eta_2 & \eta_3 \\ x_i & y_i & z_i \\ x_k & y_k & z_k \end{vmatrix} \cdot \begin{vmatrix} \eta_1 & \eta_2 & \eta_3 & 0 \\ x_1 & y_1 & z_1 & 1 \\ x_i & y_i & z_i & 1 \\ x_k & y_k & z_k & 1 \end{vmatrix}^{-1}.$$

Here (x_i, y_i, z_i) and (x_k, y_k, z_k) are the coordinates of the points M_i and M_k , respectively. Thus the ‘‘pyramidal’’ functions φ_v are continuous piecewise rational functions, with the numerator and denominator linear polynomials of degree one.

Multiresolution analysis and wavelets

Given Ω we can say that $\mathcal{T} = \mathcal{T}^0$ is a triangulation of Ω , and next we wish to consider its uniform refinement \mathcal{T}^1 . For a given triangle $[M_1 M_2 M_3]$ in \mathcal{T}^0 , let A_1, A_2, A_3 denote the midpoints of the edges $M_2 M_3, M_3 M_1$ and $M_1 M_2$, respectively. Then we consider the set

$$\mathcal{T}^1 = \bigcup_{[M_1 M_2 M_3] \in \mathcal{T}^0} \{[M_1 A_2 A_3], [A_1 M_2 A_3], [A_1 A_2 M_3], [A_1 A_2 A_3]\},$$

which is also a triangulation of Ω . Continuing in the same way the refinement process, we obtain a triangulation \mathcal{T}^j of Ω for $j \in \mathbb{N}$. We denote by V^j the set of all vertices of the triangles in \mathcal{T}^j and by E^j the set of all edges of triangles in \mathcal{T}^j . Then $V_v^j, \phi_v^j, \varphi_v^j$ and \mathcal{U}^j are defined accordingly. If we define the space \mathcal{V}^j as

$$\mathcal{V}^j = \text{span}\{\varphi_v^j, v \in V^j\}, \quad (4.7)$$

then \mathcal{V}^j will be a subspace of \mathcal{V}^{j+1} , since we have

$$\varphi_v^j = \varphi_v^{j+1} + \frac{1}{2} \sum_{w \in V_v^{j+1}} \varphi_w^{j+1}, \quad v \in V^j, \quad j \in \mathbb{N}.$$

In [92] we showed that conditions 2 and 3 in the definition of a multiresolution analysis on \mathbb{S}^2 are fulfilled.

With respect to the inner product $\langle \cdot, \cdot \rangle_{\mathcal{U}}$ the spaces \mathcal{V}^j and \mathcal{V}^{j+1} become Hilbert spaces, with the corresponding weighted norm $\| \cdot \|_{\mathcal{U}}$. The wavelet space \mathcal{W}^j will be defined as the orthogonal complement with respect to $\langle \cdot, \cdot \rangle_{\mathcal{U}}$ of the coarse space \mathcal{V}^j in the fine space \mathcal{V}^{j+1} , so that

$$\mathcal{V}^{j+1} = \mathcal{V}^j \oplus \mathcal{W}^j. \quad (4.8)$$

For each level $j \in \mathbb{N}$, the dimension of \mathcal{W}^j is $|V^{j+1}| - |V^j| = |E^j|$. We will construct a basis for \mathcal{W}^j , consisting of wavelets of small support, following the ideas in [43]. To each “new” vertex $u \in V^{j+1} \setminus V^j$, which is a midpoint of some edge $[a_1 a_2] \in E^j$, we associate a wavelet ψ_u^j in the following way:

$$\psi_u^j = s_{a_1} \varphi_{a_1}^{j+1} + s_{a_2} \varphi_{a_2}^{j+1} + \sum_{w \in V_{a_1}^{j+1}} s_w \varphi_w^{j+1} + \sum_{w \in V_{a_2}^{j+1}} t_w \varphi_w^{j+1},$$

with $s_{a_1}, s_{a_2}, s_w, t_w \in \mathbb{R}$ to be determined such that $\{\psi_u^j, u \in V^{j+1} \setminus V^j\}$ is a basis of \mathcal{W}^j . More precisely, the following orthogonality property holds for all $w \in V^j$:

$$\langle \varphi_w^j, \psi_u^j \rangle_{\mathcal{U}} = 0.$$

Explicit values for the coefficients $s_{a_1}, s_{a_2}, s_w, t_w$, which do not depend on the level j , are given in [92]. Since $\text{diam } \psi_u^j \approx 2^{-j}$, the support of each wavelet ψ_u^j is located around the “parents” a_1 and a_2 of the new vertex u and therefore we can say that we have obtained a basis of locally supported wavelets. The local support leads to sparse matrices for the reconstruction algorithms. Actually, the number of nonzero entries in each row/column of such matrix is $\max\{11, k\}$, where $k = \max\{|V_v|, v \in V\}$. These matrices are not orthogonal because the wavelets at the same level j are not orthogonal to each other. Such wavelet bases, where the wavelets belonging to different wavelet spaces \mathcal{W}^j are orthogonal but the wavelets belonging to the same wavelet space \mathcal{W}^j are not orthogonal, are called *semi-orthogonal*. Numerical manipulations with MATLAB[®] of such sparse and non-orthogonal reconstruction matrices R_j show that the product $R_j^{-1}x$ (x being a data vector) is rapidly calculated even when we deal with very large matrices (e.g. of dimension 4096×4096). Finally let us mention that the set

$$\{\varphi_u^0 : u \in V^0\} \cup \bigcup_{j=0}^{\infty} \{2^j \psi_u^j : u \in V^{j+1} \setminus V^j\}$$

forms a Riesz basis of the space

$$\bigcup_{j \geq 0} \mathcal{V}^j = \mathcal{V}^0 \oplus \bigoplus_{j=0}^{\infty} \mathcal{W}^j$$

and this space is dense in $L^2(\mathbb{S}^2)$. For more details, graphics of wavelets and numerical examples, see [92].

4.1.3 Piecewise constant wavelets on spherical triangulations

We consider again the polyhedron Π and we use the same notations and refinement procedure as in Section 4.1.2. We denote the spatial triangles of \mathcal{T}^j by T_k^j and the spherical triangles $p(T_k^j)$ of \mathcal{U}^j by U_k^j , for $k = 1, \dots, n \cdot 4^j$. Then, to each triangle U_k^j , we associate a scaling function $\varphi_{U_k^j} : \mathbb{S}^2 \rightarrow \mathbb{R}$,

$$\varphi_{U_k^j}(\eta) = \begin{cases} 1, & \text{inside the triangle } U_k^j, \\ 0, & \text{elsewhere.} \end{cases}$$

Next we define the spaces of functions $\mathcal{V}^j = \text{span} \left\{ \varphi_{U_k^j}, k = 1, 2, \dots, n \cdot 4^j \right\}$, consisting of piecewise constant functions on the triangles of \mathcal{U}^j . The set $\left\{ \varphi_{U_k^j}, k = 1, 2, \dots, n \cdot 4^j \right\}$ is a basis for \mathcal{V}^j , so $|\mathcal{V}^j| = n \cdot 4^j$. Let $U^j \in \mathcal{U}^j$ and let $U_k^{j+1} = p(T_k^{j+1})$, $k = 1, 2, 3, 4$, denote the refined triangles obtained from U^j .

We have

$$\varphi_{U^j} = \varphi_{U_1^{j+1}} + \varphi_{U_2^{j+1}} + \varphi_{U_3^{j+1}} + \varphi_{U_4^{j+1}},$$

where the equality holds in $L^2(\mathbb{S}^2)$. Thus, $\mathcal{V}^j \subseteq \mathcal{V}^{j+1}$ for all $j \in \mathbb{N}$. With respect to the scalar product $\langle \cdot, \cdot \rangle_{\mathcal{U}}$, the spaces \mathcal{V}^j and \mathcal{V}^{j+1} become Hilbert spaces, with the corresponding norm $\|\cdot\|_{\mathcal{U}}$. The wavelet space \mathcal{W}^j is defined as in (4.8). Its dimension is $|\mathcal{W}^j| = |\mathcal{V}^{j+1}| - |\mathcal{V}^j| = 3n \cdot 4^j$.

Next we will construct a basis of \mathcal{W}^j . Let us take the triangle U^j and its refinements U_1^{j+1} , U_2^{j+1} , U_3^{j+1} , U_4^{j+1} and denote by $F_{U^j}^1$, $F_{U^j}^2$, $F_{U^j}^3$ the projections onto \mathbb{S}^2 of the mid-points of the edges of the plane triangle $p^{-1}(U^j)$. To each of these points $F_{U^j}^l$ a wavelet will be associated in the following way

$$\begin{aligned} \Psi_{F_{j+1}^1, U^j} &= \alpha_1 \varphi_{U_1^{j+1}} + \alpha_2 \varphi_{U_3^{j+1}} + \beta \varphi_{U_2^{j+1}} + \gamma \varphi_{U_4^{j+1}}, \\ \Psi_{F_{j+1}^2, U^j} &= \alpha_1 \varphi_{U_4^{j+1}} + \alpha_2 \varphi_{U_1^{j+1}} + \beta \varphi_{U_2^{j+1}} + \gamma \varphi_{U_3^{j+1}}, \\ \Psi_{F_{j+1}^3, U^j} &= \alpha_1 \varphi_{U_3^{j+1}} + \alpha_2 \varphi_{U_4^{j+1}} + \beta \varphi_{U_2^{j+1}} + \gamma \varphi_{U_1^{j+1}}, \end{aligned} \quad (4.9)$$

with $\alpha_1, \alpha_2, \beta, \gamma \in \mathbb{R}$ to be determined such that the set

$$\left\{ \Psi_{F_{j+1}^k, U^j}, k = 1, 2, 3, U^j \in \mathcal{U}^j \right\}$$

is an orthonormal basis of \mathcal{W}^j with respect to the inner product $\langle \cdot, \cdot \rangle_{\mathcal{U}}$. The calculations (for more details see [93]) show that there are two classes of wavelets:

$$\begin{aligned} {}^1\Psi_{F_{j+1}^1, U^j} &= \alpha_1 \varphi_{U_1^{j+1}} + \alpha_2 \varphi_{U_3^{j+1}} + 0.5 \varphi_{U_2^{j+1}} - (0.5 + \alpha_1 + \alpha_2) \varphi_{U_4^{j+1}}, \\ {}^1\Psi_{F_{j+1}^2, U^j} &= \alpha_1 \varphi_{U_4^{j+1}} + \alpha_2 \varphi_{U_1^{j+1}} + 0.5 \varphi_{U_2^{j+1}} - (0.5 + \alpha_1 + \alpha_2) \varphi_{U_3^{j+1}}, \\ {}^1\Psi_{F_{j+1}^3, U^j} &= \alpha_1 \varphi_{U_3^{j+1}} + \alpha_2 \varphi_{U_4^{j+1}} + 0.5 \varphi_{U_2^{j+1}} - (0.5 + \alpha_1 + \alpha_2) \varphi_{U_1^{j+1}}, \end{aligned}$$

with α_1, α_2 satisfying $4(\alpha_1^2 + \alpha_1 \alpha_2 + \alpha_2^2) + 2(\alpha_1 + \alpha_2) - 1 = 0$, and

$$\begin{aligned} {}^2\Psi_{F_{j+1}^1, U^j} &= \alpha_1 \varphi_{U_1^{j+1}} + \alpha_2 \varphi_{U_3^{j+1}} - 0.5 \varphi_{U_2^{j+1}} + (0.5 - \alpha_1 - \alpha_2) \varphi_{U_4^{j+1}}, \\ {}^2\Psi_{F_{j+1}^2, U^j} &= \alpha_1 \varphi_{U_4^{j+1}} + \alpha_2 \varphi_{U_1^{j+1}} - 0.5 \varphi_{U_2^{j+1}} + (0.5 - \alpha_1 - \alpha_2) \varphi_{U_3^{j+1}}, \\ {}^2\Psi_{F_{j+1}^3, U^j} &= \alpha_1 \varphi_{U_3^{j+1}} + \alpha_2 \varphi_{U_4^{j+1}} - 0.5 \varphi_{U_2^{j+1}} + (0.5 - \alpha_1 - \alpha_2) \varphi_{U_1^{j+1}}, \end{aligned}$$

with α_1, α_2 satisfying $4(\alpha_1^2 + \alpha_1 \alpha_2 + \alpha_2^2) - 2(\alpha_1 + \alpha_2) - 1 = 0$.

Let us remark that if we choose $\alpha_1 = \alpha_2 = \alpha$, then we obtain the families of wavelets in [81], where the spherical areas are approximated with the plane areas and the authors called such wavelets ‘‘nearly orthogonal’’.

A comparison of these wavelets was realized in [96, 97]. The advantage of these piecewise constant wavelets is that they are orthogonal and locally supported, and therefore both decomposition and reconstruction matrices are orthogonal and sparse. Actually they are block matrices with only four nonzero entries on each row/column. Numerical experiments show that they can successfully detect singularities as contours.

Other piecewise constant wavelets on spherical triangulations can be obtained by transporting on \mathbb{S}^2 all the planar constructions described in Sections 1.1, 1.2 and 1.3.

We will show in the sequel the behavior of the piecewise constant wavelets obtained in Section 1.1. At each step we perform the 1-3 splitting described in Section 1.1.1 on each face of the polyhedron and then we project it onto the sphere. The spherical wavelets will be orthogonal with respect to the scalar product (4.2) and the Riesz stability property in $L^2(\mathbb{S}^2)$ holds. With the subdivisions described in Figure 1.1 performed at random, we still can obtain long and thin triangles. To avoid this, we adopt the following rule. For each triangle which has to be divided, we re-denote its vertices, obtaining the triangle ABC with $AB \geq BC \geq AC$. Then we take $M \in AB$ such that $AM = AB/3$ and $N \in BC$ such that $CN = NB$. The refined triangles will be taken as AMC, CMN, MNB .

In order to illustrate our wavelets we take a set of spherical data *topo.mat* which consists in 180×360 measurements on the sphere and we represent it in Figure 4.1. We consider as the inscribed polyhedron an octahedron with six vertices. First we approximate this data with the function $F^8 : \mathbb{S}^2 \rightarrow \mathbb{R}$, which is a piecewise constant function on the $8 \cdot 3^8$ spherical triangles at the level 8. This approximation is represented in Figure 4.1 right. The function F^8 can be therefore written as

$$F^8 = \sum_{i=1}^{8 \cdot 3^8} f_i^8 \phi_{U_i^8},$$

where U_i^8 , $i \in \mathcal{N}_8^8$ are the spherical triangles at level 8 and $\phi_{U_i^8} : \mathbb{S}^2 \rightarrow \mathbb{R}$ is the characteristic function of the spherical triangle U_i^8 . The vector $f^8 = (f_i^8)_{i \in \mathcal{N}_8^8}$ associated to the function F^8 was then decomposed, using formula (1.6), into the vectors $f^7 = (f_i^7)_{i \in \mathcal{N}_7^8}$ (containing the approximation coefficients) and $w^7 = (w_i^7)_{i \in \mathcal{M}_7^8}$ (containing the details coefficients). Figure 4.2 and Figure 4.3 left show the graphs of the functions

$$\begin{aligned} F^7 &= \sum_{i=1}^{8 \cdot 3^7} f_i^7 \phi_{U_i^7}, \\ \Psi_1^7 &= \sum_{i=1}^{8 \cdot 3^7} w_{2i-1}^7 \left(\alpha_1 \phi_{U_i^8} + \alpha_2 \phi_{U_{i+1}^8} - (\alpha_1 + \alpha_2) \phi_{U_{i+2}^8} \right), \\ \Psi_2^7 &= \frac{1}{\sqrt{3}} \sum_{i=1}^{8 \cdot 3^7} w_{2i}^7 \left((\alpha_1 + 2\alpha_2) \phi_{U_i^8} - (2\alpha_1 + \alpha_2) \phi_{U_{i+1}^8} + (\alpha_1 - \alpha_2) \phi_{U_{i+2}^8} \right), \end{aligned}$$

which satisfy the relation

$$F^8 = F^7 + \Psi_1^7 + \Psi_2^7.$$

We continue the decomposition, as we described in Section 1.1.2, obtaining in the end the vectors f^0 and w^0, w^1, \dots, w^7 . Then we performed a hard thresholding and a reconstruction, as we described in Section 1.1.2 and we measured some norms of the compression error $e^8 = f^8 - \widehat{f}^8$. These errors are tabulated in Table 1, for four choices of the parameters (α_1, α_2) . There $\gamma = (-1 + \sqrt{5})/4$, $\mu = 1/\sqrt{2}$, *thr* = the threshold of the hard thresholding, *cr* = the compression rate (the ratio of the number of nonzero coefficients to the total number of coefficients) *zc* = number of zero coefficients, *nzc* = number of nonzero coefficients. Figure 4.3 right and Figure 4.4 show the compressed data for *thr* = 100, 500 and 1000, respectively.

4.1.4 From wavelets on an interval to wavelets on the sphere

Another possible construction of spherical wavelets via radial projection can be done by using the tensor product of wavelets on an interval and by taking a cube as polyhedron Π . We will

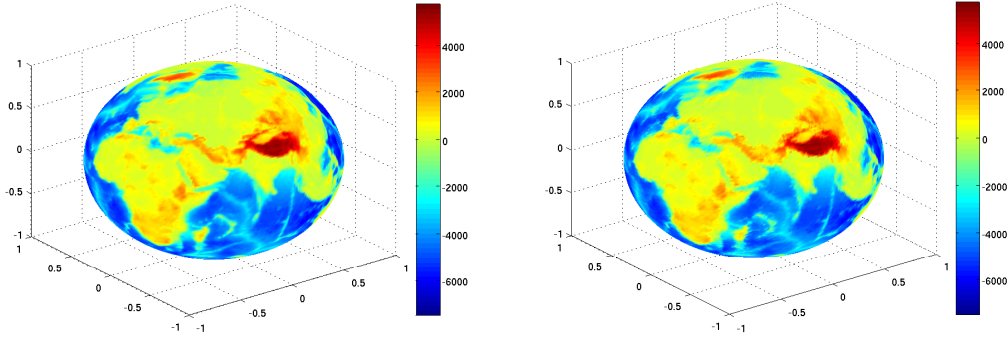


Figure 4.1: The initial data set *topo.mat* (left) and its approximation F^8 at level 8 (right).

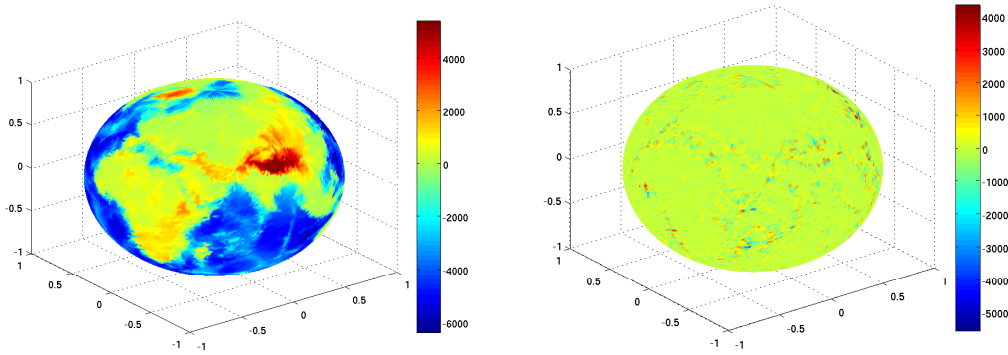


Figure 4.2: The approximation F^7 (left) and the wavelet ψ_1^7 (right).

show only the construction for Haar wavelets. Unlike the construction presented in Section 4.1.3, the wavelets will be rotations and dilations of the same function. The results were published in [99].

So let us consider as polyhedron Π the cube inscribed in \mathbb{S}^2 , having the edge $2s$, with $s = 1/\sqrt{3}$, and denote by \mathbf{C} the boundary of Π . We triangulate each face by taking one of the two diagonals. Then we denote by F_i , $i = 1, \dots, 6$, the faces of the cube situated in the planes $x = s$, $x = -s$, $y = s$, $y = -s$, $z = s$, $z = -s$, respectively, and by $\mathcal{F}_i = p(F_i)$ the corresponding spherical quadrangles. The inner product $\langle \cdot, \cdot \rangle_{\mathcal{U}}$ will have the expression

$$\begin{aligned} \langle F, G \rangle_{\mathcal{U}} &= \int_{\mathcal{F}_1 \cup \mathcal{F}_2} \frac{F(\eta)G(\eta) d\omega(\eta)}{2|\eta_1|^3} \\ &+ \int_{\mathcal{F}_3 \cup \mathcal{F}_4} \frac{F(\eta)G(\eta) d\omega(\eta)}{2|\eta_2|^3} + \int_{\mathcal{F}_5 \cup \mathcal{F}_6} \frac{F(\eta)G(\eta) d\omega(\eta)}{2|\eta_3|^3}, \end{aligned}$$

for $F, G \in L^2(\mathbb{S}^2)$.

Remark: Using the recently constructed area preserving projection \mathbf{p} from the cube C to the sphere \mathbb{S}^2 presented in Section 2.3, one can replace the weighted product $\langle \cdot, \cdot \rangle$ with the

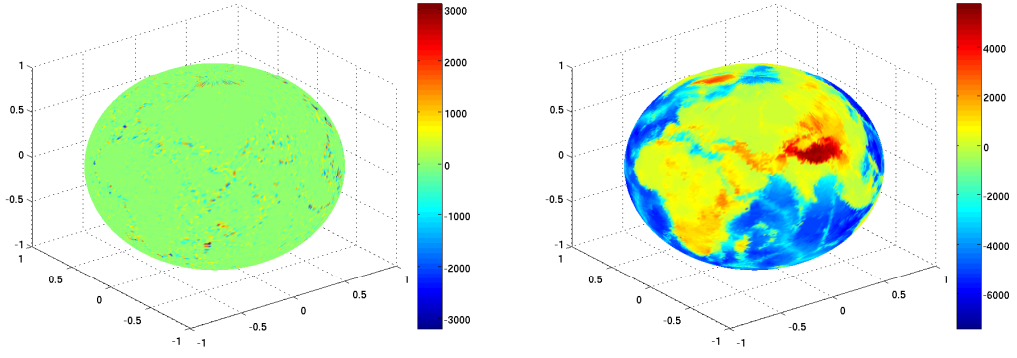


Figure 4.3: The wavelet ψ_2^7 (left) and the reconstructed function \widehat{F}^8 for the threshold $\text{thr} = 100$ (right).

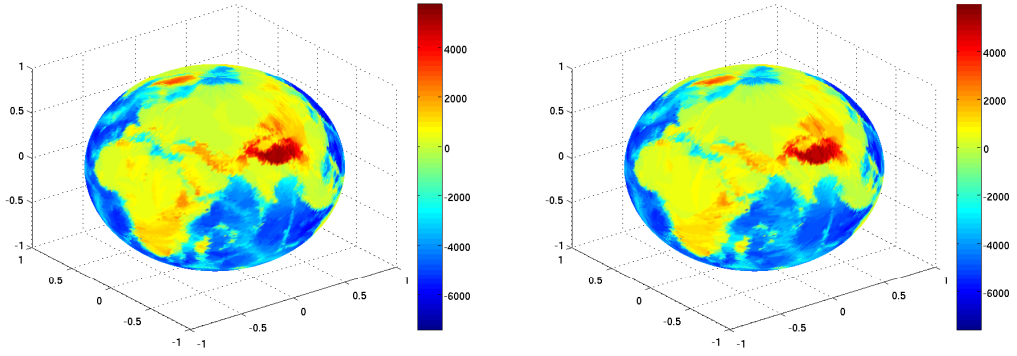


Figure 4.4: The reconstructed function \widehat{F}^8 for the thresholds $\text{thr} = 500$ (left) and $\text{thr} = 1000$ (right).

usual inner product of $L^2(\mathbb{S}^2)$. In fact, we have the equalities

$$\begin{aligned}
 \langle F, G \rangle_{L^2(\mathbb{S}^2)} &= \int_{\mathbb{S}^2} F(\eta)G(\eta) d\omega(\eta) = \sum_{i=1}^6 \int_{\mathcal{F}_i} F(\eta)G(\eta) d\omega(\eta) \\
 &= \sum_{i=1}^6 \int_{F_i} F(\mathbf{p}(\mathbf{w}))G(\mathbf{p}(\mathbf{w})) d\mathbf{w} \\
 &= \int_{F_1 \cup F_2} (F \circ \mathbf{p})(\mathbf{w})(G \circ \mathbf{p})(\mathbf{w}) dydz + \int_{F_3 \cup F_4} (F \circ \mathbf{p})(\mathbf{w})(G \circ \mathbf{p})(\mathbf{w}) dx dz \\
 &\quad + \int_{F_5 \cup F_6} (F \circ \mathbf{p})(\mathbf{w})(G \circ \mathbf{p})(\mathbf{w}) dx dy,
 \end{aligned}$$

where $d\mathbf{w}$ equals $dy dz$ on $F_1 \cup F_2$, $dx dz$ on $F_3 \cup F_4$ and $dx dy$ on $F_5 \cup F_6$. The last three terms are in fact inner products of $L^2(-L, L)$, where $2L = \sqrt{2\pi/3}$ is the edge of the cube of the same area with \mathbb{S}^2 .

(α_1, α_2)	thr	cr	nzc	zc	$\ e^8\ _2$	$\ e^8\ _1$	$\ e^8\ _\infty$
$(\gamma, 0.5)$	0.005	99.49	52213	267	0.0031	0.0257	$4.7626 \cdot 10^{-4}$
$(\gamma, 0.5)$	0.01	99.49	52212	268	0.0099	0.0399	0.0071
$(0.5, \gamma)$	0.01	99.49	52214	266	$1.4287 \cdot 10^{-9}$	$2.7103 \cdot 10^{-7}$	$1.7280 \cdot 10^{-11}$
$(0.5, \gamma)$	0.02	99.49	52213	267	0.0174	0.0282	0.0141
$(0.5, \gamma)$	0.05	99.48	52208	272	0.0831	0.3023	0.0347
$(0, \mu)$	0.01	98.61	51750	730	$1.3849 \cdot 10^{-9}$	$2.6635 \cdot 10^{-7}$	$1.5461 \cdot 10^{-11}$
$(0, \mu)$	0.25	98.59	51742	738	0.6667	6.6667	0.1111
$(0, \mu)$	0.5	98.45	51666	814	3.6540	62.6667	0.3889
$(\mu, 0)$	0.01	99.08	51997	483	$1.3746 \cdot 10^{-9}$	$2.6494 \cdot 10^{-7}$	$1.4552 \cdot 10^{-11}$
$(\mu, 0)$	0.2	99.08	51996	484	0.1361	0.6667	0.0370
$(\mu, 0)$	0.3	99.07	51990	490	0.5932	4.6667	0.1111
$(\mu, 0)$	1	98.59	51740	740	10.6069	275.5926	0.8889
$(\mu, 0)$	10	93.81	52480	3249	295.6947	$2.0958 \cdot 10^4$	13.5556
$(\mu, 0)$	100	64.45	33825	18655	$6.8759 \cdot 10^3$	$1.0094 \cdot 10^6$	162.6749
$(\mu, 0)$	500	27.54	14451	38029	$3.7898 \cdot 10^4$	$6.4781 \cdot 10^6$	812.6667
$(\mu, 0)$	1000	15.39	8077	44403	$6.9276 \cdot 10^4$	$1.1668 \cdot 10^7$	$1.5138 \cdot 10^3$

Table 4.1: Reconstruction errors for some compression rates and some wavelets.

Multiresolution analysis of $L^2(\mathbb{S}^2)$

Put $s = 1/\sqrt{3}$ and let $\varphi, f : \mathbb{R} \rightarrow \mathbb{R}$ be the functions defined by

$$\begin{aligned}\varphi &= \chi_{[0,1]}, \\ f &= a^{1/2}\varphi \circ v = a^{1/2}\chi_A,\end{aligned}$$

where $a = \sqrt{3}/2$ is a normalization factor and $v(x) = \frac{\sqrt{3}}{2}x + \frac{1}{2}$ is the linear transform which maps the interval $A = [-s, s]$ onto $[0, 1]$.

Let $j \in \mathbb{N}_0 = \mathbb{N} \cup \{0\}$ be fixed and denote $\mathcal{N}_j = \{0, 1, 2, \dots, 2^j - 1\}$. For $k \in \mathcal{N}_j$, we define the functions $\varphi_{j,k} : [0, 1] \rightarrow \mathbb{R}$ and $f_{j,k} : A \rightarrow \mathbb{R}$,

$$\begin{aligned}\varphi_{j,k} &= 2^{j/2}\varphi(2^j \cdot -k), \\ f_{j,k} &= a^{1/2}\varphi_{j,k} \circ v.\end{aligned}$$

Thus

$$f_{j,k}(x) = (a2^j)^{1/2}\varphi(2^j v(x) - k), \text{ for } x \in A.$$

Using these functions we can define the spaces of functions

$$\begin{aligned}V_{[0,1]}^j &= \text{span}\{\varphi_{j,k}, k \in \mathcal{N}_j\} \subseteq L^2([0, 1]) \text{ and} \\ V^j &= \text{span}\{f_{j,k}, k \in \mathcal{N}_j\} \subseteq L^2(A).\end{aligned}$$

Next, for $\mathbf{k} = (k_1, k_2) \in \mathcal{N}_j^2 = \mathcal{N}_j \times \mathcal{N}_j$, we construct the functions of two variables $\Phi, \Phi_{j,\mathbf{k}} : [0, 1]^2 \rightarrow \mathbb{R}$,

$$\begin{aligned}\Phi(x, y) &= \varphi(x)\varphi(y), \\ \Phi_{j,\mathbf{k}}(x, y) &= 2^j\Phi(2^j x - k_1, 2^j y - k_2) = \varphi_{j,k_1}(x)\varphi_{j,k_2}(y),\end{aligned}$$

for $(x, y) \in [0, 1]^2$ and $F, F_{j,\mathbf{k}} : A^2 \rightarrow \mathbb{R}$,

$$F(x, y) = f(x)f(y) = a\Phi(v(x), v(y)) = a\Phi(\Upsilon(x, y)), \quad (4.10)$$

$$\begin{aligned} F_{j,\mathbf{k}}(x, y) &= 2^j F(2^j x - k_1, 2^j y - k_2) \\ &= f_{j,k_1}(x)f_{j,k_2}(y) \\ &= a\varphi_{j,k_1}(v(x))\varphi_{j,k_2}(v(y)) \\ &= a \cdot 2^j \Phi(2^j v(x) - k_1, 2^j v(y) - k_2) \\ &= a\Phi_{j,\mathbf{k}}(\Upsilon(x, y)), \end{aligned} \quad (4.11)$$

for $(x, y) \in A^2$, where $\Upsilon : A^2 \rightarrow [0, 1]^2$, $\Upsilon(x, y) = (v(x), v(y))$. Using these functions, we define the spaces

$$\begin{aligned} \mathbf{V}_{[0,1]}^j &= (V_{[0,1]}^j)_x \otimes (V_{[0,1]}^j)_y = \text{span} \{ \Phi_{j,\mathbf{k}}, \mathbf{k} \in \mathcal{N}_j^2 \} \subseteq L^2([0, 1]^2), \\ \mathbf{V}^j &= V_x^j \otimes V_y^j = \text{span} \{ F_{j,\mathbf{k}}, \mathbf{k} \in \mathcal{N}_j^2 \} \subseteq L^2(A^2). \end{aligned}$$

Furthermore, we denote by D_x, D_y and D_z the orthogonal projections of the cube \mathbf{C} onto the coordinate planes $x = 0$, $y = 0$ and $z = 0$, respectively. Then we consider the function $p_c : \mathbf{C} \rightarrow D_x \cup D_y \cup D_z$, where $p_c(\mathbf{x})$ denotes the projection of the point $\mathbf{x} \in \mathbf{C}$ onto that coordinate plane which is parallel to the face of the cube which contains \mathbf{x} . If \mathbf{x} is situated on an edge, we will take as $p_c(\mathbf{x})$ one of the two possible orthogonal projections. In the following, each of the sets D_x, D_y and D_z will be identified with the set $A^2 \subseteq \mathbb{R}^2$. With this convention, for $\mathbf{k} \in \mathcal{N}_j^2$ we consider the functions $F_{j,\mathbf{k}}^S : \mathbb{S}^2 \rightarrow \mathbb{R}$,

$$F_{j,\mathbf{k}}^S = \frac{1}{a} F_{j,\mathbf{k}} \circ p_c \circ p^{-1}, \quad (4.12)$$

with $F_{j,\mathbf{k}}$ given in (4.11). With $\eta = (\eta_1, \eta_2, \eta_3)$, the function $F_{j,\mathbf{k}}^S$ can be written as

$$F_{j,\mathbf{k}}^S(\eta_1, \eta_2, \eta_3) = \frac{1}{a} \begin{cases} F_{j,\mathbf{k}} \left(\frac{\eta_2}{\sqrt{3}\eta_1}, \frac{\eta_3}{\sqrt{3}\eta_1} \right), & \text{for } \eta \in \mathcal{F}_1, \\ F_{j,\mathbf{k}} \left(-\frac{\eta_2}{\sqrt{3}\eta_1}, -\frac{\eta_3}{\sqrt{3}\eta_1} \right), & \text{for } \eta \in \mathcal{F}_2, \\ F_{j,\mathbf{k}} \left(\frac{\eta_1}{\sqrt{3}\eta_2}, \frac{\eta_3}{\sqrt{3}\eta_2} \right), & \text{for } \eta \in \mathcal{F}_3, \\ F_{j,\mathbf{k}} \left(-\frac{\eta_1}{\sqrt{3}\eta_2}, -\frac{\eta_3}{\sqrt{3}\eta_2} \right), & \text{for } \eta \in \mathcal{F}_4, \\ F_{j,\mathbf{k}} \left(\frac{\eta_1}{\sqrt{3}\eta_3}, \frac{\eta_2}{\sqrt{3}\eta_3} \right), & \text{for } \eta \in \mathcal{F}_5, \\ F_{j,\mathbf{k}} \left(-\frac{\eta_1}{\sqrt{3}\eta_3}, -\frac{\eta_2}{\sqrt{3}\eta_3} \right), & \text{for } \eta \in \mathcal{F}_6, \end{cases}$$

or, using the function $\Phi_{j,\mathbf{k}}$,

$$F_{j,\mathbf{k}}^S = \Phi_{j,\mathbf{k}} \circ \Upsilon \circ p_c \circ p^{-1}, \quad (4.13)$$

$$F_{j,\mathbf{k}}^S(\eta_1, \eta_2, \eta_3) = \begin{cases} \Phi_{j,\mathbf{k}} \left(\frac{1}{2} \left(1 + \frac{\eta_2}{\eta_1} \right), \frac{1}{2} \left(1 + \frac{\eta_3}{\eta_1} \right) \right), & \text{for } \eta \in \mathcal{F}_1, \\ \Phi_{j,\mathbf{k}} \left(\frac{1}{2} \left(1 - \frac{\eta_2}{\eta_1} \right), \frac{1}{2} \left(1 - \frac{\eta_3}{\eta_1} \right) \right), & \text{for } \eta \in \mathcal{F}_2, \\ \Phi_{j,\mathbf{k}} \left(\frac{1}{2} \left(1 + \frac{\eta_1}{\eta_2} \right), \frac{1}{2} \left(1 + \frac{\eta_3}{\eta_2} \right) \right), & \text{for } \eta \in \mathcal{F}_3, \\ \Phi_{j,\mathbf{k}} \left(\frac{1}{2} \left(1 - \frac{\eta_1}{\eta_2} \right), \frac{1}{2} \left(1 - \frac{\eta_3}{\eta_2} \right) \right), & \text{for } \eta \in \mathcal{F}_4, \\ \Phi_{j,\mathbf{k}} \left(\frac{1}{2} \left(1 + \frac{\eta_1}{\eta_3} \right), \frac{1}{2} \left(1 + \frac{\eta_2}{\eta_3} \right) \right), & \text{for } \eta \in \mathcal{F}_5, \\ \Phi_{j,\mathbf{k}} \left(\frac{1}{2} \left(1 - \frac{\eta_1}{\eta_3} \right), \frac{1}{2} \left(1 - \frac{\eta_2}{\eta_3} \right) \right), & \text{for } \eta \in \mathcal{F}_6. \end{cases} \quad (4.14)$$

The support of each spherical function $F_{j,\mathbf{k}}^S$ has a nonempty intersection with each of the spherical quadrangles \mathcal{F}_i , $i = 1, \dots, 6$. If we wish to have local support, we need to consider the functions $F_{j,\mathbf{k}}^{S,i} : \mathbb{S}^2 \rightarrow \mathbb{R}$, for $i = 1, \dots, 6$, given by

$$F_{j,\mathbf{k}}^{S,i} = F_{j,\mathbf{k}}^S \cdot \chi_{\mathcal{F}_i}. \quad (4.15)$$

Thus, the support of $F_{j,\mathbf{k}}^{S,i}$ will intersect only \mathcal{F}_i and we have the property

$$\sum_{i=1}^6 F_{j,\mathbf{k}}^{S,i} = F_{j,\mathbf{k}}^S. \quad (4.16)$$

Finally, for arbitrary $j \in \mathbb{N}_0$, we define the spaces

$$\mathcal{V}^j = \text{span}\{F_{j,\mathbf{k}}^{S,i}, \mathbf{k} \in \mathcal{N}_j^2, i = 1, \dots, 6\} \subseteq L^2(\mathbb{S}^2).$$

Let us remark that each function $F_{j,\mathbf{k}}^{S,i}$ can be obtained from $F_{j,\mathbf{k}}^{S,1}$ by applying to it a rotation around a coordinate axis, followed or not by a reflection with respect to one of the coordinate planes. This rotation followed by reflection can be replaced by a simple rotation around one of the coordinates axes if we introduce some reflections with respect to the coordinates planes in the definition of the projection p_c . So, we can conclude that the function $G^S = (\frac{1}{a}F \circ p_c \circ p^{-1}) \cdot \chi_{\mathcal{F}_1}$ generates all the spaces \mathcal{V}_j . In the following we give some properties of the functions and spaces defined above.

Theorem 4.1 *With the above notations, the set $\{\mathcal{V}^j, j \in \mathbb{N}_0\}$ constitutes a multiresolution of $L^2(\mathbb{S}^2)$, that is, the following properties hold.*

1. $\mathcal{V}^j \subseteq \mathcal{V}^{j+1}$ for $j \in \mathbb{N}_0$,
2. $\text{clos}_{L^2(\mathbb{S}^2)} \bigcup_{j=0}^{\infty} \mathcal{V}^j = L^2(\mathbb{S}^2)$,
3. The set $\{F_{j,\mathbf{k}}^{S,i}, \mathbf{k} \in \mathcal{N}_j^2, i = 1, \dots, 6\}$ is a Riesz basis of \mathcal{V}^j for each $j \in \mathbb{N}_0$, more precisely, for all sequences $\{c_{j,\mathbf{k}}^i, \mathbf{k} \in \mathcal{N}_j^2, i = 1, \dots, 6\}$ the following inequalities hold

$$\frac{2}{3\sqrt{3}} \sum_{i=1}^6 \sum_{\mathbf{k} \in \mathcal{N}_j^2} (c_{j,\mathbf{k}}^i)^2 \leq \left\| \sum_{i=1}^6 \sum_{\mathbf{k} \in \mathcal{N}_j^2} c_{j,\mathbf{k}}^i F_{j,\mathbf{k}}^{S,i} \right\|_{L^2(\mathbb{S}^2)}^2 \leq 2 \sum_{i=1}^6 \sum_{\mathbf{k} \in \mathcal{N}_j^2} (c_{j,\mathbf{k}}^i)^2.$$

Orthonormal bases of wavelets

Before giving the construction of the spherical wavelets, we briefly remind the construction of the Haar wavelets in one and two dimensions. Let $j \in \mathbb{N}_0$ be fixed. The one-dimensional mother wavelet $\psi : [0, 1] \rightarrow \mathbb{R}$,

$$\psi(x) = \varphi(2x) - \varphi(2x - 1),$$

generates the spaces

$$W_{[0,1]}^j = \text{span}\{\psi_{j,k}, k \in \mathcal{N}_j\} \subseteq L^2([0, 1]),$$

where $\psi_{j,k} = 2^{j/2}\psi(2^j \cdot -k)$. Moreover, $\{\psi_{j,k}, k \in \mathcal{N}_j\}$ is an orthonormal basis of $W_{[0,1]}^j$ and each space $W_{[0,1]}^j$ is the orthogonal complement of $V_{[0,1]}^j$ into $V_{[0,1]}^{j+1}$:

$$V_{j+1}^{[0,1]} = V_j^{[0,1]} \oplus W_j^{[0,1]}.$$

In two dimensions, the wavelets which generate the wavelet spaces are

$$\begin{aligned}\Psi^1(x, y) &= \varphi(x)\psi(y), \\ \Psi^2(x, y) &= \psi(x)\varphi(y), \\ \Psi^3(x, y) &= \psi(x)\psi(y)\end{aligned}$$

and the wavelet spaces are given by

$$\mathbf{W}_j^{[0,1]} = \text{span}\{\Psi_{j,\mathbf{k}}^\nu, \mathbf{k} \in \mathcal{N}_j^2, \nu = 1, 2, 3\} \subseteq L^2([0, 1]^2),$$

with

$$\Psi_{j,\mathbf{k}}^\nu(x, y) = 2^j \Psi^\nu(2^j x - k_1, 2^j y - k_2), \text{ for } \mathbf{k} = (k_1, k_2) \text{ and } \nu = 1, 2, 3.$$

Each of the wavelet spaces $\mathbf{W}_{[0,1]}^j$ is the orthogonal complement of $\mathbf{V}_{[0,1]}^j$ into $\mathbf{V}_{[0,1]}^{j+1}$ and $\{\Psi_{j,\mathbf{k}}^\nu, \mathbf{k} \in \mathcal{N}_j^2, \nu = 1, 2, 3\}$ is an orthonormal basis of the space $\mathbf{W}_{[0,1]}^j$.

The construction of the spherical wavelets follows the same steps as the construction of the functions $\Phi_{j,\mathbf{k}}^{S,i}$. More precisely, the spherical “generator” wavelets $\Psi^{S,\nu} : \mathbb{S}^2 \rightarrow \mathbb{R}$ are given by

$$\Psi^{S,\nu} = \Psi^\nu \circ \Upsilon \circ p_c \circ p^{-1}, \text{ for } \nu = 1, 2, 3. \quad (4.17)$$

The expressions of $\Psi^{S,\nu}$ on each of the sets \mathcal{F}_i , $i = 1, \dots, 6$, are similar with those given in (4.14), if we take the wavelet Ψ^ν instead of the scaling function Φ .

The wavelet spaces \mathcal{W}^j are defined as

$$\mathcal{W}^j = \text{span} \left\{ \Psi_{j,\mathbf{k}}^{S,\nu,i}, \mathbf{k} \in \mathcal{N}_j^2, \nu = 1, 2, 3, i = 1, \dots, 6 \right\},$$

where, for $\mathbf{k} = (k_1, k_2)$, the functions $\Psi_{j,\mathbf{k}}^{S,\nu,i} : \mathbb{S}^2 \rightarrow \mathbb{R}$ are

$$\Psi_{j,\mathbf{k}}^{S,\nu,i} = (\Psi_{j,\mathbf{k}}^\nu \circ \Upsilon \circ p_c \circ p^{-1}) \cdot \chi_{\mathcal{F}_i}.$$

The properties of the spherical wavelets are summarized in the following theorem.

Theorem 4.2 *The spherical wavelets and wavelet spaces defined above have the following properties.*

1. For each $j \in \mathbb{N}_0$, the space \mathcal{W}^j is the orthogonal complement, with respect to the inner product $\langle \cdot, \cdot \rangle_{\mathcal{U}}$, of the space \mathcal{V}^j in the space \mathcal{V}^{j+1} , that is

$$\mathcal{V}^{j+1} = \mathcal{V}^j \oplus \mathcal{W}^j,$$

2. For all $j \in \mathbb{N}_0$, the set $\left\{ \Psi_{j,\mathbf{k}}^{S,\nu,i}, \mathbf{k} \in \mathcal{N}_j^2, \nu = 1, 2, 3, i = 1, \dots, 6 \right\}$ is an orthonormal basis of \mathcal{W}^j , with respect to the inner product $\langle \cdot, \cdot \rangle_{\mathcal{U}}$.

3. With the notations $\Psi_{-1,\mathbf{0}}^{S,1,i} = F_{0,\mathbf{0}}^{S,i}$ for $i = 1, \dots, 6$, $\mathcal{N}_{-1} = \{\mathbf{0}\}$, $w(-1) = 1$ and $w(j) = 3$ for $j \in \mathbb{N}_0$, the set

$$\left\{ \Psi_{j,\mathbf{k}}^{S,\nu,i}, \mathbf{k} \in \mathcal{N}_j^2, \nu = 1, \dots, w(j), j \in \mathbb{N}_0 \cup \{-1\}, i = 1, \dots, 6 \right\}$$

is a Riesz basis in $L^2(\mathbb{S}^2)$, more precisely, the inequalities

$$\begin{aligned} \frac{2}{3\sqrt{3}} \sum_{j=-1}^{\infty} \sum_{\mathbf{k} \in \mathcal{N}_j^2} \sum_{\nu=1}^{w(j)} \sum_{i=1}^6 (c_{j,\mathbf{k}}^{\nu,i})^2 &\leq \\ \left\| \sum_{j=-1}^{\infty} \sum_{\mathbf{k} \in \mathcal{N}_j^2} \sum_{\nu=1}^{w(j)} \sum_{i=1}^6 c_{j,\mathbf{k}}^{\nu,i} \Psi_{j,\mathbf{k}}^{S,\nu,i} \right\|_{L^2(\mathbb{S}^2)}^2 &\leq 2 \sum_{j=-1}^{\infty} \sum_{\mathbf{k} \in \mathcal{N}_j^2} \sum_{\nu=1}^{w(j)} \sum_{i=1}^6 (c_{j,\mathbf{k}}^{\nu,i})^2 \end{aligned}$$

hold for all sequences

$$\{c_{j,\mathbf{k}}^{\nu,i}, \mathbf{k} \in \mathcal{N}_j^2, \nu = 1, \dots, w(j), j \in \mathbb{N}_0 \cup \{-1\}, i = 1, \dots, 6, \} \in l^2.$$

4.2 Another weighted inner product and equivalent norms

In this section we consider a more general case, where the polyhedron is not necessarily inscribed in the sphere, we show the equivalence of the norms and we give formulas for the optimal bounds of the norm equivalence. As an immediate consequence we prove that the optimal bounds of the norm equivalence remain the same when the polyhedron is scaled or rotated around the origin O . The results are published in [106].

In Section 4.1.1 (and [92]) we did not discuss the optimality of the bounds $m_{\Pi}^T, M_{\Pi}^T, m_{\Pi}, M_{\Pi}$. It can be proven that M_{Π}^T and M_{Π} are optimal, but m_{Π}^T and m_{Π} are not. However, m_{Π}^T becomes optimal in the case when the projection of O onto the triangular face T of Π falls inside T , and therefore m_{Π} becomes optimal when this condition is fulfilled for all faces of Π .

In the following we will find bounds $m_{\Pi}^T, M_{\Pi}^T, m_{\Pi}, M_{\Pi}$ for the inequalities (4.4) in the case when the polyhedron Π is not necessarily inscribed in the sphere and we also discuss the optimality of these bounds.

Norm equivalence for convex polyhedrons containing the origin in the interior

Let Γ be a polyhedron such that $O \in \text{int}\Gamma$. As in [92], let $\langle \cdot, \cdot \rangle_{\Gamma}$ be the inner product defined by

$$\langle F, G \rangle_{\Gamma} = \sum_{T \in \mathcal{T}} \int_{p(T)} F(\eta) G(\eta) w_T(\eta) d\omega(\eta) \quad (4.18)$$

for $F, G \in L^2(\mathbb{S}^2)$ and with w_T given in (4.1). The induced norm $\|\cdot\|_{\Gamma}$ has the expression

$$\|F\|_{\Gamma} = \left(\sum_{T \in \mathcal{T}} \int_{p(T)} F^2(\eta) w_T(\eta) d\omega(\eta) \right)^{1/2}.$$

The following theorem holds.

Theorem 4.3 *In $L^2(\mathbb{S}^2)$ the norms $\|\cdot\|_{L^2(\mathbb{S}^2)}$ and $\|\cdot\|_{\Gamma}$ are equivalent and*

$$m_{\Gamma} \|F\|_{L^2(\mathbb{S}^2)}^2 \leq \|F\|_{\Gamma}^2 \leq M_{\Gamma} \|F\|_{L^2(\mathbb{S}^2)}^2, \quad (4.19)$$

for all $F \in L^2(\mathbb{S}^2)$, where $m_{\Gamma} = \min_{T \in \mathcal{T}} m_{\Gamma}^T$, $M_{\Gamma} = \max_{T \in \mathcal{T}} M_{\Gamma}^T$ and

$$m_{\Gamma}^T = \begin{cases} \frac{\text{dist}^2(O, T)}{\mathcal{A}(T)}, & \text{if the projection of } O \text{ onto } T \text{ lies inside } T, \\ \frac{\min_{P \in \mathcal{B}(T)} \text{dist}^3(O, P)}{\mathcal{A}(T) \text{dist}(O, T)}, & \text{otherwise,} \end{cases}$$

$$M_{\Gamma}^T = \frac{\max^3\{r_1^T, r_2^T, r_3^T\}}{\mathcal{A}(T) \text{dist}(O, T)}.$$

Here for a given triangle $T \in \mathcal{T}$ with vertices $P_i = (x_i, y_i, z_i)$, we use the notations $r_i^T = \text{dist}(O, P_i) = \sqrt{x_i^2 + y_i^2 + z_i^2}$, $i = 1, 2, 3$ and $\mathcal{B}(T) = \overline{P_1 P_2} \cup \overline{P_2 P_3} \cup \overline{P_3 P_1}$ for the boundary of T .

Proof. Let us fix a triangle $T \in \mathcal{T}$. We need to establish bounds for the modulus of the restriction of the function $h_T : \mathbb{S}^2 \rightarrow \mathbb{R}$,

$$h_T(\eta) = a_T\eta_1 + b_T\eta_2 + c_T\eta_3 = \begin{vmatrix} \eta_1 & \eta_2 & \eta_3 & 0 \\ x_1 & y_1 & z_1 & 1 \\ x_2 & y_2 & z_2 & 1 \\ x_3 & y_3 & z_3 & 1 \end{vmatrix}$$

to the spherical triangle $U = p(T)$. A simple calculation shows that the stationary points of the function h_T are $\pm \frac{1}{2\mathcal{A}(T)}(a_T, b_T, c_T)$ and they represent the projection of O onto the plane of the triangle T and its symmetric points with respect to O , respectively. At most one of them can be situated inside $p(T)$ and the values of h_T at these points are $\pm 2\mathcal{A}(T)$. Applying the Schwarz inequality we get

$$|a_T\eta_1 + b_T\eta_2 + c_T\eta_3| \leq \sqrt{a_T^2 + b_T^2 + c_T^2} \cdot \sqrt{\eta_1^2 + \eta_2^2 + \eta_3^2} = 2\mathcal{A}(T).$$

Therefore the stationary points are points of global maximum for the function $|h_T|$ and the maximum $2\mathcal{A}(T)$ is attained by the restriction of $|h_T|$ to U if the projection of the origin O onto the plane of the triangle T is situated inside this triangle.

In the following we focus on the function $|h_T(\eta)|^{-1}$, and we determine its minimum and the maximum, when $\eta \in p(T)$.

Minimum. If the projection of O onto T is situated inside T , as we saw above, the minimum is $(2\mathcal{A}(T))^{-1}$. If this projection is not situated inside T , the maximum is attained on the boundary of the spherical triangle U . So let us consider first an arbitrary point $S = \left(\frac{x(t)}{r(t)}, \frac{y(t)}{r(t)}, \frac{z(t)}{r(t)}\right)$ situated on the spherical edge $\widetilde{U_1U_2}$, for $t \in [0, 1]$, $x(t) = x_1 + t(x_2 - x_1)$, $y(t) = y_1 + t(y_2 - y_1)$, $z(t) = z_1 + t(z_2 - z_1)$, $r(t) = (x^2(t) + y^2(t) + z^2(t))^{1/2}$. Let us remark that $r(t)$ represents the distance from the origin to the point $p^{-1}(S) \in P_1P_2$. Evaluating the function h_T at the point S , we obtain

$$h_T\left(\frac{x(t)}{r(t)}, \frac{y(t)}{r(t)}, \frac{z(t)}{r(t)}\right) = -\frac{|d_T|}{r(t)}. \quad (4.20)$$

Hence in this case, the minimum of $|h_T|^{-1}$ is

$$\frac{1}{|d_T|} \cdot \min_{P \in T} \text{dist}(O, P) = \frac{1}{|d_T|} \cdot \min_{P \in \mathcal{B}(T)} \text{dist}(O, P).$$

In conclusion,

$$\min_{\eta \in p(T)} |h_T(\eta)|^{-1} = \begin{cases} \frac{1}{2\mathcal{A}(T)}, & \text{if the projection of } O \text{ onto } T \text{ lies inside } T, \\ \frac{\min_{P \in \mathcal{B}(T)} \text{dist}(O, P)}{2\mathcal{A}(T)\text{dist}(O, T)}, & \text{otherwise.} \end{cases} \quad (4.21)$$

Maximum. In order to determine the maximum of $|h_T(\eta)|^{-1}$, when $\eta \in p(T)$, it is enough to determine the minimum of the function $|h_T|$, restricted to the spherical triangle U . From the above considerations it follows that this minimum is attained on one of the edges of U . Taking a point on the spherical edge $\widetilde{U_1U_2}$ and using formula (4.20) we obtain

$$\max_{\eta \in \widetilde{U_1U_2}} |h_T(\eta)|^{-1} = \frac{1}{|d_T|} \max_{t \in [0, 1]} r(t) = \frac{1}{|d_T|} \max\{r_1^T, r_2^T\},$$

and similar formulas for the edges $\widetilde{U_2U_3}$ and $\widetilde{U_3U_1}$. In conclusion,

$$\max_{\eta \in p(T)} |h_T(\eta)|^{-1} = \max_{\eta \in p(B(T))} |h_T(\eta)|^{-1} = \frac{1}{|d_T|} \max\{r_1^T, r_2^T, r_3^T\}. \quad (4.22)$$

Finally, using (4.21) and (4.22), for the weight function w_T we have

$$m_\Gamma^T \leq w_T(\eta) \leq M_\Gamma^T \quad (4.23)$$

for all $\eta \in p(T)$, whence the conclusion. ■

Let us remark that in the case when Γ is a polyhedron inscribed in \mathbb{S}^2 and the projection of O onto the face T of Π lies inside T , the bounds m_Γ^T and M_Γ^T coincide with m_Γ^T and M_Γ^T obtained in [92] and given in (4.5)-(4.6), that is $m_\mathcal{U}^T = m_\Gamma^T$ and $M_\mathcal{U}^T = M_\Gamma^T$. In the case when the projection lies outside T , we have only $m_\mathcal{U}^T \leq m_\Gamma^T$ and $M_\mathcal{U}^T = M_\Gamma^T$.

Corollary 4.4 *The bounds m_Γ and M_Γ given in Theorem 4.3 are optimal, i.e.*

$$m_\Gamma = \inf_{F \in L^2(\mathbb{S}^2)} \frac{\|F\|_\Gamma^2}{\|F\|_{L^2(\mathbb{S}^2)}^2} \quad \text{and} \quad M_\Gamma = \sup_{F \in L^2(\mathbb{S}^2)} \frac{\|F\|_\Gamma^2}{\|F\|_{L^2(\mathbb{S}^2)}^2}. \quad (4.24)$$

Proof. We prove only the first equality in (4.24), since similar arguments can be used for proving the second one. More precisely, we will show that, for every $\varepsilon > 0$, there exists a function $F_\varepsilon \in L^2(\mathbb{S}^2)$ such that

$$\frac{\|F_\varepsilon\|_\Gamma^2}{\|F_\varepsilon\|_{L^2(\mathbb{S}^2)}^2} \leq m_\Gamma + \varepsilon.$$

Let T_k denote a triangular face of Γ for which $m_\Gamma^{T_k} = m_\Gamma$ and let $\tilde{\eta} \in U_k = p(T_k)$ such that $w_{T_k}(\tilde{\eta}) = m_\Gamma^{T_k}$.

Let $\varepsilon > 0$. Then, by the continuity of w_{T_k} , there exists $\delta > 0$ such that

$$w_{T_k}(\eta) \leq m_\Gamma + \varepsilon, \quad \text{whenever} \quad \eta \in D = U_k \cap \overline{B}(\tilde{\eta}, \delta). \quad (4.25)$$

Here $\overline{B}(x_0, r) = \{x \in \mathbb{R}^3, \text{dist}(x_0, x) \leq r\}$ denotes the closed Euclidean ball of radius r , centered at $x_0 \in \mathbb{R}^3$. For the function $F = \chi_D \in L^2(\mathbb{R}^3)$ (the characteristic function of D), we have

$$\frac{\|F\|_\Gamma^2}{\|F\|_{L^2(\mathbb{S}^2)}^2} = \frac{\int_D w_{T_k}(\eta) d\omega(\eta)}{\int_D d\omega(\eta)} = w_{T_k}(\eta^*) \leq m_\Gamma + \varepsilon,$$

where the existence of $\eta^* \in D$ is assured by the mean theorem applied to the continuous function w_{T_k} on the domain D , and the last inequality follows from (4.25) for $\eta = \eta^* \in D$.

In conclusion, m_Γ is an optimal bound. ■

The question which arises is how the constants m_Γ and M_Γ in the relation expressing the norm equivalence change, if the polyhedron Γ is rotated and scaled.

We consider the following families of polyhedrons associated to Γ :

$$\begin{aligned} \mathcal{R}_\Gamma &= \text{the set of polyhedrons obtained by rotating } \Gamma \text{ around } O, \\ \mathcal{D}_\Gamma &= \text{the set of polyhedrons obtained by scaling } \Gamma \text{ with a factor } \alpha > 0. \end{aligned}$$

For the polyhedrons in $\mathcal{R}_\Gamma \cup \mathcal{D}_\Gamma$ we prove the following theorem.

Theorem 4.5 *Let Γ be a convex polyhedron with $O \in \text{int } \Gamma$. Let m_Γ, M_Γ be given as in Theorem 4.3. Then, for arbitrary $\Gamma' \in \mathcal{R}_\Gamma \cup \mathcal{D}_\Gamma$, the norm $\|\cdot\|_{\Gamma'}$ on $L^2(\mathbb{S}^2)$ defined in the same way as in (4.18) is equivalent to the usual norm of $L^2(\mathbb{S}^2)$. Moreover, if $m_{\Gamma'}$ and $M_{\Gamma'}$ are defined for Γ' as in Theorem 4.3, then $m_{\Gamma'} = m_\Gamma$, $M_{\Gamma'} = M_\Gamma$, and $m_{\Gamma'}$, $M_{\Gamma'}$ are optimal bounds in the inequalities*

$$m_{\Gamma'} \|\cdot\|_{L^2(\mathbb{S}^2)}^2 \leq \|\cdot\|_{\Gamma'}^2 \leq M_{\Gamma'} \|\cdot\|_{L^2(\mathbb{S}^2)}^2.$$

Proof. Clearly $\mathcal{A}(T)$, $\text{dist}(O, P)$ and $\text{dist}(O, T)$ in Theorem 4.3 are invariant with respect to rotations around O , therefore m_Γ and M_Γ rest unchanged. Further, for $\alpha > 0$ let

$$\Gamma_\alpha = \{\alpha \cdot x, x \in \Gamma\} \in \mathcal{D}_\Gamma$$

be a scaled version of Γ . If T_α denotes an arbitrary face of Γ_α , then it is immediate that

$$\begin{aligned} d_{T_\alpha} &= \alpha^3 d_T, \\ a(T_\alpha) &= \alpha^2 \mathcal{A}(T), \\ \text{dist}(O, T_\alpha) &= \alpha \text{dist}(O, T), \\ \min_{P_\alpha \in \mathcal{B}(T_\alpha)} \text{dist}(O, P_\alpha) &= \alpha \min_{P \in \mathcal{B}(T)} \text{dist}(O, P). \end{aligned}$$

In conclusion $m_{\Gamma_\alpha} = m_\Gamma$, $M_{\Gamma_\alpha} = M_\Gamma$ and

$$m_\Gamma \|F\|_{L^2(\mathbb{S}^2)}^2 \leq \|F\|_{\Gamma_\alpha}^2 \leq M_\Gamma \|F\|_{L^2(\mathbb{S}^2)}^2,$$

for all $F \in L^2(\mathbb{S}^2)$. Thus the theorem is proved. ■

Possible applications

In our previous work [92, 93, 99] we used the norm equivalence (4.4), which was generalized in this section, in order to move some constructions of wavelets from bounded domains of \mathbb{R}^2 to the sphere. In this way we constructed locally supported wavelets bases on spherical triangulations. Orthogonality with respect to the usual inner product in $L^2(\mathbb{S}^2)$ turns into orthogonality with respect to the inner product $\langle \cdot, \cdot \rangle_\Gamma$ associated to the polyhedron. The most important fact is that the decomposition and reconstruction matrices are the same in the planar and spherical cases. Thus, if a matrix involved in algorithms for \mathbb{R}^2 is orthogonal (resp. sparse), the same holds for the algorithms for \mathbb{S}^2 . The result of this section allows us to use for the sphere the results (especially regarding orthogonal wavelets) from the bounded planar domains, by considering an arbitrary convex polyhedron which satisfies minimal conditions. A review of possible approaches is presented in [98].

As shown in [93], this norm equivalence yields a mathematical proof for some constructions of wavelets on \mathbb{S}^2 , where the authors called the wavelets “nearly orthogonal” and made some approximations without studying their effects [17, 81]. It also allows us to enlarge the class of wavelets obtained in [17, 81].

A major advantage is the avoidance of distortions and singularities around the poles. This fact is nontrivial; a striking example is given by the constructions of spherical wavelets starting from periodic wavelets on $[0, \pi] \times [0, 2\pi]$ using classical spherical coordinates. Here one has to “fit” the wavelets on one meridian and a major disadvantage is the occurrence of singularities around the poles.

4.3 Wavelets on sphere-like surfaces

In this section we generalize the construction in Section 4.1 to closed surfaces, finding conditions which have to be satisfied by a closed surface to assure the Riesz stability of the wavelets. The results presented in this section are published in [94].

Consider the surface $\mathcal{S} \subseteq \mathbb{R}^3$ defined by the function $\sigma : \mathbb{S}^2 \rightarrow \mathbb{R}^3$,

$$\sigma(\eta) = \rho(\eta)\eta, \quad (4.26)$$

for all $\eta \in \mathbb{S}^2$, where $\rho : \mathbb{S}^2 \rightarrow \mathbb{R}_+$ is a continuous function. Such a closed surface is called *sphere-like surface*. We will need the inverse of σ , so we will consider $\sigma : \mathbb{S}^2 \rightarrow \mathcal{S}$, and $\sigma^{-1}(\xi)$ will be the unit vector starting at the origin, with the direction of ξ .

We intend to transport any of the wavelet bases on spherical triangulations. Actually, we try to find conditions which have to be satisfied by the function ρ to ensure the Riesz stability of these wavelets.

With the notations from Section 4.1, we project the spherical triangulations \mathcal{U}^j onto the surface \mathcal{S} , obtaining the triangulations $\mathcal{Z}^j = \{\sigma(U^j), U^j \in \mathcal{U}^j\}$ of the closed surface \mathcal{S} . For a fixed j , to each scaling function φ_k^j and wavelet ψ_k^j defined on \mathbb{S}^2 , we can associate a scaling function $\widetilde{\varphi}_k^j$ and a wavelet $\widetilde{\psi}_k^j$, defined on \mathcal{S} , in the following way:

$$\widetilde{\varphi}_k^j = \varphi_k^j \circ \sigma^{-1}, \quad \widetilde{\psi}_k^j = \psi_k^j \circ \sigma^{-1}. \quad (4.27)$$

Before we establish the orthogonality of these functions defined on \mathcal{S} , or their Riesz stability, we need to establish some equivalencies between norms.

4.3.1 Inner products and norms in $L^2(\mathcal{S})$

Consider the following parametrization of the sphere \mathbb{S}^2

$$\eta(x, y, z) \in \mathbb{S}^2 \Leftrightarrow \begin{cases} x = x(u, v) = \sin v \cos u, \\ y = y(u, v) = \sin v \sin u, \\ z = z(u, v) = \cos v, \end{cases} \quad (4.28)$$

$(u, v) \in \overline{\Delta} = [0, 2\pi] \times [0, \pi]$. Then we define the functions $r : \overline{\Delta} \rightarrow (0, \infty)$ and $X, Y, Z : \overline{\Delta} \rightarrow \mathbb{R}$ by

$$\begin{aligned} r(u, v) &= \rho(\sin v \cos u, \sin v \sin u, \cos v), \\ X(u, v) &= r(u, v)x(u, v), \\ Y(u, v) &= r(u, v)y(u, v), \\ Z(u, v) &= r(u, v)z(u, v). \end{aligned} \quad (4.29)$$

The following proposition establishes the relation between the surface element of the sphere and the surface element of \mathcal{S} .

Proposition 4.6 *Let $d\omega$ be the surface element of \mathbb{S}^2 and $d\sigma$ be the surface element of \mathcal{S} . Then, the relation between $d\omega$ and $d\sigma$ is*

$$d\sigma^2 = r^2 \left(r^2 + r_u^2 + \frac{r_u^2}{\sin^2 v} \right) d\omega^2, \quad (4.30)$$

where $r = r(u, v)$ is defined in (4.29) and $r_u, r_v : \Delta = (0, 2\pi) \times (0, \pi) \rightarrow \mathbb{R}$ denote its partial derivatives.

Proof. Let us denote

$$\begin{aligned}\eta(u, v) &= (x(u, v), y(u, v), z(u, v)), \\ R(u, v) &= (X(u, v), Y(u, v), Z(u, v)).\end{aligned}$$

An immediate calculation shows that

$$\begin{aligned}d\omega &= \|\eta_u \times \eta_v\| du dv = \sin v du dv, \\ d\sigma &= \|R_u \times R_v\| du dv = r \sin v \left(r^2 + r_v^2 + \frac{r_u^2}{\sin^2 v} \right)^{1/2} du dv,\end{aligned}$$

where $\|\cdot\|$ denotes the Euclidian norm and $u \times v$ stands for the cross product of the vectors u and v in \mathbb{R}^3 . Therefore

$$d\sigma = E(u, v)d\omega,$$

where $E : (0, 2\pi) \times (0, \pi) \rightarrow \mathbb{R}$,

$$E(u, v) = r \left(r^2 + r_v^2 + \frac{r_u^2}{\sin^2 v} \right)^{1/2}. \quad (4.31)$$

■

Definition 4.1 Let $F, G : \mathcal{S} \rightarrow \mathbb{R}$ be functions of $L^2(\mathcal{S})$. Then $\langle \cdot, \cdot \rangle_\sigma : L^2(\mathcal{S}) \times L^2(\mathcal{S}) \rightarrow \mathbb{R}$ defined by

$$\langle F, G \rangle_\sigma = \langle F \circ \sigma, G \circ \sigma \rangle_{L^2(\mathbb{S}^2)} \quad (4.32)$$

is an inner product in $L^2(\mathcal{S})$. We also consider the induced norm

$$\|\cdot\|_\sigma = \langle \cdot, \cdot \rangle_\sigma^{1/2}. \quad (4.33)$$

Regarding this norm, the following norm-equivalency is true.

Proposition 4.7 If there exist the constants $0 < m_\sigma \leq M_\sigma < \infty$ such that $m_\sigma \leq E(u, v) \leq M_\sigma$ for all $(u, v) \in \Delta$, then in $L^2(\mathcal{S})$ the norm $\|\cdot\|_{L^2(\mathcal{S})}$ is equivalent to the norm $\|\cdot\|_\sigma$.

Proof. Let $F \in L^2(\mathcal{S})$. We have

$$\begin{aligned}\|F\|_{L^2(\mathcal{S})}^2 &= \int_{\mathcal{S}} F^2(\zeta) d\sigma = \int_{\mathcal{S}} F^2(\rho(\eta)\eta) d\sigma \\ &= \iint_{\Delta} F^2(X(u, v), Y(u, v), Z(u, v)) E(u, v) \sin v du dv.\end{aligned}$$

Taking into account the inequalities $m_\sigma \leq E(u, v) \leq M_\sigma$ for $(u, v) \in \Delta$, we can write

$$\begin{aligned}m_\sigma \iint_{\Delta} F^2(X(u, v), Y(u, v), Z(u, v)) \sin v du dv &\leq \|F\|_{L^2(\mathcal{S})}^2 \leq \\ &\leq M_\sigma \iint_{\Delta} F^2(X(u, v), Y(u, v), Z(u, v)) \sin v du dv,\end{aligned}$$

and therefore

$$\begin{aligned}m_\sigma \int_{\mathbb{S}^2} F^2(\sigma(\eta)) d\omega &\leq \|F\|_{L^2(\mathcal{S})}^2 \leq M_\sigma \int_{\mathbb{S}^2} F^2(\sigma(\eta)) d\omega, \\ m_\sigma \|F \circ \sigma\|_{L^2(\mathbb{S}^2)}^2 &\leq \|F\|_{L^2(\mathcal{S})}^2 \leq M_\sigma \|F \circ \sigma\|_{L^2(\mathbb{S}^2)}^2.\end{aligned}$$

which means

$$\sqrt{m_\sigma} \|F\|_\sigma \leq \|F\|_{L^2(\mathcal{S})} \leq \sqrt{M_\sigma} \|F\|_\sigma. \quad (4.34)$$

■

Definition 4.2 Let $F, G : \mathcal{S} \rightarrow \mathbb{R}$ and let $\langle \cdot, \cdot \rangle_\Gamma$ be a scalar product in $L^2(\mathbb{S}^2)$ defined in (4.2) (or more general in (4.18)), associated to a polyhedron Γ . Then $\langle \cdot, \cdot \rangle_{\Gamma, \sigma} : L^2(\mathcal{S}) \times L^2(\mathcal{S}) \rightarrow \mathbb{R}$ defined by

$$\langle F, G \rangle_{\Gamma, \sigma} = \langle F \circ \sigma, G \circ \sigma \rangle_\Gamma \quad (4.35)$$

is an inner product in $L^2(\mathcal{S})$. We also consider the induced norm

$$\|\cdot\|_{\Gamma, \sigma} = \langle \cdot, \cdot \rangle_\sigma^{1/2}. \quad (4.36)$$

Proposition 4.8 In $L^2(\mathcal{S})$ the norm $\|\cdot\|_\sigma$ is equivalent to the norm $\|\cdot\|_{\Gamma, \sigma}$.

Proof. Let $F \in L^2(\mathcal{S})$. Then $\|F\|_{\Gamma, \sigma}^2 = \|F \circ \sigma\|_\Gamma^2$. Using now the inequalities (4.19) we can write

$$m_\Gamma \|F \circ \sigma\|_{L^2(\mathbb{S}^2)}^2 \leq \|F\|_{\Gamma, \sigma}^2 \leq M_\Gamma \|F \circ \sigma\|_{L^2(\mathbb{S}^2)}^2$$

and therefore, using the definition 4.1 we obtain

$$m_\Gamma \|F\|_\sigma^2 \leq \|F\|_{\Gamma, \sigma}^2 \leq M_\Gamma \|F\|_\sigma^2,$$

which completes the proof. ■

4.3.2 Orthogonality and Riesz stability

The relations between norms and scalar products established in the previous section allow us to establish the following results.

Proposition 4.9 Let \mathcal{I} be a finite or infinite set of indices. If the set $\{f_i, i \in \mathcal{I}\} \subset L^2(\mathbb{S}^2)$ is orthonormal with respect to the scalar product $\langle \cdot, \cdot \rangle_\Gamma$, then the set $\{f_i \circ \sigma^{-1}, i \in \mathcal{I}\} \subset L^2(\mathcal{S})$ is orthonormal with respect to the scalar product $\langle \cdot, \cdot \rangle_{\sigma, \Gamma}$.

This allows us to construct orthonormal bases of wavelets defined on \mathcal{S} , starting from orthonormal bases of wavelets defined on \mathbb{S}^2 . We remind that, even though the orthogonality is not with respect to the usual scalar product of $L^2(\mathbb{S}^2)$, the matrices involved in decomposition and reconstruction algorithm are orthogonal, and this is the important fact that assures fast and stable algorithms.

Proposition 4.10 Let \mathcal{I} be a finite set of indices and let $\{f_i, i \in \mathcal{I}\} \subset L^2(\mathbb{S}^2)$ be a set satisfying the Riesz stability conditions

$$m \sum_{i \in \mathcal{I}} c_i^2 \leq \left\| \sum_{i \in \mathcal{I}} c_i f_i \right\|_{L^2(\mathbb{S}^2)}^2 \leq M \sum_{i \in \mathcal{I}} c_i^2, \quad \text{for all } c_i \in \mathbb{R}. \quad (4.37)$$

If the numbers $m_\sigma = \min_{(u,v) \in \Delta} E(u,v)$ and $M_\sigma = \max_{(u,v) \in \Delta} E(u,v)$ are such that $m_\sigma > 0$ and $M_\sigma < \infty$, then the set $\{f_i \circ \sigma^{-1}, i \in \mathcal{I}\} \subset L^2(\mathcal{S})$ satisfy the Riesz stability property

$$m_\sigma m \sum_{i \in \mathcal{I}} c_i^2 \leq \left\| \sum_{i \in \mathcal{I}} c_i (f_i \circ \sigma^{-1}) \right\|_{L^2(\mathcal{S})}^2 \leq M_\sigma M \sum_{i \in \mathcal{I}} c_i^2.$$

Proof. We use (4.34) for $F = \sum_{i \in \mathcal{I}} c_i (f_i \circ \sigma^{-1})$ and we obtain

$$m_\sigma \left\| \sum_{i \in \mathcal{I}} c_i (f_i \circ \sigma^{-1}) \right\|_\sigma^2 \leq \left\| \sum_{i \in \mathcal{I}} c_i (f_i \circ \sigma^{-1}) \right\|_{L^2(\mathcal{S})}^2 \leq M_\sigma \left\| \sum_{i \in \mathcal{I}} c_i (f_i \circ \sigma^{-1}) \right\|_\sigma^2.$$

From the definition (4.33) of the norm $\|\cdot\|_\sigma$ we obtain

$$m_\sigma \left\| \sum_{i \in \mathcal{I}} c_i f_i \right\|_{L^2(\mathbb{S}^2)}^2 \leq \left\| \sum_{i \in \mathcal{I}} c_i (f_i \circ \sigma^{-1}) \right\|_{L^2(\mathcal{S})}^2 \leq M_\sigma \left\| \sum_{i \in \mathcal{I}} c_i f_i \right\|_{L^2(\mathbb{S}^2)}^2,$$

and finally the conclusion follows immediately using the hypothesis (4.37). ■

4.3.3 Some closed surfaces which assure the Riesz stability in $L^2(\mathcal{S})$

The question is now: *how should we choose the function ρ such that the hypotheses of Proposition 4.10 are satisfied.*

The supposition we have already made was that the function r defined in (4.29) is continuous and has partial derivatives on $\Delta = (0, 2\pi) \times (0, \pi)$. We want to see how the functions ρ or r should be taken to assure the boundness of the function $E : \Delta \rightarrow \mathbb{R}$,

$$E(u, v) = r \left(r^2 + r_v^2 + \frac{r_u^2}{\sin^2 v} \right)^{1/2}.$$

A natural choice is the following.

Proposition 4.11 *Let $\Omega \subseteq \mathbb{R}^3$ be a domain such that $\mathbb{S}^2 \subseteq \text{int}\Omega$. If the function $\rho : \Omega \rightarrow (0, \infty)$ is such that $\rho \in C^1(\Omega)$, then the function E is bounded on Δ .*

Proof. Let m_0, M_0, M_1 be real positive numbers such that

$$\begin{aligned} m_0 &\leq \rho(\eta) \leq M_0, \\ \max \{ |\rho_x(\eta)|, |\rho_y(\eta)|, |\rho_z(\eta)| \} &\leq M_1, \end{aligned}$$

for all $\eta \in \mathbb{S}^2$. Here ρ_x, ρ_y, ρ_z denote the partial derivatives of the function ρ . Evaluating r_v and r_u we obtain

$$\begin{aligned} r_v &= \rho_x \cos v \cos u + \rho_y \cos v \sin u - \rho_z \sin v, \\ \frac{r_u}{\sin v} &= -\rho_x \sin u + \rho_y \cos u, \end{aligned}$$

and further, using the Cauchy-Schwarz inequality we have

$$\begin{aligned} r_v^2 &\leq (\rho_x^2 + \rho_y^2 + \rho_z^2) (\cos^2 u \cos^2 v + \cos^2 v \sin^2 u + \sin^2 v) = \rho_x^2 + \rho_y^2 + \rho_z^2, \\ \left(\frac{r_u}{\sin v} \right)^2 &\leq (\rho_x^2 + \rho_y^2) (\sin^2 u + \cos^2 u) = \rho_x^2 + \rho_y^2. \end{aligned}$$

With these inequalities we finally get

$$m_0^2 \leq E(u, v) \leq M_0 \sqrt{M_0^2 + 5M_1^2}, \text{ for all } (u, v) \in \Delta.$$

■

4.4 Locally supported wavelet bases on the sphere via stereographic projection

The stereographic projection determines a bijection between the two-sphere, minus the North Pole, and the tangent plane at the South Pole. This correspondence induces a unitary map between the corresponding L^2 spaces. This map in turn leads to an equivalence between the continuous wavelet transform formalisms on the plane and on the sphere. More precisely, any plane wavelet may be lifted, by inverse stereographic projection, to a wavelet on the sphere. In this section we apply this procedure to orthogonal compactly supported wavelet bases in the plane and we get continuous, locally supported orthogonal wavelet bases on the sphere. As applications, we give three examples. In the first two examples, we perform a singularity

detection, including one where other existing constructions of spherical wavelet bases fail. In the third example, we show the importance of the local support, by comparing our construction with the one based on kernels of spherical harmonics. The results are published in [105].

For an efficient wavelet analysis of signals or images, including on the sphere, the following properties are desirable (a thorough discussion of this topic may be found in [7]):

- *Basis*: The redundancy of the frames leads to nonunique expansions. Moreover, the existing constructions of spherical frames (see for instance [13, 89]) are computationally heavy and often applicable only to band-limited functions. In particular, for the compression of large data sets, it is essential to have wavelet bases, not frames.
- *Orthogonality*: This is the most economical method since it leads to orthogonal reconstruction matrices. The inversion of such matrices, needed for example in data compression, is trivial (the inverse equals the adjoint). Thus, orthogonal bases are ideal for compression, but this is not always sufficient: sparsity of reconstruction matrices is still needed in the case of large data sets. We should also mention that orthogonality of a wavelet basis can be easily achieved by a Gram-Schmidt procedure, but the locality of the support is usually lost.
- *Local support*: A wavelet has *local support* if it vanishes identically outside a small region. It is *localized* if it is negligible outside a small region, so that it may have (small, but nonzero) “tails” there. Since these tails may spread in the process of approximation of data and spoil their good localization properties, local support is definitely preferred (see the example in Figure 4.8). More important, local support is crucial when working with large data sets, since it yields sparse matrices.
- *Continuity, smoothness*: These properties are always desirable in approximation, but not easily achieved.

There are many constructions in the literature that fulfil at least one of the properties above, so we have to restrict ourselves by mentioning only some of them. In [73, 31, 46, 131], smooth wavelet bases were obtained by different approaches. Besides smoothness, the wavelets constructed in [46] have local support. Orthogonal, smooth and localized (but not locally supported) wavelets were constructed in [80]. In [92, 98, 99], by making use of a radial projection, one has obtained either continuous, semi-orthogonal, locally supported wavelet bases, or piecewise constant orthogonal locally supported wavelet bases.

However, none of these methods so far has led to wavelet bases on the sphere which are *simultaneously* continuous (or smoother), orthogonal and locally supported. The aim of the present construction is precisely to fill this gap. The method we propose consists in lifting wavelets from the tangent plane to the sphere by inverse stereographic projection. It yields simultaneously smoothness, orthogonality, local support, vanishing moments. The disadvantage is that it could entail distortions around the North Pole N . Of course, mathematically the construction presented here applies to the pointed sphere $\mathbb{S}^2 := \mathbb{S}^2 \setminus \{N\}$ (and therefore we have to avoid the data around the North Pole N), but in practice this situation is harmless. Indeed, we can choose N in a region where there are no relevant data. To give an example, European climatologists routinely put the North Pole of their spherical grid in the middle of the Pacific Ocean. Actually, most of the spherical data are given in polar coordinates not containing information at the poles.

To summarize our work, we aim at detecting and quantizing *local* singularities in data, at *small* scales. This is, from the practical point of view, the main purpose of wavelet analysis. We will come back to this point in Section 4.4.3 below.

4.4.1 Preliminaries

We consider the unit sphere $\mathbb{S}^2 = \{(\eta_1, \eta_2, \eta_3) \in \mathbb{R}^3, \eta_1^2 + \eta_2^2 + (\eta_3 - 1)^2 = 1\}$ and the pointed sphere $\dot{\mathbb{S}}^2 = \mathbb{S}^2 \setminus \{(0, 0, 2)\}$, with the parametrization

$$\begin{aligned}\eta_1 &= \cos \varphi \sin \theta, \\ \eta_2 &= \sin \varphi \sin \theta, \quad \theta \in (0, \pi], \varphi \in [0, 2\pi). \\ \eta_3 &= 1 + \cos \theta,\end{aligned}$$

Let $\mathbf{p} : \dot{\mathbb{S}}^2 \rightarrow \mathbb{R}^2$ denote the stereographic projection from the North Pole $N(0, 0, 2)$ and let $\nu : \dot{\mathbb{S}}^2 \rightarrow \mathbb{R}$, $\varrho : \mathbb{R}^2 \rightarrow \mathbb{R}$ be defined as

$$\begin{aligned}\nu(\boldsymbol{\eta}) &= \frac{2}{2 - \eta_3}, \quad \text{for all } \boldsymbol{\eta} = (\eta_1, \eta_2, \eta_3) \in \dot{\mathbb{S}}^2, \\ \varrho(\mathbf{x}) &= \frac{4}{x^2 + y^2 + 4}, \quad \text{for all } \mathbf{x} = (x, y) \in \mathbb{R}^2,\end{aligned}$$

respectively. The relations between $\boldsymbol{\eta}$ and $\mathbf{x} = \mathbf{p}(\boldsymbol{\eta})$ are

$$\begin{aligned}x &= 2 \cot \frac{\theta}{2} \cos \varphi = \eta_1 \nu(\boldsymbol{\eta}), \\ y &= 2 \cot \frac{\theta}{2} \sin \varphi = \eta_2 \nu(\boldsymbol{\eta}),\end{aligned}$$

and

$$\begin{aligned}\eta_1 &= x \varrho(\mathbf{x}), \\ \eta_2 &= y \varrho(\mathbf{x}), \\ \eta_3 &= \frac{1}{2}(x^2 + y^2) \varrho(\mathbf{x}).\end{aligned}$$

Then it is easy to prove the following relations between $d\mathbf{x} = dx dy$, the area element of \mathbb{R}^2 , and $d\omega(\boldsymbol{\eta})$, the area element of \mathbb{S}^2 :

$$\begin{aligned}d\mathbf{x} &= \nu(\boldsymbol{\eta})^2 d\omega(\boldsymbol{\eta}), \\ d\omega(\boldsymbol{\eta}) &= \varrho(\mathbf{x})^2 d\mathbf{x}.\end{aligned}$$

For simplicity, we write $L^2(\dot{\mathbb{S}}^2) = L^2(\dot{\mathbb{S}}^2, d\omega(\boldsymbol{\eta})) (= L^2(\mathbb{S}^2))$, since the set $\{N\}$ is of measure zero) and $L^2(\mathbb{R}^2) = L^2(\mathbb{R}^2, d\mathbf{x})$. Then we consider the map $\pi : L^2(\dot{\mathbb{S}}^2) \rightarrow L^2(\mathbb{R}^2)$ induced by the stereographic projection, namely,

$$[\pi \mathcal{F}](\mathbf{x}) = \varrho(\mathbf{x}) \mathcal{F}(\mathbf{p}^{-1}(\mathbf{x})), \quad \text{for all } \mathcal{F} \in L^2(\dot{\mathbb{S}}^2)$$

and its inverse $\pi^{-1} : L^2(\mathbb{R}^2) \rightarrow L^2(\dot{\mathbb{S}}^2)$,

$$[\pi^{-1} F](\boldsymbol{\eta}) = \nu(\boldsymbol{\eta}) F(\mathbf{p}(\boldsymbol{\eta})), \quad \text{for all } F \in L^2(\mathbb{R}^2).$$

It is well known that π is a unitary map, whence

$$\begin{aligned}\langle \pi \mathcal{F}, \pi \mathcal{G} \rangle_{L^2(\mathbb{R}^2)} &= \langle \mathcal{F}, \mathcal{G} \rangle_{L^2(\dot{\mathbb{S}}^2)}, \\ \langle \pi^{-1} F, \pi^{-1} G \rangle_{L^2(\dot{\mathbb{S}}^2)} &= \langle F, G \rangle_{L^2(\mathbb{R}^2)},\end{aligned}$$

or, equivalently,

$$\langle \mathcal{F}, \mathcal{G} \rangle_{L^2(\dot{\mathbb{S}}^2)} = \langle \varrho \cdot (\mathcal{F} \circ \mathbf{p}^{-1}), \varrho \cdot (\mathcal{G} \circ \mathbf{p}^{-1}) \rangle_{L^2(\mathbb{R}^2)}, \quad (4.38)$$

$$\langle F, G \rangle_{L^2(\mathbb{R}^2)} = \langle \nu \cdot (F \circ \mathbf{p}), \nu \cdot (G \circ \mathbf{p}) \rangle_{L^2(\dot{\mathbb{S}}^2)}, \quad (4.39)$$

for all $\mathcal{F}, \mathcal{G} \in L^2(\dot{\mathbb{S}}^2)$, $F, G \in L^2(\mathbb{R}^2)$. The last equality allows us to construct orthogonal bases on $L^2(\dot{\mathbb{S}}^2)$ starting from orthogonal bases in $L^2(\mathbb{R}^2)$. More precisely, we will use the fact that, if the functions $F, G \in L^2(\mathbb{R}^2)$ are orthogonal, then the functions $\mathcal{F} = \nu \cdot (F \circ \mathbf{p})$ and $\mathcal{G} = \nu \cdot (G \circ \mathbf{p})$ will be orthogonal in $L^2(\dot{\mathbb{S}}^2)$.

4.4.2 Multiresolution analysis (MRA) and wavelet bases of $L^2(\dot{\mathbb{S}}^2)$

In order to fix our notations, we will briefly review in this section the standard construction of 2D orthonormal wavelet bases in the flat case, starting from a multiresolution analysis (MRA) [70].

Let D be a 2×2 regular matrix with the properties

- (a) $D\mathbb{Z}^2 \subset \mathbb{Z}^2$, which is equivalent to the fact that D has integer entries,
- (b) $\lambda \in \sigma(D) \implies |\lambda| > 1$, that is, all eigenvalues of D have modulus greater than 1.

A multiresolution analysis of $L^2(\mathbb{R}^2)$ associated to D is an increasing sequence of closed subspaces $\mathbf{V}_j \subset L^2(\mathbb{R}^2)$ with $\bigcap_{j \in \mathbb{Z}} \mathbf{V}_j = \{0\}$ and $\bigcup_{j \in \mathbb{Z}} \mathbf{V}_j = L^2(\mathbb{R}^2)$, and satisfying the following conditions:

- (1) $f \in \mathbf{V}_j \iff f(D \cdot) \in \mathbf{V}_{j+1}$,
- (2) There exists a function $\Phi \in L^2(\mathbb{R}^2)$ such that the set $\{\Phi(\cdot - \mathbf{k}), \mathbf{k} \in \mathbb{Z}^2\}$ is an orthonormal basis of \mathbf{V}_0 .

As a consequence, $\{\Phi_{j,\mathbf{k}} := |\det D|^{j/2} \Phi(D^j \cdot - \mathbf{k}), \mathbf{k} \in \mathbb{Z}^2\}$ is an orthonormal basis for \mathbf{V}_j .

For each $j \in \mathbb{Z}$, let us define the space \mathbf{W}_j as the orthogonal complement of \mathbf{V}_j into \mathbf{V}_{j+1} , i.e., $\mathbf{V}_{j+1} = \mathbf{V}_j \oplus \mathbf{W}_j$. The two-dimensional wavelets are those functions which span \mathbf{W}_0 . One can prove (see [76]) that there exist $q = |\det D| - 1$ wavelets ${}^1\Psi, {}^2\Psi, \dots, {}^q\Psi \in \mathbf{V}_1$ that generate an orthonormal basis of \mathbf{W}_0 . Therefore, $\{{}^\lambda\Psi_{j,\mathbf{k}} := |\det D|^{j/2} \cdot {}^\lambda\Psi(D^j \cdot - \mathbf{k}), \lambda = 1, \dots, q, \mathbf{k} \in \mathbb{Z}^2\}$ is an orthonormal basis of \mathbf{W}_j for each j , and $\{{}^\lambda\Psi_{j,\mathbf{k}}, \lambda = 1, \dots, q, \mathbf{k} \in \mathbb{Z}^2, j \in \mathbb{Z}\}$ is an orthonormal basis of $L^2(\mathbb{R}^2)$.

A particular case is that of tensor product wavelets, corresponding to the dilation matrix $D = \text{diag}[2, 2]$ and a 1-D MRA with scaling function and mother wavelet ϕ, ψ . In this case, $q = 3$ and one gets the 2D scaling function $\Phi(x, y) = \phi(x)\phi(y)$ and the three wavelets

$${}^h\Psi(x, y) = \phi(x)\psi(y), \quad {}^v\Psi(x, y) = \psi(x)\phi(y), \quad {}^d\Psi(x, y) = \psi(x)\psi(y).$$

If the one-dimensional functions ϕ and ψ have compact support, then obviously so have Φ and ${}^\lambda\Psi$. This is the case of the well-known Daubechies wavelets *dbn* that we will use in the sequel.

The construction of multiresolution analysis and wavelet bases in $L^2(\dot{\mathbb{S}}^2)$ is based on the equality (4.39). To every function $F \in L^2(\mathbb{R}^2)$, one can associate the function $F^s \in L^2(\dot{\mathbb{S}}^2)$ as

$$F^s = \nu \cdot (F \circ \mathbf{p}). \quad (4.40)$$

In particular, if the functions $\{F_{j,\mathbf{k}}\}_{j,\mathbf{k}}$ are orthogonal, so are

$$F_{j,\mathbf{k}}^s = \nu \cdot (F_{j,\mathbf{k}} \circ \mathbf{p}), \text{ for } j \in \mathbb{Z}, \mathbf{k} \in \mathbb{Z}^2. \quad (4.41)$$

Then, taking $F = \Phi$ and $F = \Psi$, we obtain the spherical functions

$$\Phi_{j,\mathbf{k}}^s = \nu \cdot (\Phi_{j,\mathbf{k}} \circ \mathbf{p}), \quad {}^\lambda \Psi_{j,\mathbf{k}}^s = \nu \cdot ({}^\lambda \Psi_{j,\mathbf{k}} \circ \mathbf{p}). \quad (4.42)$$

For $j \in \mathbb{Z}$, we define the spaces \mathcal{V}_j as

$$\mathcal{V}_j = \{\nu \cdot (F \circ \mathbf{p}), F \in \mathbf{V}_j\}. \quad (4.43)$$

Using (4.39) and the unitarity of the map π , it is immediate that \mathcal{V}_j is a closed subspace of $L^2(\dot{\mathbb{S}}^2)$, thus a Hilbert space. Moreover, these spaces have the following properties:

- (1) $\mathcal{V}_j \subset \mathcal{V}_{j+1}$ for $j \in \mathbb{Z}$,
- (2) $\bigcap_{j \in \mathbb{Z}} \mathcal{V}_j = \{0\}$ and $\overline{\bigcup_{j \in \mathbb{Z}} \mathcal{V}_j} = L^2(\dot{\mathbb{S}}^2)$,
- (3) The set $\{\Phi_{0,\mathbf{k}}^s, \mathbf{k} \in \mathbb{Z}^2\}$ is an orthonormal basis for \mathcal{V}_0 .

We will say that a sequence of subspaces of $L^2(\dot{\mathbb{S}}^2)$ with the properties above constitutes a *multiresolution analysis* of $L^2(\dot{\mathbb{S}}^2)$. Unlike the construction in [92], the functions $\Phi_{0,\mathbf{k}}^s$ considered here are scaled versions of the same function Φ^s . Moreover, in condition (3), we have here a genuine orthogonality of the wavelet basis, instead of the Riesz basis obtained in [92].

Remark: It should be noticed that, in the spherical MRA defined here, the scale parameter j runs over the whole of \mathbb{Z} , whereas in the usual constructions on \mathbb{S}^2 , j runs only from 0 to $+\infty$. This is due to the stereographic projection, which removes one pole, so that effectively $\dot{\mathbb{S}}^2 = \mathbb{S}^2 \setminus \{N\}$ is noncompact and thus arbitrary dilations are now allowed (see, however, Section 4.4.3 below).

Once the multiresolution analysis is determined, we construct the wavelet spaces \mathcal{W}_j in the usual manner. Let \mathcal{W}_j denote the orthogonal complement of the coarse space \mathcal{V}_j in the fine space \mathcal{V}_{j+1} , so that

$$\mathcal{V}_{j+1} = \mathcal{V}_j \oplus \mathcal{W}_j.$$

One can easily prove that, for each $j \in \mathbb{Z}$, $\{{}^\lambda \Psi_{j,\mathbf{k}}^s, \mathbf{k} \in \mathbb{Z}^2, \lambda = 1, \dots, q\}$ is an orthogonal basis for \mathcal{W}_j and therefore $\{{}^\lambda \Psi_{j,\mathbf{k}}^s, j \in \mathbb{Z}, \mathbf{k} \in \mathbb{Z}^2, \lambda = 1, \dots, q\}$ is an orthonormal basis for $\overline{\bigoplus_{j \in \mathbb{Z}} \mathcal{W}_j} = L^2(\dot{\mathbb{S}}^2)$.

The conclusion of the analysis may be summarized as follows:

- If Φ has compact support in \mathbb{R}^2 , then $\Phi_{j,\mathbf{k}}^s$ has *local support* on $\dot{\mathbb{S}}^2$ (indeed $\text{diam supp } \Phi_{j,\mathbf{k}}^s \rightarrow 0$ as $j \rightarrow \infty$).
- An *orthonormal* 2D wavelet basis leads to an *orthonormal* spherical wavelet basis.
- *Smooth* 2D wavelets lead to *smooth* spherical wavelets.
- In particular, plane tensor product Daubechies wavelets lead to locally supported and orthonormal wavelets on $\dot{\mathbb{S}}^2$, and so do plane tensor product Haar wavelets.
- The decomposition and reconstruction matrices needed in the spherical case are the same as in the plane 2D case, so that the latter can be used (with existing toolboxes).

4.4.3 Further comments

The relation $d\omega(\boldsymbol{\eta}) = \varrho(\mathbf{x})^2 d\mathbf{x}$ linking the the area elements of \mathbb{R}^2 and of \mathbb{S}^2 implies that, near the origin of the plane, corresponding to the South Pole, the areas on the sphere and on the plane are almost the same, but near the North Pole, the ratio of the areas approach infinity. In the standard cases, the elements of a planar orthogonal wavelet basis have supports of the same size all over the plane. But the corresponding spherical wavelets obtained here will have a support that almost vanishes when they are in the neighborhood of the North Pole, which corresponds to regions far away from the origin in the plane. This might clearly lead to analytical as well as numerical problems whenever the information is nearly uniform over the whole sphere, and here we see the limitation of our method. As we have precised already, we have to avoid data around the North Pole. More precisely, our method is applicable on the whole sphere, except a spherical cap $\theta \leq \theta_0$. The value of θ_0 may actually depend on the type of data.

We emphasize that, in practice, wavelet transforms are useful mainly for a *local* analysis. Thus we do not pretend that our method is the best for all kinds of applications. Actually, no construction of spherical wavelets is perfect, as we have mentioned at the beginning of this section. However, we claim that our method is more efficient than most other ones when one deals with large amounts of data, in all applications where one has to make a decomposition and a reconstruction, which implies to invert a large matrix. In the case of Daubechies wavelets, this matrix becomes orthogonal and sparse. Here we see the advantage of being able to use Daubechies wavelets rather than other 2D wavelets.

We can be more precise about the latitude effect, that is, the choice of the limiting value θ_0 . When we project stereographically onto the plane xOy spherical data situated outside of the spherical cap $\theta \leq \theta_0 \leq \pi/2$, the projected data will be situated inside the square $[-x_{\max}, x_{\max}] \times [-x_{\max}, x_{\max}]$, where $x_{\max} = 2 \cot(\theta_0/2)$. In the case of tensor product wavelets, the planar grid at level j has the dimension $n_j \times n_j$ and is taken as

$$\left\{ \left(-x_{\max} + \frac{k_1}{2^j}, -x_{\max} + \frac{k_2}{2^j} \right), \quad k_1, k_2 = 1, 2, \dots, n_j \right\}.$$

Here n_j is taken such that $-x_{\max} + \frac{n_j}{2^j} = x_{\max}$, that is $n_j = \lfloor 2^{j+1} \cdot x_{\max} \rfloor$. Table 4.2 gives the size of the planar grid for $j = 4$ and $j = 5$ (and therefore of the matrix which is used in the decomposition algorithm) for different values of θ_0 . For instance, in our first two examples below, we will use the values $\theta_0 = 8^\circ$ and $j = 4$. This gives matrices of reasonable size, yet yields good results.

4.4.4 Examples

In order to illustrate the merits of our construction, we present three examples.

In the first example, we take the function $g_{\theta_0} : \mathbb{S}^2 \rightarrow \mathbb{R}$, $g_{\theta_0}(\theta, \varphi) = g(\theta + \theta_0, \varphi)$, where

$$g(\theta, \varphi) = \begin{cases} 1, & \theta \geq \frac{\pi}{2}, \\ (1 + 3 \cos^2 \theta)^{-1/2}, & \theta \leq \frac{\pi}{2}. \end{cases}$$

The function g_{θ_0} and its gradient are continuous, but the second partial derivative with respect to θ has a discontinuity on the latitudinal circle $\theta = \frac{\pi}{2} - \theta_0$ (see Figure 4.5(a)). Detecting properly such a discontinuity requires a wavelet with two vanishing moments at least, so that none of the existing constructions of discrete wavelets mentioned at the beginning of this section could detect this discontinuity.

θ_0 (deg.)	θ_0 (rad.)	x_{\max}	dimension of planar grid n_j	
			$j = 4$	$j = 5$
1	0.0175	229.1773	7333	14666
2	0.0349	114.6015	3666	7332
3	0.0524	76.3769	2444	4888
4	0.0698	57.2725	1832	3664
5	0.0873	45.8075	1466	2932
6	0.1047	38.1623	1221	2442
7	0.1222	32.6997	1046	2092
8	0.1396	28.6013	915	1830
9	0.1571	25.4124	813	1626
10	0.1745	22.8601	731	1462
15	0.2618	15.1915	486	972
20	0.3491	11.3426	363	726

Table 4.2: Dimension of the planar grid at level j ($j = 4$ and $j = 5$), for a data set localized at a colatitude $\theta \geq \theta_0$.

Thus, following [2, 13], we take the discretized spherical CWT with the spherical wavelet $\Psi_{H_2}^s$, defined as in (4.40), associated to the plane wavelet

$$\Psi_{H_2}(x, y) = \Delta^2[e^{-\frac{1}{2}(x^2+y^2)}] = (x^4 + y^4 + 2x^2y^2 - 8(x^2 + y^2) + 8)e^{-\frac{1}{2}(x^2+y^2)}. \quad (4.44)$$

The plane wavelet (4.44) has vanishing moments of order up to 3 (here too, a simpler wavelet with less vanishing moments could not detect the discontinuity). In order to compare the two methods, we present in Figure 4.5 the analysis of the function $g_{\theta_0}(\theta, \varphi)$ for three different values of θ_0 (a) $\theta_0 = 0^\circ$; (d) $\theta_0 = 50^\circ$; (g) $\theta_0 = 80^\circ$. The second column shows, in panels (b), (e), (h), the result of the analysis with the spherical wavelet associated to the Daubechies wavelet *db3*. Finally, the third column, on panels (c), (f), (i), does the same for the analysis by the discretized CWT method with the wavelet $\psi_{H_2}^s$.

Comparing the second and the third column, it is clear that the Daubechies wavelet *db3* lifted on the sphere by (4.40) outperforms the wavelet $\Psi_{H_2}^s$ mentioned above. The precision is much better, in the sense that the width of the detected singular curve is narrower at all three latitudes. With both methods, the detection is still efficient very close to the North Pole, but the computation with the lifted *db3* wavelet then requires considering matrices of large dimension, as shown in Table 4.2.

Looking at the third column suggests to increase the resolution of the CWT method, by choosing smaller scales. In order to test this effect, we show in Figure 4.6 a systematic analysis of the function $g_{\theta_0}(\theta, \varphi)$ by the discretized CWT method with the wavelet $\psi_{H_2}^s$. Panels (a), (b), (c) and (d) present the spherical CWT at smaller and smaller scales, $a = 0.04, 0.0165, 0.012$ and 0.0085 , respectively. The discretization grids are those considered in [13]. From the panels (a)-(c), it appears that the discontinuity along the equator is detected properly, and the precision increases as the scale decreases. However, there is a limit: when the scale a is taken below $a = 0.01$, the singularity is no more detected. For instance, for $a = 0.0085$ (see panel (d)),

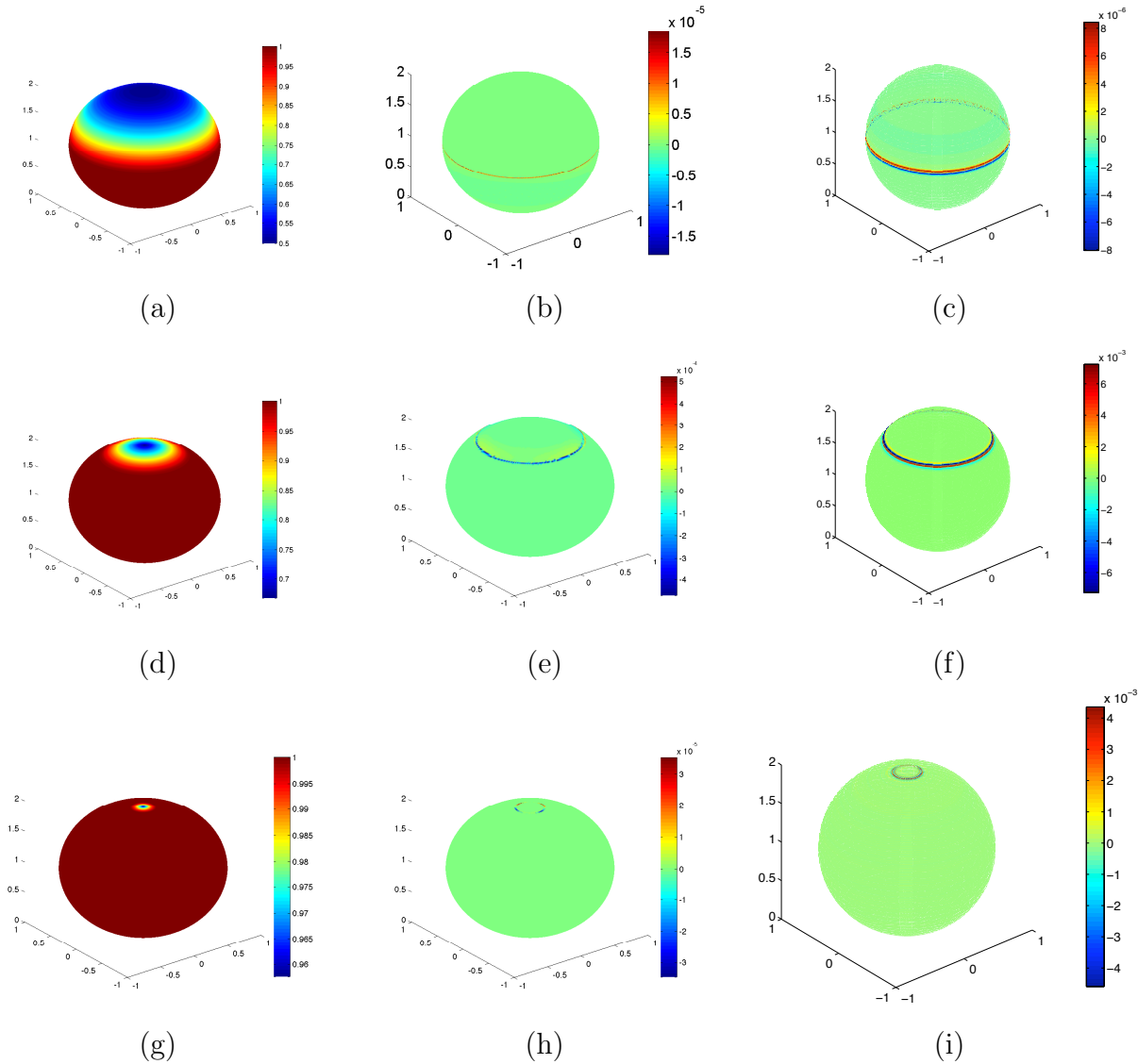


Figure 4.5: (a) The graph of the function $g_{0^\circ}(\theta, \varphi)$; (b) Its analysis with the spherical wavelet associated to the Daubechies wavelet $db3$; (c) Same analysis by the discretized CWT method with the wavelet $\psi_{H_2}^s$, at scale $a = 0.0165$; (d)-(f) The same for the function $g_{50^\circ}(\theta, \varphi)$; (g)-(i) The same for the function $g_{80^\circ}(\theta, \varphi)$.

the wavelet becomes too narrow and “falls in between” the discretization points, and “ripples” appear. This effect is described in detail in [2]. Here again, the spherical Daubechies wavelet performs better.

The next question to examine is the possible distortion in latitude around the North Pole, for a signal which is no longer invariant under rotation around the z -axis. Thus, in the second example, we take the function $f : \mathbb{S}^2 \rightarrow \{0, 1\}$,

$$f(\theta, \varphi) = \begin{cases} 0, & \text{if } \theta \geq \frac{\pi}{2}, \\ 1, & \text{if } \theta < \frac{\pi}{2}. \end{cases},$$

and then f_α , the function obtained from f by performing a rotation around the axis Ox by an angle α . We apply a tensor product Haar wavelet transform to f_α , for $\alpha = 70^\circ$. Let us proceed in two steps. First, the discontinuity is well detected in the tangent plane (where the wavelet transform is computed), as shown in Figure 4.7(a). It is indeed a circle, with uniform

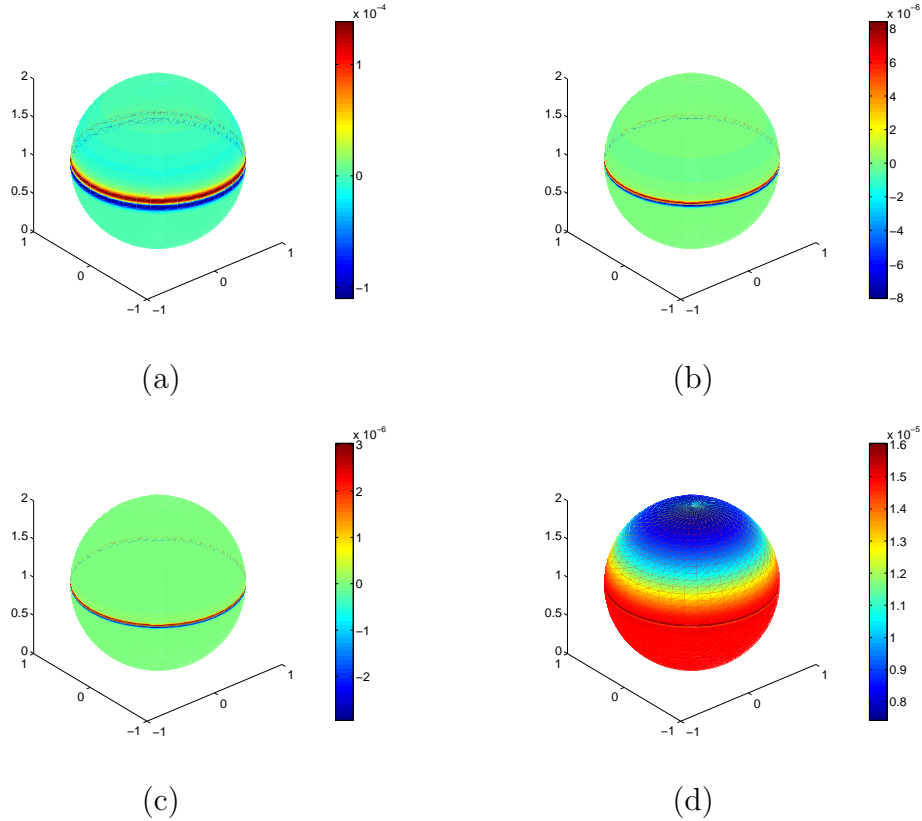


Figure 4.6: Analysis of the function $g_{0^\circ}(\theta, \varphi)$ by the discretized CWT method with the wavelet $\psi_{H_2}^s$, at scales: (a) $a = 0.04$; (b) $a = 0.0165$; (c) $a = 0.012$; and (d) $a = 0.0085$.

intensity, as it should, in virtue of the conformal character of the stereographic projection. However, when it is lifted back onto the sphere, some artifacts appear, that can be seen in Figure 4.7(b). Namely, the part of the discontinuity that lies closer to the North Pole is less clearly visible than the ones that are farther away from it and there are some gaps. This is caused by the unavoidable fact that the grids on the plane and on the sphere never match, the inverse projection does not conserve areas, so that some points are lost in the lifting process.

On the other hand, the analysis of the same function by the discretized spherical CWT, at the smallest possible scale $a = 0.0012$, shows no such effect, as seen in Figure 4.7(c). But here too, the singularity is detected by the discrete WT with a better precision. Note that, in the CWT case, simpler planar wavelets, with less vanishing moments, can be used, but the result is the same. One can also try to analyze the function obtained from g_{0° by a rotation around the axis Ox , but we don't expect much difference with the present example.

In the third example, we consider a data set from the texture analysis of crystals; see Figure 4.8(b). It consists of 180×360 measurements on the sphere and its main characteristic is that the values over the sphere are constant, except for some peaks. Figure 4.8(c) shows the approximation at level 6 using the spherical wavelet frames constructed in [89], which are localized, but not locally supported. An example of such kernel is given in Figure 4.8(a). Figure 4.8(d) shows the approximation at level 1 using the spherical wavelet associated to *db2*. One can easily see that our wavelets are more efficient in approximating the given data set and also the algorithms are much faster than the ones for spherical harmonics.

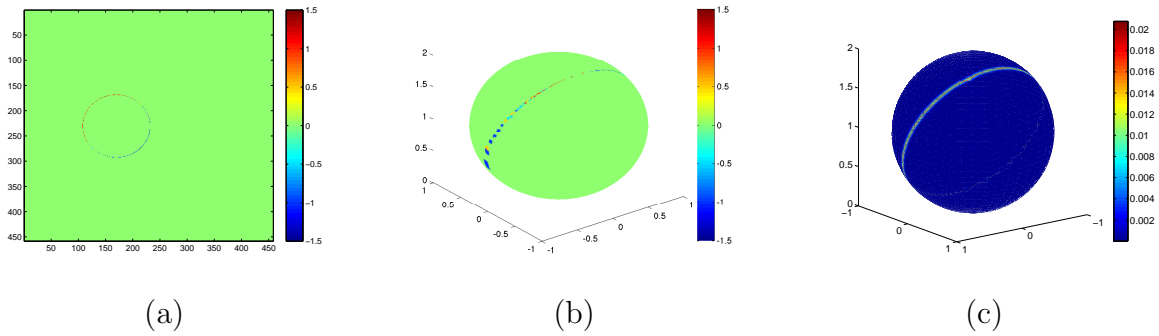


Figure 4.7: Analysis of the function $f_{70^\circ}(\theta, \varphi)$ with the spherical wavelet associated to a Haar wavelet: (a) the wavelet transform in the tangent plane; (b) the same lifted back on the sphere. (c) Analysis of the same function by the discretized CWT method with the wavelet $\psi_{H_2}^s$, at scale $a = 0.0012$.

Conclusion

We have presented a new method for constructing spherical wavelets. Its advantage over most existing methods is that it yields locally supported orthonormal bases, which is crucial when one is confronted to very large data sets. The price to pay is that one has to avoid a small region around the North Pole, whose size may depend on the data. Within that region, serious distortions may occur. However, the examples given above show that this “forbidden” region can be very small: although we have used $\theta_0 = 70^\circ$ or 80° , much higher values can be chosen without damage. Hence we believe this limitation does not prevent applying the method to practical situations. In any case, if the data are sufficiently well localized, one can always make a rotation that brings them around the South Pole, as we already mentioned. After all, one should remember that wavelet analysis is primarily a *local* analysis.

We may also mention that the method described here could detect singularities of arbitrarily high order, by choosing appropriate planar wavelets. By contrast, the other existing spherical wavelets do not have enough vanishing moments and thus are not able to detect such discontinuities.

As a final remark, we may point out that the method should work for any manifold with a bijective orthogonal projection onto a fixed plane, since the latter induces a unitary map between the respective L^2 spaces. Such are, for instance, the upper sheet of the two-sheeted hyperboloid $z^2 - x^2 - y^2 = 1$ with projection onto the plane $z = 0$ or the paraboloid $z = x^2 + y^2$ with the same projection (in addition, we have seen already that the latter case may be treated also by the stereographic projection from the sphere). It might also be extended to a local analysis on more general manifolds. A systematic discussion may be found in [8].

The case when one uses instead of the stereographic projection a projection that preserves areas have recently been considered in [109].

4.5 EPWT on triangulations of the sphere

In this section we propose a new transform for sparse representation of data on spherical surfaces, the EPWT. The results were published in [84].

The idea of the EPWT for 2D images was introduced in [83] and summarized in Section 1.4.1. We consider now a spherical triangulation, either the one described in Section 4.1.1, or an arbitrary one, constructed with the algorithm in [91]. We also need its recursive subdivision constructed in Section 4.1.2. We denote by $\mathcal{T} = \mathcal{T}^0 = \{T_1, \dots, T_M\}$ the set of faces of the

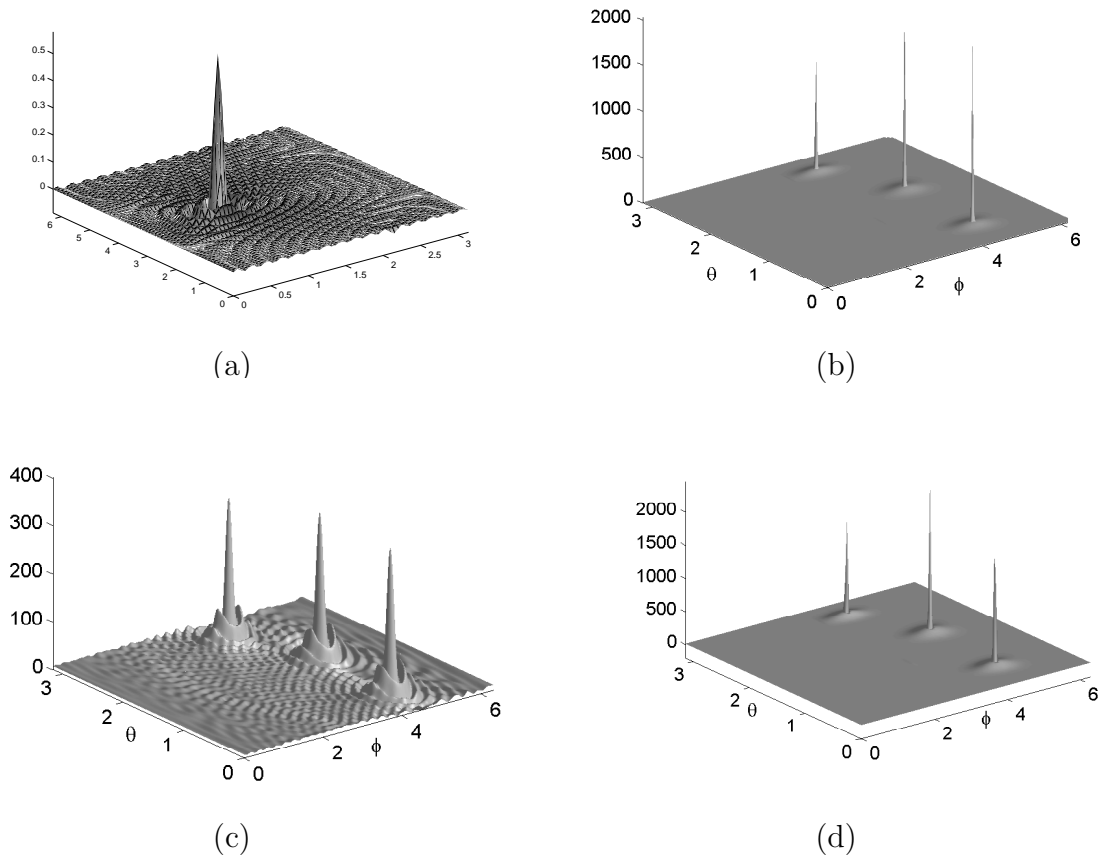


Figure 4.8: (a) An example of kernel of spherical harmonics: localized, but not locally supported; (b) The initial data set, in spherical coordinates (θ, φ) ; (c) Its approximation at level 6 using a spherical harmonics kernel; (d) Approximation at first level using the spherical wavelet associated to the Daubechies wavelet $db2$.

polyhedron Π and by V^0 the set of vertices.

For application of the EPWT we will stop the refinement process at a suitable sufficiently high (fixed) level j depending on the data set in the application. We define the set of vertices V^j accordingly. In particular, each triangle in \mathcal{T}^j is uniquely determined by its three vertices. For application of the EPWT we will also need a one-dimensional index set $J = J^j$ for the triangles in \mathcal{T}^j . Using the octahedron, for $j = 1$, this one-dimensional index set J can be assigned as shown in Figure 1 (right). Observe that for the octahedron the number of triangles at the j th level is given by $|J| = |\mathcal{T}^j| = 2^{2j+3}$.

4.5.1 Definitions and notations for the EPWT

In order to explain the idea of the EPWT for spherical triangulations, where we want to use the discrete one-dimensional wavelet transform along *path vectors* through the data, we first need some further definitions and notations.

With the notations in Section 4.1.2, let us assume that we have given a fixed refined spherical triangulation \mathcal{U}^j with a corresponding set of vertices $p(V^j)$. Further, let J be a one-dimensional index set for the spherical triangles in \mathcal{U}^j . We determine a *neighborhood* of an index $\nu \in J$ of the set of spherical triangles by

$$\mathcal{N}(\nu) = \{\mu \in J \setminus \{\nu\} : T_\mu \text{ and } T_\nu \text{ have a common edge}\}.$$

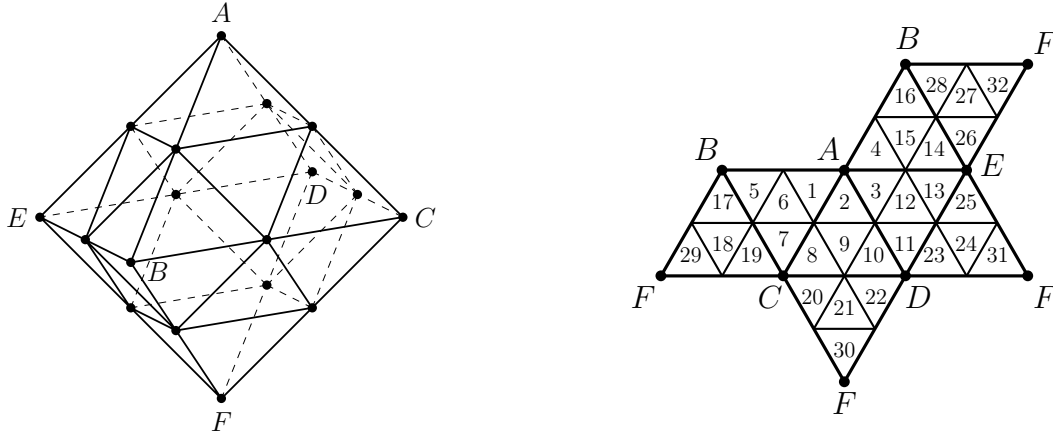


Figure 4.9: Illustration of the octahedron with \mathcal{T}^1 triangulation (left) and a fold apart version of the octahedron on the plane with a one-dimensional indexing of all faces.

Hence each index $\nu \in J$ has exactly three neighbors. One may also use a bigger neighborhood, e.g. $\mathcal{N}(\nu) = \{\mu \in J \setminus \{\nu\} : T_\mu \text{ and } T_\nu \text{ have a common edge or a common vertex}\}$, in this case each index has 12 neighbors. We also need the definition of neighborhood of subsets of an index set. We shall consider disjoint *partitions* of J of the form $\{J_1, J_2, \dots, J_r\}$, where $J_\mu \cap J_\nu = \emptyset$ for $\mu \neq \nu$ and $\bigcup_{\nu=1}^r J_\nu = J$. We then say that two different subsets J_ν and J_μ from the partition are *neighbors*, and we write $J_\nu \in \mathcal{N}(J_\mu)$, if there exist an index $l \in J_\nu$ and an index $l_1 \in J_\mu$ such that $l \in \mathcal{N}(l_1)$.

We consider a piecewise constant function $f \in \mathcal{V}$, i.e., we identify each spherical triangle in \mathcal{U}^j with a function value of f . Hence f is uniquely determined by the data vector $(f_\nu)_{\nu \in J}$. We will look for path vectors through index subsets of J and apply a one-dimensional wavelet transform along these path vectors. Any orthogonal or biorthogonal one-dimensional wavelet transform can be used here.

We say that a vector of indices (l_k, \dots, l_{k+n}) , $1 \leq k < k+n \leq |J|$, is *connected*, if we have $l_{\nu+1} \in \mathcal{N}(l_\nu)$ for $\nu = k, \dots, k+n-1$. Such a connected index vector is called *pathway*. We are interested in a *complete path* through the index set J . A complete path \mathbf{p} through J is a vector containing all indices of J in a certain order, i.e. $\mathbf{p} \in \mathbb{Z}^{|J|}$ is a permutation of $(1, 2, \dots, |J|)$. This complete path should be composed by a number of pathways, i.e. $\mathbf{p} = (\mathbf{p}_1; \dots; \mathbf{p}_r)$, where \mathbf{p}_ν , $\nu = 1, \dots, r$, are connected vectors of indices.

One simple example of such a complete path is to take just $\mathbf{p} = (1, 2, \dots, |J|)$. Using the indexing as in Figure 4.9, this path has interruptions after indices 4, 16 and 28. It is also possible to take a path without interruptions here, e.g. $(1, 2, 3, 4, 15, 16, 5, 6, 7, 8, 9, 10, 11, 12, 13, 14, 26, 25, 24, 23, 22, 21, 20, 19, 18, 17, 28, 27, 32, 31, 30, 29)$.

Example

We illustrate the idea of function decomposition with the EPWT on the sphere in the following small example. Let a set of 32 function values be given on the sphere, where each function value corresponds to a spherical triangle on the sphere that has been obtained by radial projection of the triangulated octahedron in Figure 4.9 (left). The values are given as a vector of length

32 corresponding to the one-dimensional indexing of the triangles in Figure 4.9 (right),

$$\mathbf{f} = (0.4492, 0.4219, 0.4258, 0.4375, 0.4141, 0.4531, 0.4180, 0.4258, \\ 0.4375, 0.4292, 0.4219, 0.4219, 0.4219, 0.4258, 0.4023, 0.4141, \\ 0.4219, 0.4219, 0.4297, 0.4375, 0.4141, 0.4023, 0.4258, 0.4219, \\ 0.4258, 0.4180, 0.4531, 0.4141, 0.4375, 0.4258, 0.4219, 0.4492).$$

Starting with the index 1, we now determine the first path vector. Index 1 with the function value 0.4492 has the neighbors 2, 4 and 6 with corresponding values 0.4219, 0.4375 and 0.4531, respectively (see Figure 4.10). Hence, the second index in the path is 6. Proceeding further according to Section 1.4.1 we obtain

$$\mathbf{p}^5 = (1, 6, 7, 8, 9, 10, 11, 12, 13, 14, 26, 25, 24, 31, 30, 21, 22, 23; 3, 2; 17, 18, 19, 20; \\ 4, 15, 16, 5; 28, 27, 32, 29),$$

where the pathways are separated by semicolons. This path has four interruptions and is illustrated by arrows in Figure 4.10 (left).

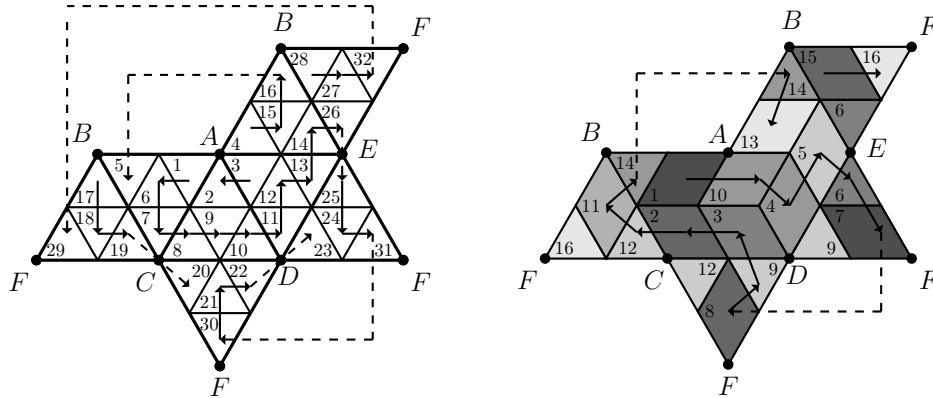


Figure 4.10: Illustration of first path through the \mathcal{T}^1 triangulation of the octahedron (left) and of the low-pass part after the first level of EPWT with Haar wavelet transform (right). Index sets at the second level are illustrated by different gray values, and path vectors are represented by arrows.

An application of the Haar wavelet transform (with unnormalized filter coefficients $h_0 = h_1 = 1/2$, $g_0 = 1/2$, $g_1 = -1/2$) along this path gives (with truncation after four digits) the low-pass coefficients

$$\mathbf{f}^4 = (0.4512, 0.4219, 0.4334, 0.4219, 0.4238, 0.4219, 0.4219, 0.4200, \\ 0.4140, 0.4238, 0.4219, 0.4336, 0.4199, 0.4141, 0.4336, 0.4434),$$

and the wavelet coefficients

$$\mathbf{g}^4 = (-0.0020, -0.0039, -0.0042, 0., -0.0020, -0.0039, 0., 0.0058, \\ -0.0118, 0.0020, 0., -0.0039, 0.0176, 0., -0.0195, 0.0058).$$

We now proceed to the second level. For the smoothed vector of function values \mathbf{f}^4 corresponding to the 16 index sets that are illustrated by gray values in Figure 4.10 (right), we obtain the next path

$$\mathbf{p}^4 = (1, 10, 4, 5, 6, 7, 8, 9, 3, 2, 12, 11, 14, 13; 15, 16),$$

illustrated by arrows in Figure 4.10 (right). The path \mathbf{p}^4 has one interruption. An application of the Haar wavelet transform along \mathbf{p}^4 gives

$$\begin{aligned}\mathbf{f}^3 &= (0.4375, 0.4229, 0.4219, 0.4170, 0.4276, 0.4278, 0.4170, 0.4385), \\ \mathbf{g}^3 &= (0.0136, -0.0010, 0., 0.0030, 0.0057, 0.0058, 0.0029, -0.0049).\end{aligned}$$

At the third level we start with the smoothed vector \mathbf{f}^3 corresponding to the 8 index sets that are illustrated by gray values in Figure 4.11 (left). We find now the path

$$\mathbf{p}^3 = (1, 5, 6, 8, 3, 2, 4; 7),$$

see Figure 4.11 (left). This leads to

$$\begin{aligned}\mathbf{f}^2 &= (0.4326, 0.4331, 0.4224, 0.4170), \\ \mathbf{g}^2 &= (0.0049, -0.0054, 0.0005, 0.).\end{aligned}$$

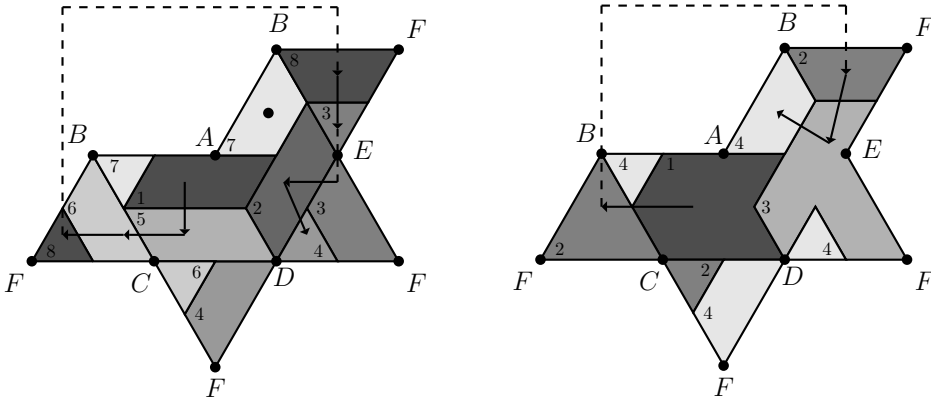


Figure 4.11: Illustration of the third path through the index sets of the octahedron (left) and of the fourth path of the obtained index sets (right) for EPWT with Haar wavelet transform. Index sets are illustrated by different gray values, and path vectors are represented by arrows.

In the fourth level we have only 4 index sets that correspond to the values in \mathbf{f}^2 , see Figure 4.11 (right). Hence we find $\mathbf{p}^2 = (1, 2, 3, 4)$ and

$$\mathbf{f}^1 = (0.4328, 0.4197), \quad \mathbf{g}^1 = (-0.0003, 0.0027).$$

Finally, with $\mathbf{p}^1 = (1, 2)$ the last transform yields $\mathbf{f}^0 = (0.4263)$ and $\mathbf{g}^0 = (0.0066)$.

4.5.2 Adaptive Haar wavelet bases on the sphere

We want to study the question, how the EPWT introduced in the previous section can be understood in terms of a multiresolution analysis on the sphere. Let $N_j := |J| = 2^L s$ with $L, s \in \mathbb{N}$ be the number of triangles in the spherical triangulation \mathcal{U}^j of \mathbb{S}^2 . For the octahedron we can take $L = 2j + 3$ and $s = 1$. We consider the space

$$\mathcal{V} = \mathcal{V}^L = \text{span} \{ \phi_i^L = \chi_{U_i}, U_i \in \mathcal{U}^j \} = \text{span} \{ \phi_i^L, i \in J \}$$

of piecewise constant functions on the fixed spherical triangulation \mathcal{U}^j . Obviously, $\{ \phi_i^L : i \in J \}$ forms an orthonormal basis of \mathcal{V}^L with respect to the scalar product $\langle \cdot, \cdot \rangle_*$ on $L^2(\mathbb{S}^2)$, defined in formula (4.2), Section 4.1.1 Further, let $f \in \mathcal{V}^L$ be a given function of the form

$$f = \sum_{\mu \in J} a_\mu^L \phi_\mu^L.$$

Let us also fix the Haar wavelet filter bank given by the analysis filters h, g with $h(0) = h(1) = 1/\sqrt{2}$ and $g(0) = -1/\sqrt{2}, g(1) = 1/\sqrt{2}$. The synthesis filters for the orthonormal Haar wavelet filter bank are given by $\tilde{h}(0) = \tilde{h}(1) = 1/\sqrt{2}$ and $\tilde{g}(0) = -1/\sqrt{2}, \tilde{g}(1) = 1/\sqrt{2}$.

As we have seen in Section 1.4.1, applying the first level of the EPWT with Haar filters, we first need to determine a path \mathbf{p}^L , i.e., a permutation of $(1, \dots, N_j)$, and then apply the one-dimensional Haar wavelet transform to the vector $(f(\mathbf{p}^L(\mu)))_{\mu=1}^{N_j}$. This transform can be interpreted by determining the new function spaces

$$\mathcal{V}^{L-1} = \text{span} \left\{ \phi_i^{L-1} := \frac{1}{\sqrt{2}} \left(\phi_{\mathbf{p}^L(2i-1)}^L + \phi_{\mathbf{p}^L(2i)}^L \right), i = 1, \dots, N_j/2 \right\}$$

and

$$\mathcal{W}^{L-1} = \text{span} \left\{ \psi_i^{L-1} := \frac{1}{\sqrt{2}} \left(\phi_{\mathbf{p}^L(2i-1)}^L - \phi_{\mathbf{p}^L(2i)}^L \right), i = 1, \dots, N_j/2 \right\}.$$

Obviously, \mathcal{V}^{L-1} is generated by characteristic functions whose supports consist of two (usually) neighbor spherical triangles along the path \mathbf{p}^L . We find $\mathcal{V}^{L-1} \subset \mathcal{V}^L$ and $\mathcal{W}^{L-1} \subset \mathcal{V}^L$, and moreover, we have

$$\mathcal{V}^{L-1} + \mathcal{W}^{L-1} = \mathcal{V}^L \quad \text{and} \quad \mathcal{V}^{L-1} \perp \mathcal{W}^{L-1},$$

where the orthogonality holds with respect to the scalar product $\langle \cdot, \cdot \rangle_*$.

We can apply the EPWT transform at L levels, thereby adaptively defining scaling spaces and wavelet spaces according to the path vectors \mathbf{p}^l , $l = L, L-1, \dots, 1$ of lengths $2^l s$. We obtain as before for $l = L, L-1, \dots, 1$,

$$\mathcal{V}^{l-1} = \text{span} \left\{ \phi_i^{l-1} := \frac{1}{\sqrt{2}} \left(\phi_{\mathbf{p}^l(2i-1)}^l + \phi_{\mathbf{p}^l(2i)}^l \right), i = 1, \dots, 2^{l-1} s \right\},$$

and

$$\mathcal{W}^{l-1} = \text{span} \left\{ \psi_i^{l-1} := \frac{1}{\sqrt{2}} \left(\phi_{\mathbf{p}^l(2i-1)}^l - \phi_{\mathbf{p}^l(2i)}^l \right), i = 1, \dots, 2^{l-1} s \right\},$$

where again $\mathcal{V}^{l-1} + \mathcal{W}^{l-1} = \mathcal{V}^l$ and $\mathcal{V}^{l-1} \perp \mathcal{W}^{l-1}$ with respect to $\langle \cdot, \cdot \rangle_*$. Observe that the spaces \mathcal{V}^l and \mathcal{W}^l are adaptively dependent on the considered original function $f \in \mathcal{V}^L$.

With the Haar filters given above, we find the decomposition of $f = f^L \in \mathcal{V}^L$,

$$f^L = f^0 + \sum_{l=0}^{L-1} g^l,$$

with $f^0 \in \mathcal{V}^0$ and $g^l \in \mathcal{W}^l$ for $l = 0, \dots, L-1$. More precisely, with the notation $f^{l+1} \in \mathcal{V}^{l+1}$ satisfying $f^{l+1} = f^l + g^l$ and with

$$f^{l+1} = \sum_{\mu=1}^{2^{l+1}r} a_{\mu}^{l+1} \phi_{\mu}^{l+1}, \quad f^l = \sum_{\mu=1}^{2^l r} a_{\mu}^l \phi_{\mu}^l, \quad g^l = \sum_{\mu=1}^{2^l r} b_{\mu}^l \psi_{\mu}^l,$$

the decomposition algorithm reads

$$a_{\mu}^l = \frac{1}{\sqrt{2}} \left(a_{\mathbf{p}^{l+1}(2\mu-1)}^{l+1} + a_{\mathbf{p}^{l+1}(2\mu)}^{l+1} \right), \quad b_{\mu}^l = \frac{1}{\sqrt{2}} \left(a_{\mathbf{p}^{l+1}(2\mu-1)}^{l+1} - a_{\mathbf{p}^{l+1}(2\mu)}^{l+1} \right), \quad \mu = 1, \dots, 2^l s.$$

Vice versa, for $l = 0, \dots, L-1$ the reconstruction algorithm is given by

$$a_{\mathbf{p}^{l+1}(2\mu-1)}^{l+1} = \frac{1}{\sqrt{2}} \left(a_{\mu}^l + b_{\mu}^l \right), \quad a_{\mathbf{p}^{l+1}(2\mu)}^{l+1} = \frac{1}{\sqrt{2}} \left(a_{\mu}^l - b_{\mu}^l \right), \quad \mu = 1, \dots, 2^l s.$$

4.5.3 Implementation issues

In order to implement the EPWT for real data sets, one is confronted with the following issues.

1. Projection of the data set or the function on the spherical triangulation with a certain fixed resolution 2^{-j} , such that each triangle in \mathcal{T}^j (resp. \mathcal{U}^j) corresponds to one data value.
2. Definition of a bijective mapping of the triangles in \mathcal{T}^j (resp. \mathcal{U}^j) to a one-dimensional index set.
3. Determination of neighbors in the one-dimensional index set.

The first issue is not related to the EPWT but occurs for all applications of spherical triangulations or on all spherical grids constructed in Chapter 2. We focus here on the second and the third issue.

Bijjective mapping to a one-dimensional index set

Usually, we consider the subdivision process separately on each of the eight triangular faces of the octahedron. Let these faces be numbered by $d \in \{1, 2, \dots, 8\}$, where the first four triangles are consecutively ordered on the northern part of the octahedron (i.e., all points of these triangles have a z -coordinate greater than or equal to zero), and the other 4 triangular faces, on the southern part of the octahedron, have numbers 5,6,7,8. Using Figure 4.9, let $T_1 = [B, C, A]$, $T_2 = [C, D, A]$, $T_3 = [D, E, A]$, $T_4 = [E, B, A]$, as well as $T_5 = [B, C, F]$, $T_6 = [C, D, F]$, $T_7 = [D, E, F]$, $T_8 = [E, B, F]$.

Let us consider for the moment only one of the faces of the octahedron. For representing the triangles after j levels of the subdivision process, we use (two-dimensional) barycentric coordinates. Let the vertices of the triangular face at hand have the coordinates $(1, 0, 0)$, $(0, 1, 0)$, $(0, 0, 1)$, where these coordinates correspond to the vertices of T_d given above in this order. For example, in T_1 we have $B = (1, 0, 0)$, $C = (0, 1, 0)$ and $A = (0, 0, 1)$ etc. The triangles T in \mathcal{T}^j are uniquely determined by the face d and by their three vertices in barycentric coordinates. Observe that the triangles $T = [d; M_1, M_2, M_3]$ in \mathcal{T}^j are either of type 1 or of type 2 with the following coordinates,

Type 1 triangle:

$$T = \left[d; \left(\frac{p+1}{2^j}, \frac{m}{2^j}, \frac{k}{2^j} \right), \left(\frac{p}{2^j}, \frac{m+1}{2^j}, \frac{k}{2^j} \right), \left(\frac{p}{2^j}, \frac{m}{2^j}, \frac{k+1}{2^j} \right) \right] \quad p, m, k = 0 \dots, 2^j - 1, \quad (4.45)$$

Type 2 triangle:

$$T = \left[d; \left(\frac{p}{2^j}, \frac{m+1}{2^j}, \frac{k+1}{2^j} \right), \left(\frac{p+1}{2^j}, \frac{m}{2^j}, \frac{k+1}{2^j} \right), \left(\frac{p+1}{2^j}, \frac{m+1}{2^j}, \frac{k}{2^j} \right) \right] \quad p, m, k = 0 \dots, 2^j - 1, \quad (4.46)$$

where in the first case $p + m + k = 2^j - 1$, and in the second case $p + m + k = 2^j - 2$. For example, the gray triangle in Figure 4.12 is of type 2, and its two direct neighbors in the row $r = 3$ are of type 1.

Let $\mathcal{T}_d^j \subset \mathcal{T}^j$ be the triangulation of one triangular face T_d . This triangulation \mathcal{T}_d^j consists of 4^j triangles. In order to define a bijective mapping of $[d; M_1, M_2, M_3]$ in \mathcal{T}^j to a one-dimensional index set, we first consider a mapping of the triangles to rows r and positions n in \mathcal{T}_d^j , i.e. a mapping $[d; M_1, M_2, M_3] \mapsto [d; r, n]$ as follows.

We say that a triangle $[d; M_1, M_2, M_3]$ is in the r th row of \mathcal{T}_d^j if the z -coordinates of M_1 , M_2 and M_3 (in the barycentric system) are all either $\frac{1}{2^j}(2^j - r)$ or $\frac{1}{2^j}(2^j - r - 1)$. Obviously, we have 2^j

rows in the triangulation \mathcal{T}_d^j , and the r th row contains $2r - 1$ triangles, see Figure 4.12 for $j = 2$. Further, with n we denote the position of a triangle in the r th row, starting with the maximal x -coordinate in the barycentric coordinate system. For example, the gray triangle in Figure 4.12 is of type 2 and uniquely given by the coordinates $[d; (1/4, 1/2, 1/4), (1/4, 1/4, 1/2), (0, 1/2, 1/2)]$, or equivalently (with $r = 3$ and $n = 4$) by $[d; 3, 4]$.

Generally, we first determine the row and then the position of a triangle in the r th row by considering its distance from the vertex $(1, 0, 0)$. We observe that the triangle of type 1 in (4.45) is mapped to the row $r = 2^j - k$ and the position $n = 2(r - p) - 1$, and the triangle of type 2 in (4.46) is mapped to the row $r = 2^j - k$ and the position $n = 2(r - p) - 2$. Conversely, for a triangle $T = [d; r, n]$ we find:

If n is odd, then T is of type 1 with

$$k = 2^j - r, \quad p = r - \frac{n+1}{2}, \quad m = 2^j - 1 - k - p;$$

if n is even, then T is of type 2 with

$$k = 2^j - r, \quad p = r - \frac{n}{2} - 1, \quad m = 2^j - 2 - k - p.$$

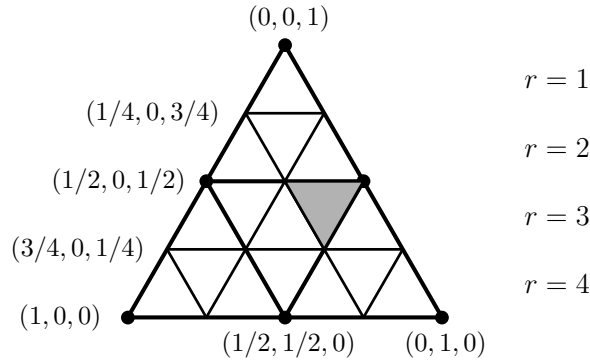


Figure 4.12: Illustration of the triangulation \mathcal{T}_d^2 on one face T_d of the octahedron with barycentric coordinates. The grey triangle is the 4th triangle in the third row.

With this preliminaries we are ready to determine the invertible mapping of triangles $T = [d; M_1, M_2, M_3]$ resp. $T = (d; r, n)$ in \mathcal{T}^j to the one-dimensional index set indicated in Figure 4.9. We restrict ourselves to the faces 1, 2, 3, 4 on the northern part of the octahedron, the other part can be done simply by reflection arguments.

Obviously, the r th row through all four northern triangular faces contains $4(2r - 1) = 8r - 4$ triangles (see e.g. Figure 4.9). Let now $T = [d; M_1, M_2, M_3]$ be an arbitrary triangle in \mathcal{T}^j with $d \in \{1, 2, 3, 4\}$, and let $(d; r, n)$ be the (face, row, position) coordinates of this triangle. Then we determine the one-dimensional index $l \in \{1, \dots, 4^{j+1}\}$ of T as

$$l := 4(r - 1)^2 + (d - 1)(2r - 1) + n. \quad (4.47)$$

Here we have used the fact that $4(r - 1)^2$ triangles belong to the first $r - 1$ rows of the triangulation \mathcal{T}^j , and $(d - 1)(2r - 1)$ triangles belong to the r th row in previous faces. So, starting at the North Pole, the one-dimensional index runs through the first row, then through the second row etc., and it ends at the South Pole (in the 2^{j+1} th row, see Figure 4.9 (right)). Conversely, a triangle T indexed by $l \in \{1, \dots, 4^{j+1}\}$ in the one-dimensional index set J is in the r th row if $4(r - 1)^2 < l \leq 4r^2$, i.e., we have

$$r := \left\lceil \frac{\sqrt{l}}{2} \right\rceil,$$

where $\lceil x \rceil$ denotes the smallest integer greater than x . Since each face has $2r - 1$ triangles in the r th row, we find with $n_1 := l - 4(r - 1)^2$ the face d of the triangle as

$$d := \left\lceil \frac{n_1}{2r - 1} \right\rceil$$

and finally the position $n := n_1 - (d - 1)(2r - 1)$.

On the southern hemisphere, the one-dimensional mapping is continued with $l \in \{4^{j+1} + 1, \dots, 2^{2j+3}\}$ by using reflection arguments, i.e., instead of l in (4.47) we take $2^{2j+3} - l + 1$.

Let us remark that this mapping $l = J([d; M_1, M_2, M_3])$ is only necessary as a preliminary step in order to relate the data vector correctly with the one-dimensional index set, and after finishing the EPWT, for correct projection of the obtained data onto the sphere.

Neighbors in the one-dimensional index set

During the transformation process using the EPWT, we work only with the one-dimensional index set and the corresponding vector of data. For this purpose, we need to determine the (one-dimensional) indices of the direct neighbors of a triangle $T_l \in \mathcal{T}^j$. We consider only the neighborhood with three neighbors, but the idea can be simply transferred to larger neighborhoods of T_l .

For $l = 1$, we find the neighborhood $\{2, 4, 6\}$ (see also Figure 4.9 (right)), and analogously, for the last index $l = 2^{2j+3}$ we obtain the neighborhood $\{2^{2j+3} - 1, 2^{2j+3} - 3, 2^{2j+3} - 5\}$. For $2 \leq l \leq 2^{2j+3} - 1$, two of the wanted neighbors are in the same row as l . If $l \leq 4^{j+1}$ and $l \neq 4\kappa^2$ (or $l > 4^{j+1}$ and $l \neq 2^{2j+3} - 4\kappa^2$) for some $\kappa \in \mathbb{N}$, then the two neighbors are immediately provided by $l - 1$ and $l + 1$. If $l = 4\kappa^2$ with $1 \leq \kappa \leq 2^j$, then the two neighbors of l are $l - 1$ and $4(\kappa - 1)^2 + 1$. Similarly, on the southern hemisphere, for $l = 2^{2j+3} - 4\kappa^2$ with $1 \leq \kappa \leq 2^j$, we have the neighbors $l - 1$ and $2^{2j+3} - 4(\kappa + 1)^2 + 1$.

The remaining third neighbor of l can be either in the previous or in the next row, depending on the type of the triangle T_l . We again use the (face, row, position) representation of the triangle T_l for determining this neighbor. We restrict ourselves to the case $l \leq 4^{j+1}$. First we observe that T_l has the representation $(d; r, n)$ with

$$r = \left\lceil \frac{l}{2} \right\rceil, \quad n_1 = l - 4(r - 1)^2, \quad d = \left\lceil \frac{n_1}{2r - 1} \right\rceil, \quad n := n_1 - (d - 1)(2r - 1).$$

For odd n , the triangle T_l is of type 1 and its third neighbor is in the next row. For $r < 2^j$, this neighbor is determined by $(d, r + 1, n + 1)$, i.e., by the one-dimensional index

$$4r^2 + (d - 1)(2r + 1) + n + 1 = l + 8r + 2d - 5.$$

In the case $r = 2^j$ the third neighbor belongs to the southern hemisphere, and has the index $l + 4(2^{j+1} - 1)$ since $4(2^{j+1} - 1)$ triangles are contained in the 2^j th row and also in the $(2^j + 1)$ th row of \mathcal{T}^j .

For even n , the triangle T_l is of type 2 and its neighbor is in the previous row. It is determined by $(d, r - 1, n - 1)$ i.e. by the one-dimensional index

$$4(r - 2)^2 + (d - 1)(2r - 3) + n - 1 = l - 8r - 2d + 13.$$

4.5.4 Numerical experiments

To illustrate the efficiency of our method, we took the data set *topo*, and we considered the regular octahedron with triangulation \mathcal{T}_6 , containing 32768 triangles. The approximation \mathbf{f}^6 on

\mathcal{U}_6 is represented in Figure 4.13 (left). Applying 4 levels of the EPWT, we obtain 2048 scaling coefficients and 30720 wavelet coefficients. We have used different thresholds to the wavelet coefficients, see Table 4.3. Figure 5 (right) shows the reconstructed data $\tilde{\mathbf{f}}^6$ using only 2265 wavelet coefficients. For comparison of the reconstructed data $\tilde{\mathbf{f}}^6$ with the original data \mathbf{f}^6 , we measured the SNR given as

$$SNR = 20 \cdot \log_{10} \frac{\|\mathbf{f}^6 - \text{mean}(\mathbf{f}^6)\|_2}{\|\mathbf{f}^6 - \tilde{\mathbf{f}}^6\|_2}.$$

The results are contained in Table 4.3, where the mean of \mathbf{f}^6 is -2329 .

threshold	number of remaining wavelet coeff.	percent of remaining wavelet coefficients	SNR
1	27732	90.27 %	84.72
100	14185	46.17 %	38.59
500	5230	17.02 %	25.30
1000	3313	10.78 %	21.17
1500	2699	8.78 %	19.18
2000	2402	7.81 %	17.89
2500	2265	7.37 %	17.10

Table 4.3: Compression results for the data set *topo*.

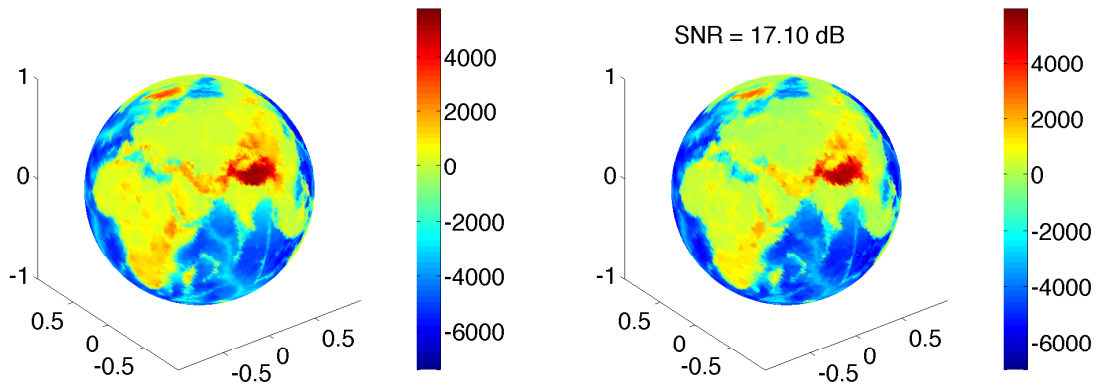


Figure 4.13: Approximation \mathbf{f}^6 at level 6 of the original data set *topo* and the compressed version $\tilde{\mathbf{f}}^6$ with threshold 2500.

Conclusions

This method is particularly efficient for compression of data sets containing texture components, as e.g. topographical data. As in the two-dimensional case, the efficiency of the EPWT depends strongly on the “cost of adaptivity”, i.e. the cost for storing the path vectors \mathbf{p}^j at each level of the transform. In order to reduce these costs, we have proposed a so-called relaxed EPWT in

[83], using the idea of “favorite directions”. This approach can be implemented on the sphere as well.

Furthermore, we want to emphasize that the EPWT can also be applied to planar triangulations and to triangulations of parts of the sphere. We only need a one-dimensional indexing of all triangles of the triangulation and a definition of neighborhood of each triangle. The application of the EPWT on the sphere is not restricted to a triangular grid.

Chapter 5

Wavelets on manifolds

We will assume data are given on a two-dimensional smooth manifold \mathcal{M} and we are given a bijective projection \mathbf{p} from \mathcal{M} (or a subset $\mathcal{N} \subset \mathcal{M}$) on a plane \mathbb{R}^2 , for instance a tangent plane or an equatorial plane. We call the projection *global* when it maps the whole manifold bijectively on the plane. Then the idea is to lift WT from \mathbb{R}^2 to \mathcal{M} by inverse projection \mathbf{p}^{-1} . When no such global projection is available, but only a restricted one, from the subset $\mathcal{N} \subset \mathcal{M}$ to the plane, the analysis may still be performed, but locally. As we will see in the sequel, this method applies both to the CWT and to the DWT. Concrete examples with global projections for \mathcal{M} we have in mind are the two-sphere \mathbb{S}^2 , the upper sheet of the two-sheeted hyperboloid \mathcal{H} and the paraboloid \mathcal{P} .

In Section 5.1.1, we describe several types of projections from the manifold \mathcal{M} on a plane, stereographic, vertical, conical, radial. Then, in Section 5.1.2, we describe the construction of a *global* CWT on \mathcal{M} . Here we have to distinguish whether \mathcal{M} admits a global isometry group, as \mathbb{S}^2 or \mathcal{H} , or does not have one, as \mathcal{P} . For the hyperboloid, \mathcal{H} , a CWT has been designed by Bogdanova *et al.* [15] using the group-theoretical approach translated from the corresponding (dual) case of the sphere and projection from \mathcal{H} onto the tangent cone. In particular, the method starts from the $\text{SO}_0(2,1)$ invariant metric on \mathcal{M} and exploits the harmonic analysis on \mathcal{M} provided by the Fourier-Helgason transform. However, the resulting CWT has not been discretized and no DWT is known. For the paraboloid \mathcal{P} , there is no global isometry group, so that the group-theoretical method is not directly applicable. A tentative has been put forward by Honnouvo [55], but it is not really conclusive (and it is again limited to the continuous transform). Further comments on this approach may be found in [6]. But in this case, or more general ones, one can only build a *local* CWT on \mathcal{M} , that is, in a (possibly large) neighborhood of a fixed point of \mathcal{M} , and this new result is described in Section 5.1.3. Here the major difficulty is of (differential) geometrical nature, namely, how to glue together the various local CWTs into a global one.

In all these methods, the measure on \mathcal{M} and the projection onto \mathbb{R}^2 are determined by geometry (group theory). However, the measure is not dilation invariant and the projection does not preserve areas, which forces one to introduce correction factors. In the method presented in Section 5.2, on the contrary, we use the projections $\mathcal{M} \rightarrow \mathbb{R}^2$ described in Section 2.4, that preserves area and is bijective. As a consequence, it induces a unitary map between $L^2(\mathcal{M})$ and $L^2(\mathbb{R}^2)$. Inverting the latter, we can then lift all operations from the plane to \mathcal{M} , in particular, producing unitary operators on $L^2(\mathcal{M})$ that implement translations, rotations and dilations in the plane. In this way, the representation of the similitude group of the plane, that underlines the 2D plane CWT, is lifted to \mathcal{M} as well. Thus we have all the necessary ingredients for constructing a multiresolution analysis and a DWT on \mathcal{M} (Section 5.2.1), that does not show distortions, due to the area preserving property. In the same way, we design

a CWT on \mathcal{M} (Section 5.2.2), with no need to use explicitly a given measure. In fact, all calculations are performed in the plane, not on \mathcal{M} , exploiting the unitarity of the map that links the corresponding L^2 spaces. This in a sense reverses the perspective and makes the method both simpler and more efficient.

5.1 Wavelet analysis on manifolds via projections onto a plane

Given a two-dimensional manifold \mathcal{M} and a bijective projection \mathbf{p} from \mathcal{M} on a fixed plane (or a subset of that plane), we will show how a wavelet transform (WT) on \mathcal{M} may be generated from a planar WT by the inverse projection \mathbf{p}^{-1} . Examples where the projection maps the whole manifold onto a plane include the two-sphere, the upper sheet of the two-sheeted hyperboloid and the paraboloid. When no such global projection is available, the construction may be performed locally, i.e., around a given point on \mathcal{M} . We apply this procedure both to the Continuous WT, already treated in the literature, and to the Discrete WT [7, 108].

5.1.1 Geometry of projections

Let \mathcal{M} be a C^1 -surface defined by the equation $\zeta = \zeta(\mathbf{x}) = (\zeta_1(x, y), \zeta_2(x, y), \zeta_3(x, y))$, $\mathbf{x} = (x, y) \in D \subseteq \mathbb{R}^2$. We consider the function $J : D \rightarrow \mathbb{R}$,

$$J(x, y) = \left| \frac{\partial \zeta}{\partial x} \times \frac{\partial \zeta}{\partial y} \right|.$$

Let $\mathbf{p} : \mathcal{M} \rightarrow D$ denote the projection of the surface \mathcal{M} onto the plane Oxy , that is

$$\mathbf{p}(\zeta_1(x, y), \zeta_2(x, y), \zeta_3(x, y)) = (x, y), \text{ for all } (x, y) \in D.$$

This projection is bijective and its inverse is obviously

$$\mathbf{p}^{-1} : D \rightarrow \mathcal{M}, \quad \mathbf{p}^{-1}(x, y) = (\zeta_1(x, y), \zeta_2(x, y), \zeta_3(x, y)).$$

We say that \mathbf{p} is global if $D = \mathbb{R}^2$, and local if D is a proper subset of \mathbb{R}^2 .

The relations between $d\mathbf{x} = dx dy$, the area element of \mathbb{R}^2 , and $d\mu(\zeta)$, the area element of \mathcal{M} , are

$$\begin{aligned} d\mu(\zeta) &= J(\mathbf{x}) d\mathbf{x}, \\ d\mathbf{x} &= \frac{1}{(J \circ \mathbf{p})(\zeta)} d\mu(\zeta), \text{ where } \zeta = (\zeta_1, \zeta_2, \zeta_3) \in \mathcal{M}. \end{aligned}$$

In $L^2(\mathcal{M})$ we define the scalar product $\langle \cdot, \cdot \rangle_*$ as

$$\langle \mathcal{F}, \mathcal{G} \rangle_* = \langle \mathcal{F} \circ \mathbf{p}^{-1}, \mathcal{G} \circ \mathbf{p}^{-1} \rangle_{L^2(D)}, \text{ for all } \mathcal{F}, \mathcal{G} \in L^2(\mathcal{M}). \quad (5.1)$$

If we consider the function $\nu : \mathcal{M} \rightarrow \mathbb{R}$, $\nu = (J \circ \mathbf{p})^{-1/2}$, then one has

$$\langle \mathcal{F}, \mathcal{G} \rangle_* = \int_D \overline{\mathcal{F}(\mathbf{p}^{-1}(x, y))} \mathcal{G}(\mathbf{p}^{-1}(x, y)) dx dy = \int_{\mathcal{M}} \overline{\mathcal{F}(\zeta)} \mathcal{G}(\zeta) \nu^2(\zeta) d\mu(\zeta).$$

Thus, the scalar product $\langle \cdot, \cdot \rangle_*$ is a weighted scalar product, with the weight function ν^2 . If we use the projection that preserves areas, recently introduced in [109] and described in Section 2.4, one can use the usual scalar product of $L^2(\mathcal{M})$ instead of the weighted one $\langle \cdot, \cdot \rangle_*$.

On the other hand, if $F, G \in L^2(D)$ are given, then

$$\langle F, G \rangle_{L^2(D)} = \int_D \overline{F(\mathbf{x})} G(\mathbf{x}) d\mathbf{x} = \int_{\mathcal{M}} \overline{F(\mathbf{p}(\zeta))} G(\mathbf{p}(\zeta)) \nu^2(\zeta) d\mu(\zeta),$$

which means that

$$\langle F, G \rangle_{L^2(D)} = \langle \nu \cdot (F \circ \mathbf{p}), \nu \cdot (G \circ \mathbf{p}) \rangle_{L^2(\mathcal{M})}, \quad (5.2)$$

or, using the definition (5.1), one can write

$$\langle F \circ \mathbf{p}, G \circ \mathbf{p} \rangle_* = \langle F \circ \mathbf{p} \circ \mathbf{p}^{-1}, G \circ \mathbf{p} \circ \mathbf{p}^{-1} \rangle_{L^2(D)} = \langle F, G \rangle_{L^2(D)}. \quad (5.3)$$

In other words, the map

$$\pi^{-1} : F \mapsto \mathcal{F} := \nu \cdot (F \circ \mathbf{p}) \quad (5.4)$$

is unitary from $L^2(D)$ onto $L^2(\mathcal{M})$ and, similarly, the map $F \mapsto F \circ \mathbf{p}$ from $L^2(D)$ onto $L^2(\mathcal{M}, *)$, i.e., \mathcal{M} with the scalar product (5.1). In particular, this implies that, if the functions $F, G \in L^2(D)$ are orthogonal with respect to the usual scalar product of $L^2(D)$, then:

- $\nu \cdot (F \circ \mathbf{p}) \in L^2(\mathcal{M})$, $\nu \cdot (G \circ \mathbf{p}) \in L^2(\mathcal{M})$ and they are orthogonal with respect to the usual scalar product of $L^2(\mathcal{M})$;
- $F \circ \mathbf{p} \in L^2(\mathcal{M})$, $G \circ \mathbf{p} \in L^2(\mathcal{M})$ and they are orthogonal with respect to the weighted scalar product defined in (5.1).

These facts will allow us to use any orthogonal wavelet basis defined on D in order to construct an orthogonal wavelet basis defined on the manifold \mathcal{M} .

An important property of the scalar product $\langle \cdot, \cdot \rangle_*$ is given in the next proposition.

Proposition 5.1 *If there exist $m, M \in (0, \infty)$ such that*

$$m \leq \nu(\zeta) \leq M, \text{ for all } \zeta \in \mathcal{M}, \quad (5.5)$$

then the norm $\| \cdot \|_ = \langle \cdot, \cdot \rangle_*^{1/2}$, induced by the scalar product $\langle \cdot, \cdot \rangle_*$, is equivalent to the usual 2-norm of $L^2(\mathcal{M})$.*

Proof. It is immediate that

$$m^2 \mathcal{F}^2(\zeta) \leq \nu^2(\zeta) \mathcal{F}^2(\zeta) \leq M^2 \mathcal{F}^2(\zeta),$$

for all $\zeta = (\zeta_1, \zeta_2, \zeta_3) \in \mathcal{M}$. Thus, integrating on \mathcal{M} , we obtain

$$m \|\mathcal{F}\|_2 \leq \|\mathcal{F}\|_* \leq M \|\mathcal{F}\|_2.$$

■

Now we consider some particular cases. If the manifold \mathcal{M} is a surface of revolution and the projection \mathbf{p} conserves the longitude, it is more natural to use polar coordinates $\zeta = (s, \varphi)$ on \mathcal{M} , with $\varphi \in [0, 2\pi)$, the longitude angle, and s a coordinate along the section $\varphi = \text{const}$. Then, in planar polar coordinates (r, φ) , the projection reads $\mathbf{p}(\zeta) = \mathbf{p}(s, \varphi) = (r(s), \varphi)$.

A. The stereographic projection

(a) Stereographic projection of the two-sphere

With the notations in Section 5.1.1, let \mathcal{M} be the pointed two-sphere $\mathring{S}^2 = \{(\zeta_1, \zeta_2, \zeta_3) \in \mathbb{R}^3, \zeta_1^2 + \zeta_2^2 + (\zeta_3 - 1)^2 = 1\} \setminus \{(0, 0, 2)\}$ and let $\mathbf{p} : \mathcal{M} \rightarrow \mathbb{R}^2$ be the stereographic projection from the North Pole $N(0, 0, 2)$ onto the tangent plane at the South Pole. If we take polar coordinates $\zeta = (\theta, \varphi)$, where $s = \theta \in [0, \pi)$ is the colatitude and $\varphi \in [0, 2\pi)$ is the longitude, then the stereographic projection is given by $r(\theta) = 2 \tan \frac{\theta}{2}$, and it is the only longitude preserving projection that is conformal [132].

Then one can easily see that

$$\nu(\zeta) = \frac{2}{2 - \zeta_3} = \frac{1}{\sin^2 \frac{\theta}{2}},$$

and this function does not satisfy the condition (5.5) in Proposition 5.1. The relations between ζ and $\mathbf{x} = \mathbf{p}(\zeta)$ are

$$x = \zeta_1 \nu(\zeta), \quad y = \zeta_2 \nu(\zeta),$$

and

$$\zeta_1 = x \varrho(\mathbf{x}), \quad \zeta_2 = y \varrho(\mathbf{x}), \quad \zeta_3 = \frac{1}{2}(x^2 + y^2) \varrho(\mathbf{x}),$$

with $\varrho(\mathbf{x}) = 4(x^2 + y^2 + 4)^{-1}$. Yet we still have a unitary map between $L^2(\mathbb{R}^2)$ and $L^2(\mathring{S}^2)$.

(b) Stereographic projection of the two-sheeted hyperboloid

Consider the upper sheet \mathcal{H}_+ of the two-sheeted hyperboloid \mathcal{H} , given by the explicit equation

$$\zeta_3 = \sqrt{1 + \zeta_1^2 + \zeta_2^2}.$$

The stereographic projection from the South Pole of \mathcal{H} maps the upper sheet \mathcal{H}_+ onto the open unit disk in the equatorial plane $\zeta_3 = 0$ (it maps the lower sheet onto the exterior of the unit disk). In terms of polar coordinates $\zeta = (\chi, \varphi)$, where $\chi \geq 0$ and $\varphi \in [0, 2\pi)$ is the longitude, the stereographic projection is given by $r(\chi) = \tanh \frac{\chi}{2}$. Then a direct computation yields

$$\nu(\zeta) = \nu(\chi, \varphi) = \frac{1}{2 \cosh^2 \frac{\chi}{2}}.$$

Thus one has $0 \leq \nu(\zeta) \leq \frac{1}{2}$ and condition (5.5) is not satisfied.

B. The vertical projection

Suppose that the surface \mathcal{M} is given by the explicit equation $z = f(\mathbf{x})$, $\mathbf{x} = (x, y) \in D \subseteq \mathbb{R}^2$. In this case we consider the vertical projection $\mathbf{p} : \mathcal{M} \rightarrow D$,

$$\mathbf{p}(x, y, f(x, y)) = (x, y), \quad \text{for all } (x, y) \in D.$$

The function ν is

$$\nu = \left[1 + \left(\frac{\partial f}{\partial x} \right)^2 + \left(\frac{\partial f}{\partial y} \right)^2 \right]^{-1/4}$$

and the relations between $\zeta = (\zeta_1, \zeta_2, \zeta_3) \in \mathcal{M}$ and $(x, y) = \mathbf{p}(\zeta)$ are

$$x = \zeta_1, \quad y = \zeta_2$$

and

$$\zeta_1 = x, \quad \zeta_2 = y, \quad \zeta_3 = f(x, y).$$

(a) Vertical projection of the two-sphere

Let \mathcal{M} be a unit sphere centered in $(0, 0, 1)$. Then the two hemispheres obey the equations

$$z = 1 \pm \sqrt{1 - x^2 - y^2}.$$

Obviously the corresponding function ν does not satisfy the condition (5.5).

(b) Vertical projection of the hyperboloid

Consider again the upper sheet of the (general) two-sheeted hyperboloid, given by the explicit equation

$$z = c\sqrt{1 + \frac{x^2}{a^2} + \frac{y^2}{b^2}}$$

(the normalized case \mathcal{H}_+ correspond to $a = b = c = 1$). The calculation shows that

$$\nu(\zeta) = \left(1 + \frac{c^2}{a^2b^2} \cdot \frac{b^4\zeta_1^2 + a^4\zeta_2^2}{b^2\zeta_1^2 + a^2\zeta_2^2 + a^2b^2}\right)^{-1/4}$$

and condition (5.5) is satisfied with

$$M = 1, \quad m = \left(1 + \frac{c^2}{\min\{a^2, b^2\}}\right)^{-1/4}$$

For the normalized case \mathcal{H}_+ , the vertical projection yields $r(\chi) = \sinh \chi$ and

$$\nu(\zeta) = \left(1 + \tanh^2 \frac{\theta}{2}\right)^{-1/4}.$$

(c) Vertical projection of the paraboloid

Consider the elliptic paraboloid with explicit equation

$$z = \frac{x^2}{a^2} + \frac{y^2}{b^2}.$$

Simple calculations show that

$$\nu(\zeta) = \frac{ab}{(4b^4\zeta_1^2 + 4a^4\zeta_2^2 + a^4b^4)^{1/4}}$$

and obviously the function ν does not satisfy condition (5.5) in Proposition 5.1.

C. The conical projection of the hyperboloid

In the case of the two-sheeted hyperboloid \mathcal{H}_+ , an alternative consists in projecting it first on its tangent half null-cone

$$\mathcal{C}_+^2 = \{\mathbf{x} = (z, x, y) \in \mathbb{R}^3 : z^2 - x^2 - y^2 = 0, z > 0\},$$

then vertically on the plane $z = 0$. The result is $r(\chi) = 2 \sinh \frac{\chi}{2}$. In fact, there is an infinite family of projections from \mathcal{H}_+ onto the plane $z = 0$, leading to $r(\chi) = \frac{1}{p} \sinh p\chi$, but the case $p = \frac{1}{2}$ seems the most natural one. More details may be found in [6, 14, 15].

The same technique can be used for the one-sheeted hyperboloid $\mathcal{H}^{1,1}$, of equation $z^2 = -1 + x^2 + y^2$, which has the same tangent null-cone $\mathcal{C}^2 = \{\mathbf{x} = (z, x, y) \in \mathbb{R}^3 : z^2 - x^2 - y^2 = 0\}$.

5.1.2 Constructing a global CWT on the manifold \mathcal{M}

In order to build a CWT on the manifold \mathcal{M} , one starts by identifying the operations one wants to perform on the finite energy signals living on \mathcal{M} , that is, functions in $L^2(\mathcal{M}, d\mu)$, where μ is a suitable measure on \mathcal{M} . Next one realizes these operations by unitary operators on $L^2(\mathcal{M}, d\mu)$. Mimicking the flat case, the required transformations are of two types: (i) *motions*, which are realized by isometries of \mathcal{M} , and (ii) *dilations* of some sort by a scale factor $a > 0$. In addition, one may look for a possible group-theoretical derivation.

For motions, we may distinguish two cases, depending whether \mathcal{M} admits a global isometry group or not. As for dilations, the problem is how to define properly them *on* the manifold \mathcal{M} itself. One possibility is to lift them, by an inverse projection, from dilations in a tangent plane or cone, that is, the dilation on \mathcal{M} is defined as

$$D_a^{(\mathcal{M})} : \mathfrak{p}^{-1} \circ d_a \circ \mathfrak{p}, \quad (5.6)$$

where \mathfrak{p} is the projection of \mathcal{M} on the plane or cone and d_a is the known dilation on the latter.

A. \mathcal{M} with global isometry group

In the first class, manifolds which admit a global isometry group, we find the two-sphere \mathbb{S}^2 and the two-sheeted hyperboloid. Their isometry group are the (compact) rotation group $\text{SO}(3)$ and the (noncompact) Lorentz-type group $\text{SO}_o(2, 1)$, respectively.

(a) *The two-sphere* \mathbb{S}^2

The construction of a CWT on the two-sphere \mathbb{S}^2 with help of the stereographic projection has been thoroughly treated in the literature [2, 3, 4], so we just quote the results.

- (1) The spherical CWT of a function $f \in L^2(\mathbb{S}^2, d\mu)$ with respect to the (admissible) wavelet ψ is defined as

$$W_f(\varrho, a) := \langle \psi_{\varrho, a}, f \rangle = \int_{\mathbb{S}^2} \overline{\psi_a(\varrho^{-1}\zeta)} f(\zeta) d\mu(\zeta), \quad \varrho \in \text{SO}(3), a > 0, \quad (5.7)$$

where μ is the usual rotation invariant measure on \mathbb{S}^2 and $\psi_a(\zeta) := \lambda(a, \theta)^{1/2} \psi(\zeta_{1/a})$, $a > 0$. In these relations, $\zeta_a = (\theta_a, \varphi)$, θ_a is defined by $\cot \frac{\theta_a}{2} = a \cot \frac{\theta}{2}$ for $a > 0$ and the normalization factor $\lambda(a, \theta)^{1/2}$ (Radon-Nikodym derivative) is needed for compensating the noninvariance of the measure μ under dilation. Clearly the operator $f(\zeta) \mapsto f(\zeta_{1/a})$ is built on the model (5.6), with \mathfrak{p} the stereographic projection.

- (2) The transform (5.7) has all the properties of the plane CWT: exact inversion (reconstruction formula), reproducing kernel, etc. In addition, it has a correct Euclidean limit. That is, if we construct the transform on a sphere of radius R and then let $R \rightarrow \infty$, the spherical CWT tends to the usual plane 2D CWT on the tangent plane at the South Pole.
- (3) The transform (5.7) can be obtained by a group-theoretical derivation (the so-called coherent state method), using the Lorentz group $\text{SO}_o(3, 1)$ (which is the conformal group both of \mathbb{S}^2 and of its tangent plane \mathbb{R}^2).
- (4) The unitary map π^{-1} defined in (5.4) allows to generate a spherical wavelet $\pi^{-1}(\psi)$ from any plane 2D wavelet ψ . Examples are the familiar Mexican hat, Difference-of-Gaussians, and Morlet wavelets. The latter, in particular, behaves on the sphere exactly as its plane counterpart does on the plane [2].

- (5) Discretization of the spherical CWT leads to various types of (generalized) frames, either half-continuous (only the scale variable is discretized) or fully discrete. Technical details may be found in [13].

(b) The two-sheeted hyperboloid \mathcal{H}

This case is entirely parallel to the previous one, replacing $\text{SO}(3)$ by the isometry group $\text{SO}_o(2, 1)$, the elements of which are of two types: (i) rotations : $x(\chi, \varphi) \mapsto (\chi, \varphi + \varphi_0)$; and (ii) hyperbolic motions : $x(\chi, \varphi) \mapsto (\chi + \chi_0, \varphi)$. As for dilations, a choice has to be made, each type being defined by one of the available projections described above. Details may be found in [14, 15].

- (1) Given an (admissible) hyperbolic wavelet ψ , the hyperbolic CWT of $f \in L^2(\mathcal{H}_+)$ with respect to ψ is

$$\mathcal{W}_f(g, a) := \langle \psi_{g,a}, f \rangle = \int_{\mathcal{H}_+} \overline{\psi_a(g^{-1}\zeta)} f(\zeta) d\mu(\zeta), \quad g \in \text{SO}_o(2, 1), a > 0. \quad (5.8)$$

As in the spherical case, $\psi_a(x) = \lambda(a, \zeta)\psi(d_{1/a}\zeta)$, with d_a an appropriate dilation, and $\lambda(a, x)$ is the corresponding Radon-Nikodym derivative. Once again, this operation is built on the model (5.6).

- (2) The key for developing the CWT is the possibility of performing harmonic analysis on \mathcal{H}_+ , including a convolution theorem, thanks to the so-called Fourier-Helgason transform. As a consequence, the usual properties hold true, for instance, an exact reconstruction formula.
- (3) However, no result is known concerning frames that would be obtained by discretization.

(c) The one-sheeted hyperboloid $\mathcal{H}^{1,1}$

The same analysis can be made for the one-sheeted hyperboloid $\mathcal{H}^{1,1}$, since it has the same isometry group $\text{SO}_o(2, 1)$, the same tangent null-cone \mathcal{C}^2 , hence the same type of conical projections, and a Fourier-Helgason-type transform with the required properties [10, 19].

B. \mathcal{M} without global isometry group

If the manifold \mathcal{M} does not admit a global isometry group, the previous method cannot be used. A case in point is the axisymmetric paraboloid \mathcal{P} , of equation $z = x^2 + y^2$. A group-theoretical tentative exists [55], based on a homeomorphism from a cylinder onto the pointed paraboloid $\dot{\mathcal{P}} := \mathcal{P} \setminus \{0\}$, but it does not produce convincing results, in particular, the formalism does not allow for a local dilation around an arbitrary point. Some additional details may be found in [6].

This being so, an alternative consists in lifting the wavelets from the tangent plane at the origin onto \mathcal{P} , using the inverse vertical projection. Another one is to define a *local* wavelet transform, as explained in the next section in the case of a general manifold.

5.1.3 CWT on a general manifold: Local wavelet transform

For simplicity, we continue to assume that \mathcal{M} is a smooth 2D surface. However, the analysis extends easily to a smooth manifold of arbitrary dimension n . Let $\mathfrak{H} = L^2(\mathcal{M}, d\mu)$ be the Hilbert space of square-integrable functions on \mathcal{M} , for a proper measure $d\mu$, with scalar product $\langle \cdot, \cdot \rangle_{\mathfrak{H}}$. In the following $T_{\zeta}(\mathcal{M})$ will denote the tangent space at $\zeta \in \mathcal{M}$.

Our construction is entirely local and rooted in differential geometry. At any point $\zeta \in \mathcal{M}$, we start by constructing a prototype wavelet. Generally speaking, this is a square integrable function $\psi^{(\zeta)} \in \mathfrak{H}$ that is compactly supported in a neighborhood \mathcal{B}_ζ of $\zeta \in \mathcal{M}$. The size of \mathcal{B}_ζ will depend on the local geometry of \mathcal{M} . The second step is to define a suitable local dilation operator. In order to exploit dilations in \mathbb{R}^n , we will equip \mathcal{M} with a local Euclidean structure by mapping \mathcal{B}_ζ to $T_\zeta(\mathcal{M})$. A simple way to implement this mapping is by *flattening* \mathcal{B}_ζ along the normal to \mathcal{M} at ζ . Let \mathfrak{p}_ζ be that local flattening map:

$$\mathfrak{p}_\zeta : \mathcal{B}_\zeta \mapsto T_\zeta(\mathcal{M}). \quad (5.9)$$

In order for that mapping to be useful, we choose the size of \mathcal{B}_ζ such that \mathfrak{p}_ζ is a diffeomorphism.

Let $\alpha \in \mathcal{B}_\zeta$. A local dilation of coordinates is defined as in (5.6):

$$\alpha \mapsto \alpha_a = \mathfrak{p}_\zeta^{-1} \circ a \circ \mathfrak{p}_\zeta(\alpha). \quad (5.10)$$

Obviously, the definition of \mathfrak{p}_ζ sets a local maximum scale $a_{\max}^{(\zeta)}$ so that (5.10) is well-defined.

We can now easily construct a dilation operator acting on functions with support in \mathcal{B}_ζ . For convenience, we will denote by $\mathfrak{H}(\mathcal{B}_\zeta)$ this subspace of \mathfrak{H} . Given $\psi^{(\zeta)} \in \mathfrak{H}(\mathcal{B}_\zeta)$, the following operator maps $\mathfrak{H}(\mathcal{B}_\zeta)$ unitarily to itself:

$$D_\zeta(a) : \psi^{(\zeta)}(\alpha) \mapsto \lambda^{1/2}(a, \alpha) \psi^{(\zeta)}(\alpha_{a^{-1}}),$$

where, as usual,

$$\lambda(a, \alpha) = \frac{d\mu(\alpha_{a^{-1}})}{d\mu(\alpha)}$$

is the corresponding Radon-Nikodym derivative that takes care of the possible noninvariance of the measure μ under dilation. For the sake of compactness, we will use the shorter notation $\psi_a^{(\zeta)} := D_\zeta(a)\psi^{(\zeta)}$. Note that, by construction, D_ζ will be continuous as a function of ζ provided the normal to \mathcal{M} at ζ varies smoothly.

Given a signal $f \in \mathfrak{H}$, we can now define its wavelet transform at $\zeta \in \mathcal{M}$ and scale a as

$$\mathcal{W}_f(\zeta, a) = \langle \psi_a^{(\zeta)}, f \rangle_{\mathfrak{H}}. \quad (5.11)$$

The inverse transform will take the general form:

$$f = \int_{\mathcal{M}} d\mu(\zeta) \int_0^{a_\psi(\zeta)} \frac{da}{a^\beta} \mathcal{W}_f(\zeta, a) \psi_a^{(\zeta)}.$$

The bound $a_\psi(\zeta)$ used in this formula is a cut-off ensuring that the support of the dilated wavelet $\psi_{a_\psi(\zeta)}^{(\zeta)}$ stays under control, i.e., $\text{supp}(\psi_{a_\psi(\zeta)}^{(\zeta)}) \subset \mathcal{B}_\zeta$. As for the exponent β , it depends on the manifold at hand and serves the same purpose.

The case of the circle

As an example of the preceding construction, but in dimension 1, we take the case where $\mathcal{M} = \mathbb{S}^1$, the unit circle in \mathbb{R}^2 and perform the calculation explicitly. The same calculation will then yield the CWT on the two-sphere generated by the vertical projection.

Construction of local dilations

In this case, $\mathfrak{H} = L^2(\mathbb{S}^1, d\alpha)$ and ζ is the angle $\varphi \in \mathbb{S}^1$. A simple calculation shows that the flattening map (5.9) has the following explicit form:

$$\mathbf{p}_\varphi(\alpha) = \sin(\alpha - \varphi).$$

Obviously, \mathbf{p}_φ coincides with the vertical projection defined in Section 5.1.1(a). In particular, for $\varphi = -\pi/2$ (the South ‘‘Pole’’), $\mathbf{p}_{-\pi/2}(\alpha) = \cos \alpha$, as it should.

This operation is defined in a neighborhood of size π centered on φ , i.e., $\mathcal{B}_\varphi = [\varphi - \pi/2, \varphi + \pi/2]$. A dilation of coordinates around φ will then be given by

$$\alpha \mapsto \alpha_a = \arcsin(a \sin(\alpha - \varphi)) + \varphi, \quad a > 0, \quad (5.12)$$

and the maximum local dilation that can be applied to a point α is $a_{\max} = |\sin(\alpha - \varphi)|^{-1}$.

In order to define the dilation operator acting on $\mathfrak{H}(\mathcal{B}_\varphi)$, we first compute the Radon-Nikodym derivative:

$$\lambda(a, \alpha) = \frac{d\alpha_{a^{-1}}}{d\alpha} = \frac{\cos(\alpha - \varphi)}{\sqrt{a^2 - \sin^2(\alpha - \varphi)}}.$$

It is easy to check that indeed it satisfies a cocycle relation: $\lambda^{-1}(a, \alpha_a)\lambda(a, \alpha) = 1$. If $\psi^{(\varphi)}$ is a bounded function compactly supported in $[\varphi - \Delta, \varphi + \Delta] \subset \mathcal{B}_\varphi$, we have

$$\psi_a^{(\varphi)}(\alpha) = \lambda(a, \alpha)^{1/2} \psi^{(\varphi)}(\alpha_{a^{-1}}), \quad (5.13)$$

and the maximal dilation applicable to the wavelet $\psi^{(\varphi)}$ is

$$a_\psi(\varphi) = |\sin(\varphi + \Delta - \varphi)|^{-1} = |\sin \Delta|^{-1}.$$

Local wavelet transform

The wavelet transform at φ then reads as follows:

$$\begin{aligned} \mathcal{W}_f(\varphi, a) &= \int_0^{2\pi} \overline{\psi_a^{(\varphi)}(\alpha)} f(\alpha) d\alpha \\ &= \int_0^{2\pi} \lambda(a, \alpha)^{1/2} \overline{\psi^{(\varphi)}(\arcsin(a^{-1} \sin(\alpha - \varphi)) + \varphi)} f(\alpha) d\alpha. \end{aligned} \quad (5.14)$$

In this particular case, we have a nice group of translations acting on the circle, so that we can write any locally defined function $\psi^{(\varphi)}$ as

$$\psi^{(\varphi)}(\alpha) = \psi(\alpha - \varphi).$$

Acting with $D_\varphi(a)$ on this function yields a simpler expression for the dilation. Namely, combining (5.13) and (5.12), we get immediately

$$\psi_a^{(\varphi)} = \psi_a(\alpha - \varphi).$$

Inserting this expression in (5.14) we see that the continuous wavelet transform takes the familiar form of a convolution between the signal f and the dilated wavelet:

$$\mathcal{W}_f(\varphi, a) = \int_0^{2\pi} d\alpha \left(\frac{\cos(\alpha - \varphi)}{\sqrt{a^2 - \sin^2(\alpha - \varphi)}} \right)^{1/2} \overline{\psi(\arcsin(a^{-1} \sin(\alpha - \varphi)) + \varphi)} f(\alpha). \quad (5.15)$$

Admissibility condition and reconstruction

We impose the following form for the reconstruction integral, to be understood in the strong sense:

$$A_\psi f(\alpha) = \int_0^{2\pi} d\varphi \int_0^{a_\psi(\varphi)} \frac{da}{a^2} \mathcal{W}_f(\varphi, a) \psi_a(\alpha - \varphi). \quad (5.16)$$

The following theorem shows that the operator A_ψ is actually a simple Fourier multiplier.

Theorem 5.2 (Admissibility condition) *Let $\psi \in \mathfrak{H}$ and $\mathfrak{m}, \mathfrak{M}$ two constants such that, for all $n \in \mathbb{Z}$, one has*

$$0 < \mathfrak{m} \leq \mathcal{A}_\psi(n) = \int_0^{a_\psi(\varphi)} |\widehat{\psi}_a(n)|^2 \frac{da}{a^2} \leq \mathfrak{M} < +\infty, \quad (5.17)$$

where $\widehat{\psi}_a(n)$ is a Fourier coefficient of ψ_a . Then the linear operator A_ψ defined in (5.16) is bounded with bounded inverse. In other words, the family of wavelets $\{\psi_a^{(\varphi)}, \varphi \in S^1, 0 < a \leq a_\psi(\varphi)\}$ is a frame, with frame bounds $\mathfrak{m}, \mathfrak{M}$. More precisely A_ψ is uniquely characterized by the following Fourier multiplier:

$$\widehat{A_\psi f}(n) \equiv \widehat{A_\psi} f(n) = \widehat{f}(n) \int_0^{a_\psi} |\widehat{\psi}_a(n)|^2 \frac{da}{a^2} = \mathcal{A}_\psi(n) \widehat{f}(n).$$

It should be noted that, here as in the standard construction [20], the admissibility condition and the reconstruction formula do *not* depend on the explicit form of dilation chosen. In all cases, the unique ingredient is the dilated wavelet $\psi_a^{(\varphi)}$ and its Fourier coefficients, no matter how the dilation is defined.

5.1.4 Generalizations

The last remark allows us to treat the case of the two-sphere exactly as in the standard derivation described at length in the papers [3, 2] and summarized briefly in Section 5.1.2 (a). The treatment extends to the n -sphere as well [5].

We may also generalize the treatment of the circle directly, using the vertical projection defined in Section 5.1.1(a). Indeed, since the two-sphere is invariant under rotation around any axis, the projection process takes place in a section of fixed longitude, that is, a circle. Let us fix the point $\zeta_0 = (\theta_0, \varphi_0) \in \mathbb{S}^2$. Then vertical projection \mathfrak{p}_{ζ_0} means projection along the axis $O\zeta_0$ onto T_{ζ_0} , the plane tangent at ζ_0 . This projection is given by

$$\mathfrak{p}_{\zeta_0}(\theta, \varphi) = (\sin(\theta - \theta_0), \varphi) \in T_{\zeta_0}, \quad \zeta_0 = (\theta_0, \varphi_0).$$

For instance, if we take $\theta_0 = \pi$ (the usual vertical projection on the plane tangent at the South Pole S), then $\mathfrak{p}_{\zeta_0}(\theta, \varphi) = (\sin \theta, \varphi)$ (in polar coordinates in the tangent plane T_S). The corresponding formula for an arbitrary point $\zeta_0 = (\theta_0, \varphi_0)$ may be obtained by performing a rotation of θ_0 around the axis Ox , but the result is not illuminating.

This being said, there remains an open problem, namely, how to go from a local WT to a global one. In other words, how can we go from one point to another one on \mathcal{M} . In the language of differential geometry, this means going from one local chart to the next one, and the tools for that are available. For example, in the case of the sphere \mathbb{S}^2 (or the circle), one needs two charts, one for each hemisphere, with an overlap around the equator, a well-known problem familiar to physicists of the 1970s in the context of a proper treatment of magnetic monopoles, for instance. Clearly, some work remains to be done here on the wavelet side.

5.1.5 Lifting the DWT onto \mathcal{M}

A similar construction may be performed for the other conic sections, the upper sheet of the two sheeted hyperboloid \mathcal{H} (using any of the conical projections described in Section 5.1.1 or the vertical projection, since the stereographic projection is somewhat pathological) and the paraboloid (using the vertical projection).

5.2 Wavelet analysis on some surfaces of revolution via area preserving projection

The results obtained in this section were published in [109]. In the sequel, we denote by \mathcal{M} a 2D surface of revolution obtained by rotating a piecewise smooth plane curve around a line in its plane, such that one end point of the curve is the only point of intersection with the line and each plane perpendicular to the line intersects the curve at most once. For the construction of a multiresolution analysis of $L^2(\mathcal{M})$ and a CWT on \mathcal{M} we also need to suppose that the curve that generates the surface has infinite length. Classical examples are the paraboloid, the two-sheeted hyperboloid, or the cone. Applied to the sphere, our projection is in fact Lambert's azimuthal projection, which has a nice geometrical interpretation. However, the present method for constructing a CWT and DWT does not apply to the sphere. But a similar approach may be designed in the case when the generating curve has finite length (thus including the case of the sphere), based on a mapping from a square onto a disc, followed by a lifting to the sphere by inverse Lambert projection [107, 112]. This case is discussed in Section 2.4.5.

We shall consider the case of a general surface of revolution, then particularize to the paraboloid, the upper sheet of the two-sheeted hyperboloid and the positive part of the cone, all axisymmetric. These three manifolds are the ones that are the most useful for applications, as we have already mentioned before.

5.2.1 Multiresolution analysis of $L^2(\mathcal{M})$

Functions in $L^2(\mathcal{M})$

We will restrict ourselves to the case when the generating curve φ has infinite length. Let \mathcal{M} be the surface of revolution considered before, given by the parametric equations

$$\xi = \xi(X, Y) = (x(X, Y), y(X, Y), z(X, Y)), \quad (X, Y) \in \mathbb{R}^2,$$

where the expressions of x, y, z are given in (2.44)-(2.46) for the paraboloid, (2.49)-(2.51) for the hyperboloid and (2.52)-(2.54) for the cone. We also consider the projection $\mathbf{p} : \mathcal{M} \rightarrow \mathbb{R}^2$ described in Section 2.4. This projection is obviously bijective and its inverse is $\mathbf{p}^{-1} : \mathbb{R}^2 \rightarrow \mathcal{M}$,

$$\mathbf{p}^{-1}(X, Y) = \xi(X, Y) = (x(X, Y), y(X, Y), z(X, Y)).$$

We have seen in Section 2.4 that \mathbf{p} preserves the area, so that the area element $d\omega(\xi)$ of \mathcal{M} equals the element area $dXdY = d\mathbf{x}$ of \mathbb{R}^2 . Therefore, for all $\tilde{f}, \tilde{g} \in L^2(\mathcal{M})$ we have

$$\begin{aligned} \langle \tilde{f}, \tilde{g} \rangle_{L^2(\mathcal{M})} &= \int_{\mathcal{M}} \overline{\tilde{f}(\xi)} \tilde{g}(\xi) d\omega(\xi) \\ &= \int_{\mathbf{p}(\mathcal{M})} \overline{\tilde{f}(\mathbf{p}^{-1}(X, Y))} \tilde{g}(\mathbf{p}^{-1}(X, Y)) dXdY \\ &= \langle \tilde{f} \circ \mathbf{p}^{-1}, \tilde{g} \circ \mathbf{p}^{-1} \rangle_{L^2(\mathbb{R}^2)} \end{aligned} \tag{5.18}$$

and similarly, for all $f, g \in L^2(\mathbb{R}^2)$ we have

$$\langle f, g \rangle_{L^2(\mathbb{R}^2)} = \langle f \circ \mathbf{p}, g \circ \mathbf{p} \rangle_{L^2(\mathcal{M})}. \quad (5.19)$$

Consider now the map $\Pi : L^2(\mathcal{M}) \rightarrow L^2(\mathbb{R}^2)$, induced by the projection \mathbf{p} , defined by

$$(\Pi \tilde{f})(X, Y) = \tilde{f}(\mathbf{p}^{-1}(X, Y)), \text{ for all } \tilde{f} \in L^2(\mathcal{M}).$$

Its inverse $\Pi^{-1} : L^2(\mathbb{R}^2) \rightarrow L^2(\mathcal{M})$ is

$$(\Pi^{-1} f)(\xi) = f(\mathbf{p}(\xi)), \text{ for all } f \in L^2(\mathbb{R}^2).$$

From equalities (5.18) and (5.19) it follows that Π is a unitary map, that is,

$$\begin{aligned} \langle \Pi \tilde{f}, \Pi \tilde{g} \rangle_{L^2(\mathbb{R}^2)} &= \langle \tilde{f}, \tilde{g} \rangle_{L^2(\mathcal{M})}, \\ \langle \Pi^{-1} f, \Pi^{-1} g \rangle_{L^2(\mathcal{M})} &= \langle f, g \rangle_{L^2(\mathbb{R}^2)}. \end{aligned}$$

Equality (5.19) is the key equality of this construction. It allows us to establish the following results, whose proof is immediate:

Proposition 5.3 *Let J be a countable set and let $\{f_k\}_{k \in J} \subseteq L^2(\mathbb{R}^2)$. For each $k \in J$ we define $\tilde{f}_k \in L^2(\mathcal{M})$ as $\tilde{f}_k = f_k \circ \mathbf{p}$. Then we have:*

1. *If $\{f_k\}_{k \in J}$ is an orthonormal basis of $L^2(\mathbb{R}^2)$, then $\{\tilde{f}_k\}_{k \in J}$ is an orthonormal basis of $L^2(\mathcal{M})$;*
2. *If $\{f_k\}_{k \in J}$ is a Riesz basis of $L^2(\mathbb{R}^2)$ with Riesz constants A, B , then $\{\tilde{f}_k\}_{k \in J}$ is a Riesz basis of $L^2(\mathcal{M})$ with the same Riesz constants;*
3. *If $\{f_k\}_{k \in J}$ is a frame of $L^2(\mathbb{R}^2)$ with frame bounds A, B , then $\{\tilde{f}_k\}_{k \in J}$ is a frame of $L^2(\mathcal{M})$ with the same frame bounds.*

Multiresolution analysis (MRA) and wavelet bases of $L^2(\mathbb{R}^2)$

In order to fix our notations, we will briefly review in this section the standard construction of 2D orthonormal wavelet bases in the flat case, starting from a multiresolution analysis (MRA) [70].

Let D be a 2×2 regular matrix with the properties

- (a) $D\mathbb{Z}^2 \subset \mathbb{Z}^2$, which is equivalent to the fact that D has integer entries,
- (b) $\lambda \in \sigma(D) \implies |\lambda| > 1$, that is, all eigenvalues of D have modulus greater than 1.

A multiresolution analysis of $L^2(\mathbb{R}^2)$ associated to D is an increasing sequence of closed subspaces $\mathbf{V}_j \subset L^2(\mathbb{R}^2)$ with $\bigcap_{j \in \mathbb{Z}} \mathbf{V}_j = \{0\}$ and $\overline{\bigcup_{j \in \mathbb{Z}} \mathbf{V}_j} = L^2(\mathbb{R}^2)$, and satisfying the following conditions:

- (1) $f \in \mathbf{V}_j \iff f(D \cdot) \in \mathbf{V}_{j+1}$,
- (2) There exists a function $\Phi \in L^2(\mathbb{R}^2)$ such that the set $\{\Phi(\cdot - \mathbf{k}), \mathbf{k} \in \mathbb{Z}^2\}$ is an orthonormal basis of \mathbf{V}_0 .

As a consequence, $\{\Phi_{j,\mathbf{k}} := |\det D|^{j/2} \Phi(D^j \cdot -\mathbf{k}), \mathbf{k} \in \mathbb{Z}^2\}$ is an orthonormal basis for \mathbf{V}_j .

For each $j \in \mathbb{Z}$, let us define the space \mathbf{W}_j as the orthogonal complement of \mathbf{V}_j into \mathbf{V}_{j+1} , i.e., $\mathbf{V}_{j+1} = \mathbf{V}_j \oplus \mathbf{W}_j$. The two-dimensional wavelets are those functions which span \mathbf{W}_0 . One can prove (see [76]) that there exist $q = |\det D| - 1$ wavelets ${}^1\Psi, {}^2\Psi, \dots, {}^q\Psi \in \mathbf{V}_1$ that generate an orthonormal basis of \mathbf{W}_0 . Therefore, $\{\lambda\Psi_{j,\mathbf{k}} := |\det D|^{j/2} \cdot \lambda\Psi(D^j \cdot -\mathbf{k}), \lambda = 1, \dots, q, \mathbf{k} \in \mathbb{Z}^2\}$ is an orthonormal basis of \mathbf{W}_j for each j , and $\{\lambda\Psi_{j,\mathbf{k}}, \lambda = 1, \dots, q, \mathbf{k} \in \mathbb{Z}^2, j \in \mathbb{Z}\}$ is an orthonormal basis of $L^2(\mathbb{R}^2)$.

A particular case is that of tensor product wavelets, corresponding to the dilation matrix $D = \text{diag}[2, 2]$ and a 1-D MRA with scaling function and mother wavelet ϕ, ψ . In this case, $q = 3$ and one gets the 2D scaling function $\Phi(x, y) = \phi(x)\phi(y)$ and the three wavelets

$${}^h\Psi(x, y) = \phi(x)\psi(y), \quad {}^v\Psi(x, y) = \psi(x)\phi(y), \quad {}^d\Psi(x, y) = \psi(x)\psi(y).$$

If the one-dimensional functions ϕ and ψ have compact support, then obviously so have Φ and $\lambda\Psi$. This is the case of the well-known Daubechies wavelets.

Multiresolution analysis and orthonormal wavelet bases of $L^2(\mathcal{M})$

The construction of multiresolution analysis and wavelet bases in $L^2(\mathcal{M})$ is based on the equality (5.19). To every function $f \in L^2(\mathbb{R}^2)$, one can associate the function $f^{\mathcal{M}} \in L^2(\mathcal{M})$ as

$$f^{\mathcal{M}} = f \circ \mathfrak{p}.$$

In particular, if the functions $\{f_{j,\mathbf{k}}\}_{j,\mathbf{k}}$ are orthogonal, so are

$$f_{j,\mathbf{k}}^{\mathcal{M}} = f_{j,\mathbf{k}} \circ \mathfrak{p}, \text{ for } j \in \mathbb{Z}, \mathbf{k} \in \mathbb{Z}^2.$$

Then, taking $f = \Phi$ and $f = \Psi$, we obtain the functions on \mathcal{M}

$$\Phi_{j,\mathbf{k}}^{\mathcal{M}} = \Phi_{j,\mathbf{k}} \circ \mathfrak{p}, \quad \lambda\Psi_{j,\mathbf{k}}^{\mathcal{M}} = \lambda\Psi_{j,\mathbf{k}} \circ \mathfrak{p}. \quad (5.20)$$

For $j \in \mathbb{Z}$, we define the spaces \mathcal{V}_j as

$$\mathcal{V}_j = \{f \circ \mathfrak{p}, f \in \mathbf{V}_j\}.$$

Using (5.19) and the unitarity of the map Π , it is immediate that \mathcal{V}_j is a closed subspace of $L^2(\mathcal{M})$, thus a Hilbert space. Moreover, these spaces have the following properties:

- (1) $\mathcal{V}_j \subset \mathcal{V}_{j+1}$ for $j \in \mathbb{Z}$,
- (2) $\bigcap_{j \in \mathbb{Z}} \mathcal{V}_j = \{0\}$ and $\overline{\bigcup_{j \in \mathbb{Z}} \mathcal{V}_j} = L^2(\mathcal{M})$,
- (3) The set $\{\Phi_{0,\mathbf{k}}^{\mathcal{M}}, \mathbf{k} \in \mathbb{Z}^2\}$ is an orthonormal basis for \mathcal{V}_0 .

We will say that a sequence of subspaces of $L^2(\mathcal{M})$ with the properties above constitutes a *multiresolution analysis* of $L^2(\mathcal{M})$.

Once the multiresolution analysis is determined, we construct the wavelet spaces \mathcal{W}_j in the usual manner. Let \mathcal{W}_j denote the orthogonal complement of the coarse space \mathcal{V}_j in the fine space \mathcal{V}_{j+1} , so that

$$\mathcal{V}_{j+1} = \mathcal{V}_j \oplus \mathcal{W}_j.$$

One can easily prove that, for each $j \in \mathbb{Z}$, $\{\lambda\Psi_{j,\mathbf{k}}^{\mathcal{M}}, \mathbf{k} \in \mathbb{Z}^2, \lambda = 1, \dots, q\}$ is an orthogonal basis for \mathcal{W}_j and therefore $\{\lambda\Psi_{j,\mathbf{k}}^{\mathcal{M}}, j \in \mathbb{Z}, \mathbf{k} \in \mathbb{Z}^2, \lambda = 1, \dots, q\}$ is an orthonormal basis for $\overline{\bigoplus_{j \in \mathbb{Z}} \mathcal{W}_j} = L^2(\mathcal{M})$.

The conclusion of the analysis may be summarized as follows:

- If Φ has compact support in \mathbb{R}^2 , then $\Phi_{j,\mathbf{k}}^{\mathcal{M}}$ has *compact support* on \mathcal{M} (indeed $\text{diam supp } \Phi_{j,\mathbf{k}}^{\mathcal{M}} \rightarrow 0$ as $j \rightarrow \infty$).
- An *orthonormal/Riesz* 2D wavelet basis leads to an *orthonormal/Riesz* basis of wavelets on \mathcal{M} .
- *Smooth* 2D wavelets lead to *smooth* wavelets on \mathcal{M} , if the curve that generates the surface is smooth.
- In particular, plane tensor product Daubechies wavelets lead to locally supported and orthonormal wavelets on \mathcal{M} , and so do plane tensor product Haar wavelets.
- The decomposition and reconstruction matrices needed in the case of \mathcal{M} are the same as in the plane 2D case, so that the latter can be used (with existing toolboxes).

5.2.2 Continuous wavelet transform on \mathcal{M}

We consider again the case when the generating curve φ has infinite length. The construction of the CWT on \mathcal{M} follows naturally from the CWT in the 2D case. So let us remind the 2D CWT [4].

In order to describe the motions in \mathbb{R}^2 , one uses the following unitary operators in the space $L^2(\mathbb{R}^2)$:

- (a) translation: $(T_{\mathbf{b}}s)(\mathbf{x}) = s(\mathbf{x} - \mathbf{b})$, $\mathbf{b} \in \mathbb{R}^2$;
- (b) dilation: $(D_a s)(\mathbf{x}) = a^{-1}s(a^{-1}\mathbf{x})$, $a > 0$;
- (c) rotation: $(R_{\theta}s)(\mathbf{x}) = s(r_{-\theta}(\mathbf{x}))$, $\theta \in [0, 2\pi)$,

where $s \in L^2(\mathbb{R}^2)$ and r_{θ} is the rotation matrix

$$r_{\theta} = \begin{pmatrix} \cos \theta & -\sin \theta \\ \sin \theta & \cos \theta \end{pmatrix}.$$

Combining the three operators, we define the unitary operator

$$U(\mathbf{b}, a, \theta) = T_{\mathbf{b}}D_aR_{\theta},$$

which acts on a given function s as

$$[U(\mathbf{b}, a, \theta)s](\mathbf{x}) = s_{\mathbf{b},a,\theta}(\mathbf{x}) = a^{-1}s(a^{-1}r_{-\theta}(\mathbf{x} - \mathbf{b})).$$

Their analogues on \mathcal{M} will be defined as follows: We define the following unitary operators in the space $L^2(\mathcal{M})$:

- (a) translation: $(\mathcal{T}_{\mathbf{b}}\tilde{s})(\eta) := T_{\mathbf{b}}(\tilde{s} \circ \mathbf{p}^{-1})(\mathbf{p}(\eta)) = (\tilde{s} \circ \mathbf{p}^{-1})(\mathbf{p}(\eta) - \mathbf{b})$, $\mathbf{b} \in \mathbb{R}^2$;
- (b) dilation: $(\mathcal{D}_a\tilde{s})(\eta) := D_a(\tilde{s} \circ \mathbf{p}^{-1})(\mathbf{p}(\eta)) = a^{-1}(\tilde{s} \circ \mathbf{p}^{-1})(a^{-1}\mathbf{p}(\eta))$, $a > 0$;
- (c) rotation: $(\mathcal{R}_{\theta}\tilde{s})(\eta) := R_{\theta}(\tilde{s} \circ \mathbf{p}^{-1})(\mathbf{p}(\eta)) = (\tilde{s} \circ \mathbf{p}^{-1})(\tilde{r}_{-\theta}(\mathbf{p}(\eta))) = \tilde{s}(\tilde{r}_{-\theta}(\eta))$, $\theta \in [0, 2\pi)$,

where $\tilde{s} \in L^2(\mathcal{M})$, $\eta \in \mathcal{M}$ and \tilde{r}_θ is the rotation matrix around Oz

$$\tilde{r}_\theta = \begin{pmatrix} \cos \theta & -\sin \theta & 0 \\ \sin \theta & \cos \theta & 0 \\ 0 & 0 & 1 \end{pmatrix}.$$

Their combination gives rise to the operator $\mathcal{U}(\mathbf{b}, a, \theta) = \mathcal{T}_{\mathbf{b}} \mathcal{D}_a \mathcal{R}_\theta$, which can be written as

$$[\mathcal{U}(\mathbf{b}, a, \theta)\tilde{s}](\eta) = a^{-1}(\tilde{s} \circ \mathbf{p}^{-1})(a^{-1}r_\theta(p(\eta) - \mathbf{b})).$$

These operators on $L^2(\mathcal{M})$ are also unitary, as follows from the unitarity of the map Π .

A wavelet Ψ on \mathbb{R}^2 is defined as a function in $L^2(\mathbb{R}^2)$ satisfying the admissibility condition

$$C_\Psi := (2\pi)^2 \int_{\mathbb{R}^2} \frac{|\widehat{\Psi}(\mathbf{y})|^2}{|\mathbf{y}|^2} d\mathbf{y} < \infty,$$

where the Fourier transform $\widehat{\Psi}$ of Ψ is defined as

$$\widehat{\Psi}(\mathbf{y}) = \frac{1}{2\pi} \int_{\mathbb{R}^2} e^{i\mathbf{x} \cdot \mathbf{y}} \Psi(\mathbf{x}) d\mathbf{x}.$$

The question now is how to define a Fourier transform on $L^2(\mathcal{M})$ and an admissible wavelet in $L^2(\mathcal{M})$. The natural way to define the Fourier transform of a signal $\tilde{s} \in L^2(\mathcal{M})$ is the following:

$$\begin{aligned} \widehat{\tilde{s}}(\eta) &:= \widehat{\tilde{s} \circ \mathbf{p}^{-1}}(\mathbf{p}(\eta)) \\ &= \frac{1}{2\pi} \int_{\mathbb{R}^2} e^{-i\mathbf{p}(\eta) \cdot \mathbf{x}} (\tilde{s} \circ \mathbf{p}^{-1})(\mathbf{x}) d\mathbf{x} \\ &= \frac{1}{2\pi} \int_{\mathcal{M}} e^{-i\mathbf{p}(\eta) \cdot \mathbf{p}(\xi)} \tilde{s}(\xi) d\omega(\xi). \end{aligned} \tag{5.21}$$

The last equality was obtained by writing $\mathbf{x} = \mathbf{p}(\xi)$, with $\xi \in \mathcal{M}$, and by taking into account the equality $d\mathbf{x} = d\omega(\xi)$, proved in Section 2.4.

Further, for the constant C_Ψ we obtain

$$\begin{aligned} C_\Psi &= (2\pi)^2 \int_{\mathbb{R}^2} \frac{|\widehat{\Psi}(\mathbf{y})|^2}{|\mathbf{y}|^2} d\mathbf{y} = \int_{\mathcal{M}} \frac{|(\widehat{\Psi} \circ \mathbf{p})(\xi)|^2}{|\mathbf{p}(\xi)|^2} d\omega(\xi) \\ &= \int_{\mathcal{M}} \frac{|(\widehat{\Psi \circ \mathbf{p}})(\xi)|^2}{l^2(\xi)} d\omega(\xi). \end{aligned}$$

In the first equality we put $\mathbf{y} = \mathbf{p}(\xi)$ and in the second we used the definition (5.21) for $\tilde{s} \circ \mathbf{p}^{-1} = \Psi$. By $l(\xi)$ we have denoted the length of the curve $\widetilde{O\xi} = \mathbf{p}^{-1}(\overline{OM'}) \subset \mathcal{M}$, $\overline{OM'}$ being the segment with endpoints O and $M' = \mathbf{p}(\xi)$.

Thus, we can define a *wavelet* $\Psi^{\mathcal{M}}$ in $L^2(\mathcal{M})$ either by $\Psi^{\mathcal{M}} = \Psi \circ \mathbf{p}$, with Ψ a wavelet in $L^2(\mathbb{R}^2)$, or, equivalently, if it satisfies the admissibility condition

$$C_{\Psi^{\mathcal{M}}} = C_\Psi = \int_{\mathcal{M}} \frac{|(\widehat{\Psi \circ \mathbf{p}})(\xi)|^2}{l^2(\xi)} d\omega(\xi) < \infty.$$

We can now proceed to the definition of CWT for functions in $L^2(\mathcal{M})$. In the 2D case, one defines

$$\begin{aligned}\Psi_{\mathbf{b},a,\theta} &= U(\mathbf{b}, a, \theta)\Psi, \text{ with } (\mathbf{b}, a, \theta) \in \mathcal{G}, \\ \mathcal{G} &= \{(\mathbf{b}, a, \theta), \mathbf{b} \in \mathbb{R}^2, a > 0, \theta \in [0, 2\pi)\},\end{aligned}$$

and one can prove (see [4], p. 35) that the set

$$\text{span}\{\Psi_{\mathbf{b},a,\theta}, (\mathbf{b}, a, \theta) \in \mathcal{G}\}$$

is dense in $L^2(\mathbb{R}^2)$. Then, the CWT of a signal $s \in L^2(\mathbb{R}^2)$ with respect to the wavelet Ψ is defined as

$$(W_{\Psi}s)(\mathbf{b}, a, \theta) := \langle \Psi_{\mathbf{b},a,\theta}, s \rangle_{L^2(\mathbb{R}^2)}.$$

For a wavelet $\Psi^{\mathcal{M}}$, we will define, for $(\mathbf{b}, a, \theta) \in \mathcal{G}$, the functions

$$\Psi_{\mathbf{b},a,\theta}^{\mathcal{M}} := \mathcal{U}(\mathbf{b}, a, \theta)\Psi^{\mathcal{M}}.$$

These functions will also satisfy the admissibility condition, so that they are also wavelets. Moreover, simple calculations show that the set

$$\text{span}\{\Psi_{\mathbf{b},a,\theta}^{\mathcal{M}}, (\mathbf{b}, a, \theta) \in \mathcal{G}\}$$

is dense in $L^2(\mathcal{M})$.

Finally, we can give the definition of CWT on \mathcal{M} .

Definition 5.1 *Given a wavelet $\Psi^{\mathcal{M}}$ and a signal $\tilde{s} \in L^2(\mathcal{M})$, the continuous wavelet transform of \tilde{s} with respect to the wavelet $\Psi^{\mathcal{M}}$ is defined as*

$$(\mathcal{W}_{\Psi^{\mathcal{M}}}\tilde{s})(\mathbf{b}, a, \theta) := \langle \Psi_{\mathbf{b},a,\theta}^{\mathcal{M}}, \tilde{s} \rangle_{L^2(\mathcal{M})}.$$

This CWT can also be written as

$$\begin{aligned}(\mathcal{W}_{\Psi^{\mathcal{M}}}\tilde{s})(\mathbf{b}, a, \theta) &= \langle \Psi_{\mathbf{b},a,\theta}^{\mathcal{M}}, \tilde{s} \rangle_{L^2(\mathcal{M})} \\ &= \langle \mathcal{U}(\mathbf{b}, a, \theta)\Psi^{\mathcal{M}}, \tilde{s} \rangle_{L^2(\mathcal{M})} \\ &= \langle U(\mathbf{b}, a, \theta)(\Psi^{\mathcal{M}} \circ \mathbf{p}^{-1}), \tilde{s} \circ \mathbf{p}^{-1} \rangle_{L^2(\mathbb{R}^2)} \\ &= \langle \Psi_{\mathbf{b},a,\theta}, s \rangle_{L^2(\mathbb{R}^2)} \\ &= (W_{\Psi}s)(\mathbf{b}, a, \theta).\end{aligned}$$

By performing a composition with \mathbf{p} on the right in the reconstruction formula for the 2D case, the following reconstruction formula holds in $L^2(\mathcal{M})$:

$$\tilde{s}(\eta) = C_{\Psi^{\mathcal{M}}}^{-1} \iiint_J \Psi_{\mathbf{b},a,\theta}^{\mathcal{M}}(\eta) (\mathcal{W}_{\Psi^{\mathcal{M}}}\tilde{s})(\mathbf{b}, a, \theta) d\mathbf{b} \frac{da}{a^3} d\theta.$$

Finally, let us mention that any discretization of the 2D CWT can be moved onto \mathcal{M} , preserving the stability properties.

Conclusion

The approach presented in this section allows us to move *any* construction of wavelets defined on \mathbb{R}^2 to a surface of revolution \mathcal{M} , which is piecewise smooth and has infinite area. Although the equal area projection \mathbf{p} that we have described in Section 2.4 has no nice geometrical interpretation as the Lambert azimuthal projection, this is not important for implementations, as long as we have explicit formulas for \mathbf{p} . Moreover, through this approach, the numerical behavior of planar 2D wavelets is inherited by the wavelets on \mathcal{M} . This implies, in particular, that both CWT and DWT on \mathcal{M} have the same properties as the usual, planar ones. For this reason, we consider that there is no need to present particular examples. Finally we note that the definition of the continuous Fourier transform on \mathcal{M} given in formula (5.21) can be used for defining a much simpler discrete Fourier transform than the one in [27].

5.2.3 Wavelets by combining two area preserving projections

The grids obtained in Section 2.4.5 can be used in constructing wavelets. More precisely, we can design constructions similar to the ones in Sections 5.2.1 and 5.2.2, if instead of projection \mathbf{p} we use the projection $\mathbf{p}^{-1} \circ T$. When applied to infinite surfaces, most of the properties are preserved. When applied to finite surfaces, there are some differences:

1. First, the multiresolution analysis is not any more the one described in Section 5.2.1, but the one described in Section 4.1 for the sphere and bounded domains. Moreover, we have to start from existing construction of wavelets on a finite 2D-interval (square) and transport them onto \mathcal{M} by the procedure described in [92, 105].

2. An adaptation of CWT by the same procedure described in Section 5.2.2 is not possible, since the operators $T_{\mathbf{b}}$ and D_a needs an infinite surface \mathcal{M} .

Perspectives

Scientific and academic career

Idealistic perspectives

The expected outcome of this Habilitation should be a promotion to the rank of Full Professor. There are several motivations for this.

1. A better hierarchical position within the department, more facilities for obtaining research grants, for traveling and attending conferences abroad, all these being vital conditions for a harmonious scientific career. In the same vein, a better access to international networks, typically EU Research/Training networks.
2. The possibility to teach graduate (Master and Doctoral) courses. My two textbooks [115, 116] are the basis of the undergraduate courses I am teaching presently. In the same way, my more recent book [114] would be a reliable support for a Master or Doctoral course on Wavelet Analysis. This is indeed a highly successful theory, with great interest, both in mathematics (e.g. approximation theory) and for applications in extremely diverse fields of physics, applied mathematics or engineering. Nowadays a lot of universities in widely diverse fields include in their curricula such a course. Moreover, during the period 2007-2011, I was an invited Professor in the third cycle (doctorate) at the Catholic University of Louvain-la-Neuve (Belgium), 4 weeks/year, teaching seminars mainly on Wavelets on the sphere and other manifolds. Therefore, it seems desirable that a course on wavelet should be included in the mathematics curricula of our technical universities, along more basic ones in Functional analysis and Approximation theory.
3. In the same vein, the possibility of supervising Master and PhD students. The Master and Doctoral theses are crucial first steps in a scientific life and also a significant source of satisfaction, both for the student and for the supervisor, especially when one meets a bright student.
4. Last, but not least of course, a better remuneration.

Realistic perspectives

Given the present circumstances, as a mathematician in a Technical University all I can hope from the Habilitation certificate is to obtain a position of Full Professor in the Department of Mathematics at Technical University of Cluj-Napoca.

Regarding future cooperation, I hope that I will have the same success in obtaining financial support from foreign universities and foreign research councils, allowing me to collaborate with foreign scientists and their PhD students, during some research visits abroad.

Prospective research

Considering the various research themes I have followed up to now and the results I have obtained, I could envisage a number of developments.

1. The idea of area preserving projections could be pursued and applied to other explicit examples. An unsolved problem, with great interest in theoretical physics, is the construction of wavelets on a torus. My method might be applicable, treating separately two half-tori, exactly as one does with the two hemispheres of the sphere.
2. The wavelet bases on the sphere or other manifolds, obtained by lifting them from the plane, should be applied explicitly to a number of situations. For instance, in optics, in the catadioptric image processing or in the treatment of omnidirectional images, which has plenty of engineering applications. In statistics also, our spherical wavelet bases should be compared with the so-called needlets [75, 117].
3. Our method should be applied to lifting from the plane to the sphere of the various generalizations of wavelets, such as ridgelets [21, 22, 125], curvelets [23, 25, 22, 26, 123, 125], wedgelets [39, 69], or shearlets [34, 51, 58, 62, 63]. This last item also raises a number of interesting mathematical questions related to the so-called coorbit method [33].
4. In the long range, our method might help to formulate for spherical data the fashionable approach of compressed sensing, based on the requirement of sparsity of representations [40].
5. For real-time applications one needs fast algorithms and a way to have them is to make use of Parallel Programming. Since most of the times the Wavelet transform is a local one, most of the wavelet algorithms can be parallelized.
6. We have introduced new grids on the sphere by transporting arbitrary grids of a square, therefore we have a rich choice of systems of uniformly or almost uniformly distributed points on the sphere. An interesting topic would be to investigate whether such points can form fundamental systems, and also to investigate the cubature formulas associated to them.
7. For the Continuous Wavelet Transform on the Hyperboloid [14, 15], no discretization leading to stable bases or to frames is known. The uniform grids on surfaces of revolutions give a large choice for the choose of the discretization points. Therefore another topic would be to investigate the numerical properties of these discretizations, more precisely to investigate whether they can lead to frames or to stable bases.

Bibliography

- [1] R. Alexander, *On the sum of distances between N points on the sphere*, Acta Math. 23 (1972), 443–448.
- [2] J-P. Antoine, L. Demanet, L. Jacques, P. Vandergheynst, *Wavelets on the sphere: Implementation and approximations*, Applied Comput. Harmon. Anal. 13 (2002) 177–200.
- [3] J-P. Antoine, P. Vandergheynst, *Wavelets on the 2-sphere: A group-theoretical approach*, Appl. Comput. Harmon. Anal. 7 (1999) 262–291 .
- [4] J-P. Antoine, R. Murenzi, P. Vandergheynst, S.T. Ali, *Two-Dimensional Wavelets and their Relatives*, Cambridge University Press, Cambridge, UK, 2004.
- [5] J-P. Antoine P. Vandergheynst, *Wavelets on the n -sphere and other manifolds*, J. Math. Phys. 39 (1998) 3987–4008.
- [6] J-P. Antoine, I. Bogdanova, P. Vandergheynst, *The continuous wavelet transform on conic sections*, Int. J. Wavelets, Multires. Inf. Proc. 6 (2007) 137–156.
- [7] J-P. Antoine, **D. Roşca**, *The wavelet transform on the two-sphere and related manifolds - A review* (invited paper), Proceedings of SPIE, Optical and Digital Image Processing, vol. 7000 (2008), B-1-15.
- [8] J-P. Antoine, **D. Roşca**, P. Vandergheynst, *Wavelet transform on manifolds: old and new approaches*, Appl. Comput. Harmon. Anal. 28, 2 (2010), 189–202.
- [9] F. Arandiga, A. Cohen, R. Donat, N. Dyn, B. Matei, *Approximation of piecewise smooth functions şi images by edge-adapted (ENO-EA) nonlinear multiresolution techniques*, Appl. Comput. Harmon. Anal. 24 (2008), 225–250.
- [10] A. Askari Hemmat and Z. Yazdani Fard, *Continuous wavelet transform on the one-sheeted hyperboloid*, preprint.
- [11] J. Beckmann, *Quadraturformeln über sphärische Dreiecke*, PhD. Thesis, Univ. Lübeck, 2010.
- [12] S.N. Bernstein, *On a system of undetermined equations*, in: Selected Papers, vol. 2: Constructive function theory, 236-242 (1956) (in Russian).
- [13] I. Bogdanova, P. Vandergheynst, J-P. Antoine, L. Jacques, M. Morvidone, *Stereographic wavelet frames on the sphere*, Appl. Comput. Harmon. Anal. 26 (2005) 223–252
- [14] I. Bogdanova, *Wavelets on non-Euclidean manifolds*, PhD thesis, EPFL, 2005.
- [15] I. Bogdanova, P. Vandergheynst, J-P. Gazeau, *Continuous wavelet transform on the hyperboloid*, Appl. Comput. Harmon. Anal. 23 (2007), 285–306.

- [16] I. Bogdanova, X. Bresson, J-Ph. Thiran, P. Vandergheynst, *Scale space analysis and active contours for omnidirectional images*, IEEE Trans. Image Process. 16,7 (2007), 1888–1901.
- [17] G-P. Bonneau, *Optimal triangular Haar bases for spherical data*, in Visualization '99 (eds. M. Gross, D.S. Ebert și B. Hamann) IEEE Computer Society Press, CA (1999), pp. 279–284.
- [18] X. Bresson, T.F. Chan, *Non-local unsupervised variational image segmentation models*, preprint, 2008.
- [19] J. Bros, U. Moschella, *Fourier analysis and holomorphic decomposition on the one-sheeted hyperboloid*, preprint, arXiv:math-ph/0311052v1 27 Nov 2003.
- [20] M. Calixto, J. Guerrero, *Wavelet transform on the circle and the real line: A unified group-theoretical treatment*, Applied Comput. Harmon. Anal. 21 (2006) 204–229.
- [21] E. J. Candès, *Ridgelets: Theory and Applications*, Ph.D. Thesis, Department of Statistics, Stanford University, 1998.
- [22] E. J. Candès and D. L. Donoho, *New tight frames of curvelets and optimal representations of objects with piecewise C^2 singularities*, Commun. Pure Appl. Math. 57 (2004) 219–266.
- [23] E. J. Candès and D. L. Donoho, *Continuous curvelet transform. I. Resolution of the wave-front set; II. Discretization and frames*, Appl. Comput. Harmon. Anal. 19 (2005) 162–197; 198–222.
- [24] E. J. Candès and L. Demanet, *The curvelet representation of wave propagators is optimally sparse*, Commun. Pure Appl. Math., 58 (2005) 1472–1528.
- [25] E. J. Candès, L. Demanet, D. Donoho and L. Ying, *Fast discrete curvelet transforms*, Multiscale Model. Simul.5 (2006) 861–899.
- [26] E.J. Candès, L. Demanet, D.L. Donoho, L. Ying, *Fast discrete curvelet transforms*, Multiscale Model. Simul. 5 (2006), 861–899.
- [27] M. Calixto, J. Guerrero, J.C. Sánchez-Monreal, *Sampling theorem și discrete Fourier transform on the hyperboloid*, J. Fourier Anal. Appl., 17, 2 (2011), 240–264.
- [28] T.F. Chan, S. Esedoglu, M. Nikolova, *Algorithms for finding global minimizers of denoising și segmentation models*, SIAM J. Appl. Math. 66 (2006), 1632–1648.
- [29] R.L. Claypole, G.M. Davis, W. Sweldens, R.G. Baraniuk (2003) *Nonlinear wavelet transforms for image coding via lifting*, IEEE Trans. Image Process. 12 (2003), 1449–1459.
- [30] A. Cohen, B. Matei, (2001) *Compact representation of images by edge adapted multiscale transforms*, Proc. IEEE Int Conf on Image Proc (ICIP), Thessaloniki, 2001, pp. 8–11.
- [31] S. Dahlke, W. Dahmen, I. Weinreich, *Multiresolution Analysis și Wavelets on S^2 și S^3* , Numer. Func. Anal. Optim. 16 (1995), 19–41.
- [32] S. Dahlke, P. Maass, *Continuous Wavelet transforms with Applications to Analyzing Functions on the Spheres*, J. Fourier Anal. Appl. 2 (1996), 379–396.
- [33] S. Dahlke, G. Kutyniok, G. Steidl, G. Teschke, *Shearlet coorbit Spaces and associated Banach frames*, Appl. Comput. Harmon. Anal. 27 (2009), 195–214.

- [34] S. Dahlke, G. Steidl, G. Teschke, *The continuous shearlet transform in arbitrary space dimensions*, J. Fourier Anal. Appl. 16 (2010), 340–364.
- [35] S. Dekel, D. Leviatan, *Adaptive multivariate approximation using binary space partitions și geometric wavelets*, SIAM J. Numer. Anal. 43 (2006), 707–732.
- [36] L. Demaret, N. Dyn, A. Iske, *Image compression by linear splines over adaptive triangulations*, Signal Process. 86 (2006), 1604–1616.
- [37] W. Ding, F. Wu, X. Wu, S. Li, H. Li, *Adaptive directional lifting-based wavelet transform for image coding*, IEEE Trans. Image Process. 16 (2007), 416–427.
- [38] M.N. Do, M. Vetterli, *The contourlet transform: An efficient directional multiresolution image representation*, IEEE Trans. Image Process. 14 (2005) 2091–2106.
- [39] D.L. Donoho (1999) *Wedgelets: Nearly minimax estimation of edges*, Ann. Stat. 27 (1999), 859–897.
- [40] D. Donoho, *Compressed sensing*, IEEE Trans. Inform. Th. 52, 4 (2006), 1289–1306.
- [41] G.C. Donovan, J.S. Jeronimo, D.P. Hardin, *Compactly supported, piecewise affine scaling functions on triangulations*, Constr. Approx. 16, 2 (2000), 201–219.
- [42] G.C. Donovan, J.S. Jeronimo, D.P. Hardin, *Orthogonal polynomials and the construction of piecewise polynomial smooth wavelets*, SIAM J. Math. Anal. 30, 5 (1999), 1029–1056.
- [43] M. Floater, E. Quak, *Piecewise linear prewavelets on arbitrary triangulations*, Numer. Math. 82 (1999), 221–252.
- [44] W. Freeden, M. Schreiner, *Spaceborne gravitational field determination by means of locally supported wavelets*, J. Geodesy, 79 (2005), 431–446.
- [45] W. Freeden, U. Windheuser, *Combined spherical harmonics and wavelet expansions - A Future Concept in Earth's Gravitational Potential Determination*, Appl. Comput. Harm. Anal. 4 (1997), 1–37.
- [46] W. Freeden, M. Schreiner, *Biorthogonal locally supported wavelets on the sphere based on zonal kernel functions*, J. Fourier Anal. Appl. 13 (2007), 693–709.
- [47] C. Geyer, K. Daniilidis, *Catadioptric projective geometry*, Int. J. Comput. Vision, 45, 3 (2001), 223–243.
- [48] K.M. Górski, B.D. Wandelt, E. Hivon, A.J. Banday, B.D. Wandelt, F.K. Hansen, M. Reinecke, M. Bartelmann, *HEALPix: A framework for high-resolution discretization and fast analysis of data distributed on the sphere*, Astrophys. J. 622, 2 (2005), p. 759.
- [49] S. Gräf, S. Kunis, D. Potts, *On the computation of nonnegative quadrature weights on the sphere*, Appl. Comput. Harmon. Anal. 27, 1 (2009), 124–132.
- [50] E.W. Grafarend, F.W. Krumm, *Map Projections, Cartographic Information Systems*, Springer-Verlag, Berlin, 2006.
- [51] P. Grohs, *Continuous shearlet tight frames*, J. Fourier Anal. Appl. 17 (2011), 506–518.

- [52] K. Guo, W.Q. Lim, D. Labate, G. Weiss, E. Wilson, *Wavelets with composite dilations*, Electr. res. Announc. of AMS 10 (2004), 78–87.
- [53] K. Guo, D. Labate, *Optimally sparse multidimensional representation using shearlets*, SIAM J. Math. Anal. 39 (2007), 298–318.
- [54] M. Holschneider, *Continuous wavelet transforms on the sphere*, J. Math. Phys. 37 (1996), 4158–4165.
- [55] G. Honnouvo, *Gabor analysis and wavelet transforms on some non-Euclidean two dimensional manifolds*, PhD Thesis, Concordia Univ., Montreal, PQ, Canada, 2007.
- [56] L. Jacques, J.-P. Antoine, *Multiselective pyramidal decomposition of images: wavelets with adaptive angular selectivity*, Int. J. Wavelets Multiresolut. Inf. Process. 5 (2007), 785–814.
- [57] K. Jetter, J. Stöckler, J.D. Ward, *Norming sets and spherical cubature formulas*, in Z. Chen, C. Micchelli, Y. Xu (Eds.) *Advances in Computational Mathematics* New York, 1998, pp. 237–245.
- [58] P. Kittipoom, G. Kutyniok, W-Q. Lim, *Irregular shearlet frames: geometry and approximation properties*, J. Fourier Anal. Appl. 17 (2011), 604–639.
- [59] J. Krommweh, *An orthonormal basis of directional Haar wavelets on triangles*, Results Math. 53, 3-4 (2009) 323–331.
- [60] J. Krommweh, G. Plonka, *Directional Haar wavelet frames on triangles*, Appl. Comput. Harmon. Anal. 27 (2009), 215–234.
- [61] J. Krommweh, *Tetrolet Transform: A New Adaptive Haar Wavelet Algorithm for Sparse Image Representation*, J. Vis. Commun. 21, 4 (2010), 364–374.
- [62] G. Kutyniok, D. Labate, *Resolution of the wavefront set using continuous shearlets*, Trans. Amer. Math. Soc. 361 (2009), 2719–2754.
- [63] D. Labate, W-Q. Lim, G. Kutyniok, G. Weiss, *Sparse multidimensional representation using shearlets*, in *Wavelets XI (San Diego, CA, 2005)*, ed. by M. Papadakis, A. Laine, and M. Unser, SPIE Proc. 5914 (SPIE, Bellingham, WA, 2005) pp. 254–262.
- [64] N. Laín Fernández, *Polynomial bases on the sphere*, Logos-Verlag, Berlin, 2003.
- [65] N. Laín Fernández, *Localized polynomial bases on the sphere*, Electron. Trans. Numer. Anal. 19 (2005), 84–93.
- [66] P. Leopardi, *A partition of the unit sphere into regions of equal area and small diameter*, Electron. Trans. on Numer. Anal. 25 (2006), 309–327.
- [67] E. Le Pennec, S. Mallat, *Bandelet image approximation și compression*, Multiscale Model. Simul. 4 (2005), 992–1039.
- [68] C. Lessig, E. Fiume, *SOHO: Orthogonal and symmetric Haar wavelets on the sphere*, ACM Transactions on Graphics 27 1 (2008) article 4.
- [69] A. Lisowska, *Moment-based fast wedgelet transform*, J. Math. Imaging Vis. 39 (2011), 180–192.

- [70] A. Louis, P. Maass, A. Rieder, *Wavelets, Theory și Applications*, Wiley, Chichester, 1997.
- [71] M. Lounsbery, T. DeRose J. Warren, *Multiresolution analysis for surfaces of arbitrary topological type*, ACM Trans. Graphics 16(1997), 34–73.
- [72] S. Mallat, *A wavelet tour of signal processing*, Academic Press, San Diego, 1999.
- [73] J. Maes, A. Bultheel, *Smooth spline wavelets on the sphere*, in: A. Cohen, J-L. Merrien, L.L. Schumaker (Eds.), *Curves și Surface Fitting: Avignon 2006*, Nashboro Press, pp. 200–209.
- [74] S. Mallat (2009) *Geometrical grouplets*, Appl. Comput. Harmon. Anal. 26 (2009), 161–180.
- [75] D. Marinucci, D. Pietrobon, A. Baldi, P. Baldi, P. Cabella, G. Kerkyacharian, P. Natoli, D. Picard, and N. Vittorio, *Spherical needlets for CMB data analysis*, Mon. Not. R. Astron. Soc. **383** (2008) 539–545
- [76] Y. Meyer, *Wavelets and Operators*, Cambridge Studies in Advanced Mathematics, vol. 37, Cambridge University Press, Cambridge, UK, 1992.
- [77] H. N. Mhaskar, F. J. Narcowich, J. D. Ward, *Spherical Marcinkiewicz-Zygmund inequalities and positive quadrature*, Math. Comp. 70 (2001), 1113–1130.
- [78] H. N. Mhaskar, Q. T. Le Gia, *Localized linear polynomial operators and quadrature formulas on the sphere*, SIAM J. Numer. Anal. 47, 1 (2008), 440–466.
- [79] F. Narcowich, J. Ward, *Nonstationary Wavelets on the m -Sphere for Scattered Data*, Appl. Comput. Harm. Anal. 3 (1996), 324–336.
- [80] F. Narcowich and J.D. Ward, *Wavelets associated with periodic basis functions*, Appl. Comput. Harmon. Anal., 3 (1996), 40–56.
- [81] G. Nielson, I. Jung, J. Sung, *Haar wavelets over triangular domains with applications to multiresolution models for flow over a sphere*, in IEEE Visualization '97, IEEE 1997, pp. 143–150.
- [82] G. Peyré, S. Mallat, *Discrete bandelets with geometric orthogonal filters*, Proceedings of ICIP'05, Vol.1, 65–68, Sept. 2005.
- [83] G. Plonka, *The easy path wavelet transform: A new adaptive wavelet transform for sparse representation of two-dimensional data*, Multiscale Model. Simul. 7 (2009), 1474–1496.
- [84] G. Plonka, **D. Roșca**, *Easy path wavelet transform on triangulations of the sphere*, Math. Geosci. 42, no. 7 (2010), 839–855.
- [85] G. Plonka, S. Tenorth, **D. Roșca**, *A new hybrid method a for image compression using the Easy Path Wavelet Transform*, IEEE Trans. Image Process., 20, 2 (2011), 372–381.
- [86] G. Plonka, S. Tenorth, A. Iske, *Optimally sparse image representation by the easy path wavelet transform*, Int. J. Wav. Multiresolut. Process., to appear.
- [87] V. Pop, **D. Roșca**, *Generalized piecewise constant orthogonal wavelet bases on 2D-domains*, Appl. Anal. 90, 3–4 (2011), 715–723.

- [88] D. Potts, M. Tasche, *Interpolatory wavelets on the sphere*, in: Approximation Theory VIII (C.K.Chui, L.L. Schumaker, eds.), World Scientific, Singapore (1995), pp. 335–342.
- [89] D. Potts, G. Steidl, M. Tasche, *Kernels of spherical harmonics and spherical frames*, in: F. Fontanella, K. Jetter, P.J. Laurent (eds.) Advanced topics in multivariate Approximation, World Scientific, Singapore, 1996, pp. 287–30.
- [90] J. Prestin, **D. Roşca**, *On some cubature formulas on the sphere*, J. Approx. Theory 142 (2006), 1–19.
- [91] R.J. Renka, *Algorithm 772: STRIPACK: Delaunay Triangulation and Voronoi diagram on the surface of a sphere*, ACM Trans. Math. Softw. 23, 3 (1997), 416–434.
- [92] **D. Roşca**, *Locally supported rational spline wavelets on the sphere*, Math. Comput., 74, 252 (2005), 1803–1829.
- [93] **D. Roşca**, *Haar wavelets on spherical triangulations*, in: N. Dogson, M. Floater, M. Sabin (eds), Advances in Multiresolution for Geometric Modelling (series Mathematics and Visualization), Springer Verlag 2005, pp. 405–417.
- [94] **D. Roşca**, *Piecewise constant wavelets defined on closed surfaces*, J. Comput. Anal. Appl. 8, 2 (2006), 121–132.
- [95] **D. Roşca**, *On the degree of exactness of some positive formulas on the sphere*, Aut. Comput. Appl. Math. 15, 1 (2006), 283–288.
- [96] **D. Roşca**, *Optimal Haar wavelets on spherical triangulations*, Pure Math. Appl. 16, 4 (2006), 429–438.
- [97] **D. Roşca**, *Some optimal wavelets with respect to the 1-norm of the compression error*, Proceedings of the 11th Symposium of Mathematics and Applications, Politehnica University of Timișoara, November 2–5, 2006, pp. 235–240.
- [98] **D. Roşca**, *Wavelet bases on the sphere obtained by radial projections*, J. Fourier Anal. Appl. 13, 4 (2007), 421–434.
- [99] **D. Roşca** *Weighted Haar wavelets on the sphere*, Int. J. Wavelets, Multiresolut. Inf. Process. 5, 3 (2007), 501–511.
- [100] **D. Roşca**, *On the solvability of some equations in \mathbb{C}* , Aut. Comput. Appl. Math. 16, 1 (2007), 133–139.
- [101] **D. Roşca**, *Piecewise constant wavelets on triangulations, obtained by 1-3 splitting*, Int. J. Wavelets, Multiresolut. Inf. Process., 6, 2 (2008), 209–222.
- [102] **D. Roşca**, J-P. Antoine, *Constructing orthogonal wavelet bases on the sphere*, 16th European Signal Processing Conference (EUSIPCO 2008), Lausanne, Switzerland, August 25–29, 2008, paper 1569102372, pp. 1–6.
- [103] **D. Roşca**, *A class of orthogonal matrices of dimension four*, Aut. Comput. Appl. Math. 17, 2 (2008), 309–316.
- [104] **D. Roşca**, *Quadrature formulas with equally distributed points on latitudinal points on the sphere*, Electron. Trans. Numer. Anal, 35 (2009), 148–163.

- [105] **D. Roşca**, J-P. Antoine, *Locally supported orthogonal wavelets on the sphere via stereographic projection*, Mathematical Problems in Engineering, vol. 2009 (2009), paper ID: 124904, 1–14.
- [106] **D. Roşca**, *On a norm equivalence in $L^2(S^2)$* , Results Math., 53, 3-4 (2009), 399–405.
- [107] **D. Roşca**, *New uniform grids on the sphere*, Astron. Astrophys., 520, A63 (2010).
- [108] **D. Roşca**, J-P. Antoine, *Constructing wavelet frames and orthogonal wavelet bases on the sphere*, in: Signal Processing, IN-Tech Press 2010, pp. 59-76.
- [109] **D. Roşca**, *Wavelet analysis on some surfaces of revolution via area preserving projection*, Appl. Comput. Harmon. Anal. 30, 2 (2011), 272–282.
- [110] **D. Roşca** *Generalized orthonormal piecewise constant wavelet bases with 1-4 splitting*, Int. J. Wavelets, Multiresolut. Inf. Process. 10, 1 (2012), 1–12.
- [111] **D. Roşca** *Area preserving maps from rectangles to elliptic domains*, Studia Univ. Babeş-Bolyai Math. 56, 2 (2011), 545-549.
- [112] **D. Roşca** *Uniform and refinable grids on elliptic domains and on some surfaces of revolution*, Appl. Math. Comput. 217, 17 (2011), 7812-7817.
- [113] **D. Roşca**, G. Plonka, *Uniform spherical grids via equal area projection from the cube to the sphere*, J. Comput. Appl. Math. 236, 6 (2011), 1033-1041.
- [114] **D. Roşca**, *Introducere în analiza wavelet*, Ed. Mediamira, Cluj-Napoca, 2010.
- [115] **D. Roşca**, *Discrete Mathematics*, Ed. Mediamira, Cluj-Napoca, 2007.
- [116] **D. Roşca**, *Matematici discrete: metode de numărare, probabilități discrete, teoria grafurilor*, Ed. Mediamira, Cluj-Napoca, 2009.
- [117] S. Scodeller, O. Rudjord, F.K. Hansen, D. Marinucci, D. Geller, A. Mayeli, *Introducing Mexican needlets for CMB analysis: Issues for practical applications and comparison with standard needlets*, The Astrophys. J., vol. 733, 12 (2011), 18pp.
- [118] P. Schröder, W. Sweldens, *Spherical wavelets: Efficiently representing functions on the sphere*, in: Computer Graphics Proceedings (SIGGRAPH 1995), 161–175.
- [119] R. Shukla, P.L. Dragotti, M.N. Do, M. Vetterli, *Rate-distortion optimized tree structured compression algorithms for piecewise smooth images*, IEEE Trans. Image Process. 14 (2005), 343–359.
- [120] I. H. Sloan, R. S. Womersley, *Extremal system of points and numerical integration on the sphere*, Adv. Comput. Math. 21, 1-2 (2004), 107–125.
- [121] J.P. Snyder, *Flattening the Earth*, University of Chicago Press, 1990.
- [122] L. Song, A.J. Kimerling, K. Sahr, *Developing an equal area global grid by small circle subdivision*, in Discrete Global Grids, M. Goodchild și A.J. Kimerling, eds., National Center for Geographic Information & Analysis, Santa Barbara, CA, USA, 2002.
- [123] J-L. Starck, E.J. Candès, D.L. Donoho, *The curvelet transform for image denoising*, IEEE Trans. Image Proc. 11 (2002) 670–684.

- [124] J.-L. Starck, M. Elad, D.L. Donoho, *Image decomposition via the combination of sparse representations and a variational approach*, IEEE Trans. Image Process. 14 (2005), 1570–1582.
- [125] J.-L. Starck, Y. Moudden, P. Abrial, M. Nguyen, *Wavelets, ridgelets and curvelets on the sphere*, Astron. Astrophys., 446 (2006) 1191–1204.
- [126] E. Stollnitz, T. DeRose, D. H. Salesin, *Wavelets for computer graphics*, Morgan Kaufmann, San Francisco, 1996.
- [127] G. Szegő, *Orthogonal Polynomials*, vol. 23 of *Amer. Math. Society Colloq. Publ.*, Rhode Island, 1975.
- [128] M. Tegmark, *An icosahedron-based method for pixelizing the celestial sphere*, Astrophys. J. 470 (1996), L81–L84.
- [129] N.A. Teanby, *An icosahedron-based method for even binning of globally distributed remote sensing data*, Comput. Geosci. 32(9) (2006), 1442–1450.
- [130] Y.G. Tian, *Estimations and optimal designs for two-dimensional Haar-wavelet regression models*, Int. J. Wavelets Multiresol. Inf. Proc. 7,3 (2009), 281–297.
- [131] I. Weinreich,(2001). *A construction of C^1 -wavelets on the two-dimensional sphere*, Appl. Comput. Harm. Anal. 10 (2001), 1–26.
- [132] Y. Wiaux, L. Jacques, P. Vandergheynst, *Correspondence principle between spherical and Euclidean wavelets*, Astrophys. J., 632 (2005), 15–28.
- [133] Y. Xu, *Quasi-orthogonal polynomials, quadrature and interpolation*, J. Math. Anal. Appl. 182, 779-799 (1994).
- [134] Y.M. Zhou, *Arrangements of points on the sphere*, PhD thesis, Mathematics, Tampa, FL, 1995.